

**BIOCHEMICAL CHARACTERIZATION  
AND FUNCTIONAL ANALYSIS OF  
PHOSPHOLIPASE D3 (PLD3)**

DISSERTATION

in partial fulfillment of the requirements for the degree “Dr. rer. nat”  
of the Faculty of Mathematics and Natural Sciences  
at the Christian-Albrechts University of Kiel

submitted by  
**ADRIANA GONZALEZ**

Institute of Biochemistry  
Kiel, February 2019





**Referee:** Prof. Dr. Paul Saftig

**Co-referee:** Prof. Dr. Thomas Röder / PD Dr. Markus Damme

**Date of oral presentation:** 16<sup>th</sup> April, 2019

**Approved for publication:** 16<sup>th</sup> April, 2019

Kiel, April 2019



*"It is not joy that makes us grateful, it is gratitude that makes us joyful."*

*-David Steindl-Rast*

*"Enjoy the little things, for one day you may look back  
and realize they were the big things."*

*-Robert Brault*

*This is for you, Mom*

---



---

## TABLE OF CONTENTS

<b>LIST OF ABBREVIATION .....</b>	<b>VI</b>
<b>SUMMARY.....</b>	<b>IX</b>
<b>ZUSAMMENFASSUNG.....</b>	<b>X</b>
<b>1 INTRODUCTION.....</b>	<b>1</b>
1.1 Lysosomes .....	1
1.1.1 Transport of lysosomal membrane proteins.....	2
1.1.2 Transport of soluble lysosomal proteins .....	3
1.1.3 Protein transport pathways to the yeast vacuole.....	6
1.2 The ESCRT pathway .....	7
1.3 Lysosomal degradation of intracellular nucleic acids .....	9
1.4 Phospholipase D family.....	1
1.4.1 Enzymes with PLD activity.....	1
1.4.2 PLD nucleases.....	13
1.4.3 Phospholipase D3 (PLD3).....	13
1.5 Alzheimer's disease .....	14
1.5.1 PLD3 and Alzheimer's disease.....	15
1.6 PLD3 and spinocerebellar ataxia.....	16
1.7 Aim of the study .....	16
<b>2 MATERIAL AND METHODS.....</b>	<b>18</b>
2.1 Material.....	18
2.1.1 Laboratory chemicals .....	18
2.1.2 Frequently used solutions and buffers.....	18
2.1.3 Reagents, solutions, media and buffers .....	19
2.1.4 Cell lines.....	20
2.1.5 Transgenic mouse lines .....	21
2.1.6 Bacterial strains .....	21
2.1.7 Antibodies.....	21
2.1.8 Protein and DNA standards.....	23
2.1.9 Enzymes.....	23
2.1.10 Substrates for lysosomal enzyme activity .....	23
2.1.11 Plasmids.....	24

---

2.1.12	Oligonucleotides .....	25
2.1.13	Equipment .....	28
2.1.14	Software.....	29
2.1.15	Other material.....	29
2.2	Molecular biology methods.....	30
2.2.1	Commercial kits.....	30
2.2.2	Site directed mutagenesis.....	30
2.2.3	Isolation of plasmid DNA (MiniPrep).....	31
2.2.4	Determination of nucleic acid concentration .....	31
2.2.5	Purification of plasmid DNA .....	31
2.2.6	Agarose gel electrophoresis.....	32
2.3	Cell biology methods.....	32
2.3.1	Maintenance of cell lines .....	32
2.3.2	Cryo-preservation of cell lines.....	33
2.3.3	Transient transfection of cells with Polyethylenimine (PEI) .....	33
2.3.4	siRNA transfection .....	33
2.3.5	Generation of stable PLD3 knockout cell line (CRISPR-Cas9).....	34
2.3.6	Isolation of mouse embryonic fibroblast (MEFs).....	35
2.3.7	Coating of culture dishes with Poly-L-Lysine (PLL).....	35
2.3.8	Preparation of primary mix co-culture from mouse hippocampi .....	35
2.3.9	Immunocytochemistry (ICC) .....	37
2.4	Histological methods.....	37
2.4.1	Fluorescence staining of mouse tissue (Immunohistochemistry) .....	37
2.4.2	X-gal-staining of brain sections .....	38
2.5	Protein biochemistry methods.....	38
2.5.1	Generation of cell lysates for protein extraction .....	38
2.5.2	Preparation of tissue homogenates .....	39
2.5.3	Determination of protein concentration with a Bicinchoninic acid (BCA) assay .....	39
2.5.4	Membrane separation .....	40
2.5.5	Co-immunoprecipitation (CO-IP) .....	40
2.5.6	Tandem ubiquitin-binding entities (TUBES).....	41
2.5.7	SDS-polyacrylamide gel electrophoresis (SDS-PAGE).....	42
2.5.8	Western blotting and immunodetection .....	43
2.5.9	Percoll density gradient centrifugation .....	44
2.5.10	Enzymatic deglycosylation.....	45
2.5.11	In vitro measurement of lysosomal hydrolase activity.....	45

---

2.5.12	Nuclease activity assay.....	45
2.6	Animal experimentation.....	46
2.6.1	Animal housing.....	46
2.6.2	Breeding strategies.....	46
2.6.3	Tail or ear biopsy and isolation of genomic DNA.....	48
2.6.4	Genotyping by polymerase chain reaction (PCR).....	48
2.6.5	Mice perfusion for organ extraction and euthanasia.....	49
2.6.6	Behavioral studies.....	50
2.7	Microscopy.....	50
2.7.1	Confocal and fluorescence microscopy.....	50
2.7.2	Electron microscopy.....	50
2.8	Quantification of Western blot bands and immunocytochemistry/immunohistochemistry images.....	51
	Pearson correlation coefficient (PCC).....	51
	Western blot analysis by densitometry.....	51
	Quantification of microglial/astrocytes markers in brain sections.....	51
2.9	Statistical analyses.....	52
<b>3</b>	<b>RESULTS</b> .....	<b>54</b>
3.1	Cellular and biochemical characterization of phospholipase D3 (PLD3).....	54
3.1.1	PLD3 is a lysosomal protein.....	54
3.1.2	Proteolytic processing of PLD3.....	58
3.1.3	Intracellular transport of PLD3.....	69
3.2	Pld3 expression in mouse tissues and characterization of the Pld3 <sup>tm1e</sup> (EUCOMM)Wtsi mouse model.....	85
3.2.1	Pld3 is abundantly expressed in the brain.....	85
3.2.2	Pld3 is mainly expressed in the cortex and hippocampus.....	86
3.2.3	Pld3 is a neuronal protein.....	88
3.2.4	Pld3-deficient mice exert subtle changes in the activity of lysosomal enzymes.....	91
3.2.5	Pld3 deficiency leads to a localized microgliosis in the dentate gyrus (DG).....	92
3.2.6	Pld3 deficient mice show a depression-like behavior.....	98
3.3	Functional analysis of PLD3.....	101
3.3.1	Pld3 deficient mice show subtle alterations in lipid species.....	101
3.3.2	PLD3 is a 5'-exonuclease.....	102
3.3.3	PLD3 is the main 5'-exonuclease in the brain.....	112

---

3.4	Role of PLD3 variants as a genetic risk factor of Alzheimer’s disease development .....	113
3.4.1	Described Pld3 variants in AD patients exhibit different proteolytic processing and nuclease activity .....	114
3.4.2	Characterization of Pld3 deficiency in the 5XFAD Alzheimer’s mouse model .....	117
3.5	PLD3 and spinocerebellar ataxia .....	120
3.5.1	A Pld3 variant linked to spinocerebellar ataxia shows altered proteolytic processing, intracellular localization and nuclease activity .....	120
3.5.2	Pld3-deficient mice show unaltered cerebellar morphology or cerebellar dysfunction .....	125
<b>4</b>	<b>DISCUSSION .....</b>	<b>129</b>
4.1	Biochemical characterization of PLD3 .....	129
4.1.1	PLD3 is a lysosomal protein .....	129
4.1.2	PLD3 is proteolytically processed into a stable soluble form .....	130
4.1.3	ESCRT-dependent delivery of PLD3 to lysosomes .....	134
4.2	<i>In vivo</i> characterization of PLD3 function .....	138
4.2.1	Pld3 is a neuronal protein .....	139
4.2.2	Pld3-deficient mice show a subtle phenotype .....	140
4.2.3	Pld3 is a 5’ exonuclease .....	142
4.2.4	Pld3 is the main 5’ exonuclease in the brain .....	146
4.3	PLD3 and its role in neurodegenerative disorders .....	149
4.3.1	PLD3 and Alzheimer’s disease .....	149
4.3.2	PLD3 and spinocerebellar ataxia .....	150
4.4	Concluding remarks .....	150
<b>5</b>	<b>REFERENCES .....</b>	<b>152</b>
<b>6</b>	<b>SUPPLEMENTARY INFORMATION .....</b>	<b>180</b>
<b>7</b>	<b>LIST OF FIGURES AND TABLES .....</b>	<b>189</b>
7.1	List of figures .....	189
7.2	List of tables .....	192
<b>8</b>	<b>DECLARATION .....</b>	<b>193</b>
<b>9</b>	<b>CURRICULUM VITAE .....</b>	<b>195</b>
<b>10</b>	<b>PUBLICATIONS AND SCIENTIFIC PARTICIPATION .....</b>	<b>196</b>
<b>11</b>	<b>ACKNOWLEDGEMENTS .....</b>	<b>199</b>





---

## LIST OF ABBREVIATIONS

A $\beta$	Amyloid-beta
aa	Amino acids
AD	Alzheimer's disease
ADAM	A desintegrin and metalloprotease
AICD	APP intracellular domain
APP	Amyloid precursor protein
AP	Adaptor protein
APS	Amoniumpersulfate
Bace1	$\beta$ -site APP cleaving enzyme 1
BSA	Bovine serum albumin
CLEAR	Coordinated lysosomal expression and regulation
CMA	Chaperone-mediated autophagy
CNS	Central nervous system
CO-IP	Co-immunoprecipitation
CRISPR	Clustered Regularly Interspaced Palindromic Repeats
CTF	C-terminal fragment
DABCO	1,4-diazabicyclo[2.2.2]octane
DAPI	4',6-diamidino-2-phenylindole
DIV	Days in vitro
DNA	Deoxyribonucleic acid
DMEM	Dulbecco's Modified Eagle's Medium
DMSO	Dimethyl sulfoxide
<i>E. coli</i>	<i>Escherichia coli</i>
EDTA	Ethylenediaminetetraacetic acid
EEA1	Early endosome antigen 1
ER	Endoplasmic reticulum
ESCRT	Endosomal sorting complexes required for transport
FACS	Fluorescence-activated cell sorting
FBS	Fetal bovine serum
fl	Full-length
GAPDH	Glyceraldehyde 3-phosphate dehydrogenase

---

GFP	Green fluorescence protein
GM130	Golgi superfamily A member 2 / cis-Golgi matrix protein
GPI	Glycosylphosphatidylinositol
HBSS	Hank's Balanced Salt Solution
HA	Hemagglutinin
HeLa	Henrietta Lacks (cervical cancer cell line)
KDEL	ER marker
ICC	Immunocytochemistry
Ig	Immunoglobuline
ILV	Intraluminal vesicle
kDa	Kilodalton
KO	Knockout
LAMP-1/-2	Lysosomal-associated membrane glycoprotein-1 /-2
LBPA/BMP	Lyso bis-phosphaditic acid / bis-(monoacylglyceryl)-phosphate
LIMP-1/-2	Lysosomal integral membrane protein-1/-2
LMP	Lysosomal membrane protein
MEF	Mouse embryonic fibroblast
MeOH	Methanol
min	Minutes
mRNA	Messenger ribonucleic acid
mtDNA	Mitochondrial DNA
MVB	Multivesicular body
N2a	Neuro-2a (murine neuroblastoma cell line)
NaCl	Sodium chloride
NaOH	Sodium hydroxide
NeuN	Neuronal nuclei
NP-40	Nonidet P-40
nt	nucleotide
PAGE	Polyacrylamide gel electrophoresis
PB	Phosphate buffer
PBS	Phosphate-buffered saline
PCC	Pearson correlation coefficient
PCR	Polymerase chain reaction

---

PEI	Polyethylenimine
PFA	Paraformaldehyde
PLD	Phospholipase D
PMEL	Premelanosome protein
PNGaseF	Peptide N-glycosidase F
Rab5	Ras-related protein Rab5A
RDA	RNautophagy/DNautophagy
rpm	Revolutions per minute
rRNA	Ribosomal RNA
RT	Room temperature
RNA	Ribonucleic acid
ROS	Reactive oxygen species
s	Seconds
sAPP	Soluble APP
siRNA	Small interference RNA
SCA	Spinocerebellar ataxia
SDS	Sodium dodecyl sulfate
SDS-PAGE	SDS-polyacrylamide gel electrophoresis
SEM	Standard deviation of the mean
SV40	Simian virus 40
siRNA	Small interfering ribonucleic acid
SH-SY5Y	Neuroblastoma cell line
TAE	Tris-acetate-EDTA
TBS	Tris buffered saline
TFEB	Transcription factor EB
TGN	Trans-Golgi network
TMD	Transmembrane domain
Tris	Tris(hydroxymethyl)aminomethane
TUBES	Tandem ubiquitin-binding entities
WES	Whole exome sequencing
WT	Wild type

## SUMMARY

Rare coding variants in the *PLD3* gene coding for Phospholipase D3 were recently identified to increase the risk of developing late onset Alzheimer's disease (LOAD). In order to address in more detail a possible influence of PLD3 on AD development, it was important to perform a fundamental biochemical characterization of PLD3 that provides a better understanding of its potential function. In this project evidence was provided that the type II transmembrane protein PLD3 is transported through the secretory and endocytic route to reach lysosomes. Using a newly described pathway, PLD3 is delivered to lysosomes via the endosomal sorting complex required for transport (ESCRT) machinery. An ubiquitination of PLD3 is required for its sorting into intraluminal vesicles of multivesicular bodies (MVBs). After fusion of MVBs with lysosomes, PLD3 is proteolytically processed into a stable luminal domain, to exert its main enzymatic function in this compartment.

In the course of this project, PLD3 was identified as a lysosomal 5' single-stranded acid exonuclease in immune cells. We could reveal that PLD3 is predominantly expressed in the brain, with highest expression in the hippocampus and the cerebral cortex. It could be further shown that PLD3 is the main 5'-exonuclease in the mouse brain. Almost absent 5' exonuclease activity was observed in the brain lysates of *Pld3* knockout (KO) mice.

*Pld3* KO mice did not show cerebellar dysfunction, suggesting that a previously reported PLD3 mutation is not causative for spinocerebellar ataxia. In *Pld3*-deficient mice, microglia alterations in the dentate gyrus of the hippocampus and the subventricular zone, both sites of adult neurogenesis, and a depression-like behavior were revealed. This suggests an important role of PLD3 in neuronal homeostasis, possibly affecting the onset and course of LOAD. *Pld3* KO mice were bred with the 5xFAD Alzheimer's disease (AD) mouse model. Although *Pld3* was enriched in amyloid plaques (a hallmark of AD), no obvious changes on APP protein levels or cleavage products were observed in 5xFAD *Pld3*<sup>-/-</sup> mice, suggesting a more complex role of PLD3 in the etiology of AD.

## ZUSAMMENFASSUNG

Seltene Varianten im *PLD3*-Gen, welches für die Phospholipase D3 kodiert, wurden kürzlich als Risikofaktor einer spät einsetzenden Alzheimer-Erkrankung ('late onset Alzheimer's disease', LOAD) identifiziert. Um einen möglichen Einfluss von PLD3 auf die Pathogenese des Morbus Alzheimers zu verstehen, war es wichtig, eine grundlegende biochemische Charakterisierung von PLD3 vorzunehmen, die ein besseres Verständnis seiner potenziellen Funktion ermöglicht. In diesem Projekt wurde der Nachweis erbracht, dass das Typ-II-Transmembranprotein PLD3 über den sekretorischen und endozytotischen Weg zu den Lysosomen transportiert wird. PLD3 wird mittels der Transportmaschinerie der ESCRT-Proteine ('endosomal sorting complexes required for transport') an Lysosomen geliefert, ein Transportweg der bislang nur für vakuoläre Proteine in Hefe bekannt war. Für die Sortierung in intraluminale Vesikel innerhalb multivesikulärer Körper ('multivesicular bodies', MVBs) ist eine Ubiquitinierung von PLD3 erforderlich. Nach der Fusion von MVBs mit Lysosomen wird dann proteolytisch die luminaire Domäne von PLD3 abgespalten, welche ihre enzymatische Funktion in den Lysosomen ausübt.

Während dieses Projektes wurde PLD3 als lysosomale saure 5' Exonuklease mit Spezifität für einzelsträngige Nukleinsäuren in Immunzellen identifiziert. Es konnte gezeigt werden, dass PLD3 vorwiegend im Gehirn exprimiert wird, wobei die höchste Expression im Hippokampus und in der Großhirnrinde nachweisbar ist. Weiterhin wurde der Nachweis erbracht, dass Pld3 die primäre 5'-Exonuklease im Gehirn von Mäusen ist. In Gehirnlisaten von Pld3-Knockout (KO) -Mäusen wurde nur geringe 5'-Exonuklease-Aktivität beobachtet.

Pld3-KO-Mäuse zeigten keine cerebelläre Dysfunktion, was darauf hindeutet, dass eine zuvor beschriebene PLD3-Mutation nicht ursächlich für eine spinocerebelläre Ataxie ist. In Pld3 KO-Mäusen zeigten sich neben einem Depressions-ähnlichem Verhalten, Mikroglia-Veränderungen im Gyrus dentatus des Hippocampus und der subventrikulären Zone, beides Bereiche der adulten Neurogenese. Dies lässt auf eine wichtige Rolle von PLD3 bei der neuronalen Homöostase schließen, was möglicherweise den Beginn und den Verlauf der LOAD beeinflusst. Pld3-KO-Mäuse wurden mit dem

5xFAD Alzheimer-Mausmodell gekreuzt. Obwohl Pld3 in Amyloid-Plaques angereichert war, wurden bei 5xFAD Pld3<sup>-/-</sup> Mäusen keine offensichtlichen Änderungen der APP-Protein-Spiegel oder APP proteolytischen Spaltprodukte beobachtet, was auf eine komplexere Rolle von PLD3 in der Ätiologie der Alzheimer Erkrankung hindeutet.





---

## 1 INTRODUCTION

### 1.1 Lysosomes

Lysosomes were first described in 1955 by Christian de Duve. These ubiquitous organelles are considered the cell's degradation center primarily responsible for the breakdown of various macromolecules (Bainton, 1981; Barrett, 1980; De Duve et al., 1955; Wartosch et al., 2015). Lysosomes mediate the degradation of extracellular substrates obtained through endocytosis and phagocytosis and of intracellular components from autophagy (Bonifacino, 2004; Dell'Angelica et al., 2000). The digestion of the macromolecules occurs in the lumen of lysosomes, catalyzed by a cocktail of more than 50 hydrolytic enzymes with characteristic acidic pH-optima (Saftig and Klumperman, 2009; Winchester, 2001). The lysosomal membrane separates this potent catalytic activity from the cytosol (Lübke et al., 2009). Around 25 lysosomal membrane proteins (LMPs) have been extensively characterized. However, proteomics analyses have identified around 300 lysosomal membrane candidates which might be involved in lysosomal function (Callahan et al., 2009; Chapel et al., 2013; Schröder et al., 2007). Although lysosomes are considered the digestive system of the cell, increasing evidence suggest that LMPs play essential roles in a number of cellular events linked to processes occurring along the endocytic and biosynthetic pathways, ranging from autophagy, phagocytosis, plasma membrane repair, pathogen defense and cell signaling (Saftig and Klumperman, 2009; Schwake et al., 2013). Moreover, proper transport and delivery of lysosomal hydrolases and lysosomal membrane proteins is pivotal to regulate lysosomal distribution and size, ion homeostasis, membrane potential, catabolite export and sensing nutrient availability (Xu and Ren, 2015).

Newly synthesized lysosomal hydrolases and lysosomal membrane proteins are transported throughout the secretory and endocytic pathway following specific and regulated pathways. Defects in degradation, export or trafficking results in lysosomal dysfunction underlying the pathogenesis of many lysosomal storage disorders (LSDs) and other metabolic disorders (Shen et al., 2012; Slaugenhaupt, 2002; Stauber and Jentsch, 2013).

### 1.1.1 *Transport of lysosomal membrane proteins*

The great majority of lysosomal membrane proteins (LMPs) are highly glycosylated. This post-translational modification is important to preserve their own stability and the integrity of the lysosome (Schwake et al., 2013). The lysosomal associated membrane proteins LAMP-1 and LAMP-2 are heavily glycosylated at their luminal domain, containing 19 and 16 potential *N*-glycosylation sites, respectively (Carlsson et al., 1988; Chen et al., 1988; Fukuda et al., 1988). These glycoproteins represent ~50 % of all proteins of the lysosomal membrane (Marsh et al., 1987). Two major pathways have been described for the transport of LMPs to lysosomes, referred as the “direct” and the “indirect” pathway (Figure 1A). After synthesis in the endoplasmic reticulum (ER), LMPs can follow the constitutive “indirect” transport from the trans Golgi network (TGN) to the plasma membrane, followed by internalization into early endosomes (EE) and further delivery to late endosomes and lysosomes (Braulke and Bonifacino, 2009; Janvier and Bonifacino, 2005). Alternatively, in the “direct” pathway LMPs can be transported directly from the TGN to either early or late endosomes to finally reach lysosomes (Carlsson and Fukuda, 1992; Harter and Mellman, 1992).

Both sorting pathways are mediated by the specific interaction of cytosolic adaptor protein complexes that recognize peptide motifs in the cytosolic domain of transmembrane proteins. Two major sorting signals consisting of short, linear arrays of amino acid residues have been described (Bonifacino and Traub, 2003). Tyrosine-based sorting signals, formed by the NPXY or YXXØ consensus motifs (where Ø correspond to any amino acid), are recognized by the heterotetrameric adaptor protein (AP) complexes AP-1, AP-2, AP-3 and AP-4. On the other hand, dileucine-based sorting signals, formed by the [DE]XXXL[LI] or DXXLL consensus motifs, are recognized by another family of adaptors known as Golgi-localized, gamma-ear containing, ADP-ribosylation factor binding proteins (GGAs) (Braulke and Bonifacino, 2009).

Depending on the cargo protein, sorting of LMPs is initiated by its interaction with AP-1/AP-3 with clathrin or GGA-clathrin complexes. This facilitates the exit of the complex from the TGN to the plasma membrane or directly to early or late endosomes (Figure 1A) (Janvier and Bonifacino, 2005). The contribution of each transport pathway depends on the cell type (Peden et al., 2004), the type of cargo protein and its expression level

---

(Carlsson and Fukuda, 1992; Groux-Degroote et al., 2008; Janvier and Bonifacino, 2005) and the cellular conditions.

Members of the LAMP family, as well as members of the lysosomal integral membrane proteins (LIMPs), are typical examples of LMPs transported via the direct pathway through the interaction of AP/clathrin complexes (Harter and Mellman, 1992; Lippincott-Schwartz and Fambrough, 1987). However, transport of these proteins via the indirect pathway has been reported as a salvage route for a small population of molecules that are not correctly sorted from the TGN to endosomes (Harter and Mellman, 1992). On the other hand, transport of the lysosomal acid phosphatase (LAP), is a well-described example of proteins sorted via the indirect pathway (Braun et al., 1989). LAP is transported from the TGN to the cell surface, followed by several cycles of endocytosis and recycling, dependent on AP-2 (Obermüller et al., 2002; Peters et al., 1990). In each cycle, LAP is sorted to lysosomes where proteolytic processing releases a soluble form (Peters et al., 1990).

A very different mechanism of sorting to lysosomes has been reported for the lysosomal transmembrane protein LPTM5. This protein contains three L/PPXY motifs that bind the ubiquitin ligase Nedd4 and GGA-3, both acting as lysosomal targeting adaptors (Pak et al., 2006).

### **1.1.2 *Transport of soluble lysosomal proteins***

Lysosomes are composed of several acid hydrolases responsible for the breakdown of proteins, polysaccharides, complex lipids, nucleic acids, etc., into their respective building blocks: amino acids (AAs), monosaccharides, free fatty acids and nucleotides (Huotari and Helenius, 2011; Luzio et al., 2007). The well characterized mannose 6-phosphate receptor (M6PR) pathway mediates the transport of most lysosomal hydrolases. However, alternative M6PR-independent pathways have been described (Figure 1B).

Once in late endosomes/lysosomes, several hydrolases undergo proteolytic processing dependent on the presence of lysosomal endopeptidases. For some hydrolases this proteolytic cleavage is associated with conversion to active and stable forms. However, for many hydrolases, processing does not affect their hydrolytic activity (Ishidoh and Kominami, 2002; Roberts, 2005).

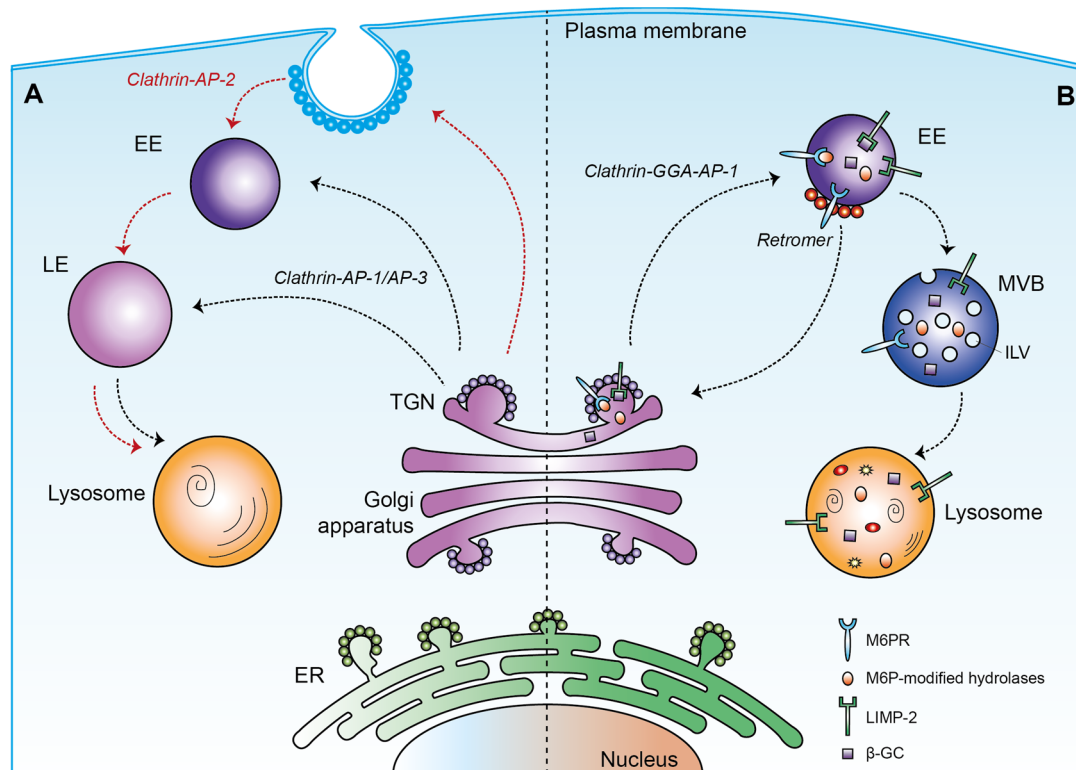


**Figure 1 | Schematic representation of lysosomal protein sorting pathways.** *A*, lysosomal membrane proteins (LMPs) can be sorted to lysosomes via a “direct” (black arrows) or “indirect” (red arrows) pathway. In the “direct” pathway, proteins are directly transported from the trans Golgi network (TGN) to early (EE) or late (LE) endosomes in a clathrin/AP-1/AP-2-dependent manner. In the “indirect” pathway, LMPs are first transported to the plasma membrane, followed by clathrin/AP-2-dependent endocytosis and further sorting to late endosomes/lysosomes. *B*, lysosomal hydrolases can be transported via the mannose 6-phosphate receptor (M6PR) –dependent or –independent pathway. In the first pathway, mannose 6-phosphate (M6P)-modified hydrolases are recognized by the M6PR in the TGN and transported to EE via clathrin-GGA-AP-1-containing vesicles. Invagination of the limiting membrane of endosomes leads to the formation of multivesicular bodies (MVBs) containing intraluminal vesicles (ILVs). Due to the acidic pH of lysosomes (~4.5-5), M6P-modified hydrolases are released in the lumen of lysosomes and M6PR are recycled back for further rounds of transport. Transport of  $\beta$ -glucocerebrosidase ( $\beta$ -GC) is a typical example of a M6PR-independent pathway. In the TGN,  $\beta$ -GC is recognized by its receptor (LIMP-2) following a similar route along the endocytic pathway to reach lysosomes. In contrast to M6PRs, LIMP-2 ends up as a component of the limiting membrane of lysosomes, following the described “direct” pathway of LMPs.

### 1.1.2.1 Mannose 6-phosphate receptor-dependent transport

Soluble lysosomal proteins are synthesized in the ER as precursor polypeptides. In this compartment, asparagine (Asn)-linked oligosaccharides (*N*-glycosylation) undergo extensive processing necessary for protein folding, oligomerization, quality control, sorting and transport (Helenius and Aebi, 2001; Ruddock and Molinari, 2006). Upon arrival in the Golgi, oligosaccharide chains of lysosomal enzymes are either trimmed and modified resulting in complex-type sugars, or selected mannose residues are modified with phosphate groups (Braulke and Bonifacino, 2009). The attached mannose 6-

phosphate (M6P) tag is catalyzed by the sequential action of two enzymes: (1) *N*-acetylglucosaminyl-1-phosphotransferase (GlcNac-1-phosphotransferase), which transfers GlcNac-1-phosphate to hydroxyl groups of mannose residues (Lazzarino and Gabel, 1989), and (2) *N*-acetylglucosamine-1-phosphodiesterase  $\alpha$  *N*-acetylglucosaminidase (known as “uncovering” enzyme, UCE), which removes a covering *N*-acetylglucosamine (GlcNac) from the M6P recognition marker on lysosomal hydrolases (Kornfeld et al., 1999; Rohrer and Kornfeld, 2001). The M6P residues of lysosomal enzymes are then recognized by ubiquitously expressed M6P-receptors (M6PR) in the TGN (Figure 1B) (Kornfeld and Mellman, 1989; von Figura and Hasilik, 1986). After endosome-mediated transport of the M6PR-ligand complex, due to the low pH in these organelles (<5.5), the complex dissociates and hydrolases are released into the endosomal lumen (van Meel and Klumperman, 2008). MPRs recycle to the TGN for further rounds of transport. Several proteins are decorated with M6P residues, but no lysosomal function or localization has been assigned, making them candidates for lysosomal storage diseases of unknown etiology (Della Valle et al., 2006; Sleat et al., 2006).

#### 1.1.2.2 *Mannose-6-phosphate receptor-independent transport*

Patients with I-cell disease (mucopolipidosis type II) are defective in GlcNac-1-phosphotransferase, thus some lysosomal hydrolases do not acquire M6P tags (Hasilik et al., 1981; Waheed et al., 1982). Nevertheless, analysis of I-cell diseased cells, such as hepatocytes, Kupffer cells and lymphocytes, and tissues of these patients showed normal lysosomal enzyme levels in many organs. Similar observations were observed in GlcNac phosphotransferase-knockout mice and mice deficient of both MPRs (Dittmer et al., 1999; S. Kornfeld, 2001). Increasing number of studies have reported different M6P-independent transport routes of lysosomal proteins, as well as the identification of alternative receptors to lysosomes (Braulke and Bonifacino, 2009). An example of such receptor is sortilin, which mediates lysosomal trafficking of prosaposin and acid sphingomyelinase (Körner et al., 1994; Rosorius et al., 1993). Another M6PR-independent pathway is the sorting of  $\beta$ -glucocerebrosidase ( $\beta$ -GC). Its transport to lysosomes is dependent on the direct interaction with the integral membrane protein LIMP-2 (Figure 1B) (Reczek et al., 2007).

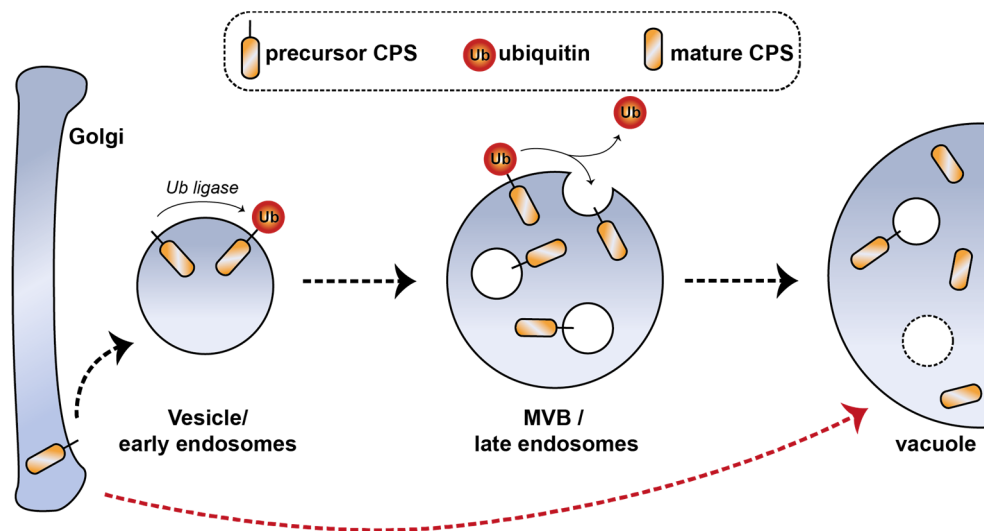
### 1.1.3 Protein transport pathways to the yeast vacuole

*S. cerevisiae* is one of the most studied and best characterized yeast species, sharing a complex intracellular organization with higher eukaryotes. Proteins synthesized in the Golgi apparatus are either sorted to the plasma membrane, secreted or targeted to the vacuole (the yeast equivalent of the lysosome) (Bonifacino and Glick, 2004; Feyder et al., 2015; Novick et al., 1981). Protein sorting to the vacuole can occur via endosomes (vacuolar sorting pathway or CPY pathway) or directly (alkaline phosphatase or ALP pathway). Specific sorting to the vacuoles via the ALP pathway requires the function of the AP-3 adaptor protein (Cowles et al., 1997; Stepp et al., 1997). AP-3 binds to an acidic di-leucine sorting signal found in the cytoplasmic tail of the cargo proteins (Darsow et al., 1998; Honing et al., 1998) and directs these cargoes into Golgi-derived vesicles that are then transported to the vacuole (Rehling et al., 1999). The CPY pathway transports different vacuolar proteins, either membrane-bound as the CPS (carboxypeptidase S) or soluble as the CPY (carboxypeptidase Y) pro-protease (Feyder et al., 2015).

CPS- and CPY-containing vesicles are transported to endosomes where they fuse and liberate CPS to the endosomal membrane and CPY into the lumen (Bonifacino and Glick, 2004; Novick et al., 1981). CPS transport to vacuoles (Figure 2) requires ubiquitination as a sorting signal for the ESCRT (endosomal sorting complexes required for transport) machinery (see section 1.2), which will cluster CPS into invaginated endosomal membranes and pinching off vesicles for the formation of multivesicular bodies (MVBs). Fusion of the MVBs with the vacuole releases their content. This process is dependent on the phosphatidylinositol(3)-P 5-kinase activity of the Fab1p, highlighting the significant role of phosphoinositides in the regulation of protein trafficking (Odorizzi et al., 1998; Reggiori and Pelham, 2001). An equivalent for the CPS pathway in mammals has yet not been identified.

---

▼ **Figure 2 | Schematic representation of carboxypeptidase S (CPS) biogenesis.** In yeast, protein vacuolar sorting from the Golgi can occur via endosomes (CPY pathway) or directly to the vacuole (ALP pathway, red arrow). An example of the CPY pathway (black arrows) is the transport of the carboxypeptidase S (CPS) protein. In early endosomes, precursor CPS is ubiquitinated for sorting transport into multivesicular bodies (MVBs). Fusion of MVBs with the vacuole releases a mature form of CPS into the lumen of the vacuole.



## 1.2 The ESCRT pathway

The endosomal sorting complexes required for transport (ESCRT) assemble into a multisubunit machinery that performs a topologically unique membrane bending and scission reaction away of the cytoplasm, leading to the biogenesis of multivesicular bodies (MVBs) (Figure 3) (Gruenberg and Stenmark, 2004; Hurley, 2008; Piper and Katzmann, 2007; Wollert et al., 2009). MVBs are formed at early endosomes by the inward budding of the limiting membrane into the lumen. The resulting intraluminal vesicles (ILVs) can carry cytoplasmic proteins in temporary storage or serve as a device to deliver the entire protein to the lysosomes for degradation (Piper and Katzmann, 2007).

The ESCRT machinery consists of five protein complexes ESCRT-0, ESCRT-I, ESCRT-II, ESCRT-III and Vps4-Vta1 (Hurley, 2008; Saksena et al., 2009; Williams and Urbé, 2007). ESCRT-0, ESCRT-I, ESCRT-II and Vps4-Vta1 are soluble complexes that cycle between cytosolic and membrane-bound states. By contrast, the subunits of ESCRT-III are soluble monomers that assemble in membranes into tightly bound filaments, tubes and spirals that can only be released by the ATP-dependent action of Vps4-Vta1 (Ghazi-Tabatabai et al., 2008; Hanson et al., 2008; Lata et al., 2008; Wollert et al., 2009a).

Ubiquitination is the molecular signal that designates cargo for the ESCRT pathway for lysosomal degradation. The ESCRT proteins interact with ubiquitinated receptors and other ubiquitinated cargo through various motifs, including the ubiquitin interacting motif (UIM) and the double-sided ubiquitin-interacting motif (DUIM) of the yeast and

human Hrs subunits of ESCRT-0 (Hurley, 2008; Williams and Urbé, 2007). The complexes of the ESCRT machinery were first characterized in yeast through the analysis of vacuolar protein sorting (*vps*) mutants which could no longer transport proteins to the vacuoles (Wollert et al., 2009a). Biochemical characterization of these mutants first resulted in the identification of ESCRT-I complex (Katzmann et al., 2001) and subsequently defined the ESCRT-II and ESCRT-III complexes (Babst et al., 2002a; Babst et al., 2002b). These studies were preceded by the identification of the AAA (ATPase associated with various cellular activities) ATPase Vps4 in 1997, which disassembles the ESCRT complexes from endosomes for delivery of cargo to the vacuoles/MVBs and recycles them back to the cytoplasm to maintain the function of the MVB pathway (Figure 3) (Hurley, 2008; Stuchell-Brereton et al., 2007).

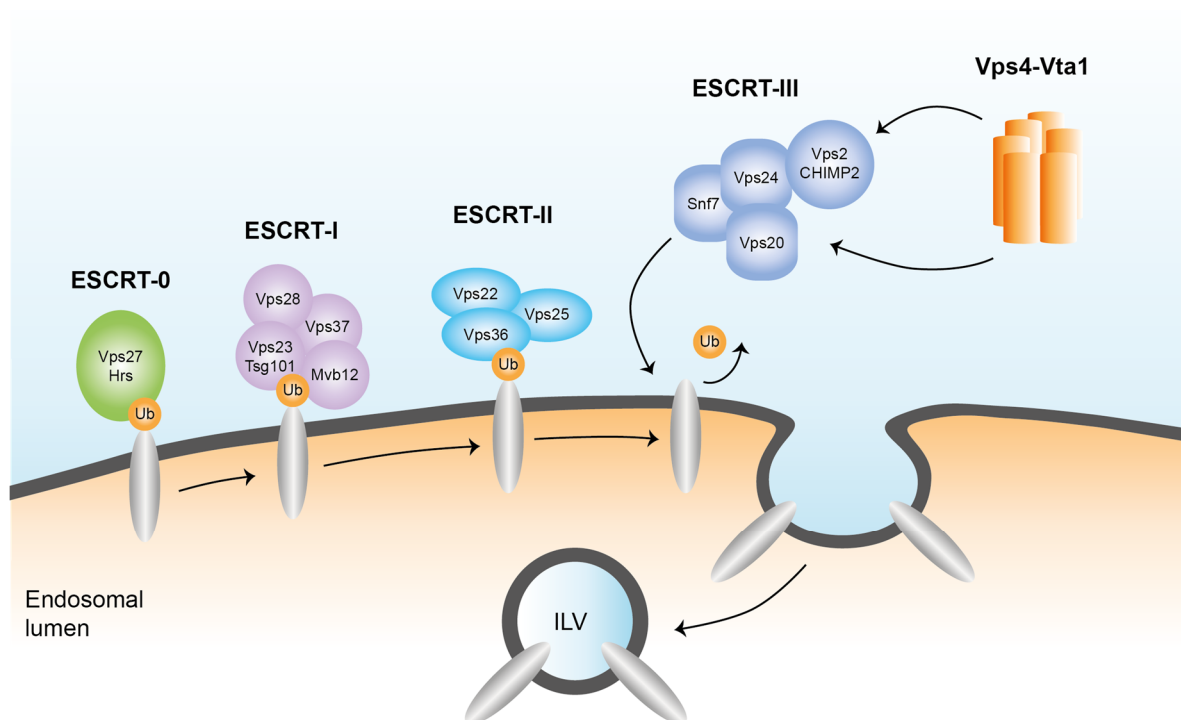


**Figure 3 | Scheme of ubiquitin-dependent sorting of proteins by the ESCRT machinery.** The different ESCRT complexes are sequentially recruited at the limiting membrane of endosomes for the recognition and sorting of ubiquitin-modified transmembrane proteins (gray oval). The Vps4-Vta1 complex is responsible for the disassembly of the ESCRT complexes and further delivery of ubiquitinated cargo to intraluminal vesicles (ILVs). Modified from Vingtdoux et al., 2012.



### 1.3 Lysosomal degradation of intracellular nucleic acids

A variety of cellular components are delivered to lysosomes or the vacuole for the hydrolysis of macromolecules (Fujiwara et al., 2017). This process of “self-eating” is called autophagy, a regulated process that involves the formation of an autophagosome that captures random or selective targets for degradation. Fusion of the autophagosome with lysosomes leads to proteolytic degradation of engulfed substrates by lysosomal enzymes (Axe et al., 2008; Mizushima, 2007; Saftig et al., 2008). Despite the diversity of hydrolases observed within the lysosome, studies on selective autophagy have been mainly focused on its protein-targeting machineries and less attention has been devoted to the degradation of other macromolecules such as nucleic acids (Dice, 2007; Johansen and Lamark, 2011; Sahu et al., 2011). Three kinds of autophagy have been described: macroautophagy, microautophagy and chaperone-mediated autophagy (CMA). In macroautophagy, cytosolic components are sequestered by autophagosomes and delivered to lysosomes by membrane fusion. In microautophagy, substrates are entrapped in lysosomes by invagination of the lysosomal membrane. Conversely, CMA is a highly selective form of autophagy where specific cytosolic proteins containing a KFERQ-like motif are unfolded by a chaperone complex and directly imported into lysosomes via a lysosomal membrane receptor, LAMP2A (Mizushima and Komatsu, 2011).

DNA and RNA can be selectively delivered to lysosomes/vacuoles as a component of larger structures such as ribosomes, mitochondria, a portion of the nucleus and RNA granules (Figure 4) (Fujiwara et al., 2017). Approximately 80 % of total RNA in living cells is ribosomal RNA (rRNA, Warner, 1999). Kraft et al. proposed a selective degradation of ribosomes by macroautophagy which they termed “ribophagy” (Kraft et al., 2008). Later, NUFIP1 (nuclear fragile X mental retardation-interacting protein 1) was identified as a receptor for the selective autophagy of ribosomes (Wyant et al., 2018). Another pathway of DNA delivery to lysosomes is a process called “mitophagy”. As a consequence of ATP production, mitochondria generate large amounts of reactive oxygen species (ROS) as byproducts (Loschen et al., 1971). As a result, mitochondrial DNA (mtDNA) is frequently exposed to ROS, leading to higher DNA damage, thus elimination of damaged mitochondria is critical for cell survival (Yakes and Van Houten, 1997).

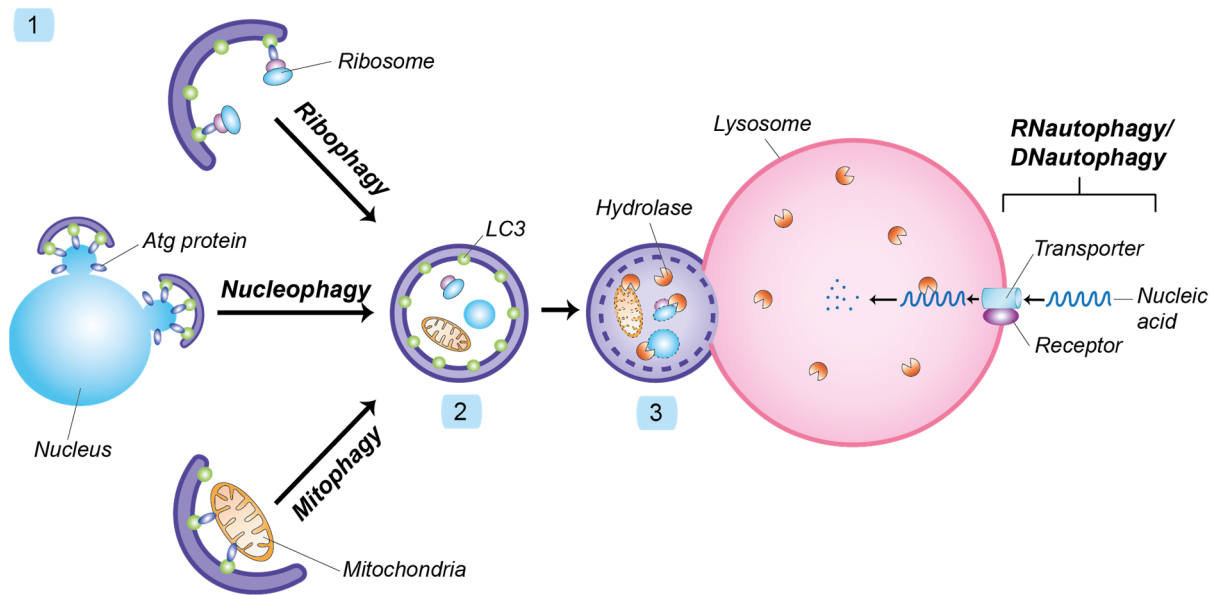


**Figure 4 | Schematic diagram of selective delivery of DNA and RNA to lysosomes.** DNA and RNA can be delivered to lysosomes as a component of larger structures such as ribosomes (*ribophagy*), mitochondria (*mitophagy*) and a portion of the nucleus (*nucleophagy*). (1) Stress conditions and damage of cellular components activates the formation of the phagophore. Vesicle nucleation and expansion of the phagophore requires the recruitment of the LC3 (the microtubule-associated protein light chain 3) and Atg (autophagy-related protein), important for the recognition of the autophagic cargos. The resulting autophagosome (2) fuses with lysosomal compartments, forming the autolysosome (3). In *RNautophagy/DNautophagy*, nucleic acids are directly transported into the lumen of the lysosome via the interaction with receptor proteins and transporters. In all described processes, the autophagic cargo is degraded by lysosomal acidic hydrolases.

Similar to ribosomes and mitochondria, the existence of macroautophagy in selective degradation of the nucleus, or “nucleophagy” has been described (Ivanov et al., 2013).

In addition to the canonical types of autophagy, a type of autophagy that directly delivers RNA and DNA into lysosomes, processes termed “RNautophagy” and “DNautophagy”, respectively, has been tentatively described (abbreviated as RDA) (Figure 4) (Fujiwara et al., 2013b, 2013a). Both pathways are ATP-dependent and the lysosomal membrane protein LAMP2C may serve as a receptor, directly binding to nucleic acids. Additionally, the same group found that SIDT2, a putative nucleic acid transporter, mediates direct uptake of RNA and DNA by lysosomes (Aizawa et al., 2016a; Aizawa et al., 2016b).

After translocation to the lysosomal lumen, autophagic substrates undergo degradation by catabolic enzymes. RNase T2 and DNase II are well-characterized lysosomal RNases and DNases, respectively (Fujiwara et al., 2017). RNase T2 is an endonuclease that cleaves single-stranded RNA into mono- or oligo-nucleotides with generally little sequence specificity (Deshpande and Shankar, 2002). DNase II is an endonuclease that cleaves

double-stranded DNA with low sequence specificity (Evans and Aguilera, 2003). Turnover of DNA and RNA molecules produces nucleotides that are further catabolized to nucleosides as catabolic end-products. Recycling of nucleosides is important for the 'salvage' pathway, required for the synthesis of new nucleic acids (Möhlmann et al., 2010). In human and mouse, ENT3 (equilibrative nucleoside transporter 3) protein promotes the export of nucleosides from the lysosomal lumen (Baldwin et al., 2005).

## 1.4 Phospholipase D family

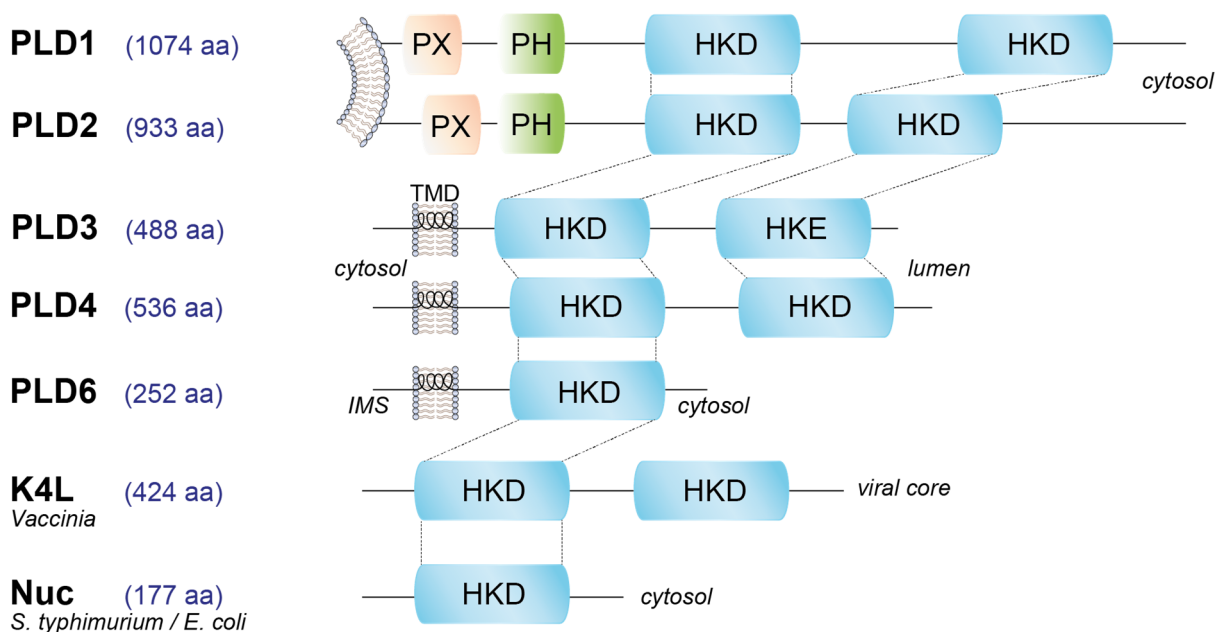
The phospholipase D (PLD) lipid-signaling enzyme superfamily has long been studied for its role in cell communication and a wide range of cell biological processes. The most commonly studied PLD activity entails hydrolysis of phosphatidylcholine (PC), the most abundant membrane phospholipid, to yield choline and the second messenger signal lipid phosphatidic acid (PA) (Peng and Frohman, 2012). However, other members of this family, like the *Vaccinia* virus protein KL4, can function as endonucleases (Huang et al., 2011; Voigt et al., 2012). A large subset of enzymes with PLD activity share a conserved HxKxxxDx6GSxN motif (HKD), or a variation thereof, which is involved in mediating catalytic activity (Figure 5) (Koonin, 1996; Ponting and Kerr, 1996). HKD enzymes sharing this conserved catalytic domain have a similar structural core that contributes to the hydrolysis of phosphodiester bonds with a similar reaction mechanism for a range of substrates (Liscovitch et al., 2000; Selvy et al., 2011).

### 1.4.1 Enzymes with PLD activity

PLD family members are found in organisms ranging from viruses to bacteria, yeast, plants and animals (Jenkins and Frohman, 2005). In mammals, PLD1 and PLD2, two isoforms attached to the cytosolic leaflet of the membranes via palmitoyl anchors (Figure 5), are responsible for the PC-hydrolyzing activity described above (Peng and Frohman, 2012). PLD1 and PLD2, which are 50 % identical in protein sequence and have almost the same protein domain organization, are widely expressed in different tissues and cell types that are activated by a variety of signaling molecules (Colley et al., 1997; Du et al., 2000; Jenkins and Frohman, 2005). The two HKD motifs are essential for PLD enzymatic activity (Sung et al., 1997), while the other consensus domains like the phox sequence

(PX) and the pleckstrin homology (PH) domain (Figure 5) are lipid binding domains that regulate PLD subcellular localization (Du et al., 2003; Jang et al., 2012). PLD1 and PLD2 modulate many cell signaling-driven processes, such as regulated exocytosis, endocytosis, Golgi-ER trafficking, proliferation, cell migration, autophagy and apoptosis (Brown et al., 1998; Hughes and Parker, 2001; Nelson and Frohman, 2015). PLD1 and PLD2 polymorphisms, as well as upregulated activity levels, have been linked to development of cancer, cardiovascular, neurodegenerative and infectious diseases, making these proteins of high interest as therapeutic targets (Frohman, 2015).

Several viral and bacterial proteins are known to exert PLD activity. They are involved in a range of different processes including bacterial invasion, survival enhancement, host cell invasion and increased infectivity (Selvy et al., 2011). For example, a protein of the *Vaccinia* virus, named p37, is known to have lipase activity and PC specificity. This enzymatic activity is important to facilitate viral trafficking to the host cell plasma membrane and release at the extracellular enveloped virus (EEV) (Eckert et al., 2005; Hiller et al., 1981). *Yersinia pestis*, an enteric Gram-negative bacterium, encodes in its genome the cytosolic protein Ymt which belongs to the PLD superfamily and consist of two HKD motifs (Ponting and Kerr, 1996). *In vitro* characterization of this enzyme revealed its capability of hydrolyzing PC, phosphatidylethanolamine (PE) and other phospholipids (Rudolph et al., 1999).



---

**▲ Figure 5 | Domain alignment of different PLD superfamily enzymes.** The HKD motifs responsible of the PLD catalytic activity are conserved among different family members and species. PLD1 and PLD2 are attached to the membrane via palmitoyl anchors. PLD3, PLD4 and PLD6 contain a transmembrane domain, although with different topology. K4L is found in the viral core, while Nuc is localized in the cytosol of bacteria. aa, amino acid; PX, phox sequence, PH, pleckstrin sequence; TMD, transmembrane domain; IMS, mitochondrial intermembrane space.

---

### 1.4.2 *PLD nucleases*

Several proteins that do not act as phospholipases belong to the PLD family because they contain one or two HKD motifs (Figure 5). PLD6, also named MitoPLD, functions as an endonuclease (via phosphodiesterase action) to generate microRNAs (miRs) known as piwi-interacting RNAs, which are critical during spermatogenesis (Huang et al., 2011; Voigt et al., 2012). The genome of the *Vaccinia* virus also encodes a protein named K4L, containing two HKD motifs (Figure 5). K4L was reported to exhibit nuclease and viral DNA condensation function (Eckert et al., 2005). Subsequently, the K4L gene product was also determined to be the previously described nick-joining enzyme (DeMasi et al., 2001; Reddy and Bauer, 1989). The plasmid DNA of *Salmonella typhimurium* and *Escherichia coli* encodes a protein called Nuc, an ATP-independent, non-specific endonuclease. Crystal structure studies revealed that Nuc contains one HKD motif that forms a homodimer (Figure 5) (Stuckey and Dixon, 1999). Nuc endonucleases non-specifically hydrolyzes internal phosphodiester bonds within the backbone of single and double-stranded duplex DNA and RNA (*in vitro* and *in vivo*) in the bacterial periplasm during DNA conjugation (Winans and Walker, 1983).

### 1.4.3 *Phospholipase D3 (PLD3)*

The mammalian enzyme PLD3 is another member of the PLD family. The human *PLD3* gene is localized in the long arm (q) of chromosome 19 at position 13.2 (19q13.2), and it is expressed as a 488 amino acid protein. PLD3, also known as Hu-K4, has a type II transmembrane protein orientation with a short N-terminal tail of 38 amino acids exposed to the cytosol, and a large C-terminus with multiple predicted glycosylation sites (Munck et al., 2005). The C-terminus contains two HxKxxxD/E motifs, where the aspartate of one motif is mutated to glutamate (Figure 5).

PLD3 was first identified as a human homolog of the K4L protein of *Vaccinia* virus mentioned before, sharing a significant sequence homology (48 %). Yet, K4L is a nonessential protein in the life cycle of the virus and its viral function remains unclear. On the other hand p37, encoded by the same virus, shares 25 – 30 % of homology with PLD3, being p37 the closest relative with known function (Cao et al., 1997). The conservation of the HKD motifs and the high similarity between PLD3 and the proteins K4L and p37 suggests that these viral proteins have evolved from one or more eukaryotic genes that were involved in similar cellular processes (Cao et al., 1997). However, the closest homologues of PLD3 are found in other mammals, where the murine protein (denoted as SAM9) has 93 % identical amino acid residues. More distantly related proteins are found in *Xenopus* (54 %) and *Drosophila* (48 %).

The mechanism of action or any type of catalytic activity exerted by PLD3 are unknown. Initial studies have suggested that PLD3 is localized to the ER and the secretory pathway (Munck et al., 2005). However, PLD3 was identified as a direct target of the CLEAR (Coordinated Lysosomal Expression and Regulation) gene network, together with a partial overlapping localization of PLD3 with lysosomes in HeLa cells (Palmieri et al., 2011). Moreover, PLD3 was identified as a glycoprotein that may contain mannose 6-phosphate (M6P) as a target for lysosomal delivery (Sleat et al., 2013). PLD3 has been also reported in granules in an insulin pancreatic  $\beta$ -cell line (Brunner et al., 2007). Additionally, PLD3 was shown to play a role in myogenesis during myotube formation, potentially in the events involving ER reorganization (Osisami et al., 2012).

## 1.5 Alzheimer's disease

Alzheimer's disease (AD) is a chronic progressive neurodegenerative disease and represents the most common form of age-related dementia (Bertram and Tanzi, 2005). Genetically, the disease is divided into familial cases and sporadic cases. The familial form (~5 % of total AD cases) is due to mutations in three major genes: amyloid precursor protein (APP), presenilin 1 (PSEN1) and presenilin 2 (PSEN2) (Bekris et al., 2010; Varvel et al., 2008). In contrast, many genetic and environmental factors may contribute to determining the sporadic AD cases (Piaceri et al., 2013). Dementia in AD is characterized by progressive neurodegeneration of the central nervous system that eventually leads to gradual decline of cognitive functions (DeKosky and Scheff, 1990; DeKosky et al., 1996).

This is accompanied by the extracellular accumulation of amyloid- $\beta$  ( $A\beta$ ) deposits and intracellular aggregation of neurofibrillary tangles in the brain (Bertram and Tanzi, 2005). Accumulation of  $A\beta$  peptide, which is derived from proteolysis of the amyloid precursor protein (APP), is the result of an imbalance between the levels of  $A\beta$  production, aggregation and clearance (Crews and Masliah, 2010). APP is proteolytically processed at several different subcellular sites (Chow et al., 2010; Weidemann et al., 1989). Three major proteases, termed  $\alpha$ -,  $\beta$ - and  $\gamma$ -secretase, are involved in these processing steps, which give rise to two independent pathways, the non-amyloidogenic and the amyloidogenic pathway (Haass, 2004). In the first pathway, sequential cleavage of  $\alpha$ - and  $\gamma$ -secretase, release a soluble sAPP $\alpha$  fragment and a short P3 peptide, shown to have synaptotrophic and neuroprotective functions (Nikolaev et al., 2009; Turner et al., 2003). In the amyloidogenic pathway, sequential cleavage of  $\beta$ - and  $\gamma$ -secretase, generate a soluble sAPP $\beta$  ectodomain and the  $A\beta$  peptide (Müller and Zheng, 2012). Both pathways also lead to the generation of an APP intracellular domain (AICD) which is released into the cytosol and it may function in intracellular signaling (Cao and Südhof, 2001; von Rotz et al., 2004).  $A\beta$  is then liberated and found in intracellular fluids such as plasma and cerebrospinal fluid (Seubert et al., 1992). APP is transported throughout the constitutive secretory pathway. Once it reaches the plasma membrane (PM), it is rapidly internalized and subsequently trafficked to endocytic and recycling organelles, transported back to the PM or retrogradely to the TGN. A small fraction is also degraded in lysosomes (Haass et al., 2012).

### 1.5.1 *PLD3 and Alzheimer's disease*

PLD3 is highly expressed in the brain, including mature neurons of the forebrain, hippocampus and cortex (Cruchaga et al., 2014; Hawrylycz et al., 2012; Lein et al., 2007). Rare coding variants in the *PLD3* gene have been associated with late onset AD in 14 families of European ancestry and African Americans (Cruchaga et al., 2014). More specifically, a putative loss-of-function polymorphism (V232M) was proposed to increase the secretion of the amyloid peptide ( $A\beta$ ), hence increasing the risk of late-onset AD development. In addition, PLD3 was found to interact with APP after transfection of both plasmids in HEK293T cells (Cruchaga et al., 2014). PLD3 protein expression is downregulated in AD brains (Kong et al., 2009; Satoh et al., 2014) and in cortical

membrane lipid rafts prepared from the 3xTgAD murine model of AD (Chadwick et al., 2010). Notably, PLD3 was found to be constitutively expressed in cortical neurons, hippocampal pyramidal granular neurons but not in microglia. A high accumulation of PLD3 immunoreactivity was also observed in neuritic plaques of AD brains (Sato et al., 2014). Other groups were not able to successfully reproduce the genetic association of *PLD3* polymorphisms with late-onset AD (Heilmann et al., 2015; Hooli et al., 2015; van der Lee et al., 2015). Moreover, loss-of-function of *Pld3* in the background of an AD mouse model (*App<sup>ki</sup> Pld3<sup>ko</sup>*), did not show any alterations on APP expression and processing (Fazzari et al., 2017). Thus, the genetic link between PLD3 and AD is still under debate.

## 1.6 PLD3 and spinocerebellar ataxia

Autosomal dominant cerebellar ataxias (ADCA) are hereditary neurodegenerative disorders that are known as spinocerebellar ataxias (SCA) in genetic nomenclature (Schöls et al., 2004). The term SCA has been used to denote recessive and sporadic disorders characterized from patients that suffer from coordination, loss of balance, gait abnormalities and slurred speech (Durr, 2010; Klockgether, 2011). In 2017, Nibbeling et al., through a combination of exome sequencing in genetically undiagnosed families, reported *PLD3* as a novel ataxia gene, more specifically, they identified the PLD3 variant p.Leu308Pro (Nibbeling et al., 2017). Further cell-based analysis suggested that this overexpressed PLD3 variant localized to the endoplasmic reticulum (ER). However, no alterations on protein stability were observed. Moreover, Nibbeling et al. reported that the PLD3 L308P variant led to a reduction of phospholipase D activity, based on a colorimetric assay. These results proposed a role of *PLD3* in the etiology of SCA.

## 1.7 Aim of the study

Lysosomes are the main organelles responsible of the catabolism of a number of macromolecules. Several studies support an increasing emergence of undescribed lysosomal hydrolases and lysosomal membrane proteins. The phospholipase D3 (PLD3) protein has been identified as a type II transmembrane protein mainly localized in the endoplasmic reticulum. However, independent proteomic analyses suggested that PLD3



---

is a lysosomal protein. An aim of the present study was to perform a detailed biochemical and cell biological characterization of PLD3 with a special focus on its subcellular localization, intracellular transport, post-translational modifications and intracellular proteolytic cleavage. Another objective of this thesis was to analyze PLD3 expression *in vivo* in different organs and cell types. To investigate how the absence of PLD3 affects the physiology of the mouse, a phenotype analysis of a *Pld3*-deficient mouse model was performed. Due to the linkage of *PLD3* variants with the development of late-onset Alzheimer's disease (AD), the influence of *in vivo* PLD3 deletion, especially on the brain phenotype, should be evaluated. Since PLD3 downregulation was found to promote increased amyloid- $\beta$  release, the effect of *Pld3* deficiency on APP proteolysis in the background of the 5xFAD AD mouse model was also investigated.

PLD3 is part of the phospholipase superfamily because it contains two HKD motifs. However, no canonical PLD activity or substrate has been specified. Interestingly, during the course of this project, PLD3 and PLD4 were described to have 5'-exonuclease in the spleen responsible of cleaving single-stranded DNA (Gavin et al., 2018). We hypothesized that this nuclease activity might be tissue-specific, thus a thorough *in vitro* and *in vivo* description of PLD3 nuclease activity was performed.

## 2 MATERIAL AND METHODS

### 2.1 Material

#### 2.1.1 Laboratory chemicals

The chemicals not listed on Table 1 were purchased with the purity grade *pro analysi* (*p.a.*) from the firma Carl Roth.

**Table 1. List of laboratory chemicals**

<i>Chemical</i>	<i>Reference</i>
DABCO	Sigma-Aldrich
DAPI	Sigma-Aldrich
Glutaraldehyde	Merck
LE Agarose	Biozym
Mowiol 4-88	Calbiochem
NP-40	Calbiochem
Triton X-100	Sigma-Aldrich

#### 2.1.2 Frequently used solutions and buffers

##### LB medium

1 % (w/v) Trypton / Pepton

0.5 % (w/v) Yeast extract

1 % (w/v) NaCl

pH 7.0

##### LB agar

1.5 % (w/v) Agar-agar

In LB medium

##### 0.1 M Phosphate buffer (PB)

84 mM Na<sub>2</sub>HPO<sub>4</sub>

16 mM KH<sub>2</sub>PO<sub>4</sub>

pH 7.2 – 7.4

10X Phosphate-buffered saline (PBS)100 mM Na<sub>2</sub>HPO<sub>4</sub>18 mM KH<sub>2</sub>PO<sub>4</sub>

1.37 M NaCl

27 mM KCl

pH 6.8

10X Tris-buffered saline (TBS)

200 mM Tris/HCl pH 7.0

1.5 M NaCl

Mounting solution

1x PBS pH 7.4

17 % (w/v) Mowiol 4-88

33 % (v/v) Glycerol

20 mg/ml 1,4-Diazabicyclo-[2.2.2]-octane (DABCO)

**2.1.3 Reagents, solutions, media and buffers****Table 2. List of reagents, solutions, media and buffers**

<i>Name</i>	<i>Reference</i>
5x Phusion HF/GC Buffer	Thermo Fisher Scientific
6x DNA Loading Dye	Thermo Fisher Scientific
10 x DreamTaq Buffer	Thermo Fisher Scientific
Albumin Fraction V	Roth
Bafilomycin A1	Sigma-Aldrich
B-27™ Supplement (50X), serum free	Thermo Fisher Scientific
Bovine serum albumin (BSA)	Carl Roth
Brefeldin A	Sigma-Aldrich
Chloroquine	Sigma-Aldrich
DirectPCR® Lysis Reagent (Mouse Tail)	Viagen Biotech
Dynabeads Protein G	Thermo Fisher Scientific
cOmplete™ Protease Inhibitor Cocktail	Roche
DNaseI	Roche
dNTP Mix, 10 mM each	Thermo Fisher Scientific

Dulbecco's Modified Eagle Medium (DMEM)	Gibco
DMEM (with D-Glucose and Sodium Pyruvate)	Gibco
DMEM/F-12, HEPES	Gibco
E64D	Enzo
Endoglycosidase H	Roche
Fetal bovine serum (FBS)	Biochrom
GlutaMAX™ Supplement	Thermo Fisher Scientific
Glutathione Sepharose 4B	Thermo Fisher Scientific
GW4869	Sigma-Aldrich
Hank's Balanced Salt Solution (HBSS)	Gibco
INTERFERin® siRNA transfection reagent	Polyplus
Ketamine 10 %	Bremer Pharma
Leupeptin	Enzo
Neurobasal™-A Medium	Thermo Fisher Scientific
N-glycosidase F	Roche
<i>Silencer</i> ® Select Pre-designed siRNA	Life Thecnologies
Penicillin/Streptomycin	Thermo Fisher Scientific
Pepstatin A	Enzo
PMSF	Sigma-Aldrich
Polyethylenimin Max (PEI)	Polysciences
Poly-L-Lysine	Sigma-Aldrich
Rompun 2 %	Bayer
Sodium Pyruvate (100 mM)	Thermo Fisher Scientific
SYBR™ Gold Nucleic Acid Gel Stain	Thermo Fisher Scientific
Trypsin/EDTA	Sigma-Aldrich
Wortmannin	Sigma-Aldrich

### 2.1.4 Cell lines

**Table 3. List of cell lines**

<i>Cell line</i>	<i>Description</i>
<i>HeLa</i>	Human cervical cancer cell line
<i>Pld3 KO HeLa</i>	PLD3-deficient human cervical cancer cells
<i>Neuro2a</i>	Mouse neuroblastoma cell line

<i>SH-SY5Y</i>	Human neuroblast-like subclone
<i>MEF</i>	Mouse embryonic fibroblasts
<i>BV-2</i>	Mouse microglia cell line

### 2.1.5 Transgenic mouse lines

**Table 4. List of transgenic mouse lines**

<i>Mouse strain</i>	<i>Mouse strain (full name)</i>	<i>Source</i>	<i>Refererence</i>
Pld3 KO	<i>Pld3<sup>tm1e(EUCOMM)Wtsi</sup></i>	EUCOMM	Skarnes et al., 2011
5XFAD	B6SJL-Tg (APP <sup>SwFlLon</sup> , PSEN1* <sup>M146L</sup> * <sup>L286V</sup> ) 6799Vas/Mmjax	The Jackson Lab	Oakley et al., 2006
TLR9	<i>Tlr9</i> <sup>-/-</sup>	Dr. Shizuo Akira and Dr. Melanie Brinkmann	Hemmi et al., 2000

### 2.1.6 Bacterial strains

Amplification of plasmid DNA was conducted using the *Escherichia coli* XL1-blue strain (Agilent Technology).

Genotype: *recA1 endA1 gyrA96 thi-1 hsdR17 supE44 relA1 lac* [F' *proAB lacIqZΔM15 Tn10* (Tet<sup>r</sup>)].

### 2.1.7 Antibodies

**Table 5. List of primary antibodies**

<i>Antigen</i>	<i>Clonality</i>	<i>Host</i>	<i>Dilution</i>	<i>Reference</i>
APP (22C11)	Monoclonal	Mouse	1:5000 (WB)	eBioscience
APP (A8717)	Polyclonal	Rabbit	1:1000 (WB)	Sigma-Aldrich
APP (6E10)	Monoclonal	Mouse	1:500 (IHC)	BioLegend
β-glucocerebrosidase	Monoclonal	-	1:100 (WB)	Johannes Aerts
Bace1 (D10E5)	Monoclonal	Rabbit	1:1000 (WB)	Cell Signaling
Cathesin D	-	Rabbit	1:200 (IF) 1:1000 (WB)	Andrej Hasilik

CD68 (FA 11)	-	Rat	1:500 (IHC)	BioLegend
Doublecortin	Polyclonal	Goat	1:50 (IHC)	Santa Cruz
EEA1	Monoclonal	Rabbit	1:100 (IF)	Cell Signaling
GAPDH (FL-335)	Polyclonal	Rabbit	1:5000 (WB)	Santa Cruz
GFAP (G-A-5)	Monoclonal	Mouse	1:500 (IF, IHC)	Sigma-Aldrich
GFP (D5.1)	Monoclonal	Rabbit	1:500 (IF) 1:1000 (WB)	Cell Signaling
GST (P1A12)	Monoclonal	Mouse	1:500 (WB)	Hybridoma Bank
HA (3F10)	Monoclonal	Rat	1:1000 (WB)	Roche
Hrs (A-5)	Monoclonal	Mouse	1:500 (WB)	Enzo Life Science
Iba1 (GTX100042)	Polyclonal	Rabbit	1:500 (IHC)	GeneTex
Ki67	Monoclonal	Rat	1:300 (IHC)	eBioscience
LAMP1	-	Mouse	1:500 (EM)	Pharmingen
LAMP1 (1D4B)	Monoclonal	Rat	1:500 (IF, IHC) 1:100 (WB)	Hybridoma Bank
LAMP2 (H4B4)	Monoclonal	Mouse	1:500 (IF, IHC) 1:100 (WB)	Hybridoma Bank
LBPA (6C4)	-	Mouse	1:50	Jean Gruenberg
MAP2 (HM-2)	Monoclonal	Mouse	1:500 (IHC)	Sigma-Aldrich
Myc (9B11)	Monoclonal	Mouse	1:1000 (WB)	Cell Signaling
NeuN (MAB377)	Monoclonal	Mouse	1:200 (IF)	Merck
Pld3 (N-term)	Polyclonal	Rabbit	1:500 (IF) 1:3000 (WB)	Pineda Service
Pld3 (HPA012800)	Polyclonal	Rabbit	1:400 (IF) 1:300 (WB)	Sigma-Aldrich

EM: electron microscopy, IF: immunofluorescence, IHC: immunohistochemistry, WB: Western blot

**Table 6. List of secondary antibodies**

<i>Antigen</i>	<i>Coupled to</i>	<i>Host</i>	<i>Dilution</i>	<i>Reference</i>
Anti-mouse	Horseradish-Peroxidase	Goat	1:10000	Dianova
Anti-rabbit		Goat		
Anti-rat		Goat		
Anti-mouse	AlexaFluor® 488, 594, 647	Goat/donkey	1:500	Cell Signaling Technology
Anti-rabbit		Goat		
Anti-rat		Goat		
Anti-rabbit	Protein A gold	-	1:500	G. Posthuma, University Medical Center Utrecht
Anti-mouse				

### 2.1.8 Protein and DNA standards

**Table 7. List of protein and DNA standards**

<i>Name</i>	<i>Reference</i>
PageRuler™ Prestained Protein Ladder	Thermo Fisher Scientific
GeneRuler™ Ultra Low Range DNA Ladder	Thermo Fisher Scientific
GeneRuler™ 100 pb Plus DNA Ladder	Thermo Fisher Scientific
Albumin Standard	Thermo Fisher Scientific

### 2.1.9 Enzymes

**Table 8. List of enzymes**

<i>DreamTaq™ DNA Polymerase</i>	<i>Thermo Fisher Scientific</i>
Phusion DNA Polymerase	Thermo Fisher Scientific
DreamTaq DNA Polymerase	Thermo Fisher Scientific
Proteinase K	Roche
DpnI	Thermo Fisher Scientific
HindIII	Thermo Fisher Scientific
XbaI	Thermo Fisher Scientific

### 2.1.10 Substrates for lysosomal enzyme activity

**Table 9. List of artificial substrates for lysosomal enzyme activity**

<i>Substrate</i>	<i>Enzyme</i>	<i>Reference</i>
p-nitrophenyl-N-acetyl-β-D-glucosaminide	β-hexosaminidase	Sigma-Aldrich
2-nitrophenyl-β-D-glucopyranoside	β-glucocerebrosidase	Sigma-Aldrich
p-nitrophenyl-α-D-glucuronidase	β-glucuronidase	Sigma-Aldrich

2.1.11 *Plasmids***Table 10. List of plasmids**

<i>Plasmid</i>	<i>Resistance</i>	<i>Reference</i>
pcDNA <sup>TM</sup> 3.1/Hygro(+)	Ampicillin	Huang, Morielli and Peralta, 1993
pEGFP-C1	Kanamycin	T. T. Yang et al., 1988
pCMV	Ampicillin	Matsuda T, Cepko CL 2004
pFrog	Ampicilin	-
pCMV-Cas9-GFP	Kanamycin	Sigma-Aldrich

**Table 11. List of expression constructs**

<i>Construct</i>	<i>Vector</i>	<i>Reference</i>
Dynamin-WT	pCR3.1	Juan Bonifacino & Stephan Storch
Dynamin-K44A	pCR3.1	Juan Bonifacino & Stephan Storch
Hrs-GFP	pEGFP-C1	Sylvie Urbe & Andreas Kallinos
hPLD3-WT	pcDNA <sup>TM</sup> 3.1/Hygro(+)	Sebastian Jagdmann
hPLD-K2R	pcDNA <sup>TM</sup> 3.1/Hygro(+)	Generated in this work
hPLD-K4R	pcDNA <sup>TM</sup> 3.1/Hygro(+)	Generated in this work
hPLD-M6R	pcDNA <sup>TM</sup> 3.1/Hygro(+)	Generated in this work
hPLD3-Y7A	pcDNA <sup>TM</sup> 3.1/Hygro(+)	Generated in this work
hPLD-K11R	pcDNA <sup>TM</sup> 3.1/Hygro(+)	Generated in this work
hPLD-K30R	pcDNA <sup>TM</sup> 3.1/Hygro(+)	Generated in this work
hPLD-K34R	pcDNA <sup>TM</sup> 3.1/Hygro(+)	Generated in this work
hPLD-K35R	pcDNA <sup>TM</sup> 3.1/Hygro(+)	Generated in this work
hPLD-G63S	pcDNA <sup>TM</sup> 3.1/Hygro(+)	Cedric Cappel
hPLD-P76A	pcDNA <sup>TM</sup> 3.1/Hygro(+)	Generated in this work
hPLD-G92A	pcDNA <sup>TM</sup> 3.1/Hygro(+)	Generated in this work
hPLD-L93A	pcDNA <sup>TM</sup> 3.1/Hygro(+)	Generated in this work
hPLD-D94A	pcDNA <sup>TM</sup> 3.1/Hygro(+)	Generated in this work
hPLD-F95A	pcDNA <sup>TM</sup> 3.1/Hygro(+)	Generated in this work
hPLD-P96A	pcDNA <sup>TM</sup> 3.1/Hygro(+)	Generated in this work
hPLD-N97A	pcDNA <sup>TM</sup> 3.1/Hygro(+)	Generated in this work
hPLD-N102A	pcDNA <sup>TM</sup> 3.1/Hygro(+)	Generated in this work



hPLD-N132A	pcDNA <sup>TM</sup> 3.1/Hygro(+)	Generated in this work
hPLD-K228R	pcDNA <sup>TM</sup> 3.1/Hygro(+)	Generated in this work
hPLD-V232M	pcDNA <sup>TM</sup> 3.1/Hygro(+)	Generated in this work
hPLD-N236A	pcDNA <sup>TM</sup> 3.1/Hygro(+)	Generated in this work
hPLD-N236S	pcDNA <sup>TM</sup> 3.1/Hygro(+)	Generated in this work
hPLD-N284A	pcDNA <sup>TM</sup> 3.1/Hygro(+)	Generated in this work
hPLD-N284S	pcDNA <sup>TM</sup> 3.1/Hygro(+)	Generated in this work
hPLD-L308P	pcDNA <sup>TM</sup> 3.1/Hygro(+)	Generated in this work
hPLD-N387A	pcDNA <sup>TM</sup> 3.1/Hygro(+)	Generated in this work
hPLD-K418R	pcDNA <sup>TM</sup> 3.1/Hygro(+)	Generated in this work
hPLD-E423A	pcDNA <sup>TM</sup> 3.1/Hygro(+)	Cedric Cappel
hPLD-T426A	pcDNA <sup>TM</sup> 3.1/Hygro(+)	Generated in this work
hPLD-N432A	pcDNA <sup>TM</sup> 3.1/Hygro(+)	Generated in this work
hPLD-K1-6R	pcDNA <sup>TM</sup> 3.1/Hygro(+)	Generated in this work
Rab5-WT	pFrog	Michael Schwake
Rab5-Q79L	pFrog	Michael Schwake
Ubiquitin-HA	pcDNA <sup>TM</sup> 3.1/Hygro(+)	Jan Riemer
Vps4a-WT-3XFlag	pCMV	Nobuyuki Tanaka
Vps4a-E228Q-3Xflag	pCMV	Nobuyuki Tanaka
Vps4a-WT-GFP	pEGFP-C1	John McCullough
Vps4a-K173Q-GFP	pEGFP-C1	John McCullough

### 2.1.12 Oligonucleotides

**Table 12. Oligonucleotides used for genotyping**

<i>Oligonucleotide name</i>	<i>Length (Nt.)</i>	<i>5' → 3' sequence</i>
Pld3 forward	19	GGGGCCTCAAGGGAGAGTC
Pld3 WT reverse	24	CAAGCTCTCACTGAGTTCTTCTGG
Pld3 CAS R1	20	TCGTGGTATCGTTATGCGCC
TLR9 WT2	28	GTGGAGGGACTTTTGGCCACATTCTATA
TLR9 extra	27	GCAATGGAAAGGACTGTCCACTTTGTG
TLR9 Neo	27	ATCGCCTTCTATCGCCTTCTTGACGAG
5XFAD transgene forward	20	AGGACTGACCACTCGACCAG
5XFAD transgene reverse	19	CGGGGGTCTAGTTCTGCAT

5XFAD internal positive control forward	24	CTAGGCCACAGAATTGAAAGATCT
5XFAD internal positive control reverse	25	GTAGGTGGAAATTCTAGCATCATCC

**Table 13. Oligonucleotides used for site directed mutagenesis**

<i>Amino acid change position</i>	<i>Length (nt.)</i>		<i>5' → 3' sequence</i>
hPLD-K2R	42	Forward	ACATCAGTTTAGGCCTCATAAGCTTAAGTTTAAACGCTAGCC
		Reverse	GGCTAGCGTTTAAACTTAAGCTTATGAGGCCTAAACTGATGT
hPLD-K4R	37	Forward	GCTCCTGGTACATCAGTCTAGGCTTCATAAGCTTAAG
		Reverse	CTTAAGCTTATGAAGCCTAGACTGATGTACCAGGAGC
hPLD-M6R	35	Forward	CCTTCAGCTCCTGGTACCTCAGTTTAGGCTTCATA
		Reverse	TATGAAGCCTAAACTGAGGTACCAGGAGCTGAAGG
hPLD3-Y7A	38	Forward	GGCACCTTCAGCTCCTGGGCCATCAGTTTAGGCTTCAT
		Reverse	ATGAAGCCTAAACTGATGGCCCAGGAGCTGAAGGTGCC
hPLD-K11R	30	Forward	TGCAGGCACCCTCAGCTCCTGGTACATCAG
		Reverse	CTGATGTACCAGGAGCTGAGGGTGCCTGCA
hPLD-K30R	31	Forward	CTTTTCCGCAGCCCTCCACGCCTCAATCTCA
		Reverse	TGAGATTGAGGCGTGGAGGGCTGCGGAAAAG
hPLD-K34R	29	Forward	CCCAGCGGGCTTTCCTTCCGCAGCCTTC
		Reverse	GAAGGCTGCGGAAAAGGAAAGCCCGCTGGG
hPLD-K35R	30	Forward	CCAGCGGGCTCTCTTTTCCGCAGCCTTCCA
		Reverse	TGGAAGGCTGCGGAAAAGAGAGCCCGCTGG
hPLD-G63S	38	Forward	CAAAGAGATGCAAGTCGCTGTATTCCCATAGAAACAGC
		Reverse	GCTGTTTCTATGGGAATACAGCGACTTGCATCTCTTTG
hPLD-P76A	25	Forward	GGTCATAGCAGGCGGCTGGGCGCTG
		Reverse	CAGCGCCCAGCCGCCTGCTATGACC
hPLD-G92A	27	Forward	GGGGAAGTCCAGGGCCTCAGGAATGCT
		Reverse	AGCATTCCTGAGGCCCTGGACTTCCCC
hPLD-L93A	32	Forward	GCATTGGGGAAGTCCGCGCCCTCAGGAATGCT
		Reverse	AGCATTCCTGAGGGCGCGGACTTCCCCAATGC
hPLD-D94A	27	Forward	GGCATTGGGGAAGGCCAGGCCCTCAGG

		Reverse	CCTGAGGGCCTGGCCTTCCCCAATGCC
hPLD-F95A	30	Forward	TGGAGGCATTGGGGGCGTCCAGGCCCTCAG
		Reverse	CTGAGGGCCTGGACGCCCCCAATGCCTCCA
hPLD-P96A	27	Forward	GTGGAGGCATTGGCGAAGTCCAGGCC
		Reverse	GGGCCTGGACTTCGCCAATGCCTCCAC
hPLD-N97A	28	Forward	CCCCGTGGAGGCAGCGGGGAAGTCCAGG
		Reverse	CCTGGACTTCCCCGCTGCCTCCACGGGG
hPLD-N102A	28	Forward	GCTGGTGAAGGGGCCCCGTGGAGGCA
		Reverse	TGCCTCCACGGGGGCCCCCTCCACCAGC
hPLD-N132A	34	Forward	CTGGACCCTCACCAACGCTGACACCCACACGCAG
		Reverse	CTGCGTGTGGGTGTCAGCGTTGGTGAGGGTCCAG
hPLD-K228R	27	Forward	GCCCAGCTCCCTGACCTGGGTCAGTGA
		Reverse	TCACTGACCCAGGTCAGGGAGCTGGGC
hPLD-V232M	33	Forward	CAGTTGTACATGACCATGCCAGCTCCTTGACC
		Reverse	GGTCAAGGAGCTGGGCATGGTCATGTACAAC TG
hPLD-N236A	32	Forward	GCCAGGCAGCTGCAGGCGTACATGACCACGCC
		Reverse	GGCGTGGTCATGTACGCTGCAGCTGCCTGGC
hPLD-N236S	29	Forward	CCAGGCAGCTGCAGCTGTACATGACCACG
		Reverse	CGTGGTCATGTACAGCTGCAGCTGCCTGG
hPLD-N284A	36	Forward	CCAGAGCAGGGGTTCCAGCGAGGCAGATCTCCATTG
		Reverse	CAATGGAGATCTGCCTCGCTGGAACCCCTGCTCTGG
hPLD-N284S	33	Forward	CAGGGGTTCCACTGAGGCAGATCTCCATTGGTG
		Reverse	CACCAATGGAGATCTGCCTCAGTGGAAACCCCTG
hPLD3-L308P	29	Forward	TGAGTAGAGCCTTCGGGTCTGGAGTGCGG
		Reverse	CCGCACTCCAGACCCGAAGGCTCTACTCA
hPLD-N387A	32	Forward	TCAGAGTGGGTATGGGCGTCACGCAGGGCAGC
		Reverse	GCTGCCCTGCGTGACGCCATACCCACTCTGA
hPLD3-K418R	35	Forward	GTTCAGTCACCATGTACCTGTTGTGGTTGACACGG
		Reverse	CCGTGTCAACCACAACAGGTACATGGTGACTGAAC
hPLD-E423A	33	Forward	GATGTAGGTGGCGCGTGCAGTCACCATGTACTT
		Reverse	AAGTACATGGTGACTGCACGCGCCACCTACATC
hPLD-T426A	29	Forward	GGTCCGATGTAGGCGGCGGTTTCCAGTCA
		Reverse	TGACTGAACGCGCCGCTACATCGGAACC
hPLD-N432A	36	Forward	AGTAGTTGCCAGACCAGGCGGAGGTTCCGATGTAGG
		Reverse	CCTACATCGGAACCTCCGCTGGTCTGGCAACTACT

**Table 14. Oligonucleotide used for nuclease activity assay**

<i>Name</i>	<i>Length (Nt.)</i>	<i>5' → 3' sequence</i>
5'-ssDNA	55	ACCATGACGTTCTGATGCTAAGTATGCACTTCATCGTCAAGCAATGCTATG*C*A*T

\* indicates internucleotide phosphorothioate (PS) modifications

### 2.1.13 Equipment

**Table 15. List of equipment**

<i>Name</i>	<i>Description</i>	<i>Reference</i>
Blot Imager	Odyssey FC	LI-COR
Cell culture centrifuge	Universal 32	Hettich Zentrifugen
Cell incubator	HERA cell 150	Thermo Electron Corporation
Cold centrifuge	Centrifuge 5415R	Eppendorf
Confocal Microscope	FV1000D	Olympus
Confocal Microscope lens	UPLSAPO 100x	Olympus
Electron Microscope	EM902	Zeiss
Electron Microscope camera	MegaViewIII	A. Tröndle, Moorenweis
Flow Cytometer	FACSaria	BD Biosciences
Gel Imager	Amersham 680	GE Healthcare Life Sciences
Gel Imager	LAS 4000	GE Healthcare Life Sciences
Homogenizer	-	B. Braun
Light microscope	LEICA DMi8	Leica
Light microscope camera	DFC7000T	Leica
Microplate reader	Synergy HT	BioTek
Orbital shaker	-	Edmund Bühler
PCR machine	FlexyCycler <sup>2</sup>	analytic jena
Perfusion pump	11 Plus	Harvard Apparatus
SDS-PAGE chamber	-	BIO-RAD
Sliding microtome	SM 2000R	Leica
Sonifier	Branson 450	Emerson Industrial Automation
Table centrifuge	Centrifuge 5424	Eppendorf
Thermo block	TherMixer F1.5	Eppendorf
Ultracentrifuge	Optima™ LE-89IL	Beckmann

Ultracentrifuge	Optima™ TLX	Beckmann
UV transilluminator	UV-Systeme	Intas®
Water bath (37 °C)	-	GFL®

### 2.1.14 Software

**Table 16. List of software**

<i>Software</i>	<i>Version</i>	<i>Reference</i>
FV10-ASW	Version 4.2	Olympus
GraphPad Prism	Version 7.04	GraphPad Software Inc.
ImageJ (Fiji)	Version 1.8.0_66	Wayne Rasband / BioVoxxel
Odyssey Image Studio	Version 4.0	LI-COR

### 2.1.15 Other material

**Table 17. List of consumables**

<i>Name</i>	<i>Reference</i>
Carbon-Formvar-coated nickel grids	Science Services GmbH, Germany
C-chip disposable hemocytometer	NanoEntek
Cell culture plates and dishes	SARTEDT
Cell scraper	SARTEDT
Cryogenic freezing tubes	SARTEDT
Falcon tubes	SARTEDT
Needles (20G & 26G)	Fine-Ject
Microscope Cover Glasses 13 mm	Asistent
Nitrocellulose membrane	GE Healthcare Life Sciences
Pasteur pipettes	Assistant
Scalpel	B. Braun
Serological pipettes	SARTEDT
Syringe	B. Braun
Whatman blotting paper	GE Healthcare Life Sciences

## 2.2 Molecular biology methods

### 2.2.1 Commercial kits

**Table 18. List of commercial kits**

<i>Name</i>	<i>Reference</i>
ECL Advanced™ Western Blotting Detection Kit	GE Healthcare
GeneJET Plasmid Miniprep Kit	Thermo Fisher Scientific
Pierce™ BCA Protein Assay Kit	Thermo Fisher Scientific
Pure Yield™ Plasmid Midiprep System	Promega
HighPure PCR Product Purification Kit??	Roche

### 2.2.2 Site directed mutagenesis

In order to address the effect of different point mutations, amino acid changes were generated by site directed mutagenesis. Primer sequences were design using the online QuickChange Primer Design tool from Agilent. With the PLD3 WT sequence as a template, a Polymerase Change Reaction (PCR) was performed by mixing 1x GC or HF buffer, 6.4  $\mu$ M dNTPs, 3% DMSO, 0.2  $\mu$ M forward and reverse primers, 10 ng plasmid DNA and 0.02 units of Phusion Polymerase in a total reaction volume of 50  $\mu$ l. The PCR program was set as: (1) 5 min of initiation at 98 °C, (2) 30 s of denaturation at 98 °C, (3) 30 s of annealing at 68 °C, (4) 2000 bp/min of elongation at 72 °C and (5) a final elongation of 10 min at 72 °C; steps 2 to 4 were repeated 35 times. The PCR product was further incubated with 1  $\mu$ l DpnI enzyme (10 U/ $\mu$ l) for 1 h at 37 °C to digest the parental methylated DNA, which does not contain the newly introduced mutation. Further, a transformation was performed by incubating 5  $\mu$ l of the digested PCR product with 50  $\mu$ l chemo-competent E. coli XL1 blue bacteria for 20 min on ice, followed by a heat shock for 45 s at 42 °C. The bacteria/PCR product mixture was then incubated with 300  $\mu$ l LB-media without antibiotics for 1 h at 37 °C, shaking at 125 rpm. The bacteria suspension was spun down for 1 min at 8000 rpm at room temperature (RT), 200  $\mu$ l of the media was discarded and the pellet was resuspended with the remaining volume and plated on a LB-agar plate containing ampicillin (50  $\mu$ g/ml) and incubated upside-down overnight at 37 °C. For further purpose, the plate was stored at 4 °C.

### **2.2.3 Isolation of plasmid DNA (MiniPrep)**

A single colony was inoculated in 3 ml LB-media containing ampicillin (100 µg/ml) and incubated overnight at 37 °C in a rotor. Isolation of plasmid DNA was done following the manufacture's protocol (GeneJET Plasmid MiniPrep Kit, Thermo Fischer Scientific). Plasmid DNA concentration was measured (section 2.2.4) and sent for sequencing (Eurofins Genomic).

### **2.2.4 Determination of nucleic acid concentration**

DNA concentration was measured photometrically (Synergy HT, BioTek) in a microplate reader. The maximal absorption of nucleic acids is 260 nm. An absorbance of 1.0 reflects a concentration of 50 ng/µl of double stranded DNA and a concentration of 40 ng/µl for RNA. An absorbance of 280 nm was used to measure the purity of the nucleic acid preparation with respect to protein contaminants; a A<sub>260</sub>/280 ratio should range between 1.7 and 2.0.

### **2.2.5 Purification of plasmid DNA**

In order to obtain higher concentrations of the plasmid DNA, chemo-competent E. coli XL1 blue bacteria were transformed as described in section 2.2.1. Instead, the bacteria-plasmid mixture was inoculated in 200 ml of LB-media containing ampicillin (50 µg/ml) and incubated overnight at 37 °C. The plasmid DNA was later purified following the manufacture's protocol described by the PureYield™ Plasmid Midiprep System (Promega). Nucleic acid concentration was measured as described in section 2.2.4.

### **2.2.6 Agarose gel electrophoresis**

#### 50x Tris-acetate-EDTA (TAE) buffer

2 M Tris/HCl pH 8.0

5.5 % (v/v) acetic acid

50 mM EDTA

For the visualization and separation of DNA, an agarose gel electrophoresis was performed. Hence, nucleic acid samples were mixed with 6x DNA loading dye (Thermo

Fisher Scientific) to adjust the sample density and track the migration during the electrophoresis. Agarose gels were cast in 1x TAE buffer with a final concentration between 1 % and 3 % (w/v) and 500 ng/ml ethidium bromide. Separation was done by using a voltage of 120 V. The length of the separated products was compared with a standard DNA ladder (GeneRuler™ 100 pb Plus DNA Ladder, Thermo Scientific). Detection of DNA was achieved using UV light ( $\lambda = 312$  nm) and documented with a Gel Jet Imager (Intas®).

## 2.3 Cell biology methods

### 2.3.1 Maintenance of cell lines

#### Culture medium

DMEM (containing 4 mM L-glutamine and 4.5 g/l D-glucose)

10 % (v/v) FBS

1x Penicillin/Streptomycin

All cell lines used during this study were kept at 37 °C in a humidified atmosphere at 5 % (v/v) CO<sub>2</sub>. Handling of cells and sterile material was always performed under a laminar flow clean bench. HeLa, Neuro-2a (N2a) and MEF cells were cultivated in fresh *culture medium* and maintained by two passages per week at 100 % confluency. Where indicated, SH-SY5Y cell were differentiated to neuronal-like cells with 20 mM retinoic acid for 4 days. Medium including retinoic acid was changed every two days. Therefore, cells were rinsed once with phosphate-buffered saline (PBS) and incubated with 1 ml trypsin/EDTA (0.5 mg/ml – 0.22 mg/ml in PBS) for 3 min at 37 °C for cell detach. Cells were dissociated in fresh medium by pipetting several times up and down and seeded onto new culture dishes in a dilution between 1:5 and 1:30 depending on the cell type and cell growth.

### 2.3.2 Cryo-preservation of cell lines

#### Freezing medium

DMEM (containing 4 mM L-glutamine and 4.5 g/l D-glucose)

20 % (v/v) FBS

10 % DMSO

All cell lines were cryo-preserved on liquid nitrogen. Accordingly, cultured cells with confluence between 60 – 80 % were first detach with trypsin/EDTA (section 2.3.1),



resuspended in fresh medium and transferred into a 15 ml Falcon tube for further centrifugation at 800 rpm for 5 min at RT. The supernatant was removed and cell pellet was resuspended in 1ml *freezing medium* and pipetted into cryogenic freezing tubes. Tubes were frozen at -80 °C and for longer storage cells were kept on a liquid nitrogen container at -196 °C.

### 2.3.3 *Transient transfection of cells with Polyethylenimine (PEI)*

For the evaluation of transient gene expression, cells were transfected with polyethylenimine (PEI). Therefore, cells must have an approximate confluency of 60 – 80% at the moment of transfection. An incubation was performed for 20 min at RT by mixing 300 µl DMEM medium without any additive, 1 mg/ml PEI (3 µl / µg of DNA) and plasmid DNA. The complete mixture was added to the cells containing fresh culture medium and incubated at 37 °C for up to 5 h. Culture medium was changed again and cell harvesting (section 2.5.1) was performed 24 h or 48 h post-transfection.

### 2.3.4 *siRNA transfection*

Transfection of siRNA (Thermo Fisher Scientific) was performed with Interferin (VWR). Briefly, 5 nM siRNA was mixed with DMEM without additive and Interferin, incubated for 20 min at RT and added to the cells. The specific amount of transfection reagents are listed on Table 19. After 48 h, a second siRNA transfection was performed and 24 h afterwards cells were further analyzed by immunocytochemistry (ICC, section 2.3.9) or harvested (section 2.5.1).

**Table 19. *siRNA transfection volumes per dish/well***

	<i>6-well plate</i>	<i>6 cm dish</i>
DMEM only	200 µl	400 µl
siRNA	5 nM (5,5 µl)	5 nM (11 µl)
Interferin	5 µl	10 µl
Medium total	2 ml	4 ml

### 2.3.5 Generation of stable *PLD3* knockout cell line (CRISPR-Cas9)

#### FACS buffer

PBS

0.5% (w/v) BSA

2 mM EDTA

Generation of *Pld3* knockout (KO) in HeLa cells was performed by CRISPR-Cas9 technology (Clustered Regularly Interspaced Short Palindromic Repeats). Cells were transfected with the vector U6gRNA-Cas9-2A-GFP (Sigma-Aldrich) containing the target site ACGCCTCAATCTCATTTCATGGG, located on exon 4 of *Pld3* (Figure 6). Isolation of clonal cell population from transfected cells was performed by fluorescence-activated cell sorting (FACS) at the Institute of Immunology (University Hospital Schleswig-Holstein), where cell pellets were resuspended in *FACS buffer* filtered with a cell strainer, sorted in 96 well plates with a FACSaria high speed flow cytometer (BD Bioscience) and expanded for 2-3 weeks in culture medium supplemented with 10 % conditioned medium. When reaching 60% confluency, cells were passaged into a 24-well plate and functional testing was performed by Sanger sequencing (GATC Biotech) and Western blot (section 2.5.8).

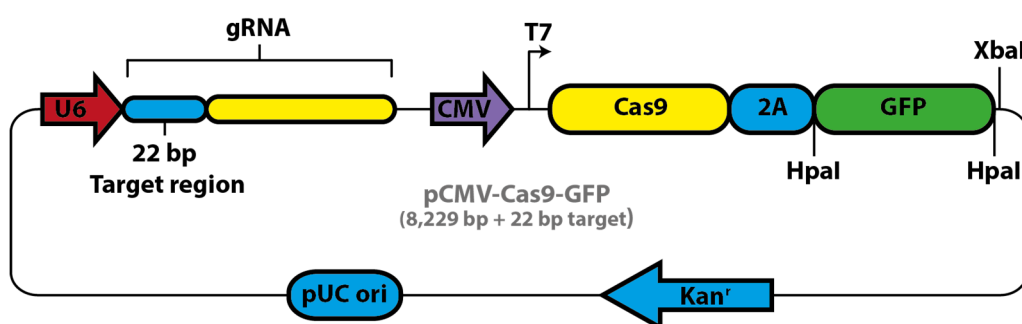


**Figure 6** | Schematic representation of CRISPR-Cas9 plasmid for the generation of stable *PLD3*-deficient HeLa cells.

### 2.3.6 Isolation of mouse embryonic fibroblast (MEFs)

For the preparation of mouse embryonic fibroblasts, pregnant female mice were sacrificed at day E13.5 *post coitum*. Embryos were placed in a Petri dish containing sterile PBS. The placenta and the amniotic sac of each embryo was taken out, together with the heart, the liver and other red organs. A washing step with PBS was performed to remove the blood. The head of the embryos was used for further genotyping (section 2.6.4), if

necessary. The remaining tissue of each embryo was incubated for 15 min at 37 °C with 2 ml trypsin/EDTA after prior cell dissociation with the help of a scalpel. The mesh was resuspended and mixed with 13 ml warm culture medium (DMEM, 10 % FBS and 1x Penicillin/Streptomycin) and cells were centrifuged at 800 rpm for 5 min at RT. Supernatant was discarded and cell pellet was resuspended in 10 ml fresh culture medium. When cells reached a confluence of approximately 60 %, a transient transfection was performed with a SV40 Large T antigen plasmid as described on section 2.3.3, in order to immortalize the cells.

### **2.3.7 Coating of culture dishes with Poly-L-Lysine (PLL)**

A PLL stock solution (10 mg/ml) was prepared in autoclaved ddH<sub>2</sub>O, aliquoted and stored at -20 °C. Working solution (0.1 mg/ml) was freshly prepared in autoclaved ddH<sub>2</sub>O. The solution was added in the 24-well plates (for ICC experiments) or cell cultures dishes (for protein biochemistry) and incubated for 4 h under the bench at RT. Next, 5x washing steps with ddH<sub>2</sub>O were performed, DMEM/F12 medium was added and plates or culture dishes were kept in the incubator at 37 °C for up to 1 week for further preparation of the primary mix co-culture (section 2.3.8).

### **2.3.8 Preparation of primary mix co-culture from mouse hippocampi**

#### Dissociation medium

0.025 % trypsin/EDTA in 1X HBSS

#### Plating medium

DMEM (containing 25 mM D-Glucose and 1 mM Sodium Pyruvate)

1X Penicillin/Streptomycin

10 % FBS

#### Growing medium

Neurobasal A

1X B-27™ Supplement

1X GlutaMAX™ Supplement

1 mM Sodium Pyruvate

For the preparation of hippocampal co-culture of neurons, microglia and astrocytes, 1-day-old mice were used. Therefore, embryos were transferred to a Petri dish containing 1X Hank's Balanced Salt Solution (HBSS) placed on ice and the head was cut using a scissor. The head was fixed by piercing the eyes with the tips of a curved forceps and the skin, the skull and meninges were cut with the help of a straight forceps. The brain was removed and the hippocampus was isolated as described on Figure 7. Hippocampi were collected in a tube containing 500  $\mu$ l 1X HBSS. After isolation was completed, *dissociation medium* was added and incubated for 20 min at 37 °C mixing in between every 5 min. Afterwards, 2x washes with HBSS were followed and tissue were resuspended in 1 ml warm *plating medium*. Tissue were gently triturated using two different needles (yellow 20G and brown 26G) with the help of a 2 ml syringe until big clumps of tissue were not observed (3 – 4 times each, dropwise). Cells were counted using a Neubauer chamber (C-chip, Biochrom) and desired amount of cells (80.000 cells/ml for immunofluorescence analysis) were resuspended in the required volume of *plating medium*. Hippocampal neuron suspension was plated in PLL-coated (section 2.3.7) 18 mm diameter coverslips placed in a 24-well-plate. Culture plates were incubated for 1 h at 37 °C and media was changed with *growing medium*. Cells were further processed at DIV 15.

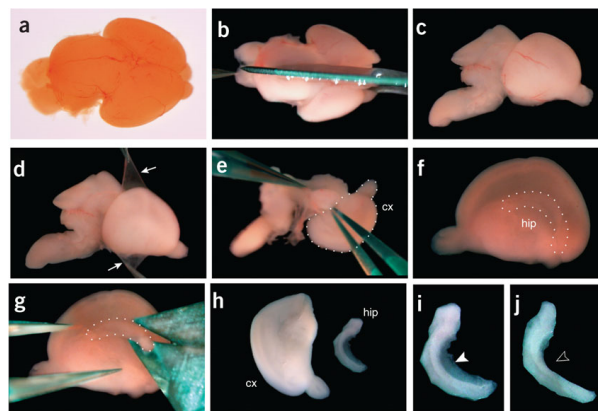


**Figure 7 | Isolation of hippocampus and cortex.** *a*, brain was removed by cutting the skin, the skull. *b*, brain was cut in half; *c*, half brain was placed with the cortex to the upper part. *d*, the meninges was removed. *e*, cortex was separated from the rest of the brain. *f*, *g* and *h*, cortex was placed upside down and hippocampus was isolated. *i* and *j*, hippocampus was get rid of remaining meninges. From: (Melling and Westermayer, 2011).

### 2.3.9 Immunocytochemistry (ICC)

Semi-confluent cultures of cells grown on coverslips were fixed with 99% (v/v) p.a cold Methanol (Roth) or 4% (w/v) paraformaldehyde solution (PFA; Roth) for 20 min at RT.

Cells were permeabilized with 0.2% (w/v) Saponin (Roth) in PBS and natural fluorescence was reduced by adding 0.12% (w/v) Glycine (Roth) in 0.2% Saponin/PBS. Cells were blocked for 1 h with 10% FBS in 0.2 % Saponin/PBS. Coverslips were incubated overnight at 4 °C with 40 µl of the indicated primary antibody diluted in 0.2% Saponin/PBS. The secondary antibody (1:500 in 0.2% Saponin/PBS) coupled to Alexa-Fluor-488/594/647 (Thermo Fisher Scientific) was added for 1 h at RT, followed by embedding of coverslips in 17% (w/v) Mowiol 4-88 mounting Solution (Calbiochem) containing 20 mg/ml DABCO (1,4-Diazabicyclo-[2.2.2]-octane; Sigma-Aldrich) and 5 µg/ml DAPI (Sigma-Aldrich) for nuclear staining.

## 2.4 Histological methods

### 2.4.1 Fluorescence staining of mouse tissue (Immunohistochemistry)

#### Blocking solution

0.1 M PB (phosphate buffer)

0.5 % (v/v) Triton X-100

4 % goat serum

#### Washing buffer

0.1 M PB

0.25 % (v/v) Triton X-100

Tissue sections were obtained from mice previously perfused with 4 % (w/v) PFA (section 2.6.5). The Sliding Microtome (Leica SM 2000 R) was pre-cooled with dry ice and tissue was placed on a thin layer of 5 % sucrose and further embedded with a 30 % sucrose solution using a brush. Tissue sections were cut in 35 µm and stored in a 24-well plate containing 0.1 M PB / 0.02 % (w/v) sodium azide. For antibody staining, sections were first incubated in *blocking solution* for 2 h followed by overnight primary antibody incubation at 4 °C. For staining of Pld3 with the commercial C-terminal antibody, antigen retrieval was performed by incubation of sections in pre-heated (85 °C) sodium citrate buffer (10 mM, pH 8.5) for 30 min, washed 2x with 0.1 M PB (10 min each) and incubated overnight with primary antibody. Next, sections were washed 3x with *washing buffer* (10 min each) and incubated 2 h with Alexa-coupled secondary antibody (1:500) prepared in *washing buffer* and protected from the light. After the incubation time, sections were

washed 3x with *washing buffer* (10 min each), where the second washing step was used for nuclear staining with DAPI. Finally, sections were carefully transferred to a microscope slide and embedded with a 17 % (w/v) Mowiol mounting solution containing 20 mg/ml DABCO.

#### **2.4.2 X-gal-staining of brain sections**

##### Permeabilization solution

0.01 % Na-deoxycholate

0.02 % NP40 in PBS

##### X-gal staining solution

5mM K<sub>3</sub>Fe(CN)<sub>6</sub>

5mM K<sub>4</sub>Fe(CN)<sub>6</sub>

2 mM MgCl<sub>2</sub>

1 mg/ml X-gal in PBS

Free floating sections (35 µm) were washed with 1x PBS and incubated for 10 min at RT with *permeabilization solution*. Sections were further washed with 1x PBS for 10 min at RT and stained overnight at 37 °C with *X-gal staining solution* protected from light. Sections were washed twice with PBS, 10 min each. Finally, brain sections were embedded with a 17 % (w/v) Mowiol mounting solution containing 20 mg/ml DABCO.

## **2.5 Protein biochemistry methods**

### **2.5.1 Generation of cell lysates for protein extraction**

#### Cell lysis buffer

1x cOmplete protease inhibitor

1 % (v/v) Triton X-100

1x PBS

In order to prepare protein lysates from cells, a lysis was performed with a buffer containing the non-ionic surfactant (Triton X-100) which disrupt the lipid barrier and solubilize the integral membrane proteins. The corresponding culture dishes with transfected cells were first washed 2x with cold PBS and cells were detached with the help of a cell scraper and resuspended in 500 µl 1xPBS containing 1x cOmplete protease

inhibitor. Cells were centrifuged down at 3.000 rpm for 10 min at 4 °C. Supernatant was discarded and cell pellet was resuspended in 100 – 300 µl *cell lysis buffer*, sonicated 3x 20 s and incubated on ice for 1 h. To spin down the cell debris, a centrifugation step was performed at 13.000 rpm for 10 min at 4 °C. The supernatant (cell lysate) was transferred into a new Eppendorf and protein concentration was determined (section 2.5.3). Lysates were kept at -20 °C for long term storage.

### **2.5.2 Preparation of tissue homogenates**

#### Cell lysis buffer

1x cOmplete protease inhibitor

1 % (v/v) Triton X-100

1x TBS (tris buffered saline)

Protein extraction from mouse tissue was achieved by homogenization. Therefore, organs were weighed and homogenized in 6x volumes of *cell lysis buffer* using 10 up-and-down strokes (1.000 U/min, B. Braun), sonicated 3x 20 s and incubated on ice for 30 min (with vortex in between). A centrifugation step was followed at 13.000 rpm for 10 min at 4 °C and the soluble fraction was further quantified (section 2.5.3) and analyzed by Western blot (section 2.5.8).

### **2.5.3 Determination of protein concentration with a Bicinchoninic acid (BCA) assay**

Protein concentration was measured using the Pierce™ BCA Protein Assay according to the manufacturer's instructions. The assay relies on the formation of Cu<sup>2+</sup>-protein complexes under alkaline conditions, followed by the reduction of Cu<sup>2+</sup> from the copper sulfate (CuSO<sub>4</sub>) to Cu<sup>1+</sup>. This reduction occurs via cysteine, tryptophan, tyrosine and peptide bonds. Thus, the amount of reduction is proportional to the protein amount. BCA will form a purple-colored complex with Cu<sup>1+</sup> in an alkaline environment, thus providing a basis to monitor the reduction of Cu<sup>2+</sup> by proteins at a wavelength of 562 nm. Briefly, diluted (1:10) samples were mixed with 200 µl of the BCA assay mixture and incubated at 37 °C for 20 min and measured photometrically with a Synergy HT (BioTek) microplate reader. Sample absorption values were related to a calibration curve based on Albumin standard concentrations ranging from 0 to 2 mg/ml to determine the protein amount.

#### 2.5.4 *Membrane separation*

##### Lysis buffer

10 mM Tris pH 7,5

140 mM NaCl

250 mM sucrose

1x cOmplete protease inhibitor

Cell pellets (generated as described on section 2.5.1) were resuspended in 500  $\mu$ l *lysis buffer*, passed 10 times through a 27G x 3/4" gauge needle (0.4 x 20 mm, FineJet) using a 1 ml syringe (Omnifix, B. Braun Medical Inc.) and sonicated 3x 10 s. From the cell suspension, 200  $\mu$ l were further processed to generate the cell lysate as described above. The remaining 300  $\mu$ l were sonicated 3x 10s and centrifuged for 1 h at 55.000 rpm at 4°C (Beckmann Optima™ TLX Ultracentrifuge, rotor TLA 55) and supernatant was collected (soluble fraction). Same procedure was repeated by resuspension of the pellet on 200  $\mu$ l *lysis buffer*, and both soluble fractions were mixed. The pellet was resuspended in 100  $\mu$ l *lysis buffer* containing 1% (v/v) Triton X-100 and 0.5 % (w/v) SDS and sonicated to obtain the membrane fraction. Further analysis was performed by Western blot (section 2.5.6 and 2.5.8).

#### 2.5.5 *Co-immunoprecipitation (CO-IP)*

##### EBC buffer (pH 7.4)

120 Mm NaCl

50 Mm Tris

0.5 % NP-40

1x cOmplete protease inhibitor

After 48 h of transfection, cell pellets were resuspended in *EBC buffer* at 4 °C, and cell lysates were generated as described above (section 2.5.1). For the IP, 800 – 1.000 mg of protein was incubated overnight with 1.5 mL of the indicated antibody at 4 °C. Dynabeads Protein G (Thermo Fisher Scientific) were blocked in 3% Albumin Fraction V (Roth) in *EBC buffer*, and 50 mL of the magnet beads were added to the cell lysate and incubated for 2 h at RT. The beads were finally washed with *EBC buffer*, proteins were eluted with Lämmli buffer, heated for 30 min at 60 °C and separated on a SDS-PAGE (section 2.5.7).



### 2.5.6 *Tandem ubiquitin-binding entities (TUBES)*

#### Cell lysis buffer

- 50 mM Tris/HCl pH 7.5
- 0.15 M NaCl
- 1 mM EDTA
- 1 % (v/v) NP-40
- 10 % (v/v) Glycerol
- 1x cOmplete protease inhibitor (added fresh)

#### Resin wash buffer

- 20 mM Tris/HCl pH 8.0
- 0.15 M NaCl
- 0.1 % (v/v) Tween-20 (TBS-T)
- 1x cOmplete protease inhibitor

#### Glutathione Affinity Resin (GSH beads)

Glutathione Sepharose 4B slurry

For the analysis of PLD3 ubiquitination, a GST-TUBE approach was performed as previously described by Hjerpe et al., 2009. After 48 h of transfection (section 2.3.3), 300 µl of *cell lysis buffer* containing 100 mg GST-TUBE or 100 mg GST only (as a negative control) were added to the cells, resuspended and incubated for 30 min on ice. Cell suspension was centrifuged at 13.000 rpm for 10 min at 4 °C and the supernatant was further mixed with 100 µl slurry of *glutathione affinity resin* and incubated overnight at 4 °C. GSH beads were collected by centrifugation at 2.000 rpm for 5 min at 4 °C, supernatant (unbound fraction) was discarded and beads were washed 3x with *resin wash buffer* for 10 min in a rotator, collecting the beads by low centrifugation as described above. All liquid was carefully aspirated and beads were resuspended in 40 µl 1X Lämmli buffer containing 1 % (v/v) 2-Mercaptoethanol at 95 °C for 10 min and further analyzed by Western blot (section 2.5.8).

### 2.5.7 *SDS-polyacrylamide gel electrophoresis (SDS-PAGE)*

#### 5x Lämmli loading buffer

- 1% (w/v) SDS
- 10 % (v/v) glycerol

125 mM Tris

1 % 2-Mercaptoethanol

Bromophenol blue

Separating gel buffer

1.5 M Tris/HCl pH 8.8

0.4 % (w/v) SDS

Stacking gel buffer

0.5 M Tris/HCl pH 6.8

0.4 % (w/v) SDS

10X SDS gel electrophoresis running buffer

0.25 M Tris

2M Glycine

1 % (w/v) SDS

In order to perform the electrophoretic separation of proteins, cell lysates were previously denatured by the addition of the anionic detergent sodium dodecyl sulfate (SDS) to add a negative charge to the linearized proteins, which will move towards the positive pole through a polymer of acrylamide monomers. Therefore, 20 µg of protein (cell lysates) was mixed with *Lämmli loading buffer* to get a 1X final concentration and denatured at 95 °C for 5 min. Proteins were separated by SDS-PAGE (10 – 15 %, Table 20) in a vertical chamber containing 1X *SDS gel electrophoresis running buffer* applying a current between 80 – 100 V (BIO-RAD). A protein ladder (PageRuler™ Prestained Protein Ladder, Thermo Fisher Scientific) was included next to the samples as known-size-standards to monitor the progress of the electrophoresis and estimating the approximate size of separated proteins.

**Table 20. Composition of SDS polyacrylamide gels**

<i>Separating gel</i>					
		10 %	12.5 %	15 %	<i>Stacking gel</i>
Separating/stacking gel buffer	[µl]	-	-	-	675
30 % (w/v) Acrylamide / bisacrylamide Rotiphorese Gel 30 (37,5:1)	[ml]	3.3	4.2	5.0	0,8
Water	[ml]	4.0	3.1	2.3	3.4

10 % (w/v) APS	[ $\mu$ l]	60	60	60	30
TEMED	[ $\mu$ l]	30	30	30	15

APS, ammonium persulfate

### 2.5.8 Western blotting and immunodetection

#### 10X Transfer buffer

250 mM Tris

2 M Glycine

add 20 % (v/v) MeOH

#### 10X Tris-buffered saline (TBS)

200 mM Tris/HCl pH 7.0

1.5 M NaCl

#### TBS-T

1X TBS

0.1 % (w/v) Tween<sup>®</sup> 20

#### Detection solution A

0.1 M Tris/HCl pH 8.6

0.025 % (w/v) Mowiol

#### Detection solution B

0.11 % (w/v) p-Coumaric acid

In DMSO

For the specific immunodetection of proteins via Western blot, an immunoblotting into a nitrocellulose membrane (GE Healthcare Life Sciences) was performed. Therefore, two sheets of Whatman<sup>®</sup> blotting paper, a nitrocellulose membrane, the SDS polyacrylamide gel and another two sheets of Whatman<sup>®</sup> blotting paper (all equilibrated in 1X *transfer buffer*) were mounted on a semi-dry transfer chamber, beginning at the anode and sealed with the cathode. The transfer was performed at a constant current of 1.5 mA per cm<sup>2</sup> of nitrocellulose membrane for 120 min. The membranes were further probed overnight at 4 °C with the indicated antibodies diluted in 5% (w/v) milk powder prepared in *TBS-T*. Membranes were washed 3x with *TBS-T* (10 min each), incubated with HRP-conjugated secondary antibodies (1:10.000, prepared in 5% milk powder / *TBS-T*) for 1 h at RT and washed again 3x with *TBS-T*. Immunodetection of horseradish peroxidase was performed by mixing 100  $\mu$ l of each solution provided on the ECL Advanced<sup>™</sup> Western Blotting

Detection Kit (GE Healthcare Life Sciences), 1 ml *detection solution A*, 100  $\mu$ l *detection solution B* and 3.5  $\mu$ l H<sub>2</sub>O<sub>2</sub>. Image acquisition was performed with the ImageQuant LAS 4000 Analyzer or the Amersham Imager 680 (GE Healthcare Life Sciences). Signal intensities were quantified with the ImageJ software (section 2.8.)

### **2.5.9 Percoll density gradient centrifugation**

#### Buffer I

250 mM sucrose

3 mM Imidazole pH 7.4

#### Buffer P

90 % (v/v) Percoll (GE Healthcare Life Sciences)

2.5 M sucrose

30 mM Imidazole pH 7.4

Subcellular fractionation of PLD3 transfected cells was performed with a 30% (v/v) Percoll density gradient. Cell pellet (corresponding to 10 mg total protein) was resuspended in 600  $\mu$ l *buffer I*, passed 10 times through a 27G x 3/4" gauge needle (0.4 x 20 mm, Fine-Jet) using a 1 ml syringe (Omnifix, B. Braun Medical Inc.) and homogenate was centrifuged 10 min at 1000 x g. Supernatant (post-nuclear fraction; PNS) was transferred to a new Eppendorf tube and procedure was repeated by resuspension of pellet with 400  $\mu$ l *buffer I*. Both PNS fractions were mixed. 0.9 ml of PNS was mixed with 1.98 ml *buffer P* and 6.12 ml *buffer I*, followed by centrifugation for 90 min at 18100 rpm (Beckman, Optima™ LE-89K Ultracentrifuge, rotor 70TI/70.1TI). From the total volume, 12 fractions (750  $\mu$ l each) were taken, 1% (v/v) Triton X-100 was added to each fraction and incubated for 30 min. Fractions were either mixed with 1X Lämmli buffer for Western blot analysis (section 2.5.8) or further used for measurement of  $\beta$ -hexosaminidase activity (section 2.5.11).

### **2.5.10 Enzymatic deglycosylation**

To a final volume of 10  $\mu$ l, cell lysates (20  $\mu$ g) were digested with 0.5% (w/v) SDS and 0.25 M  $\beta$ -mercaptoethanol followed by incubation at 95 °C for 5 min. Cell lysates were cooled down at RT and 0.25 M Tris/HCl, 100 mM EDTA (pH 7.4), 2.5 mM Phenylmethane-

sulphonylfluoride protein inhibitor (PMSF; Sigma-Aldrich) and either 1 unit of N-Glycosidase F (PNGFase, Roche) or 0.05 units of Endoglycosidase H (EndoH, Roche) were added. Samples were incubated overnight at 37°C in an orbital shaker at 125 rpm. The reaction was stopped by heating the samples for 5 min at 95 °C. Further analyses were performed by Western blot (section 2.5.8).

### **2.5.11 *In vitro* measurement of lysosomal hydrolase activity**

For the measurement of lysosomal hydrolase activity, 10 µl of brain lysate was mixed with 100 µl substrate solution (10 mM) listed on Table 9 and incubated for 30 min ( $\beta$ -hexosaminidase) or 3 h ( $\beta$ -glucocerebrosidase and  $\beta$ -glucuronidase) at 37 °C in an orbital shaker (125 rpm). As a blank value, samples were incubated without substrate. The reaction was stopped by addition of 1000 µl 0.4 M glycine/NaOH pH 10.4. Absorbance of each sample was measured at 405 nm using a Synergy HT spectrometer (Biotek) and percentage of enzyme activity was further calculated.

### **2.5.12 *Nuclease activity assay***

#### MES buffer

50 mM MES, pH 4.5

100 mM NaCl

#### 10X TBE buffer

1 M Tris

1 M Boric acid

0.02 M EDTA

Pld3 nuclease activity was analyzed by denaturing polyacrylamide gel electrophoresis as previously described by Gavin et al., 2018. Therefore, 50 µg of lysate (section 2.5.1) was incubated with 5 µM ssDNA (Table 14) in *MES buffer* pH 4.5 for the indicated time at 37 °C. Nuclease reaction was deactivated by incubation at 95 °C for 5 min and sample was mixed with 6X DNA loading dye. DNA was separated on a vertical chamber using a 20 % denaturing polyacrylamide gel in 1X Tris-Borate-EDTA (*TBE buffer*) applying a current of 60 V for 6 h. To monitor the progress of the electrophoresis, a GeneRuler Ultra Low Range DNA Ladder was used. DNA gel was either incubated at RT in 1X SYBR™ Gold Nucleic

Acid Gel Stain for 5 min or in an Ethidium Bromide (EtBr) bath for 30 min. For EtBr staining, gels were visualized under UV light. For SYBR Gold staining, acquisition was performed with the Odyssey® FC Imaging system at 600 nm and visualized with the Image Studio Software (LI-COR).

## 2.6 Animal experimentation

### 2.6.1 Animal housing

Animal housing was established at the “Victor-Hensen-Haus” at the University of Kiel under the special care of animal keepers. All mice were kept in individually ventilated cages (IVC) to generate a pathogen free environment. The temperature of the room was maintained between 19 – 22 °C with a humidity of 45 – 60 % and conditions of 12 hours with light followed by 12 hours of darkness. Animal handling and care was performed in agreement with the German animal welfare law according to the guidelines of the Christian Albrecht University of Kiel. Experiments with mice were approved by the Ministry of Energy, Agriculture, Environment and Rural Areas of Schleswig Holstein under the reference numbers V242-4255/2018 (mice with deficient lysosomal proteins and proteases) and V242-18325/2016 (generation of KO lysosomal proteins in the 5XFAD Alzheimer mouse model).

### 2.6.2 Breeding strategies

The *Pld3*-deficient mouse used for this study was purchased from the Wellcome Trust Sanger Institute, corresponding to the allele *Pld3<sup>tm1e(EUCOMM)Wtsi</sup>*. The knockout (KO) strategy is based in gene trap technology, by the insertion of a reporter-tagged cassette in intron 9 containing an artificial 5'-splice acceptor (SA) followed by an IRES:*lacZ* reporter coding for  $\beta$ -galactosidase (Figure 8). Splicing from the splice donor sites in the chromosomal gene to the splice acceptor sites in the reporter gene results in the fusion of *Pld3* upstream exon sequences to the reporter gene, disrupting the gene function. *Pld3* KO mice were already available when this study was initiated.

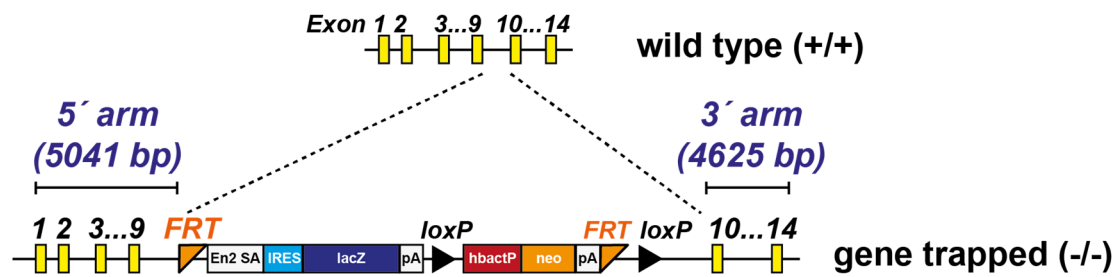


**Figure 8** | Schematic representation of the gene-trap cassette for the generation of Pld3 KO mice.

### Generation of 5xFAD Pld3<sup>-/-</sup> mice

The 5xFAD mouse (Tg6799 line) was purchased from The Jackson Laboratory. These transgenic mice overexpress mutant human APP(695) with the Swedish (K670N, M671L), Florida (I716V), and London (V717I) Familial Alzheimer's Disease (FAD) mutations along with human PS1 harboring two FAD mutations, M146L and L286V. Both transgenes are regulated by the mouse *Thy1* promoter to drive overexpression in the brain (Oakley et al., 2006). Schematic representation of 5xFAD Pld3<sup>-/-</sup> is shown in Figure 9.

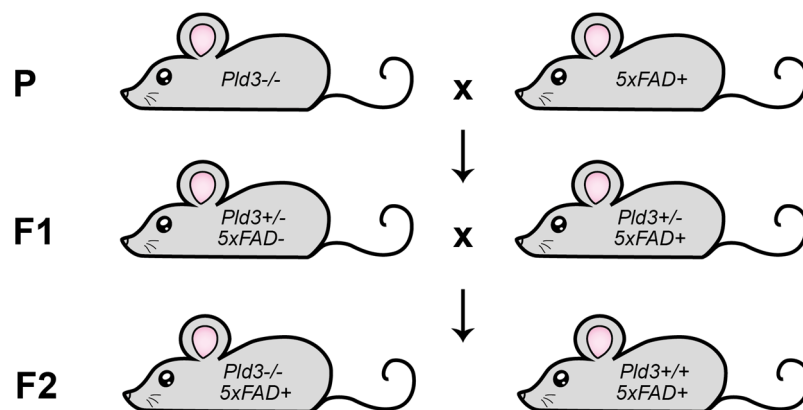


**Figure 9** | Schematic representation of 5xFAD Pld3<sup>-/-</sup> mice.

To maintain the breeding colony with the desired phenotype of the mice used for this study, a one-to-one long term mating was performed until pregnancy. After birth, the litters were weaned three weeks after and an ear or tail biopsy was taken for further genotyping (section 2.6.3).

### 2.6.3 Tail or ear biopsy and isolation of genomic DNA

For mice genotyping, either a tail or an ear biopsy was taken. Tail biopsy was collected between weeks 4 and 6 after birth. Ear biopsies were taken at any time point after weaning. The tissue was digested overnight in DirectPCR® Lysis Reagent Tail (Viagen Biotech) containing 0.3 mg/ml proteinase K at 55 °C and vigorous shaking. The next day, inactivation of proteinase K was performed at 85 °C for 45 min and debris was pelleted by centrifugation at 13.000 rpm for 2 min. Isolated genomic DNA was directly used for genotyping (section 2.6.4).

### 2.6.4 Genotyping by polymerase chain reaction (PCR)

In order to distinguish between the mutant and the wild-type alleles of *Pld3*, *TLR9* and *5xFAD*, genotyping of the different mouse lines used in this study were analyzed by polymerase chain reaction (PCR). Therefore, isolated genomic DNA (section 2.6.3) was incubated with specific oligonucleotides (Table 12) and a heat-stable DNA polymerase (Table 21 and Table 22) and PCR product was further visualized by agarose gel electrophoresis (section 2.2.6).

**Table 21. PCR components for genotyping determination**

<i>Pld3</i>	µl	<i>TLR9</i>	µl	5xFAD	µl
10X DreamTaq™ buffer	5	10X DreamTaq™ buffer	5	10X DreamTaq™ buffer	5
dNTP Mix (10 mM)	1.25	dNTP Mix (10 mM)	1.25	dNTP Mix (10 mM)	1
Fw primer (20 µM)	0.95	WT2 primer (10 µM)	0.5	Transgene fw (20 µM)	2.5
WT rev. primer (20 µM)	0.63	Extra primer (10 µM)	0.5	Transgene rev. (20 µM)	2.5
CAS R1 primer (20 µM)	0.63	Neo primer (10 µM)	0.5	Internal pos. control fw	1.3
Template DNA	2	Template DNA	1	Internal pos. control rev	1.3
DreamTaq™ (5 U/µl)	0.38	DreamTaq™ (5 U/µl)	0.38	Template DNA	3
H <sub>2</sub> O ad 50 µl	39.2	H <sub>2</sub> O ad 50 µl	40.9	DreamTaq™ (5 U/µl)	0.33
				H <sub>2</sub> O ad 50 µl	33.2



**Table 22. PCR cycle conditions applied for genotyping**

	<i>Pld3</i>			<i>TLR9</i>			<i>5xFAD</i>		
Step	° C	t (s)		° C	t (s)		° C	t (s)	
<i>Initiation</i>	94	180		94	180		94	180	
<i>Denaturation</i>	94	30		94	30		94	30	
<i>Annealing</i>	62	40	35 x	62	40	35 x	52	60	35 x
<i>Extension</i>	72	40		72	40		72	60	
<i>Final extension</i>	72	180		72	180		72	120	
<i>Hold</i>	4	∞		4	∞		4	∞	

### 2.6.5 Mice perfusion for organ extraction and euthanasia

Mice perfusion was performed in order to rapidly and uniformly preserve the tissues in a life-like state. Accordingly, mice were anesthetized via intraperitoneal injection (30G, 0.3 mm x 8 mm, BD Micro-Fine™) with a Ketamin/Rompun mixture (10 % Ketamine and 2 % Rompun) prepared in 0.9 % (w/v) NaCl and mice received a dosage of 10 µl per g body weight. Once the animal reached a surgical plane of anesthesia, an incision was done through the abdominal wall and further through the diaphragm to expose the pleural cavity. The ribs were cut along the sides and the sternum was lifted away to provide a major view of the heart. The perfusion needle was passed through the left ventricle and finally an incision was made to the animal's right atrium using a scissor. Mouse was first perfused with 20 ml of 0.1 M PB and further fixed with 30 ml of fresh prepared 4 % PFA with a rate of 5 ml/min (11 Plus, Harvard Apparatus). After proper fixation, desired tissues were collected and post-fixed for 4 h with 4 % PFA at RT and later stored at 4 °C. For fluorescence staining, tissues were incubated overnight with a 30 % sucrose solution at 4 °C and protocol was followed as described (section 2.4.1). For the analysis of tissue biochemistry, mice were sacrificed by cervical dislocation.

### 2.6.6 Behavioral studies

Motor coordination and equilibrium were tested on an accelerating rotarod (MED Associates Inc., St. Albans, Vermont, US). A training with constant speed (4 rpm, 2 min) was performed, followed by four 5-min trials with 10-min intertrial intervals. Rotaring

rod was accelerated from 4 to 40 rpm in 5 min, and the time until they dropped from the rod was recorded. Additionally, the standard deviation of standardized drop latencies for each animal was calculated to evaluate the variability of performance. All behavioral studies were performed in collaboration with Dr. Stijn Stroobants.

## **2.7 Microscopy**

### **2.7.1 *Confocal and fluorescence microscopy***

Cell images were analyzed with an Olympus FV1000D Laser Scanning Confocal Microscope (Model: FV10-292-115, inverted microscope) with a 100x lens (UPLSAPO 100x NA: 1.40) and 2.5% zoom. Acquisition was performed with the FV10-ASW 4.2 Viewer software (Olympus Europa GmbH, Germany). Tissue images were analyzed with the Inverted Microscope Leica DMI8 (20x lens) and acquisition was performed with the LAS X Software (Leica).

### **2.7.2 *Electron microscopy***

Cells were first fixed with warm 8% paraformaldehyde (PFA) and 0.2% glutaraldehyde (GA, Merck KGaA) in PB solution (pH 7.4). After 5 min, fixative was replaced with 4% PFA and 0.1% GA solution in PB for 1 h. Cells were washed with PBS, scratched with a cell scraper, transferred to an Eppendorf tube and centrifuged at 1.000 rpm. Supernatant was replaced with 2% PFA solution. Further sample processing was performed with the collaboration of Michaela Schweizer at the Center of Molecular Neurobiology, University Medical Center Hamburg-Eppendorf. In brief, for post-embedding double immunogold-labeling, small pieces of cryoprotected cell pellets (2.3 M sucrose) were mounted on specimen holders and immersed in liquid nitrogen. Ultrathin sections (70 nm) were cut and labeled according to Slot and Geuze, 2007. Briefly, sections were collected on Carbon-Formvar-coated nickel grids (Science Services GmbH, Germany). Antibodies, mouse anti-LAMP1 (Pharmingen) and rabbit anti PLD3, were detected with 15 nm and 10 nm large protein A gold secondary antibodies (G. Posthuma, University Medical Center Utrecht), respectively. Ultrathin sections (60 nm) were examined in an EM902 (Zeiss, Germany). Pictures were taken with a MegaViewIII digital camera (A. Tröndle, Moorenweis, Germany).

## 2.8 Quantification of Western blot bands and immunocytochemistry /immunohistochemistry images

### *Pearson correlation coefficient (PCC)*

Co-localization analyses with different intracellular markers were quantified by Pearson correlation coefficient (PCC) using the Olympus FV10-ASW 4.2 Viewer software.

### *Western blot analysis by densitometry*

For Western blot analyses by densitometry, the integrated density was calculated with ImageJ. Raw values were used for the quantification of the respective ratios of the proteolytic fragments, and the average of the untreated cells was set as 100% and represented as 1 in each independent experiment (untreated; n = 3). The ratio of the treated cells is shown relative to the untreated cells.

### *Quantification of microglial/astrocytes markers in brain sections*

CD68 and GFAP intensity quantification was analyzed by Fiji, with special plugins provided by Dr. Jan Brocher, BioVoxel 2017-2018. Therefore, all pictures were taken with the same acquisition parameters as described on section 2.7.1. Image processing was performed by applying the following steps: (1) The region of interest was drawn using the freehand selection tool, (2) >Filter Menu >Median...(radius=2 pixels), (3) >Process >Subtract background...(Rolling ball radius=100 pixels), (4) >Process >Enhance contrast...(saturated pixels=0.1 %, normalize active), (5) >Adjust Menu >Auto Threshold (method=Intermodes white), (6) Measure (Area, Mean). The <Area> and <Mean> output values were multiplied and further normalized to the wild-type.

## 2.9 Statistical analyses

All experiments were repeated at least three times and data analyses were performed with unpaired, two-tailed t-test using the GraphPad Prism 7.04. Significant values were considered at  $p < 0.05$ . Values are expressed as mean  $\pm$  SEM, and significance is designated as \* $p < 0.05$ , \*\* $p < 0.005$ , and \*\*\* $p < 0.0001$ .



### 3 RESULTS

#### 3.1 Cellular and biochemical characterization of phospholipase D3 (PLD3)

Due to the structural similarities with phospholipase D-related proteins, including the presence of two conserved HKD motifs, PLD3 has been grouped as a member of the phospholipase D family. PLD3 was characterized as a type II transmembrane protein associated with the endoplasmic reticulum (Munck et al., 2005; Osisami et al., 2012), but no canonical substrate has been identified. Independent genetic and proteomic approaches have identified PLD3 as a lysosomal protein (Sleat et al., 2008; Lübke et al., 2009; Palmieri et al., 2011; Sleat et al., 2013). Therefore, we first aimed to make a detail description of PLD3 at the cellular and biochemical level.

##### 3.1.1 *PLD3 is a lysosomal protein*

In order to analyze the expression and subcellular distribution of PLD3, an antibody was generated against an N-terminal peptide of murine PLD3 (mPLD3) encompassing the amino acids between position 1 and 20 (referred along the text as N-terminal specific PLD3 antibody, Figure 10A, upper panel). Additionally, a commercial antibody raised against the luminal domain of human PLD3 (hPLD3) was used (referred along the text as luminal specific PLD3 antibody, Figure 10A, lower panel). To check for PLD3 expression, HeLa cells and Neuroblastoma 2a (Neuro2a) cells were transfected with either human PLD3 (*hPLD3*) or mouse PLD3 (*mPLD3*) and further analyzed by Western blot using both described antibodies. Untransfected cells were used as a negative control to test for antibody specificity (Figure 10B). With the N-terminal specific anti-PLD3 antibody, a signal was observed at around 70 kDa, with a double band pattern corresponding to the full-length (fl) protein, probably caused by different glycosylation forms. A signal with a lower molecular weight (~12 kDa) was detected with the same antibody (designated as “nt”). Using the PLD3 antibody directed against the luminal domain, a similar signal was observed at ~70 kDa (fl PLD3, Figure 10B). Interestingly, another PLD3-specific polypeptide appeared at ~50 kDa (designated as “soluble”). The same protein pattern is recognized with both mouse and human PLD3 as well as in both cell types. It should be noted that, the 12 kDa signal is slightly lower for *mPLD3* compared to *hPLD3* transfected

cells, which might be due to three amino acid changes within the N-terminal sequence possibly leading to a lower migration. These differential protein pattern observed with both antibodies suggest that PLD3 is proteolytically processed and/or modified by posttranslational modifications, like glycosylation.

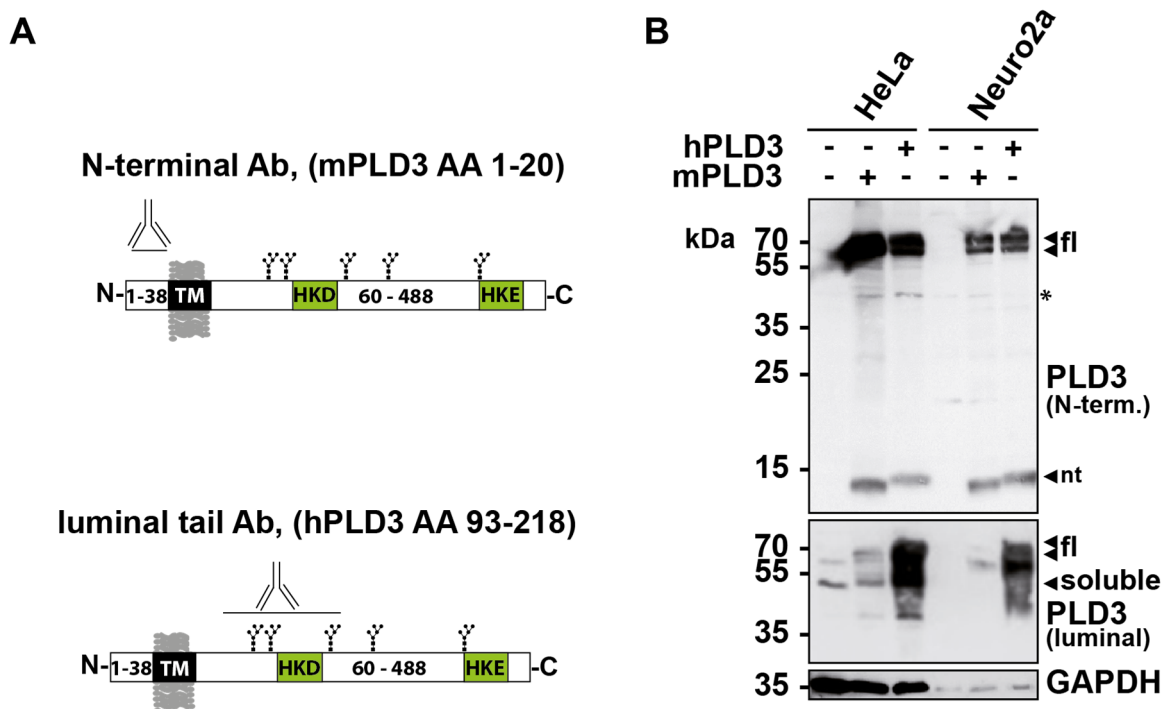


**Figure 10 | Western blot analysis of PLD3 transfected cells.** *A*, Schematic representation of the epitope binding sites of PLD3 antibodies. hPLD3, human PLD3; mPLD3, mouse PLD3. *B*, human and murine *PLD3* cDNA were transiently transfected in HeLa or Neuro2a cells followed by detection with the antibodies directed against the N-terminal and luminal domain of PLD3. Specific PLD3 signals are indicated with black arrowheads. \* indicates nonspecific signal. fl, full-length; nt, N-terminus; TM, transmembrane domain; HKD, HxKxxxxD motif; Ab, antibody; AA, amino acids. GAPDH is presented as a loading control.

Next, the subcellular distribution of PLD3 was analyzed. To this end, HeLa cells were transfected with *hPLD3* and immunolabeled with both N-terminal and luminal specific PLD3 antibodies together with antibodies against proteins from the endoplasmic reticulum (KDEL), Golgi apparatus (GM130), early endosomes (EEA1), late endosomes (LBPA) and lysosomes (LAMP2). Quantification of co-localization was determined by Pearson correlation coefficient (PCC) as a degree of linear relationship between the localization of PLD3 and each marker (Figure 11).

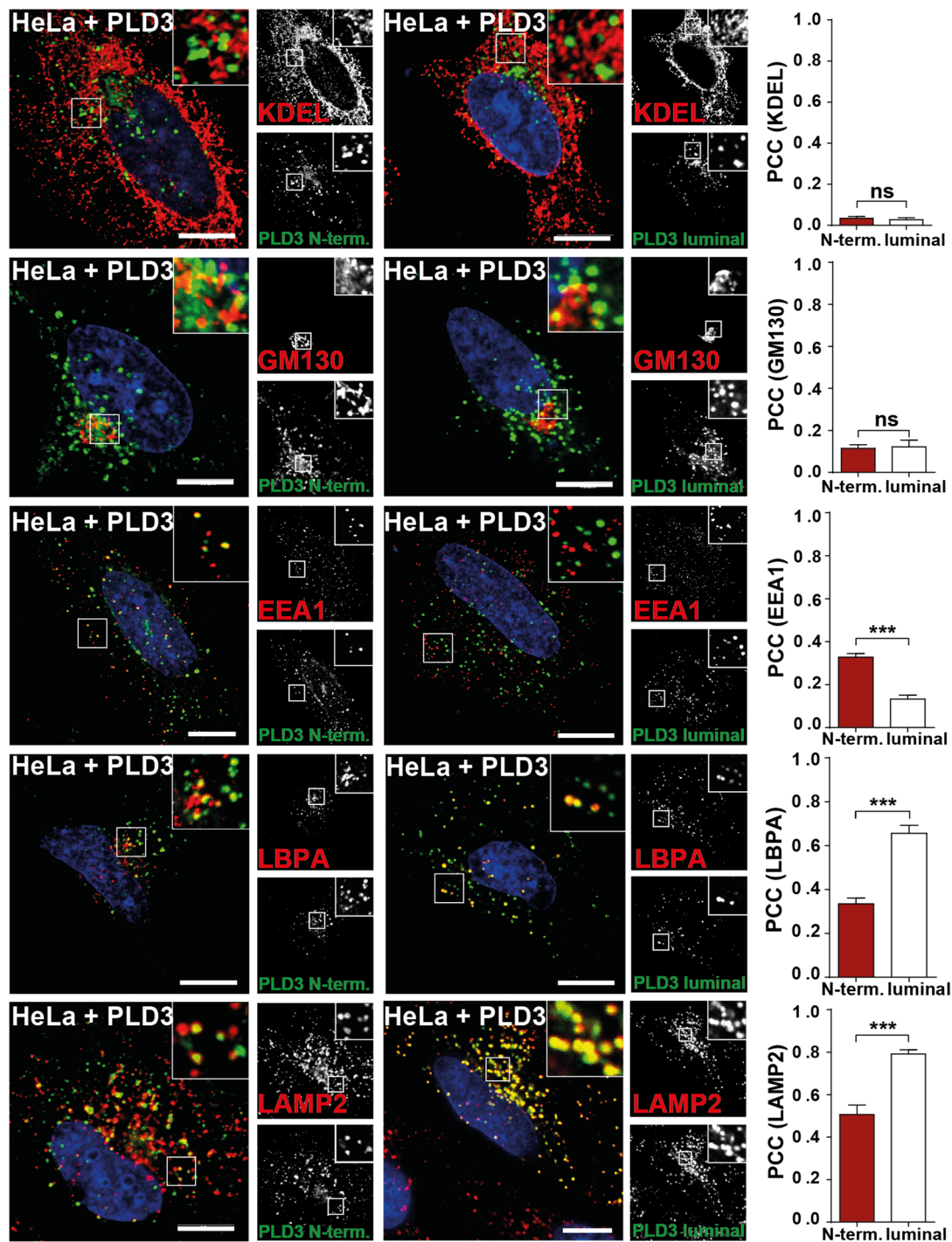


**Figure 11 | PLD3 localizes to late endosomes and lysosomes.** HeLa cells were transiently transfected with *hPLD3* and co-stained with the indicated PLD3 antibodies against the N-terminal and luminal domain of PLD3 (green) and different markers against intracellular proteins (anti-KDEL, anti-GM130, anti-EEA1, anti-LBPA and anti-LAMP2 antibodies, red). The nucleus was stained with DAPI (blue). Insets show enlarged regions of the cell. In the graphs, the Pearson correlation coefficient (PCC) was calculated for each PLD3 specific antibody staining and each corresponding intracellular marker. Error bars represent SEM. \*\*\* $p < 0.001$ ; unpaired Student's t test ( $n = 12$ ). Scale bar, 10  $\mu\text{m}$ .

Confocal images and its respective quantification (PCC) revealed only minor co-localization of both PLD3 specific antibody staining with the endoplasmic reticulum (ER) and Golgi organelle markers (Figure 11). A partial co-localization with early endosomes (EE) was observed only with the anti-PLD3 N-terminal antibody, which was higher in comparison with the staining of antibody against the PLD3 luminal domain. In contrast, an increase in co-localization between the staining of the luminal specific anti-PLD3 antibody and late endosomes was detected, which was even more pronounced with the lysosomal marker (PCC ~0,8). These results suggest that PLD3 has a differential vesicular distribution in subcellular compartments. While full-length and N-terminal PLD3 are localized to early and late endosomes, a possible soluble fraction of PLD3 is preferentially localized to lysosomes.

To validate the PLD3 localization at the endogenous level, cells from the neuroblastoma cell line SH-SY5Y (Figure 12A) or human brain sections (Figure 12B) were stained with the luminal specific anti-PLD3 antibody and the lysosomal marker anti-LAMP1 antibody. No endogenous staining with the PLD3 specific N-terminal antibody was detected (data not shown). Confocal microscopy images and PCC quantification confirm that PLD3 is found in lysosomes under endogenous conditions (Figure 12A). Interestingly, in the stained cortical human brain region, PLD3 was mostly found in neuronal-like cells (in accordance with their cellular shape (Figure 12B).

### **3.1.2 *Proteolytic processing of PLD3***

#### *3.1.2.1 PLD3 is proteolytically processed, yielding a stable soluble form*

The distinctive PLD3 signal patterns observed with the different N-terminal and luminal specific antibodies (Figure 10B) suggest that posttranslational modifications are implicated. To test if the 50 kDa PLD3 signal detected with the luminal specific antibody correspond to a possible N-glycosylated polypeptide or if it is derived from proteolytic processing, lysates of *hPLD3* transfected HeLa cells (Figure 13A) or mouse brain tissue (Figure 13B) were treated with either endoglycosidase H (EndoH), which cleaves asparagine-linked mannose rich oligosaccharides, or with N-glycosidase F (PNGaseF), which cleaves all types of N-linked (Asn-linked) glycans generated in the Golgi apparatus (O'Neill, 1996).



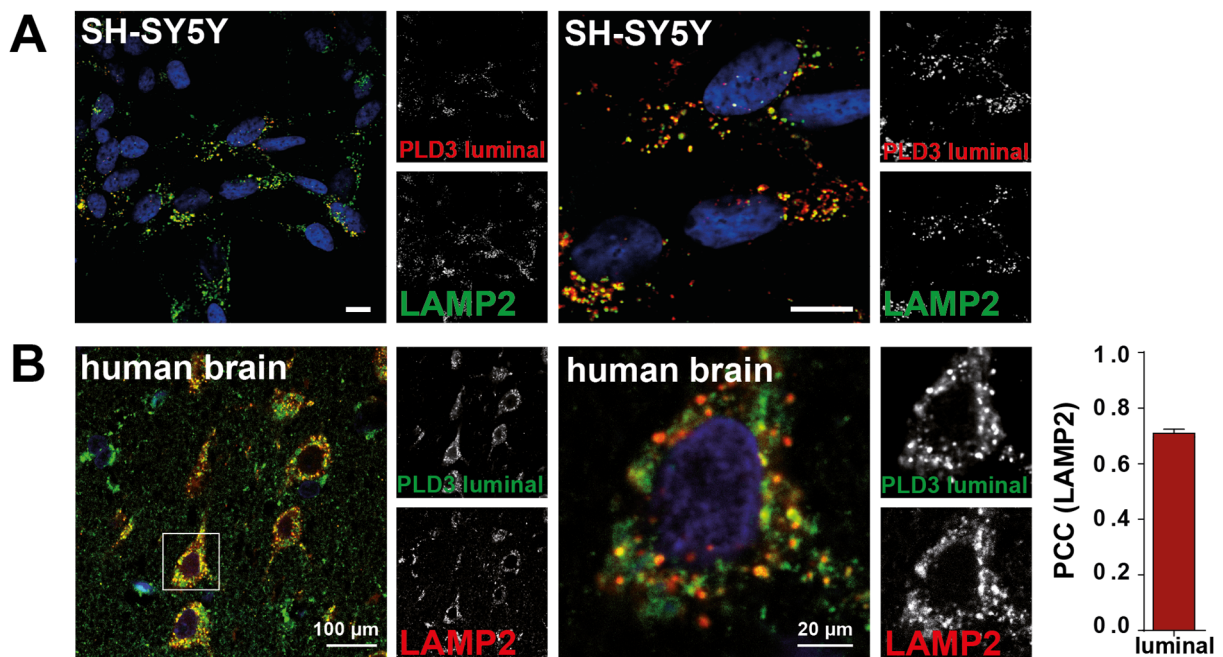


**Figure 12 | Endogenous PLD3 localizes to lysosomes.** PLD3 was co-stained endogenously in SH-SY5Y cells (A) and human brain (B) with the antibody against the luminal domain of PLD3 and an antibody against the intracellular lysosomal marker (LAMP2). *A*, neuroblastoma SH-SY5Y cells were differentiated for 4 days with retinoic acid (20 μM) and co-stained with the luminal PLD3 antibody (red) and the lysosomal marker LAMP2 (green). Scale bar, 10 μm. *B*, immunofluorescence of human brain sections (cerebral cortex) shows co-localization of endogenous PLD3 (green) and LAMP2 (red). Staining of human brain sections was performed by Christian Bernreuther (Institute of Pathology, UKE, Hamburg, Germany). Pearson correlation coefficient (PCC) is shown in the graph.

Western blot analyses of EndoH-treated samples revealed that only a partial shift of full-length but not of the luminal (50 kDa) PLD3 was detected using the N-terminal specific anti-PLD3 antibody. In contrast, a complete shift of full-length and soluble PLD3 were observed in samples treated with PNGaseF, detected with both antibodies. As a positive control of glycosidase treatment, an antibody against  $\beta$ -glucocerebrosidase ( $\beta$ -GC) was used, which is known to be modified by both complex- and high-mannose-type glycans (Erickson et al., 1985). This experiment led to the conclusion that the 50 kDa-form of PLD3 is derived from proteolytic processing and that PLD3 is mainly modified with complex-type glycans.

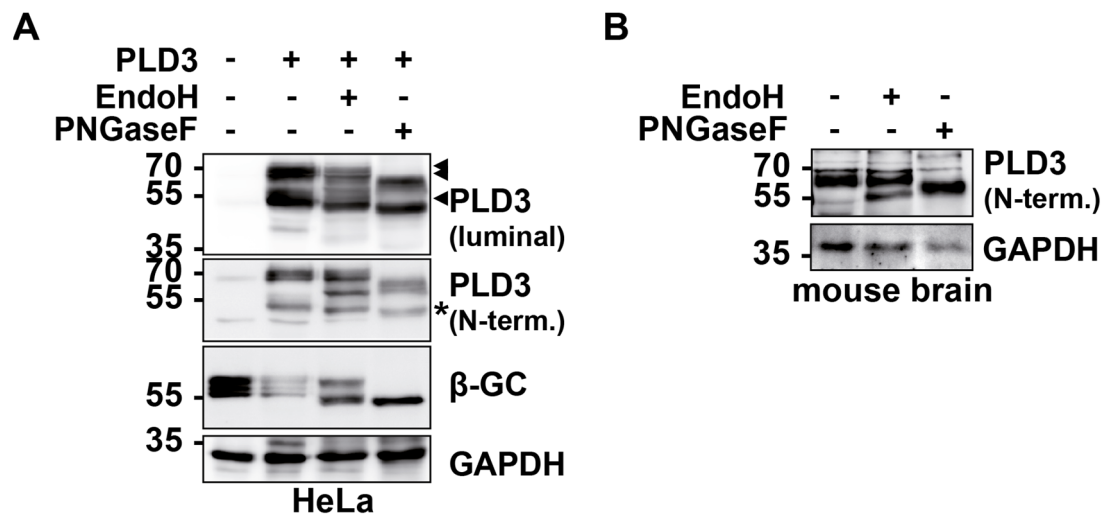


**Figure 13 | PLD3 is N-glycosylated.** *PLD3* transfected HeLa cells (A) and mouse brain (B) were treated with the glycosidases EndoH and PNGaseF followed by immunodetection with both N-terminal and luminal specific anti-PLD3 antibodies (specific signals are shown with arrowheads).  $\beta$ -glucocerebrosidase ( $\beta$ -GC), known to be modified with both complex – and high – mannose – type glycans, is included as a positive control of glycosidase treatment. \* indicates a signal derived from previous incubation with the luminal antibody and inefficient stripping of the membrane. GAPDH is presented as a loading control.

To gain a deeper insight which positions are *N*-glycosylated, single *PLD3* mutants were generated by substitution of each asparagine amino acid to alanine. Sequence analysis predicts 7 consensus *N*-glycosylation sites in the full-length *PLD3* protein (N97, N102, N132, N236, N284, N387 and N432). Accordingly, HeLa cells were transfected with either *PLD3 WT* or with each of the single glycosylation mutants (*PLD3 N97A*, *PLD3 N102A*, *PLD3 N132A*, *PLD3 N236A*, *PLD3 N284A* and *PLD3 N432A*). In addition, a PNGaseF treated sample was included as a positive control of complete glycan cleavage (Figure 14). Western blot analyses showed that the full-length and soluble *PLD3* signals of several *N*-glycosylation mutants shifted to a slightly lower molecular weight, except for the *PLD3 N102* expressing mutant. Different molecular weight signals of full-length *PLD3* were also observed with both antibodies, suggesting that *PLD3* is not only *N*-glycosylated at multiple sites, but that different combinations of *N*-glycosylation might occur at different asparagine positions (Figure 14). Of note, in a longer exposed membrane, several mutants showed an additional signal at ~40 kDa, peptide that also shifted with the PNGaseF-treated sample, arguing for a possible, less pronounced, alternative cleavage site for *PLD3*. For the N236 and N432A mutants, *PLD3* cleavage was strongly reduced, suggesting that these amino acids are highly conserved and important for proper *PLD3* folding and subsequent

proteolytic processing. It is worth mentioning that the PLD3 N-terminal peptide did not shift for any of the *N*-glycosylation mutants and neither after PNGaseF-treatment. This observation suggests that PLD3 cleavage occurs before amino acid 97, leading to the generation of an N-terminal peptide with a theoretical molecular weight of ~11 kDa.

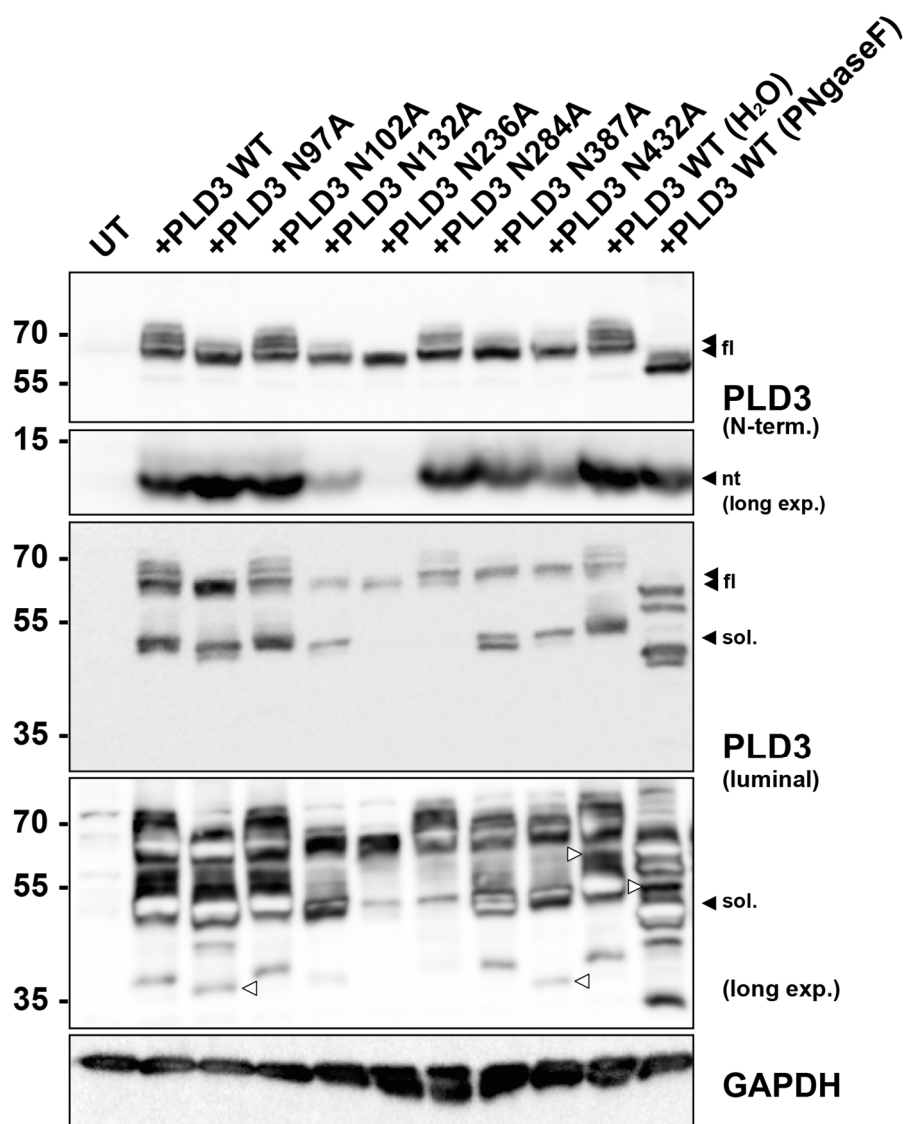


**Figure 14 | PLD3 is N-glycosylated at multiple sites.** Western blot analysis of HeLa cells transiently transfected with *PLD3* WT and different *N*-glycosylation mutants where the asparagine (N) amino acid was mutated to alanine (A). Additionally, *PLD3* transfected cells were treated with PNGaseF as a positive control cleaving all protein glycans. Immunodetection was performed with both N-terminal and luminal specific anti-*PLD3* antibodies (specific signals are shown with arrowheads). Open arrowheads represent possible alternative cleavage site of *PLD3*. \* indicates unspecific signal. GAPDH is presented as a loading control. fl, full-length *PLD3*; sol., soluble *PLD3*; long exp., long exposure.

To investigate if the N-terminus of PLD3 is linked to the soluble domain via disulfide bonds, lysates of *hPLD3* transfected HeLa cells were analyzed by immunoblot under reducing and non-reducing conditions (with/without  $\beta$ -mercaptoethanol,  $\beta$ -ME) (Figure 15). After detection with both PLD3 specific antibodies, only a small shift of full-length and luminal PLD3 was observed, which might be explained by different denatured conformations of the protein or intramolecular disulfide bonds with or without the reducing agent. This experiment led to the conclusion that the N-terminal and C-terminal PLD3 peptides are not linked via disulfide bonds and that mostly proteases are involved in the generation of the PLD3 cleavage products.

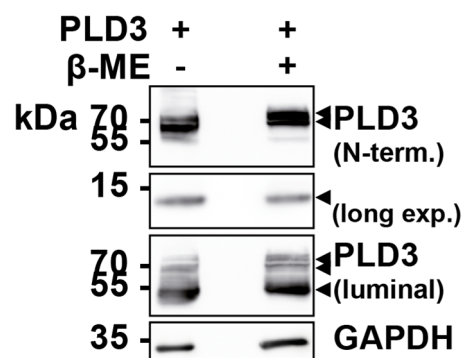


**Figure 15 | Reducing conditions do not affect the generation of PLD3 cleavage products.** Western blot analysis of *PLD3* transfected HeLa cells treated with or without  $\beta$ -mercaptoethanol ( $\beta$ -ME) do not reveal major changes on the generation of PLD3 fragments. Arrowheads indicate the PLD3 signal with both N-terminal and luminal anti-PLD3 specific antibodies. GAPDH is presented as a loading control.

To address the distribution of PLD3 in more detail, *hPLD3* transfected lysates of HeLa cells were fractionated using ultracentrifugation to separate them into a membrane and cytoplasmic (soluble) cell fraction. Immunoblot analyses revealed that full-length and N-terminal PLD3, both containing the transmembrane domain, are enriched in the membrane fraction, but no signal of these peptides was observed in the soluble fraction (left panel, Figure 16). On the other hand, the immunoblot incubated with the luminal PLD3 specific antibody (right panel, Figure 16) shows an enrichment of soluble PLD3, although a smaller signal was also detected in the membrane fraction. Antibodies against LAMP2 and GAPDH were used as a positive control of membrane bound- and cytosolic-proteins, respectively, indicating a suitable fractionation procedure.

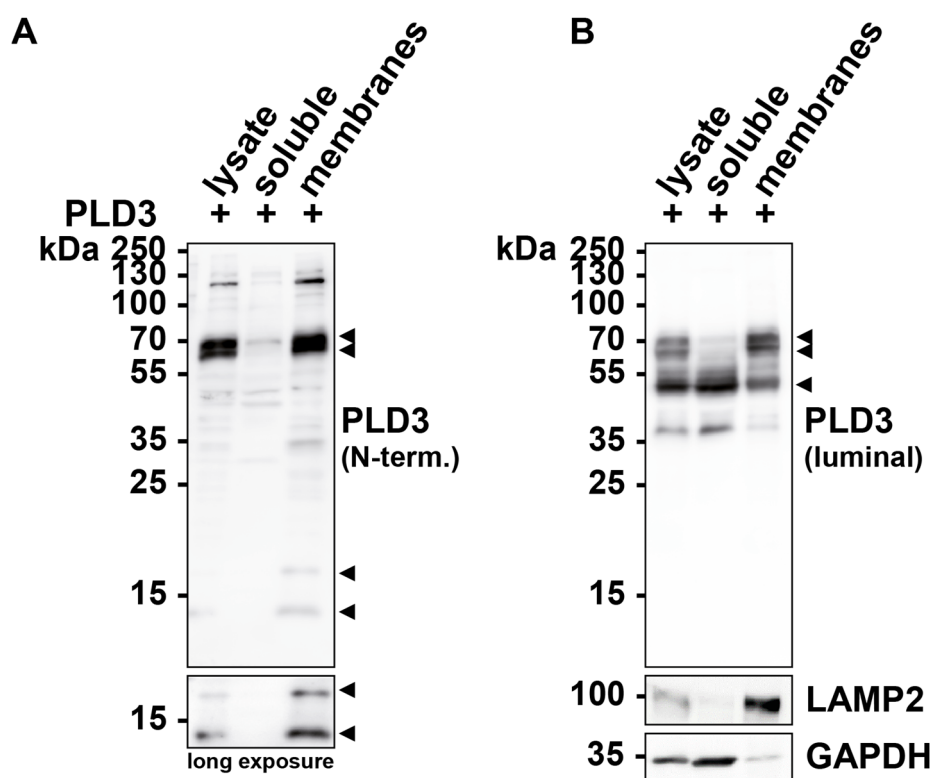


**Figure 16 | Membrane separation of *PLD3* transfected HeLa cells.** Transiently transfected *PLD3* HeLa lysates were subjected to membrane separation by ultracentrifugation into soluble and membrane proteins fractions and further immunoblotted using the N-terminal (A) or luminal (B) *PLD3*-specific antibodies. Arrowheads indicate *PLD3*-specific signals. GAPDH was used as a loading control and control for soluble proteins. LAMP2 is represented as a membrane protein control.

These findings were corroborated by immunofluorescence analysis of HeLa cells transfected with *hPLD3* and either myc-tagged *Rab5-WT* or *Rab5-Q79L*. Cells were further co-stained with specific antibodies against *PLD3* and antibodies against the intracellular membrane proteins myc (to recognize *Rab5*, Figure 17A) or against LAMP2 (Figure 17B). *Rab5-Q79L* represents a dominant active form of *Rab5* known to impair the maturation of early endosomes, leading to an enlargement of endo-/lysosome-positive vesicles upon overexpression, allowing better to distinguish between membrane-bound and cytosolic protein localization (Stenmark et al., 1994). A weak co-localization between *PLD3* and *Rab5-WT* was observed (Figure 17A, upper panels). In cells co-transfected with *Rab5-Q79L*, *PLD3* staining was mainly found in membrane-bound vesicles positive for *Rab5* (Figure 17A) and LAMP2 (Figure 17B), when labeled with the N-terminal specific *PLD3* antibody. On the other hand, labeling with the *PLD3* specific luminal antibody led to a homogenous soluble staining within the enlarged vesicles.



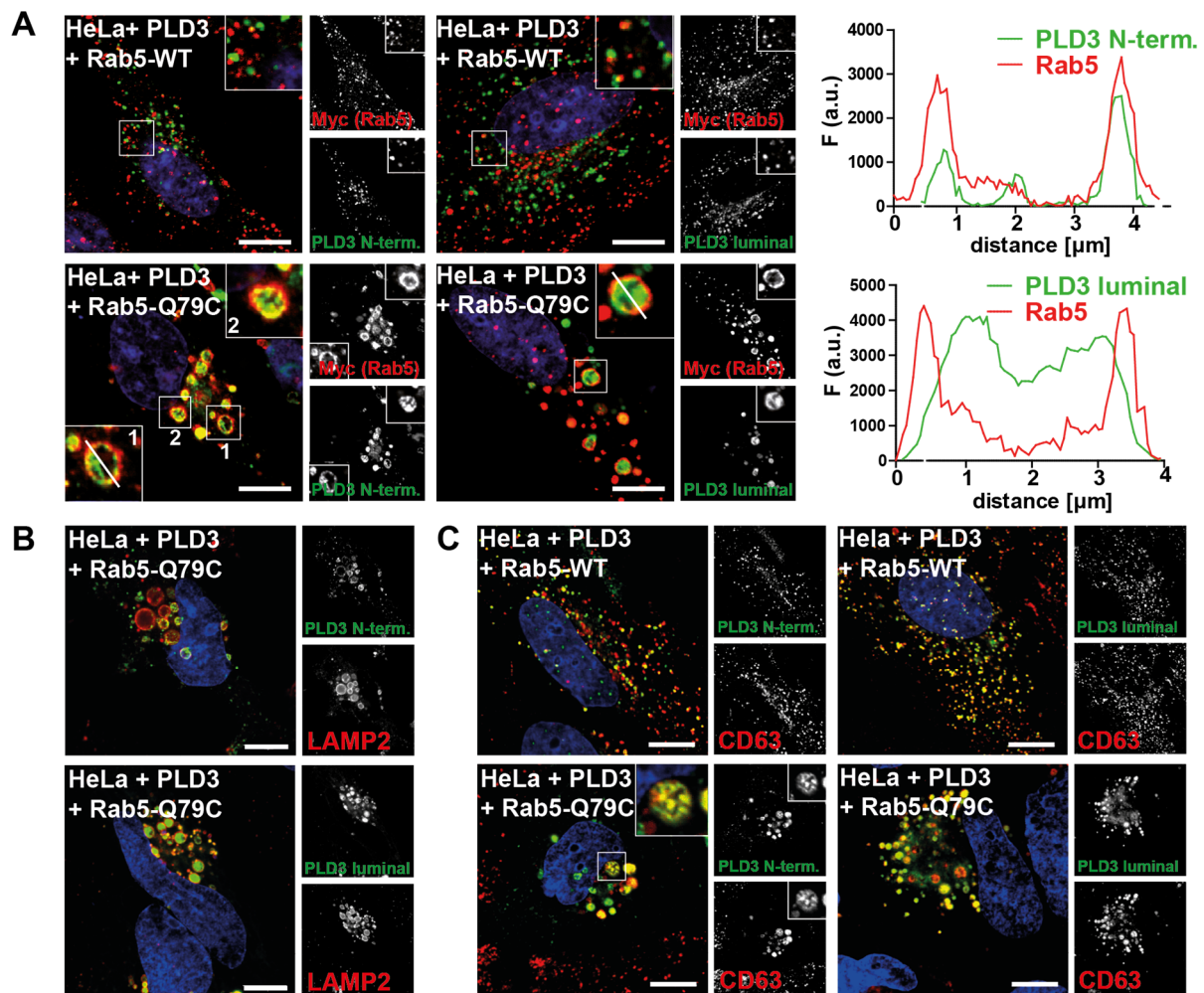


**Figure 17 | Membrane-bound and soluble PLD3 show different compartmentalization in lysosomes.** *A*, confocal microscopy of transfected HeLa cells with *PLD3* and myc-*Rab5* WT (upper panel) or the negative dominant mutant myc-*Rab5* Q79L (lower panel, red), followed by co-staining with the N-terminal and luminal *PLD3*-specific antibodies (green). Nuclei are stained with DAPI (blue). Inset 1: staining of membrane-bound *PLD3* with the N-terminal specific antibody. Inset 2: additional intraluminal vesicle-like staining is observed with the *PLD3* specific luminal antibody. For the vesicles labeled with a white line, profile plots are shown from a sequence of equi-spaced vertical spikes ( $\mu$ m) corresponding to each indicated antibody. F, fluorescence; a.u., arbitrary units. *B* and *C*, *PLD3* and *Rab5* co-transfected HeLa cells were stained using both *PLD3*-specific antibodies (green) and LAMP2 as a membrane-bound positive control (*B*) or CD63 as a marker of intraluminal vesicles (*C*). Scale bar, 10  $\mu$ m.

Of note, in addition to membrane-bound staining of *PLD3* with the *PLD3* specific N-terminal antibody, a distinctive punctate staining was also detected, which is clearly different from that observed with the *PLD3* specific luminal antibody, also shown in the profile plots (Figure 17A, right panel). This particular staining looks similar to intraluminal vesicles (ILVs), structures that are formed by membrane deformation and scission on the surface of endosomes (Henne et al., 2011). Indeed, after co-staining of

PLD3 with an anti-CD63 antibody (marker for intraluminal vesicles), a high level of co-localization was detected (Figure 17C). Percoll density centrifugation and subsequent analysis of *hPLD3* transfected HeLa cells confirmed the subcellular distribution of PLD3 (Figure 18). Western blot analyses of a series of Percoll fractions reveal that soluble PLD3 is progressively enriched in the later fractions (fractions 8 – 12), corresponding to lysosomal fractions, as observed by activity measurement of the  $\beta$ -hexosaminidase hydrolase (Figure 18, lower panel). Little co-fractionation was observed between the PLD3 luminal domain and the endoplasmic reticulum marker protein disulfide isomerase (PDI). In contrast, full-length PLD3 is distributed along the different fractions (fractions 1 – 10), except the lysosomal ones. These data suggest that membrane-bound PLD3 (either full-length or N-terminal PLD3 fragment) and its luminal domain are differentially distributed in the cell.

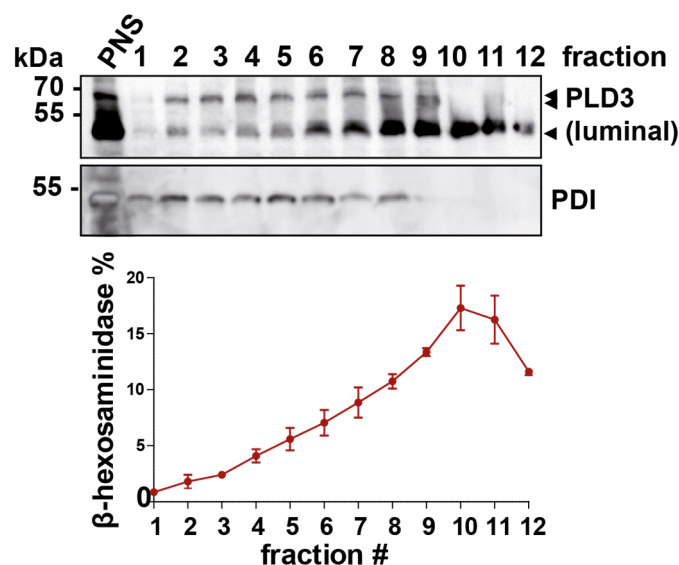


**Figure 18 | PLD3 shows distinct subcellular distribution as visualized by Percoll density centrifugation experiment.** *PLD3*-transfected HeLa cells were subjected to Percoll density centrifugation for organelle fractionation and further analyzed by immunoblotting using the PLD3-specific luminal antibody. The endoplasmic reticulum marker was detected with an antibody against PDI. PNS, post-nuclear supernatant.

### 3.1.2.2 Proteolytic processing of PLD3 is mediated by acidic cysteine proteases

To investigate in more detail the proteolytic processing of PLD3, different inhibitors affecting cellular sorting, acidification and proteolysis were added to the media of *hPLD3*-transfected HeLa cells and analyzed by Western blot. Further quantification of the luminal / full-length PLD3 ratio (Figure 19) as well as immunofluorescence analyses were performed (Figure 20). When applying inhibitors of intracellular trafficking like Brefeldin A and monensin, known to restrain the transport from endoplasmic reticulum to Golgi apparatus (Misumi et al., 1986) and from Golgi to early endocytic compartments (Tartakoff et al., 1978), respectively, a significant decrease of PLD3 cleavage products was observed using both PLD3-specific antibodies (Figure 19A). This result argues that protease cleavage occurs after PLD3 has left the ER.

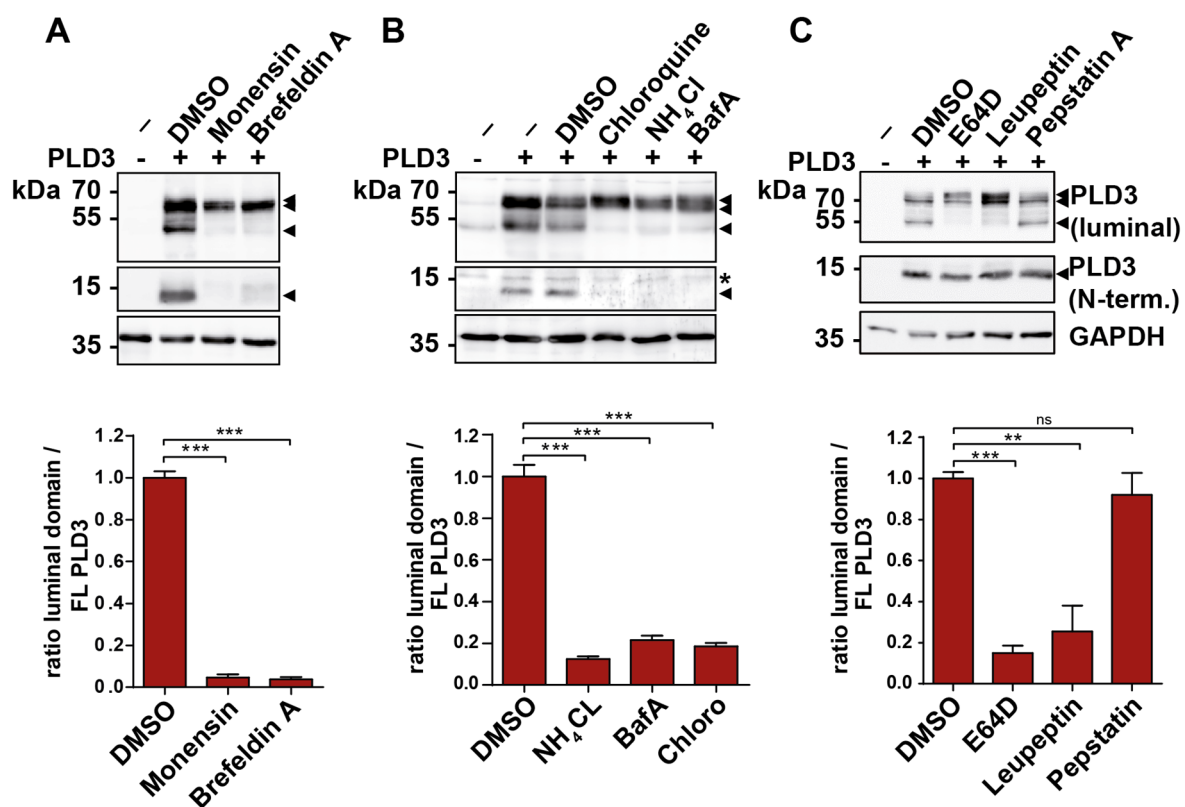


**Figure 19 | Proteolytic processing of PLD3 is mediated by acidic cysteine proteases.** Western blot analysis of *PLD3*-transfected cells treated with different inhibitors of intracellular transport monensin and brefeldin A (A), inhibitors interfering with lysosomal acidification chloroquine, NH<sub>4</sub>Cl and bafilomycin (B) and protease inhibitors E64D, leupeptin and pepstatin A (C) followed by immunodetection with the PLD3-specific N-terminal and luminal antibodies (specific PLD3 signal is shown with arrowheads). \* indicates unspecific signal. GAPDH is shown as a loading control. For each inhibitor, the ratio between the luminal domain and the full-length (fl) PLD3 is presented after densitometric quantification (lower panel). Error bars represent SEM. \*\*\*p < 0.001; \*\*p < 0.01; unpaired Student's t test (n = 3). ns, not significant.



A similar effect was observed with the different inhibitors of lysosomal acidification chloroquine, ammonium chloride (NH<sub>4</sub>Cl) and Bafilomycin A (Poole and Ohkuma, 1981), indicating that an acidic environment is required for the protease(s) involved in PLD3 cleavage, and that this process takes place in post-Golgi compartments (Figure 19B). To narrow down which classes of protease(s) are responsible for PLD3 cleavage, more specific inhibitors were used (Figure 19C). As shown by Western blot and its respective quantification, an effect on PLD3 proteolytic processing was only observed after addition of E64D, a potent cysteine protease inhibitor (Tamai et al., 1981) and leupeptin, a reversible and competitive inhibitor of cysteine, serine and threonine proteases (Aoyagi et al., 1969; Zimmerman and Schlaepfer, 1982). No changes on PLD3 processing were observed with pepstatin A, an aspartate protease inhibitor (Greenbaum and Sutherland, 1983). Interestingly, levels of the PLD3 N-terminus did not change upon incubation with E64D or leupeptin, suggesting that proteases of these classes are involved in the degradation of this short peptide. Analysis by immunofluorescence with the specified inhibitors revealed PLD3 retention in the ER after treatment with Brefeldin A (Figure 20). As expected, a decrease in the co-localization of PLD3 and LAMP2 was detected in Bafilomycin A-treated HeLa cells. A higher co-localization between PLD3 and LAMP2 was observed in cells treated with E64D (Figure 20).

### *3.1.2.3 Degradation of the PLD3 N-terminus is mediated by Cathepsin B and L*

As observed in Western blot analyses of E64D- and Leupeptin-treated HeLa cells (Figure 19C), there seems to occur a stabilization of the PLD3 N-terminus. To further address this observation, brain lysates of mouse strains deficient for the most abundant cysteine proteases cathepsin B (CtsB), cathepsin H (CtsH), cathepsin L (CtsL), legumain and the aspartate protease cathepsin D (CtsD) were analyzed by immunoblot (Figure 21A). Using both anti-PLD3-specific antibodies for detection, a cleavage of PLD3 could still be observed, even in the absence of the different proteases. However, only for the mouse brain lysates deficient for both cathepsin B and L, a striking increase of the PLD3 N-terminus was observed, together with a less pronounced increase of the luminal and full-length PLD3 (Figure 21A, lower panel, arrowheads), suggesting that these proteases might degrade the N-terminal short peptide.

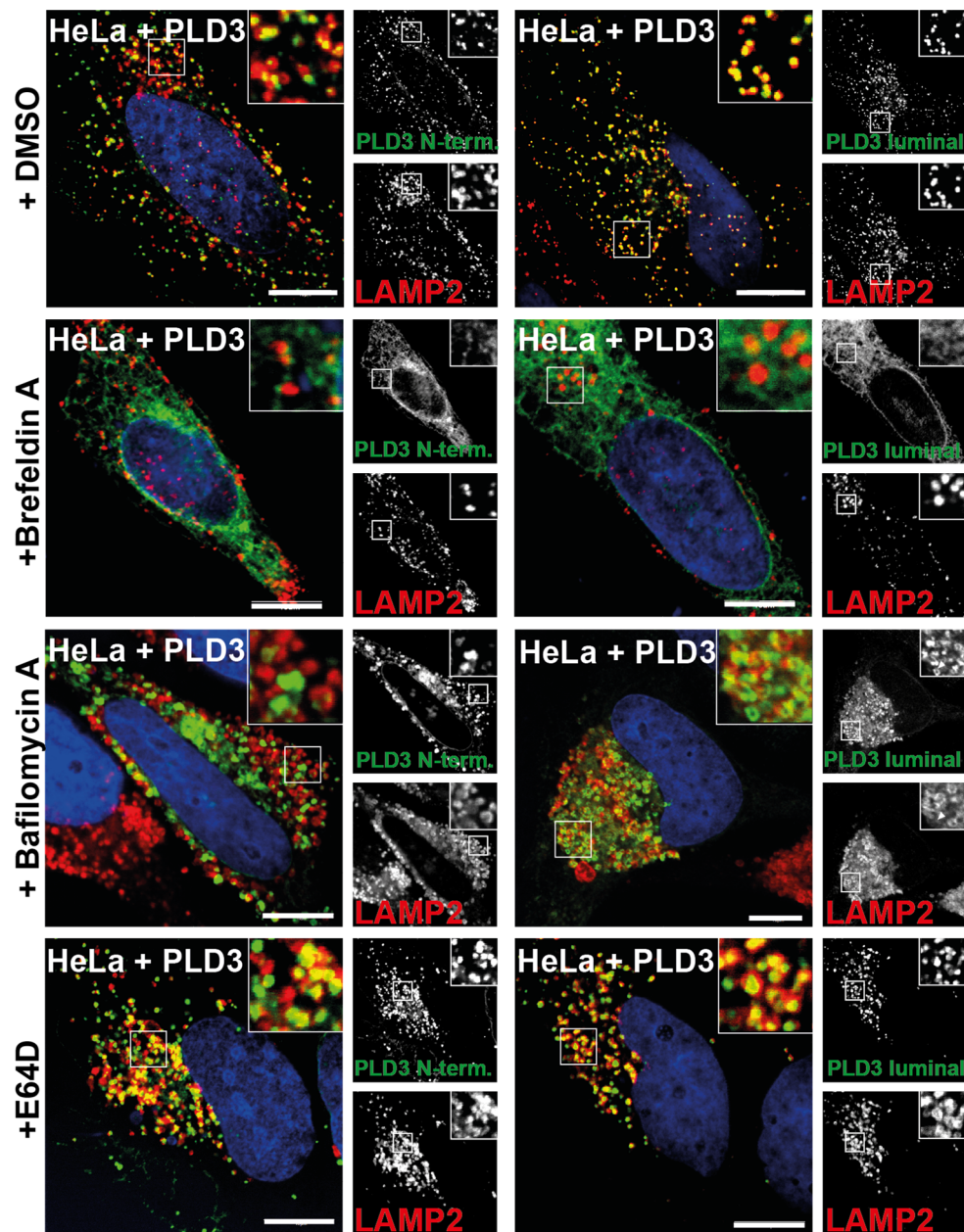


**Figure 20 | Confocal images of *PLD3*-transfected HeLa cells with different inhibitors.** *PLD3*-transfected cells were co-stained with the *PLD3*-specific N-terminal and luminal antibodies (green) and an antibody against the lysosomal marker LAMP2 (red) after overnight treatment with the indicated inhibitors. DMSO was used as a negative control. Nuclei are stained with DAPI (blue). Insets show enlarged regions of the cell. Scale bar, 10  $\mu$ m.

After transfection of *hPLD3* in wild-type (WT) or *CtsB*-, *CstL*- or *CtsB/L*-deficient mouse embryonic fibroblast (MEF) cells, a cleavage of the luminal *PLD3* domain was detected, along with an increase of the *PLD3* N-terminus in *CtsB/L* KO MEFs. These data indicate that cathepsin B and L are involved in the degradation of the *PLD3* N-terminus, but not in the initial *PLD3* cleavage or luminal peptide turnover, which is more stable and resistant to lysosomal proteolysis.

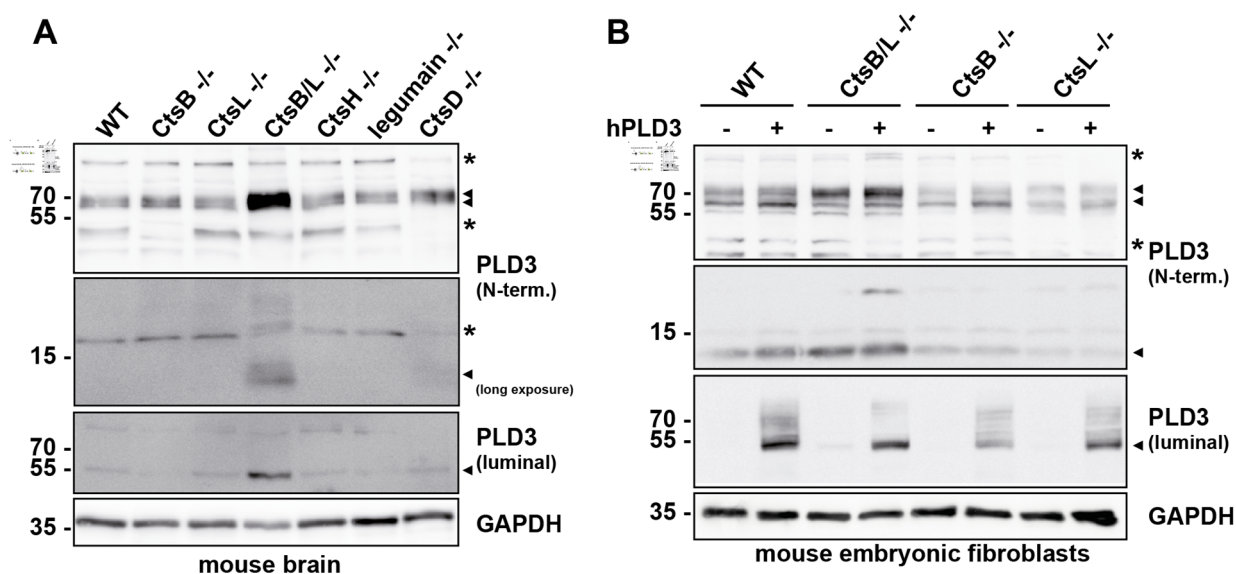


**Figure 21 | Degradation of PLD3 N-terminus is mediated by cathepsin B and L.** *A*, Western blot analysis of brain lysates of WT and mouse strains deficient for different cysteine proteases (CtsB, CtsL, CtsB/L, CtsH, CtsD and Legumain) were immunodetected with the PLD3-specific antibodies. *B*, Western blot analysis of wild-type (WT), cathepsin B, cathepsin L and cathepsin B/L mouse embryonic fibroblasts (MEF) transfected with *hPLD3* followed by detection with the indicated PLD3-specific antibodies. GAPDH is represented as a loading control. Arrowheads shown specific PLD3 signal. \* indicates unspecific signals.

### 3.1.3 Intracellular transport of PLD3

#### 3.1.3.1 PLD3 is partially sorted to the plasma membrane (PM) before reaching lysosomes

We further investigated if PLD3 is transported en route to lysosomes through the plasma membrane (PM). Different membrane proteins are transported through the PM mediated by the interaction with adaptor proteins (AP), which recognize sorting signals contained within the cytosolic domain of the proteins. One of the very well conserved motifs is the tyrosine-based sorting signals, with the consensus motif YXX $\Phi$  (Canfield et al., 1991; Marks et al., 1997).

Alignment of the cytosolic tails of PLD3 homologs and LAMP1, reveal a similar tyrosine motif for PLD3 (Figure 22A). Therefore, a PLD3 tyrosine mutant was generated by its substitution to alanine at position 7. Immunoblots analyses of HeLa cells transfected with the *hPLD3 Y7A* mutant showed normal PLD3 proteolytic processing. An absence of the PLD3 N-terminus and a decrease of full-length PLD3 might be due to a lower binding strength of the antibody due to the epitope change in the very N-terminal region (Figure 22B). Nonetheless, confocal images of the tyrosine mutant revealed an increased staining of PLD3 at the PM using both PLD3-specific antibodies (Figure 22C).

Despite of its transient appearance at the PM, PLD3 is still able to reach lysosomes, as revealed by its co-localization with the marker LAMP2, indicating that PLD3 is partially transported throughout the plasma membrane. As an indirect approach, electron microscopy analyses of *hPLD3*-transfected HeLa cells, labeled with the luminal PLD3-specific antibody followed by secondary antibody immunogold labeling, detected several gold particles at the PM (Figure 22D). These data support the idea that PLD3 is partially transported through the PM, but independent trafficking pathways may also be involved in its direct transport from the Golgi to late endosomal and lysosomal compartments.

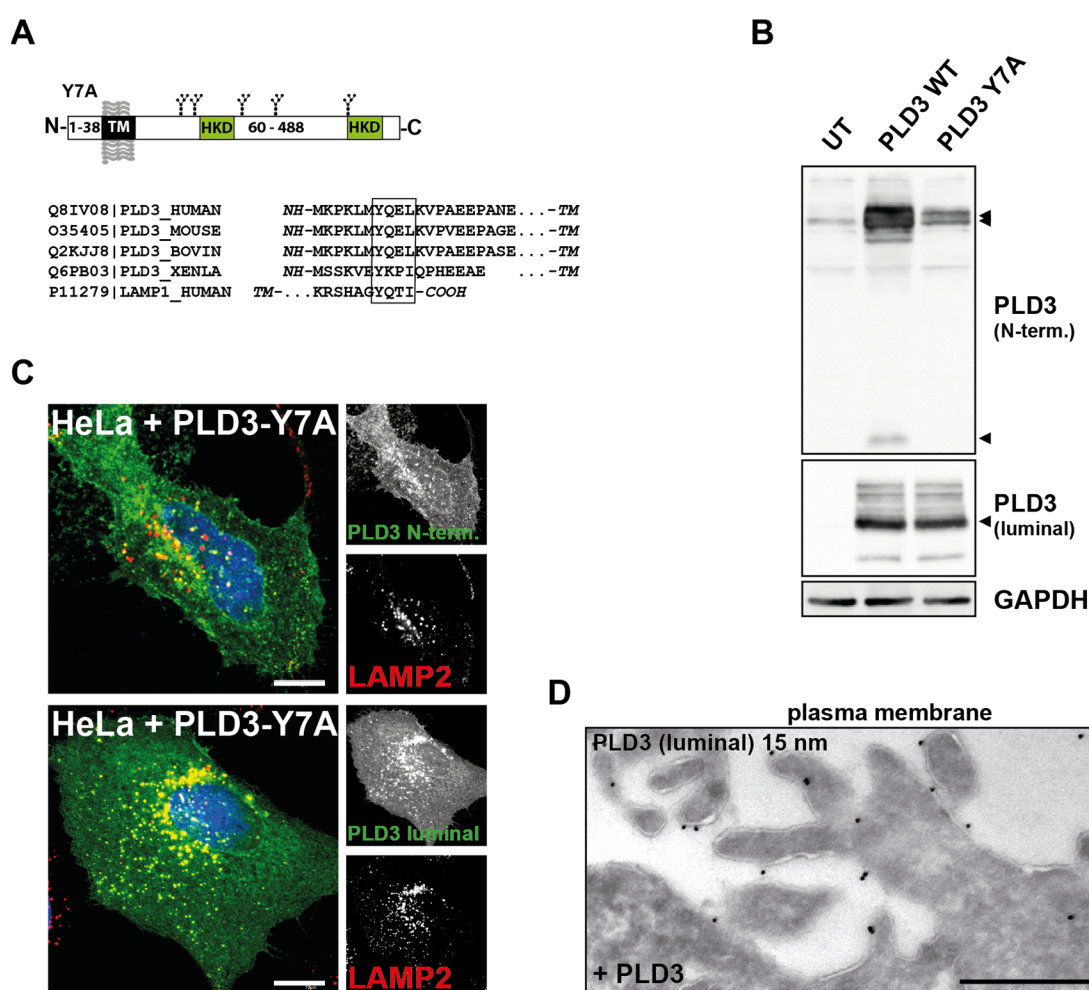
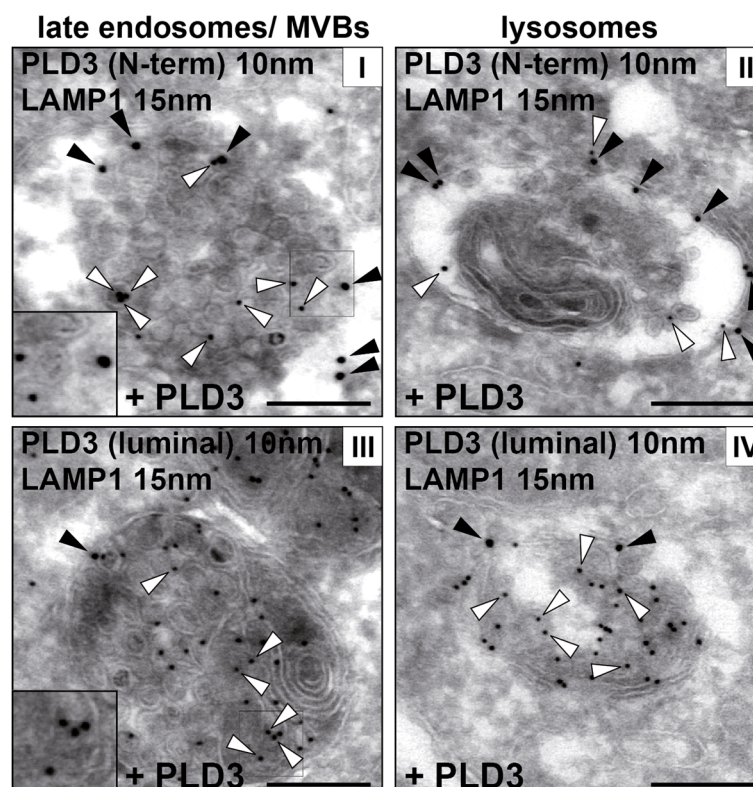


**Figure 22 | PLD3 is partially sorted to the plasma membrane (PM).** *A*, Schematic representation of the PLD3 protein and alignment of the N-terminal amino acids (1-20) of different orthologues of PLD3 and the C-terminus of LAMP1 showing the highly conserved tyrosine sorting motif (boxed). *B*, western blot analysis of HeLa cells transfected with *hPLD3* WT and *hPLD3* Y7A and further immunodetected with both N-terminal-specific and luminal-specific PLD3 antibodies. GAPDH is presented as a loading control. *C*, immunofluorescence images of HeLa cells transfected with the *PLD3* Y7A tyrosine mutant and co-labeled with the indicated anti-PLD3-specific antibodies and the lysosomal marker (anti-LAMP2 antibody). Scale bar, 10  $\mu$ m. *D*, electron microscopy image showing the plasma membrane of *PLD3*-transfected HeLa cells followed by immunogold labeling with the luminal-specific PLD3 antibody (15 nm gold particles). Scale bar, 500 nm.



### 3.1.3.2 *PLD3 is sorted into intraluminal vesicles (ILVs) of multivesicular bodies (MVBs) in a PtdIns(3)P-dependent manner*

Having observed that PLD3 is localized in ILV-positive vesicles upon transfection of the Rab5 mutant Q79L (Figure 17C), the possible sorting of PLD3 into these structures was analyzed. *hPLD3* transfected HeLa cells were analyzed by electron microscopy using both PLD3-specific antibodies and co-immunolabeled with an anti-LAMP1 antibody (Figure 23). Immunogold staining with the PLD3-specific N-terminal antibody showed localization of PLD3 in intraluminal vesicles (ILVs) of multivesicular bodies (MVBs, Figure 23, I) or at the limiting membrane of lysosomes where it co-localized with LAMP1-positive gold particles (Figure 23, II). It is important to consider that with this antibody it is not possible to distinguish between the full-length PLD3 or the N-terminal peptide of PLD3. Gold particles stained with the PLD3 luminal-specific antibody showed similar localization to ILVs of MVBs (Figure 23, III), whereas most of the soluble peptide was found in the lumen of lysosomes (Figure 23, IV). In contrast, LAMP1 labeling was exclusively found at the limiting membrane of lysosomes. These data indicate that the full-length and the N-terminal peptide of PLD3 are localized into ILVs of MVBs, where possible processing might occur before the delivery of the luminal domain of PLD3 into lysosomes.



▲ **Figure 23 | PLD3 is localized to ILVs of MVBs.** Co-immunogold labeling of *PLD3*-transfected HeLa cells with the N-terminal-specific (I and II) and luminal-specific (III and IV) *PLD3* antibodies (10 nm gold particles, white arrowheads) and *LAMP1* (15 nm gold particles, black arrowheads) showing its localization in lysosomes and intraluminal vesicles (ILVs) of multivesicular bodies (MVBs). Scale bar, 500 nm. Electron microscopy images were performed in collaboration with Dr. Michaela Schweizer at the Center of Molecular Neurobiology (ZMNH), Hamburg.

Three mechanisms have been reported regarding the sorting of proteins into ILVs: (1) involvement of the tetraspanin *CD63* (Theos et al., 2006; van Niel et al., 2011), (2) utilization of the sphingolipid ceramide (Trajkovic et al., 2007) and (3) transport through the ESCRT pathway (Odorizzi et al., 1998; Nickerson et al., 2010). To narrow down which of these mechanisms is involved in the transport of *PLD3* into ILVs, wild-type (WT) or *CD63*-deficient MEF cells (Schröder et al., 2009) were transfected with *hPLD3* and further analyzed by immunofluorescence. *CD63* deficiency did not abrogate the proper transport of *PLD3* to lysosomes, as revealed by co-localization of *PLD3* with an anti-*LAMP1* antibody (Figure 24). To analyze if *PLD3* is transported to ILVs via the sphingolipid ceramide, *hPLD3* transfected HeLa cells were treated with the neutral sphingomyelinase (nSMase) inhibitor GW4869 (Trajkovic et al., 2007). As shown by Western blot analysis and immunofluorescence experiments, normal processing and lysosomal localization of *PLD3* was observed (Figure 25, A and B).

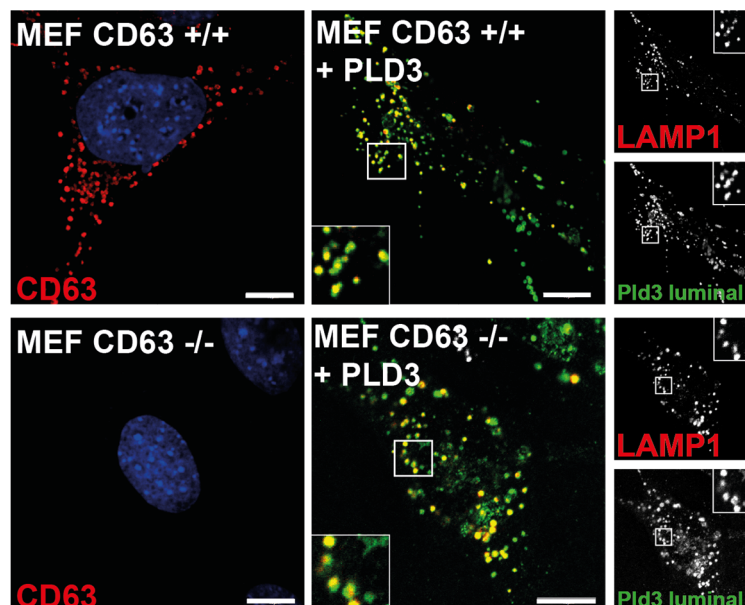


**Figure 24 | *PLD3* reaches lysosomes in *CD63* deficient MEFs.** Confocal images of WT (upper panel) and *CD63*-deficient (lower panel) mouse embryonic fibroblast (MEF) cells transfected with *hPLD3* and further co-stained with the luminal-specific *PLD3* antibody (green) and the lysosomal marker (anti-*LAMP1* antibody). Staining with an anti-*CD68* antibody is depicted as a control of appropriate *CD63* knockout. Scale bar, 10  $\mu$ m.

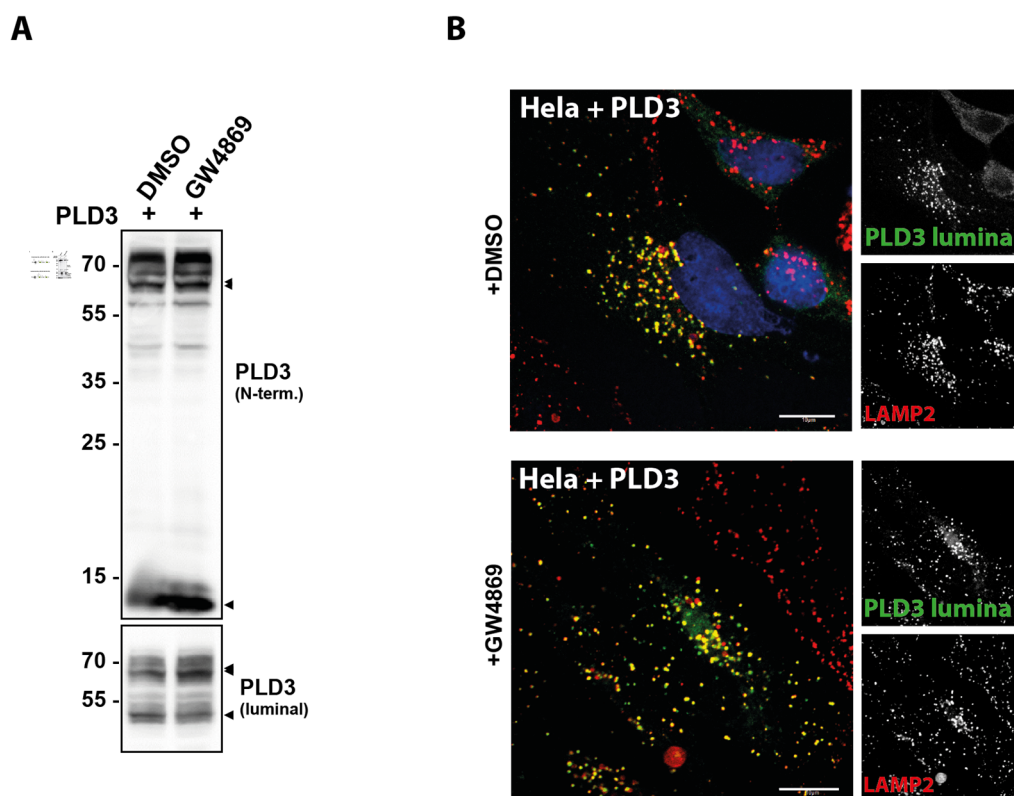


**Figure 25 | Effect of the ceramide inhibitor GW4869 on the processing and localization of PLD3.** HeLa cells were transfected with *hPLD3* and treated with the ceramide inhibitor GW4869 or DMSO as a negative control. *A*, Western blot analysis was performed using the indicated anti-PLD3 specific antibodies showing the respective cleavage products (arrowheads). *B*, confocal images of HeLa cells were generated by co-staining with the PLD3 luminal-specific antibody (green) and the anti-LAMP2 lysosomal antibody (red). Scale bar, 10  $\mu$ m.

The third mechanism through which PLD3 may be delivered to ILVs is the ESCRT pathway. Four large protein complexes are involved in ESCRT sorting (ESCRT-0, ESCRT-I, ESCRT-II and ESCRT-III; Katzmann et al., 2001; Babst et al., 2002a, 2002b). Several steps during this process critically depend on phosphatidylinositol 3-phosphate (PtdIns3P or PIP3) - and its derivative PtdIns(3,5)P<sub>2</sub>, products of the class III phosphatidylinositide 3-kinase Vps34 (Gill et al., 2007). *hPLD3* transfected HeLa cells were treated with the fungal metabolite Wortmannin, an inhibitor of Vps34 (Brown et al., 1995). This metabolite induces the swelling of vesicles and further inhibits the invagination and/or pinching off of ILVs. In cells treated with Wortmannin, PLD3 was exclusively found in the limiting membrane of endosomes and not in ILVs (Figure 26A), similar to CD63 (Figure 26B), used as a positive control. These results suggest that transport of PLD3 to ILVs of MVBs is PtdIns(3)P- and PtdIns(3,5)P<sub>2</sub>-dependent and that members of ESCRT machinery are involved.

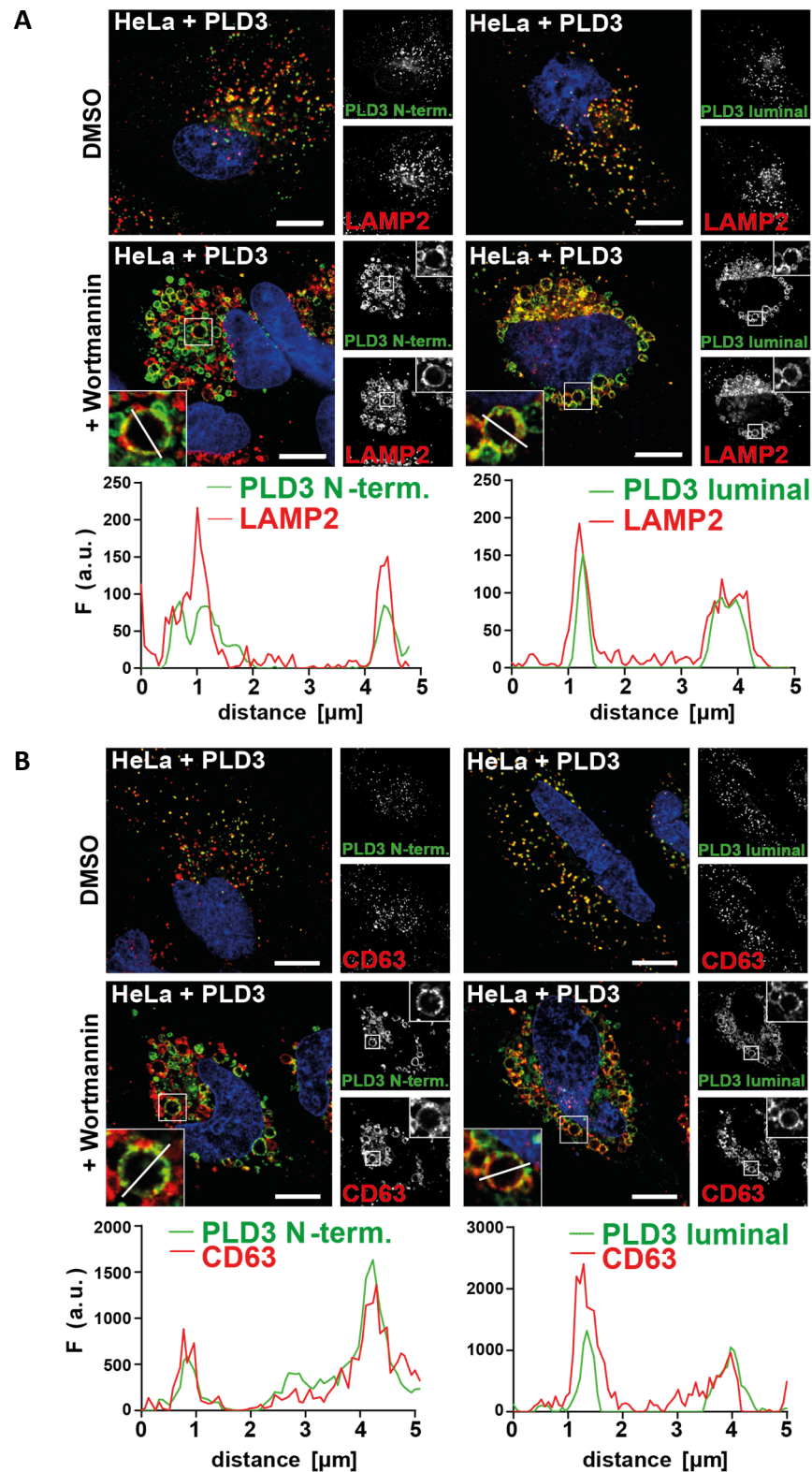


**Figure 26 | PLD3 is transported to MVBs dependent on PtdIns(3)P.** *A* and *B*, *hPLD3*-transfected HeLa cells were treated with DMSO (negative control) or wortmannin and co-stained with the PLD3-specific antibodies (green) and antibodies against the lysosomal marker anti-LAMP2 (*A*) or the ILV marker anti-CD63 (*B*) depicted in red. Insets of wortmannin-treated cells in *A* and *B* show enlarged vesicles with a white line further represented in a profile plot between fluorescence (*F*) in arbitrary units (a.u.) and distance ( $\mu\text{m}$ ). Scale bar, 10  $\mu\text{m}$ .



### 3.1.3.3 *PLD3 transport to lysosomes is ESCRT-dependent*

From the previous results, it can be hypothesized that PLD3 is transported to MVBs using the ESCRT machinery for final delivery of the luminal peptide to lysosomes. A straight forward approach to address this assumption is by interfering with the function of some key components of this machinery, either by overexpression or knock down experiments. Hrs plays a key role in the initiation of the MBV pathway, not only because it binds to the ubiquitinated cargo, but it also recruits the ESCRT-I complex (Schmidt and Teis, 2012). Overexpression of Hrs prevents efficient formation of ILVs, therefore preventing the sorting of cargo proteins to MVBs. Increased recruitment of clathrin leads to the formation of enlarged endosomes (Bishop et al., 2002; Urbé et al., 2003), making this Hrs overexpression approach suitable for the distinction between intracellular signal and localization at the limiting membrane of endosomes.

Using both anti-PLD3-specific antibodies, PLD3 was found in the limiting membrane of endosomes when co-transfected with GFP-tagged Hrs. No obvious PLD3 staining in the lumen was observed (Figure 27, upper panel). Additionally, no co-localization between PLD3 and LAMP2 was detected, arguing for its retention in enlarged endosomes and no further transport to lysosomes (Figure 27, lower panel). Immunoblot analyses revealed that co-transfection of *hPLD3* with *eEGFP-C1-Hrs* led to decreased proteolytic cleavage of PLD3, shown also by quantification (Figure 28). This result is in agreement with the altered delivery of PLD3 to lysosomes, suggesting that cleavage takes place in a later step after MVB formation.

To independently prove the contribution of the ESCRT machinery on PLD3 delivery to ILVs, HeLa cells were co-transfected with *hPLD3* and dominant-negative forms of Vps4a, a AAA(+) ATPase protein required for the final step of MVB vesicle formation by dissociation of the ESCRT-III complex (Babst et al., 1997). Overexpression of both the 3x-FLAG-tagged *Vps4a-E228Q* and the GFP-tagged *Vps4a-K173Q* led to significant reduction of PLD3 delivery to lysosomes (Figure 29A) and abrogated PLD3 cleavage (Figure 30). Of note, overexpression of the Vps4a mutants did not abolish the transport to lysosomes of the soluble protein cathepsin D (CtsD) (Figure 29B) and neither affected its maturation or proteolytic processing (Figure 30).

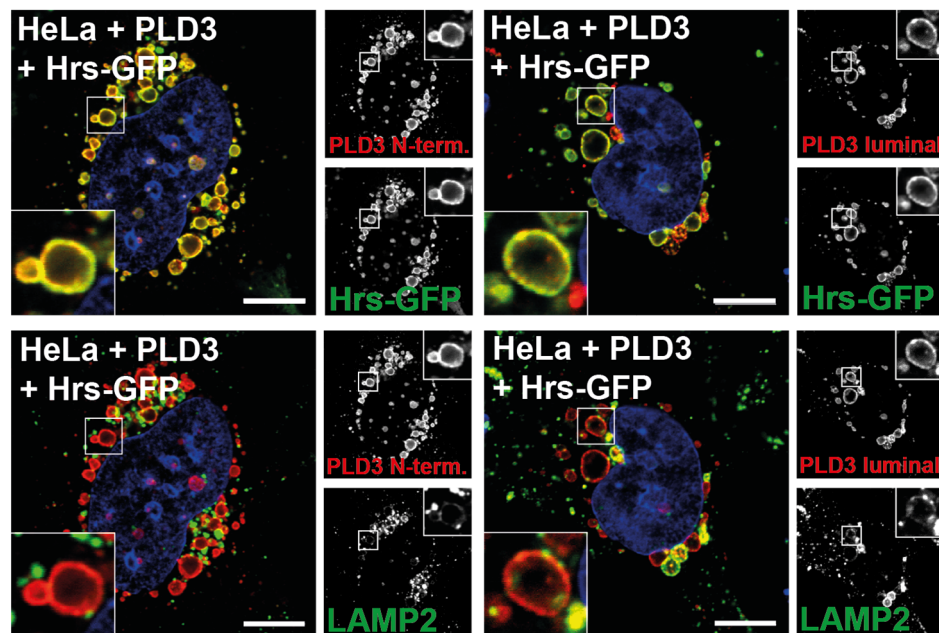


**Figure 27 | PLD3 is retained in intracellular membranes upon co-expression of Hrs.** HeLa cells were co-transfected with *PLD3* and the ESCRT-0 member *Hrs-GFP* and further co-stained with N-terminal and luminal anti-PLD3-specific antibodies (red) and an antibody against the lysosomal marker LAMP2 (green). Insets represent enlarged lysosomes. Scale bar, 10  $\mu$ m.

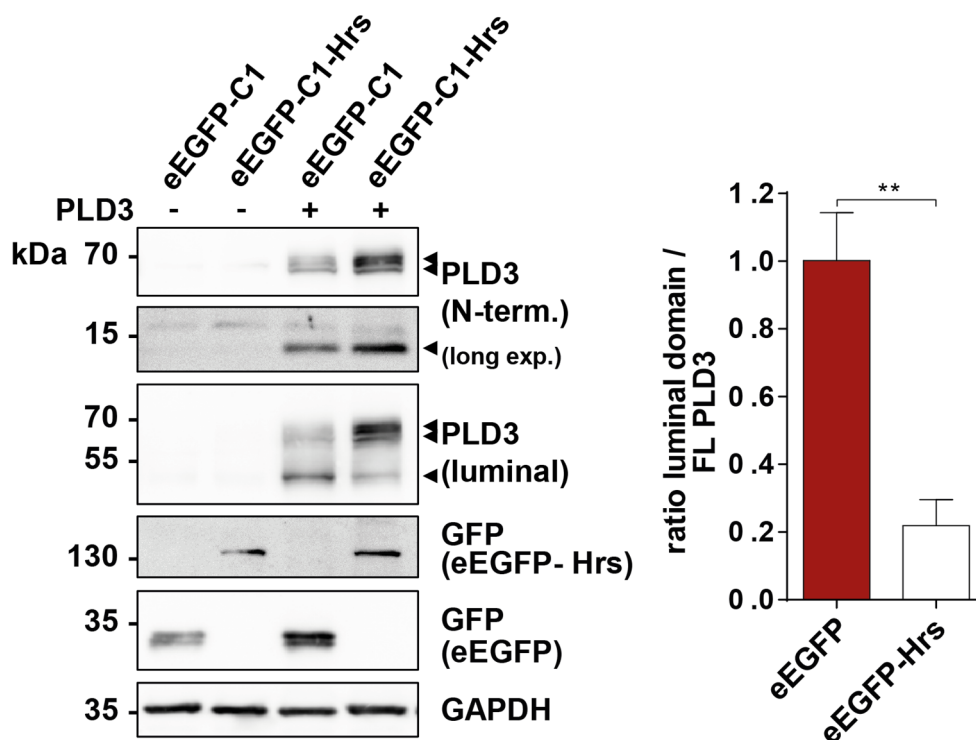


**Figure 28 | PLD3 processing is altered upon co-expression with Hrs.** HeLa cells co-transfected with *PLD3* and *eGFP-C1-Hrs* were further immunoblotted and detected with the N-terminal and luminal PLD3 specific antibodies. GFP is depicted as a positive control of transfection and GAPDH as loading control. Arrowheads represent PLD3 specific signals. The ratio of PLD3 luminal domain and full-length PLD3 of eEGFP and eEGFP-Hrs is shown in a graph after densitometric quantification. Error bars represent SEM. \*\*\*p < 0.001; \*\*p < 0.01; unpaired Student's t test (n = 3).

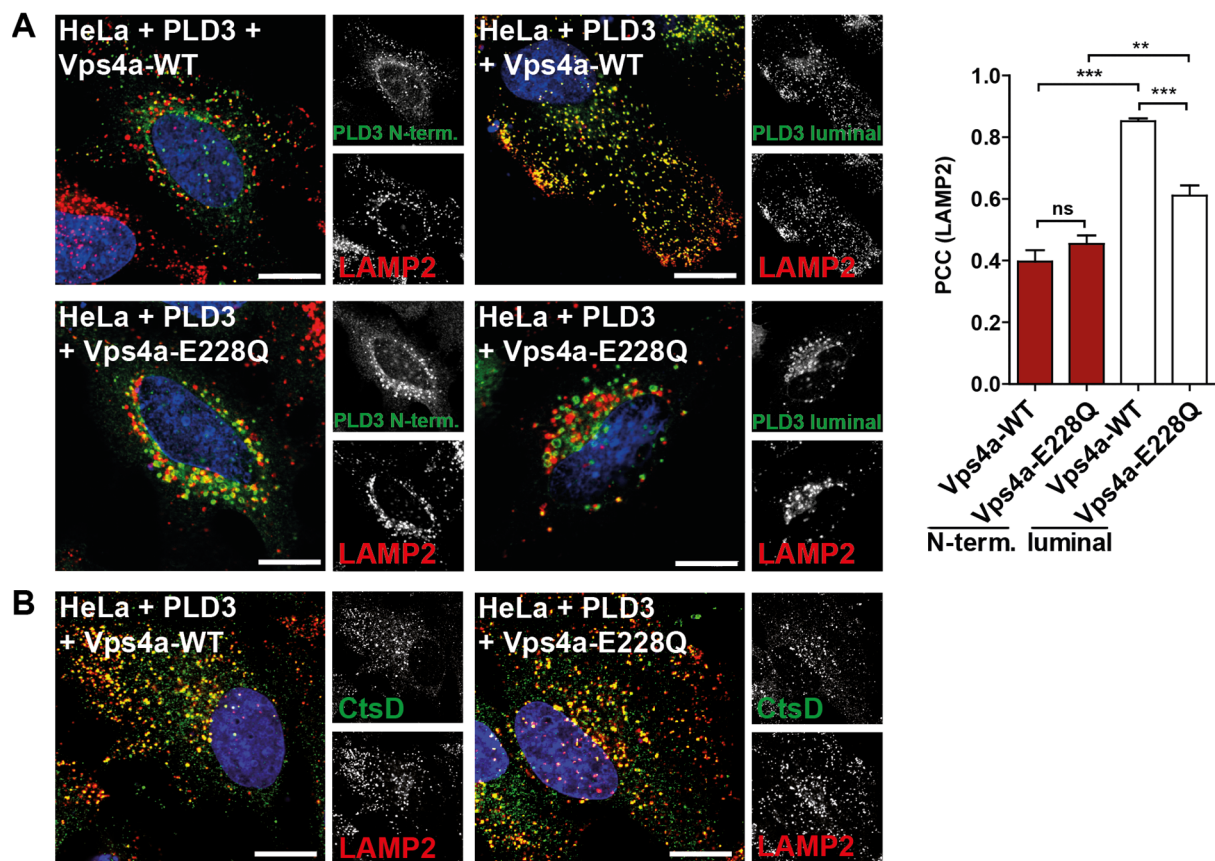


**Figure 29 | PLD3 transport to lysosomes is altered upon co-expression with Vps4a.** Immunofluorescence analysis of HeLa cells co-transfected with *PLD3* and a WT or a 3x-FLAG -tagged dominant negative mutant (E228Q) of the ESCRT-III member *Vps4a*. *A*, cells were co-labeled with indicated anti-PLD3-specific antibodies (green) and an anti-LAMP2 lysosomal antibody (red). *B*, as a control for normal lysosomal delivery, cells were co-stained with antibodies against cathepsin D (CtsD) and LAMP2. Scale bar, 10  $\mu$ m. The Pearson correlation coefficient (PCC) between LAMP2 and the different transfection plasmids is presented in a graph. Error bars represent SEM. \*\*\* $p < 0.001$ ; \*\* $p < 0.01$ ; unpaired Student's *t* test ( $n = 12$ ). ns, not significant.

The effect of PLD3 proteolytic cleavage and localization was also evaluated by knockdown of *Hrs*. An almost 80 % reduction of *Hrs* gene expression by transient transfection of *Hrs* siRNA reduced the levels of the processed forms of PLD3 (Figure 31A and B). In addition, PLD3 was mostly found in the limiting membrane of vesicle-like structures after *Hrs* siRNA transfection (Figure 31C). Our data indicate that PLD3 transport to lysosomes is ESCRT-dependent, in contrast to the conventional trafficking of lysosomal membrane proteins (e.g. LAMP2) or soluble enzymes (e.g. cathepsin D).

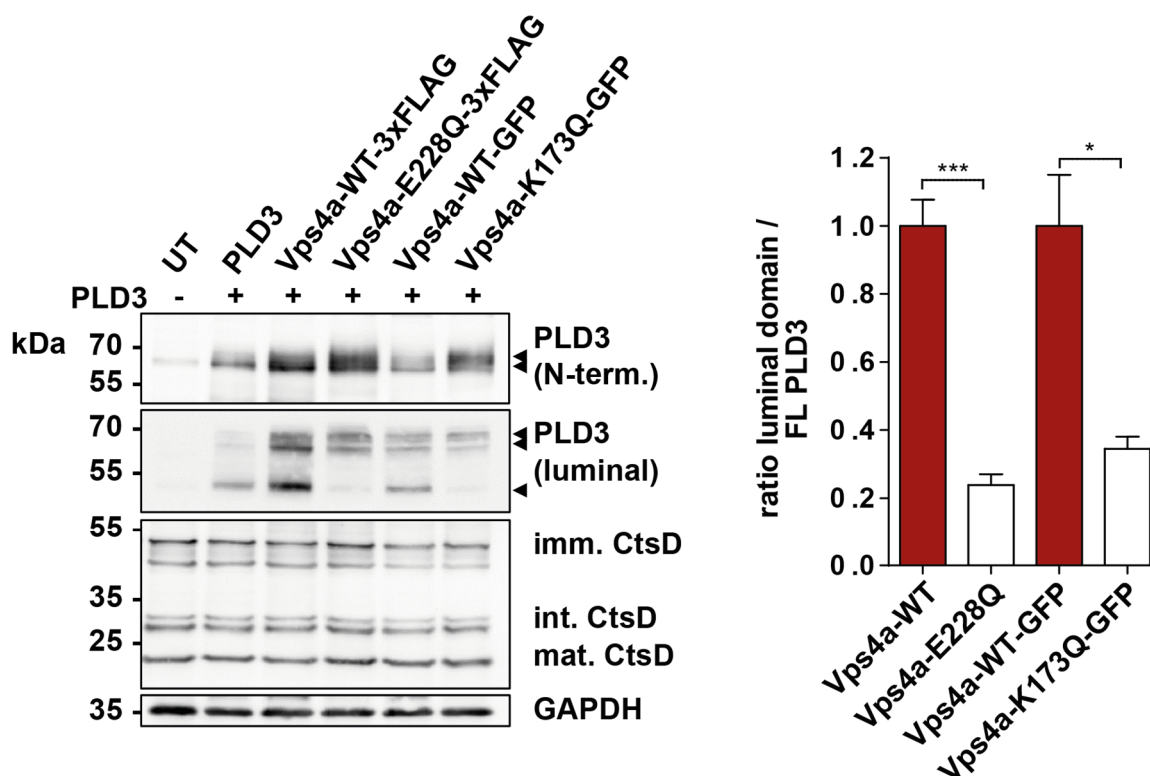


**Figure 30 | PLD3 processing is altered upon co-expression with Vps4a.** HeLa cells were co-transfected with *PLD3* and the WT and dominant negative mutants (E228Q and K173Q) of *Vps4a* and further immunodetected with both anti-PLD3-specific antibodies (shown with arrowheads). Antibodies against cathepsin D and GAPDH are depicted as positive control or loading control, respectively. The ratio of the luminal domain and full-length PLD3 of the different *Vps4a* mutants is presented as a graph after densitometric quantification. Error bars represent SEM. \*\*\* $p < 0.001$ ; \* $p < 0.1$ ; unpaired Student's t test ( $n = 3$ ).

#### 3.1.3.4 Sorting of PLD3 into ILVs is ubiquitin-dependent

Cargo proteins sorted via the ESCRT pathway require its prior ubiquitination. Therefore, PLD3 might be post-translationally modified with ubiquitin molecules covalently linked to the protein. A co-immunoprecipitation (CO-IP) assay by overexpression of *hPLD3* with a hemagglutinin (HA)-tagged ubiquitin (*Ub-HA*) construct was performed. Transfected cell lysates were incubated with the PLD3 N-terminal-specific antibody and further immunoblotted with a HA antibody, where a specific signal of ubiquitinated full-length PLD3 is observed (Figure 32A, upper panel, lane 8). As a negative control, cells were transfected with either *Ub-HA* (lane 6) or *PLD3* (lane 7) constructs alone or an isotype control antibody (cAb, lane 9). In all cases, no PLD3-specific signal was detected.

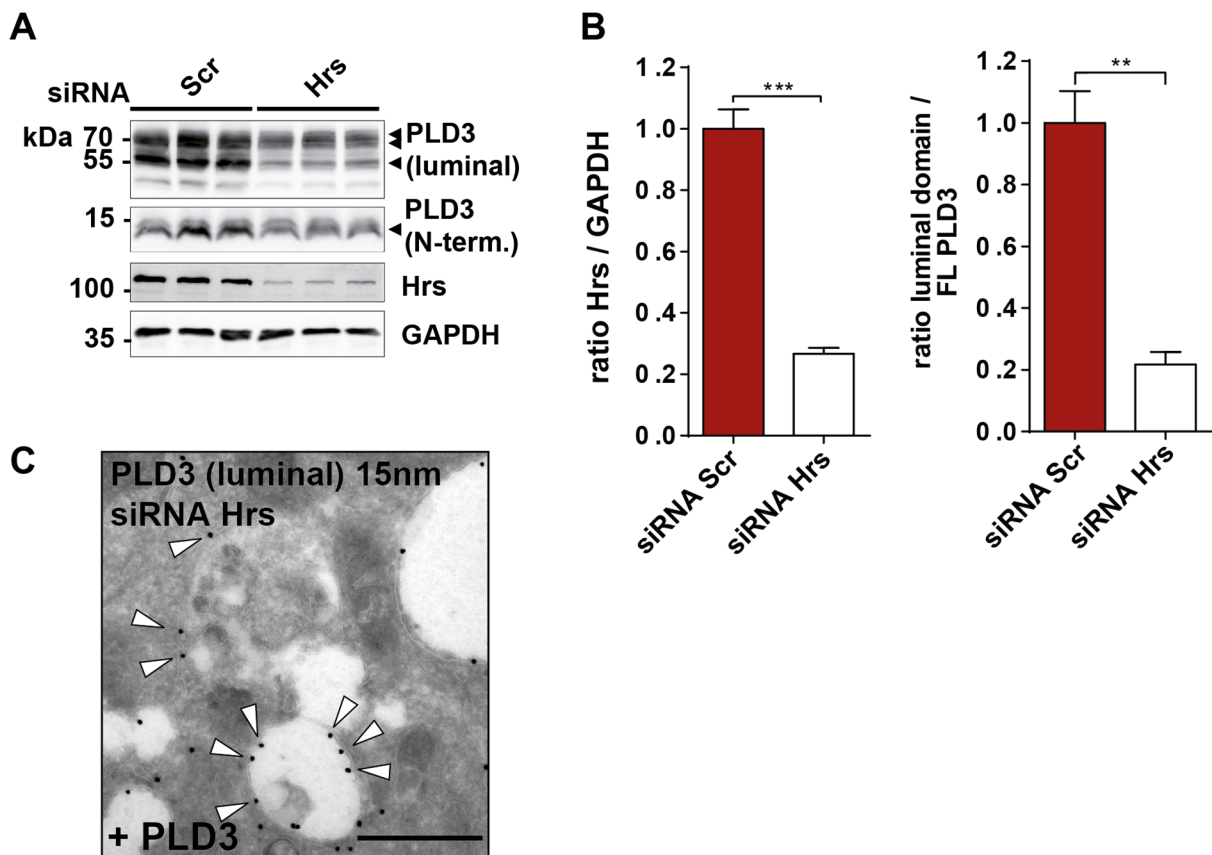


**Figure 31 | PLD3 processing and localization is altered upon Hrs knockdown.** *A*, *PLD3*-transfected HeLa cells were transfected with scrambled (Scr) siRNA or Hrs siRNA and analyzed by Western blot by immunodetection with the *PLD3*-specific N-terminal and luminal antibodies (shown with arrowheads). An anti-Hrs antibody was used as a positive control to show the Hrs knockdown. *GAPDH* was presented as a loading control. *B*, the graphs show the ratio of Hrs / *GAPDH* for the control and Hrs knockdown (left) and ratio of luminal domain / FL *PLD3* (right) from the blots shown in *A*. Error bars represent SEM. \*\*\* $p < 0.001$ ; \*\* $p < 0.01$ ; unpaired Student's *t* test ( $n = 3$ ). *C*, immunogold labeling of siRNA-mediated knockdown of Hrs in *PLD3*-transfected cells using the luminal *PLD3*-specific antibody (15 nm gold particles, white arrowheads). Scale bar, 500 nm. Electron microscopy image was performed in collaboration with Dr. Michaela Schweizer at the Center of Molecular Neurobiology (ZMNH), Hamburg.

To corroborate *PLD3* ubiquitination, immunoprecipitation was also performed in the opposite direction, *i.e.* by incubation of cell lysates with a HA antibody and additional immunodetection with the *PLD3* N-terminal specific antibody. Similarly, a signal of ubiquitinated full-length *PLD3* was detected using the anti-*PLD3* specific N-terminal antibody (Figure 32B, lower panel, lane 8). For the control of proper transfection of indicated constructs, both antibodies (anti-HA and anti-*PLD3* N-terminal) were used.



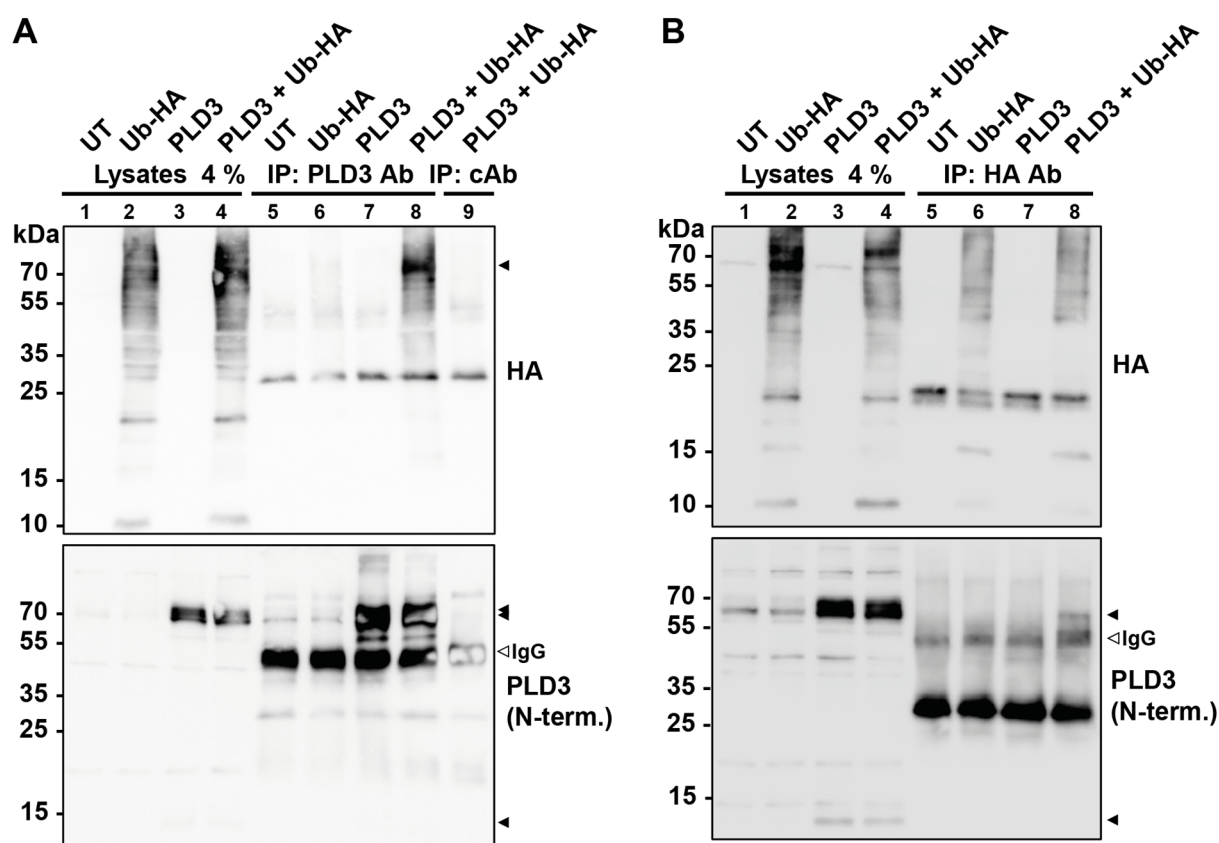


**Figure 32 | PLD3 is ubiquitinated.** HeLa cells transfected with *PLD3* and/or *ubiquitin-HA* and further immunoprecipitated (IP) with the N-terminal PLD3-specific antibody (A) or an anti-HA antibody (B). Membranes were immunoblotted with the indicated antibodies. Lines 1 to 4, 4 % of indicated transfected lysates were loaded. Lines 5 to 8, immunoprecipitated lysates. Black arrowhead indicates the full-length PLD3-specific ubiquitinated signal. Open arrowheads show the signal of immunoglobulin G (IgG). cAb, control antibody (lane 9).

PLD3 contains six lysine residues (K2, K4, K11, K30, K34, K35) which can be modified with a single ubiquitin (Ub) in a single lysine (mono-ubiquitination) or a single Ub on multiple lysines (multi-ubiquitination). These positions are conserved among different species (Figure 33A). To analyze which position(s) undergo ubiquitination, single lysine mutants were generated by substitution with an arginine residue to keep the positive charged side chains. Additionally, a mutant of all lysine residues (K1-6R) was generated to avoid any lysine conjugation of ubiquitin molecules. Following the same co-immunoprecipitation (CO-IP) approach, each single and full lysine mutants were co-expressed with *Ub-HA* (Figure 33B). For all mutants, a normal PLD3 processing was observed. Interestingly, a

slight increase of full-length PLD3 was detected for the K11R mutant, an observation that was consistent in independent experiments, although not significant (data not shown). After immunoprecipitation (IP) with the anti-HA antibody, a signal of ubiquitinated PLD3 was observed for all mutants. However, no signal at the same molecular weight was detected for the K1-6R mutant, indicating that PLD3 is multi-ubiquitinated.

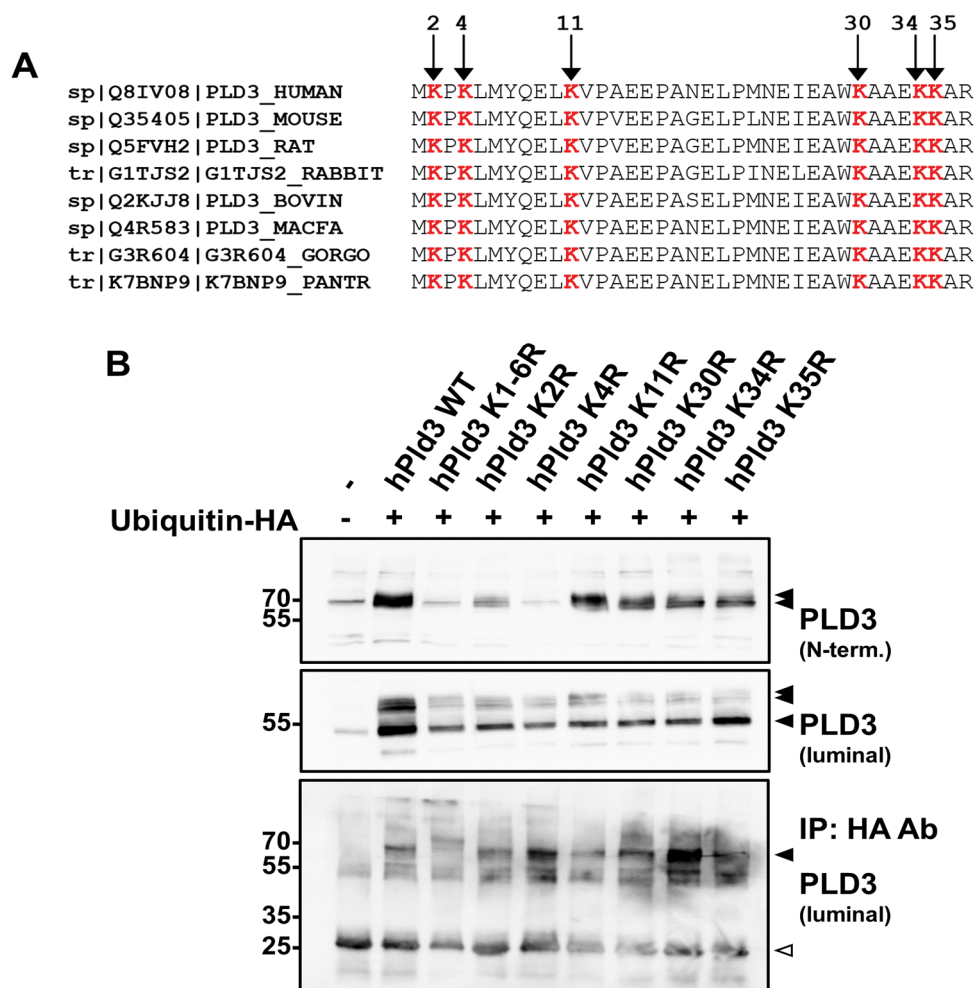


**Figure 33 | PLD3 is ubiquitinated at multiple lysine (K) residues.** *A*, alignment of the PLD3 cytosolic N-terminal sequencing (amino acids 1-38) from different species, highlighting the lysine (K) residues for possible ubiquitination events. *B*, HeLa cells were co-transfected with *ubiquitin-HA* and *PLD3* WT, *PLD3* K1-6 (full lysine mutant) or the indicated single lysine mutants (*K2R*, *K4R*, *K11R*, *K30R*, *K34R*, *K35R*). Cell lysates were analyzed by Western blot with the N-terminal and luminal PLD3-specific antibodies, either for the input lysates (two upper blots) or the immunoprecipitated lysate (lower blot). Black arrowheads indicate PLD3 specific signal. White arrowhead indicates immunoglobulin G (IgG).

To test for an indirect pathway of PLD3 ubiquitination, we applied the tandem-repeated ubiquitin-binding entities (TUBEs)-based assay. This approach is based on the generation of a construct with four tandem ubiquitin-associated (UBA) domains of ubiquitin 1, fused to glutathione S-transferase (GST; Hjerpe et al., 2009). Thus, ubiquitin-modified proteins will interact with higher affinity to GST-TUBE. After GST-pulldown with a Glutathione Sepharose resin, ubiquitinated proteins can be detected. As expected, for the *hPLD3* transfected cell lysates, a specific signal of ubiquitinated PLD3 was observed but not in the lane with GST-only (Figure 34A), used as a negative control, indirectly proving that PLD3 is post-translationally modified with ubiquitin molecules.

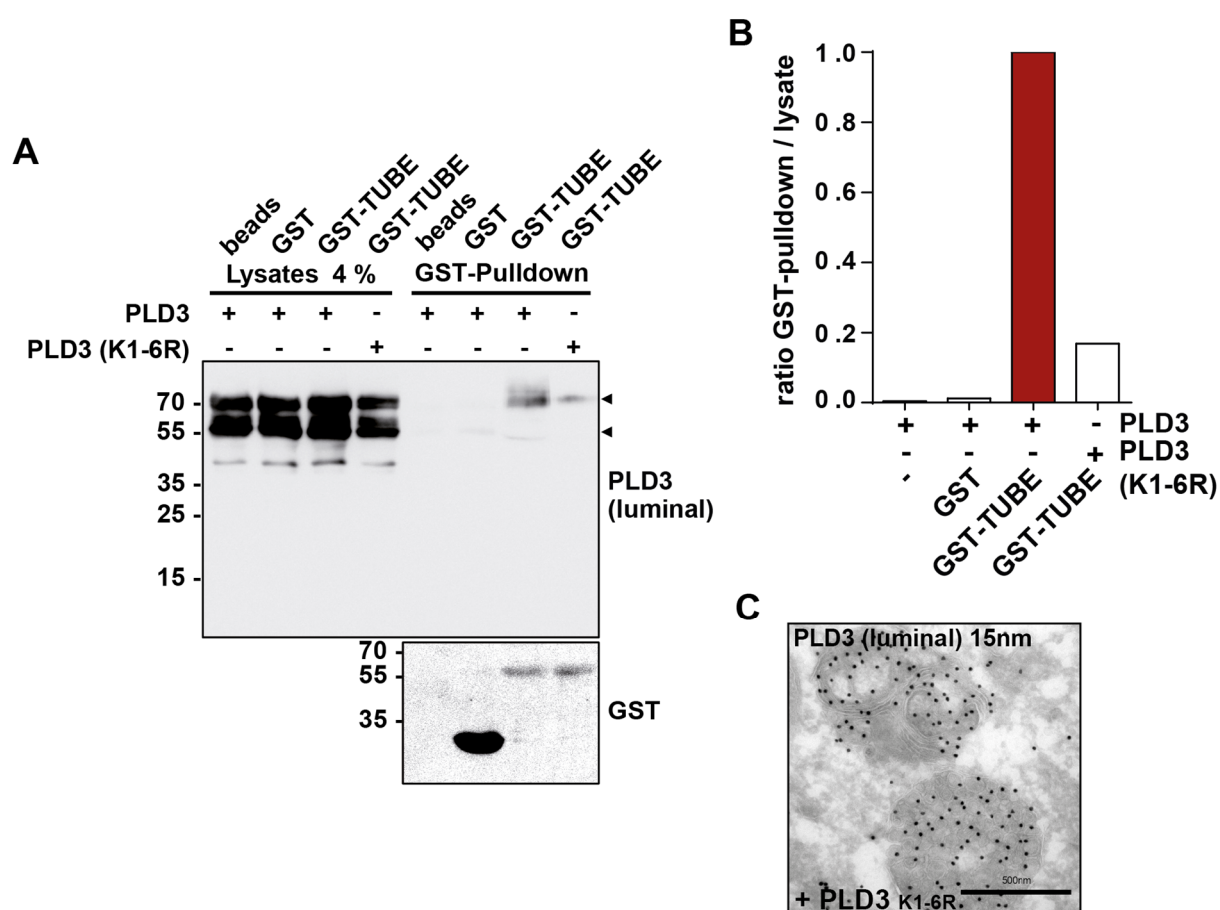


**Figure 34 | PLD3 ubiquitination is altered after mutation of all N-terminal lysine (K) residues.** *A*, Ubiquitination assay using tandem ubiquitin-binding entity (TUBE). HeLa cells were transfected with either *PLD3* WT or the full lysine mutant *PLD3* K1-6R, followed by the addition of GST or GST-TUBE. Cell lysates or affinity purified protein with a glutathione resin (GST) were further immunoblotted with the PLD3-specific luminal antibody or an anti-GST antibody as a positive control of the pulldown. *B*, the ratio of the GST-pulldown and lysate is shown. *C*, electron microscopy image of HeLa cells transfected with the full lysine mutant *PLD3* K1-6R immunolabeled with the PLD3-specific luminal antibody coupled to 15 nm gold particles.



A weaker signal was detected in the GST-pulldown of *hPLD3 K1-6R* transfected cell lysates, arguing for an abrogation of PLD3 ubiquitination (Figure 34A, GST-pulldown and Figure 34B). A blot with the PLD3-specific N-terminal antibody is not shown due to amino acid changes in the PLD3 epitope. Moreover, the full lysine mutant was still cleaved (Figure 34A, luminal) and found in MVBs (Figure 34C), indicating that processing does not depend on ubiquitination and that alternative sorting pathways than lysine ubiquitination are involved. Mutation of each single lysine residue only had a little effect on the overall PLD3 ubiquitination. Of note, an increase in full-length PLD3 (Figure 35, upper panel) and a slight decrease of ubiquitination (Figure 35, lower panel) was observed for the PLD3 K11R mutant, suggesting that this residue is a key player of PLD3 ubiquitination, however the signal was not completely abrogated.

Altogether, our data indicate that PLD3 is ubiquitinated and transported through the recruitment of the ESCRT-0 complex and formation of MVBs to finally reach lysosomes.

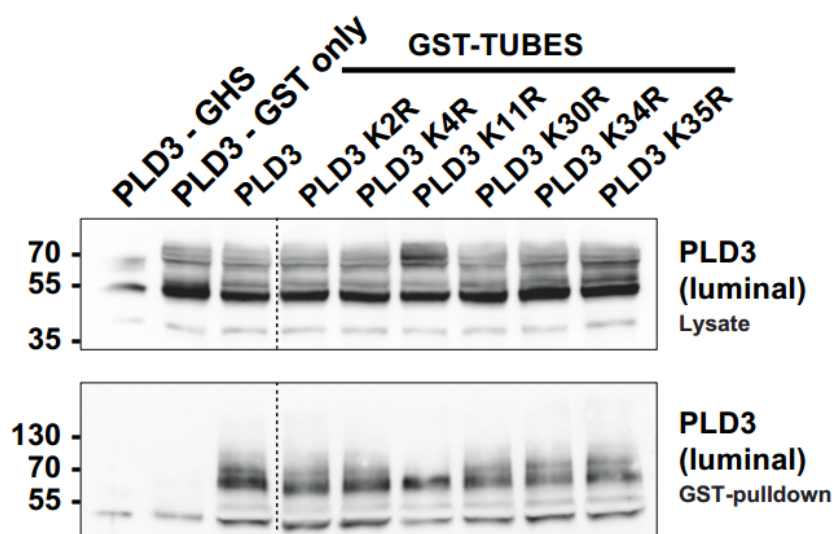


**Figure 35 | Lysine residue 11 (K11) might be a key residue of PLD3 ubiquitination.** GST-TUBE pulldown of HeLa cell lysates transfected with *PLD3 WT* and the single lysine mutants (*K2R*, *K4R*, *K11R*, *K30R*, *K34R*, *K35R*) and further analyzed by Western blot with the anti-PLD3 specific antibodies. GST only was used as a negative control.

## 3.2 Pld3 expression in mouse tissues and characterization of the Pld3<sup>tm1e(EUCOMM)Wtsi</sup> mouse model

Having provided a detail the intracellular transport of PLD3 in cells, we wanted to further investigate PLD3 expression and function *in vivo*. Is PLD3 expressed ubiquitously or is PLD3 expression tissue- and cell-type dependent? To address these question and further analyze possible functions, we generated a Pld3-deficient mouse strain (*Pld3<sup>tm1e(EUCOMM)Wtsi</sup>*), based on a targeted non-conditional mutant strategy (see section 2.6.2, Material and Methods), where the lacZ-tagged allele reports expression of the endogenous PLD3 promoter, leading to a null allele.

### 3.2.1 Pld3 is abundantly expressed in the brain

Northern blot analyses have shown a strong hybridization signal for PLD3 mRNA in brain tissues of adult mice, but not with RNA purified from non-nervous tissues (Pedersen et al., 1998). In order to investigate if a similar Pld3 expression pattern occurs at the protein level and to validate Pld3 deficiency, different mouse tissues from wild-type (WT) and Pld3 knockout (KO) mice were evaluated. Western blot analysis revealed a strong Pld3-specific signal in the mouse brain lysate at ~70 kDa (indicated with the black arrowhead, Figure 36). Additionally, a specific but weaker Pld3 signal was detected in the spleen, bone marrow (BM) and lungs. Very faint Pld3 signals were also observed in the kidney and the liver, but not in the heart.

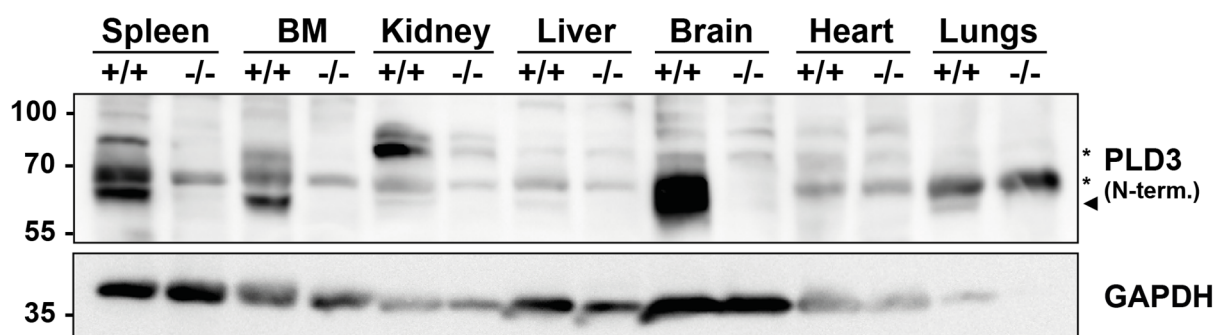


**Figure 36 | Pld3 is highly expressed in the brain.** Cell lysates of different mouse tissues from WT (+/+) and Pld3-deficient mice (-/-) were analyzed by Western blot and immunodetected with the anti-Pld3-specific N-terminal antibody. Black arrowhead represents specific full-length Pld3 signal. \* indicates unspecific signal. GAPDH is presented as a loading control.

As a control for the antibody specificity and validation of Pld3 deficiency, no signal at 70 kDa was detected in the Pld3  $-/-$  tissue lysates (Figure 36). Fluorescence histology images of Pld3 expression in visceral tissues only revealed a Pld3-specific signal in the spleen, especially in the red pulp and in a small population of cells in the white pulp (Figure 37). No specific Pld3 staining was observed in the kidney, liver, lung and the heart (data not shown). These results indicate that Pld3 is mainly expressed in the brain, but also a significant expression is observed in the spleen.

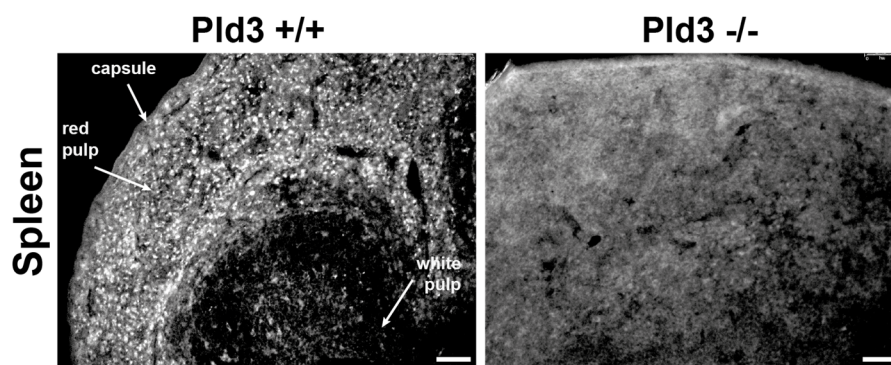


**Figure 37 | Pld3 is expressed in the spleen.** Immunohistochemistry images of spleen of Pld3 WT (+/+) and Pld3 KO (-/-) sections labeled with the Pld3-specific luminal antibody. Prior to Pld3 labeling, heat-induced antigen retrieval was performed (see section 2.4.1, Material and Methods). The main regions of the spleen are listed. Scale bar, 50  $\mu\text{m}$ .

### 3.2.2 *Pld3 is mainly expressed in the cortex and hippocampus*

After comparing different tissues, Pld3 is highest expressed in the brain. Therefore, Pld3 distribution in this organ was analyzed in more detail. The brain of WT mice was dissected in different regions, including the cerebellum, the medulla, the olfactory bulb, the hippocampus and the cerebral cortex. Western blot analysis of lysates from the main brain regions and further immunoblotting with the anti-PLD3-specific N-terminal antibody revealed that Pld3 is expressed highest in the hippocampus and the cerebral cortex, but at low levels in the cerebellum. Quantification of the relative Pld3 levels are shown in Figure 38A.

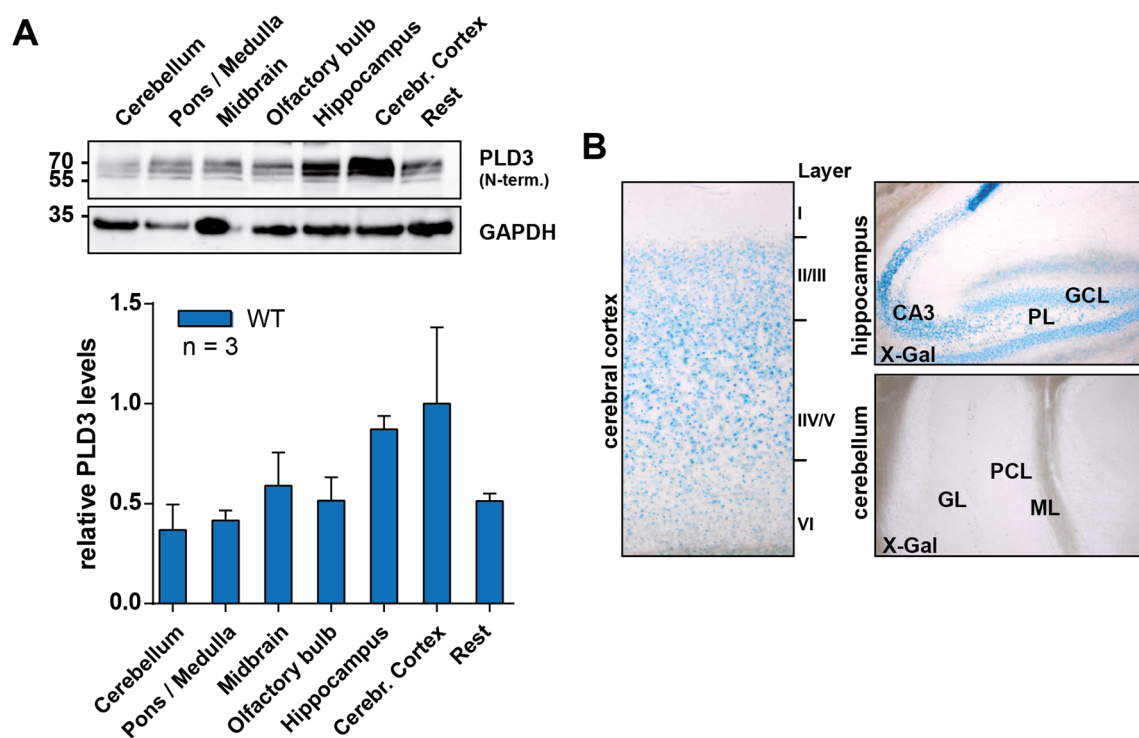


**Figure 38 | Pld3 is mainly expressed in the cortex and the hippocampus.** *A*, Pld3 full-length protein levels of different brain regions were analyzed via Western blot by immunoblotting with the N-terminal specific Pld3 antibody. GAPDH is presented as a loading control. Relative PLD3 levels of independent biological replicates ( $n = 3$ ) is shown. Values were normalized to Pld3 levels in the cerebral cortex. *B*, Immunohistochemistry images of  $\beta$ -galactosidase activity in the cerebral cortex, the hippocampus and the cerebellum, using X-gal as a colorimetric substrate. The layers of the cerebral cortex (I-VI) are labeled. CA3, *Cornu Ammonis* area 3; GCL, granular cell layer; PCL, Purkinje cell layer; GL, granular layer; ML, molecular layer.

X-gal staining, used to detect the reporter *lacZ* gene expression, also confirmed this result (Figure 38B). In this assay,  $\beta$ -galactosidase cleaves X-gal into galactose and 5-bromo-4-chloro-3-hydroxyindole; this second compound is then oxidized into 5,5'-dibromo-4,4'-dichloro-indigo (Burn, 2012). As its name suggest, the final product is blue in color, as seen in Figure 38B, where X-gal staining was distributed along the cerebral cortex and the hippocampus, particularly in the dentate gyrus and the CA3 region. In contrast, barely any staining was observed in the cerebellum. Of note, within the hippocampus, Pld3 is predominantly expressed in cells distributed along the granular cell layer (gcl). To get a broader overview of the Pld3 expression within the brain, an immunofluorescence staining was performed. Analysis of PLD3 expression by immunofluorescence of brain sections showed showed an increased Pld3 immunoreactivity along the different layers of the cerebral cortex and in the hippocampus (Figure 39). Additionally, Pld3-specific

fluorescence signal was observed in sub-regions of the hypothalamus, the striatum, the medulla and the anterior olfactory nucleus (AON, Figure 39). The presence of Pld3 in these sub-regions might explain the lower Pld3 protein signal observed in the Western blot analysis compared to the cortex and the hippocampus (Figure 38A), probably derived from a sub-population of specific cell types.

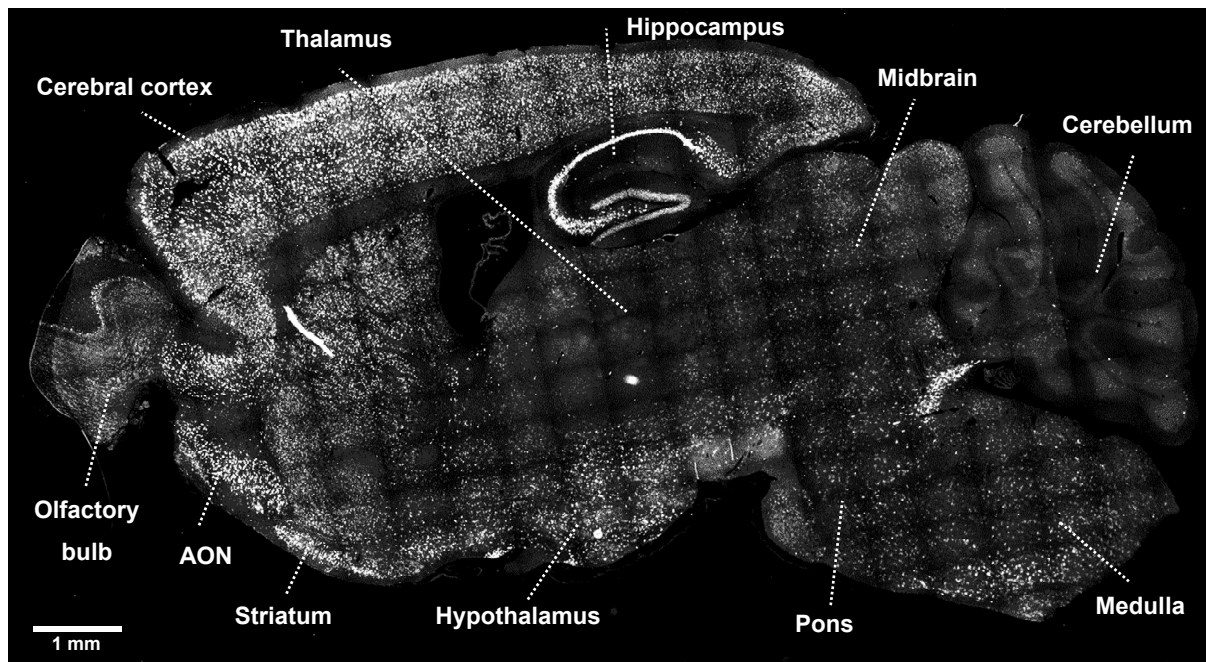


**Figure 39 | Image stitching of Pld3 expression in the brain.** Paraffin embedded WT brain sections (9 months old) were stained with the luminal-specific Pld3 antibody and more than 300 single fluorescence images were acquired to generate a full picture of the brain by stitching overlapping image tiles. A high *Pld3* expression is observed in the hippocampus and cerebral cortex. All main brain regions are named. AON, anterior olfactory nucleus.

### 3.2.3 *Pld3* is a neuronal protein

The central nervous system (CNS) contains a large variety of cell types, each with a unique morphology, physiology and function (Lein et al., 2007). Within the CNS, the two main types of cells are neurons and glia cells. Within the neuronal population, it has been reported that 50 – 250 neuronal sub-cell types exist (Ascoli et al., 2007; Kandel et al., 2012; Dimou and Götz, 2014). On the other hand, glia cells make up about 90 % of cells within the CNS. Astrocytes, oligodendrocytes and microglia are the major cell types.

Considering the cell morphology, immunohistochemistry images of human brain sections suggests that Pld3 is expressed mainly in neurons (Figure 12A). To confirm this observation, mouse brain sections were co-stained with the luminal Pld3-specific antibody and a neuronal nuclear marker (anti-NeuN antibody). Fluorescence images of Pld3-stained brain regions with the highest immunoreactivity (hippocampus and cortex) revealed that Pld3 is expressed in NeuN positive cells (Figure 40). Within the hippocampus, Pld3 is mostly concentrated in cells of the Striatum Pyramidale (CA3 region) and in the hilus of the dentate gyrus. Although Pld3 was expressed in all cerebral cortical layers (Figure 39), a stronger staining was observed in layers II and III, which might be due to the presence of a population of large pyramidal cells (Figure 40).

For Pld3 staining in tissue sections, heat-induced antigen retrieval is required (see section 2.4.1, Material and Methods). Therefore, only co-staining with the NeuN marker was possible. Thus, no co-staining of Pld3 with glia markers was viable. To investigate if Pld3 is expressed in other cell types, a primary co-culture of neurons, astrocytes and microglia was prepared from newborn WT mouse embryos. Accordingly, Pld3 localized to MAP2- (microtubule-associated protein 2) positive cells, used as a neuronal marker (Figure 41). However, no co-localization of Pld3 was observed in cells positive for the marker proteins expressed in astrocytes (anti-GFAP antibody, glial fibrillary acidic protein) or in microglial cells (anti-CD68 antibody). This result confirms that Pld3 is exclusively expressed in neurons. Additionally, Pld3 protein levels of WT and Pld3 KO mouse brain lysates were directly compared with BV-2 WT cells (Figure 42). This murine cell line (BV-2) has been previously generated by infecting primary microglia cell cultures with a *v-raf/v-myc* oncogene carrying retrovirus (J2), resulting in the generation of a cell line exhibiting morphological, phenotypical and functional properties of active microglial cells (Blasi et al., 1990).

Western blot analysis revealed a faint signal in BV-2 cells at the size of Pld3, especially with the luminal Pld3-specific antibody (Figure 42). No Pld3 was detected by immunofluorescence analysis of BV-2 cells (data not shown). In brief, these data indicate that Pld3 is a neuronal protein, although a low expression in microglia cells cannot be excluded.



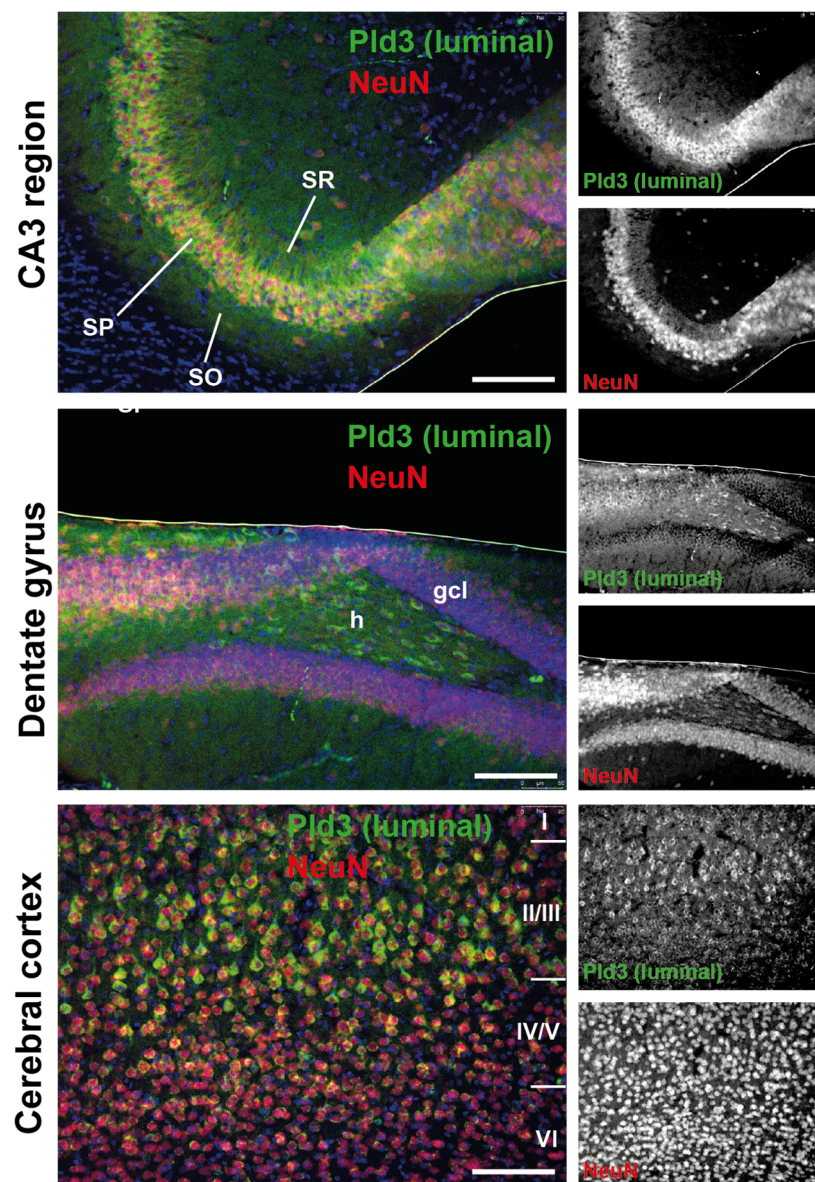


**Figure 40 | Pld3 is mainly expressed in neuronal cells.** Fluorescence images of the CA3 region and dentate gyrus of the hippocampus and the cerebral cortex (layers numbered). Sections were treated with heat-induced antigen retrieval and further co-labeled with the Pld3-specific luminal antibody (green) and the neuronal nuclear protein marker anti-NeuN (red). SO, Stratum Oriens; SP, Stratum Pyramidale; SR, Stratum Radiatum; h, hilus; gcl, granular cell layer. Scale bar, 50  $\mu$ m.

▼ **Figure 41 | Pld3 is highly expressed in neurons.** Mixed co-culture of neuronal, astroglia and microglia cells co-stained with the luminal Pld3-specific antibody (green) and antibodies against the microtubule-associated protein 2 (MAP2, neuronal dendrites marker), the glial fibrillary acidic protein (GFAP, astrocyte marker) and the cluster of differentiation protein 68 (CD68, microglia marker) depicted in red (upper panel). The lower panels correspond to enlarged regions for each cell type (dashed square). Images of astrocytes and microglia cells were acquired at the same region. Scale bar, 10  $\mu$ m.

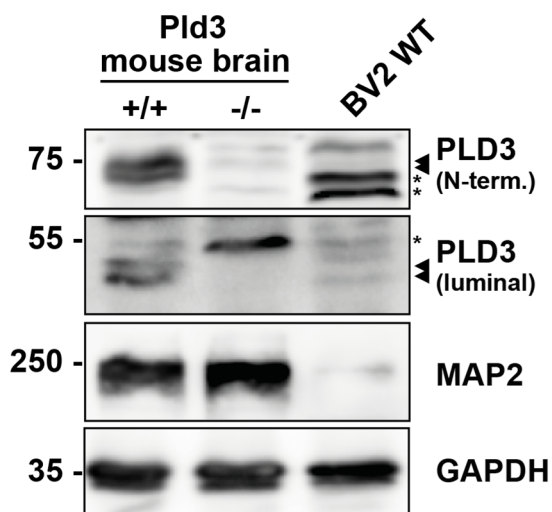
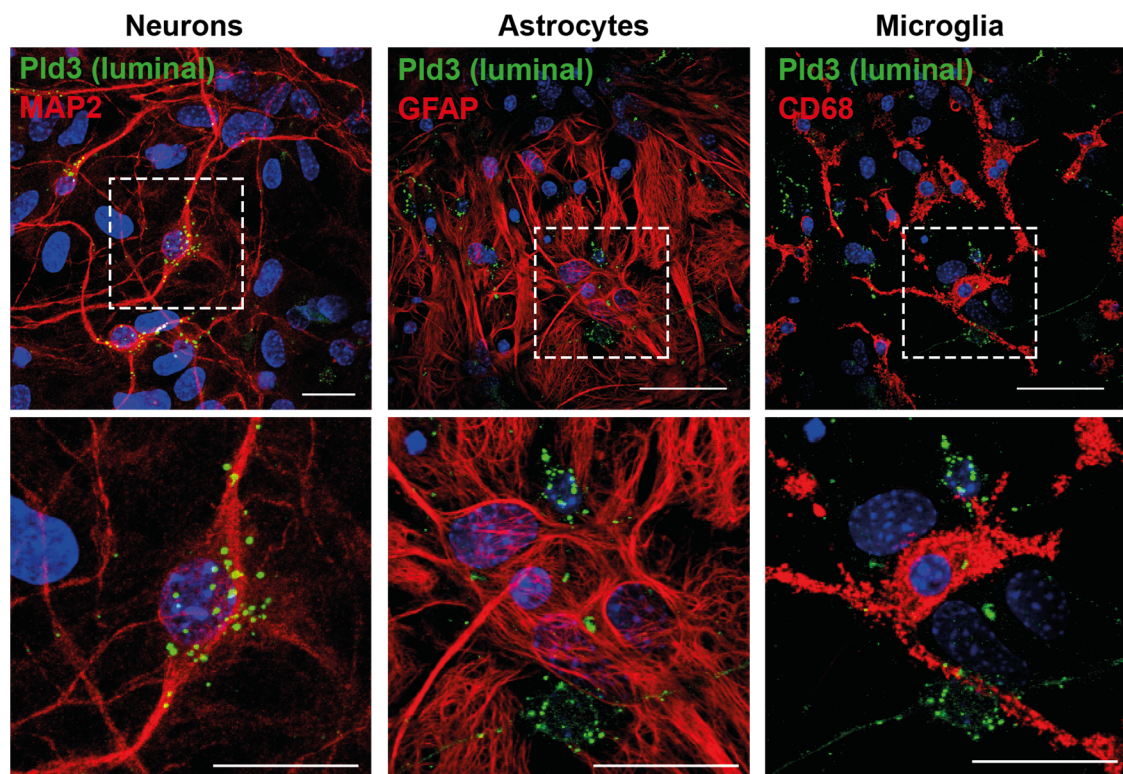


**Figure 42 | Pld3 is hardly expressed in microglia cells.** Western blot analysis of Pld3 WT and KO brain lysates compared to BV-2 WT microglia cell lysate. Pld3 signal detected with the N-terminal and luminal Pld3-specific antibodies is indicated with black arrowheads. \* denotes unspecific signal. MAP2 is presented as a positive control of neuronal cell specificity. GAPDH was used as a loading control.

### 3.2.4 *Pld3*-deficient mice exert subtle changes in the activity of lysosomal enzymes

Lysosomes are the primary degradative compartment of the cell, containing more than 50 hydrolases with utilize specific substrates (Saftig and Klumperman, 2009). In order to test if Pld3 deficiency leads to changes in the activity of lysosomal enzymes, e.g. due to higher number of lysosomes, the activities of three different lysosomal enzymes ( $\beta$ -



hexosaminidase,  $\beta$ -glucuronidase and  $\beta$ -glucocerebrosidase) were analyzed (Figure 43). Considering that Pld3 may have phospholipase D activity, its deficiency could lead to the accumulation of specific substrates and subsequent alteration of other lysosomal hydrolases.  $\beta$ -Hexosaminidase catalyzes the hydrolysis of  $\beta$ -glycosidically linked *N*-acetylglucosamine and *N*-acetylgalactosamine residues from the non-reducing end of a number of glycoconjugates (Wendeler and Sandhoff, 2009).  $\beta$ -glucuronidase catalyzes the hydrolysis of  $\beta$ -D-glucuronic acid residues from the non-reducing termini of glycosaminoglycans (Fratz-Berilla et al., 2017).  $\beta$ -glucocerebrosidase catalyzes the hydrolysis of glucosylceramide to form ceramide and glucose (Motabar et al., 2012). All assays used to analyze the activity of these enzymes were based on the use of chromogenic artificial substrates, thereby producing a product that can be detected spectrophotometrically at 405 nm to determine enzymatic activity. These analyses were performed using brain lysates of 3 months old and 6 months old WT and Pld3 KO mice. For most of the enzymes evaluated, a significant decrease of the specific activity (mU/mg protein) was observed in the lysates of Pld3 KO mice when compared to WT lysates (Figure 43).

### **3.2.5 *Pld3* deficiency leads to a localized microgliosis in the dentate gyrus (DG)**

As described above, Pld3 is highly expressed in neuronal cells of the hippocampus and the cortex (3.2.1, 3.2.2 and 3.2.3). Moreover, *PLD3* variants have been associated as risk factors for the development of Alzheimer's disease (AD) (Cruchaga et al., 2014). Neuroinflammation is proposed as one of the mechanisms by which AD pathology leads to neuronal death and dysfunction (Griffin, 2006).

Microglia cells are the resident immune cells of the brain and play a major role in the neuroinflammatory response in AD (Hopperton et al., 2018). Despite low expression of Pld3 in microglia, Pld3 WT (+/+) and KO (-/-) brain sections were stained with an antibody against CD68 to analyze any sign of neuroinflammation (Figure 44). Although there is some expression of CD68 in resting microglia (Lee et al., 2002), it is commonly considered a maker for activated phagocytic microglia (Walker and Lue, 2015).

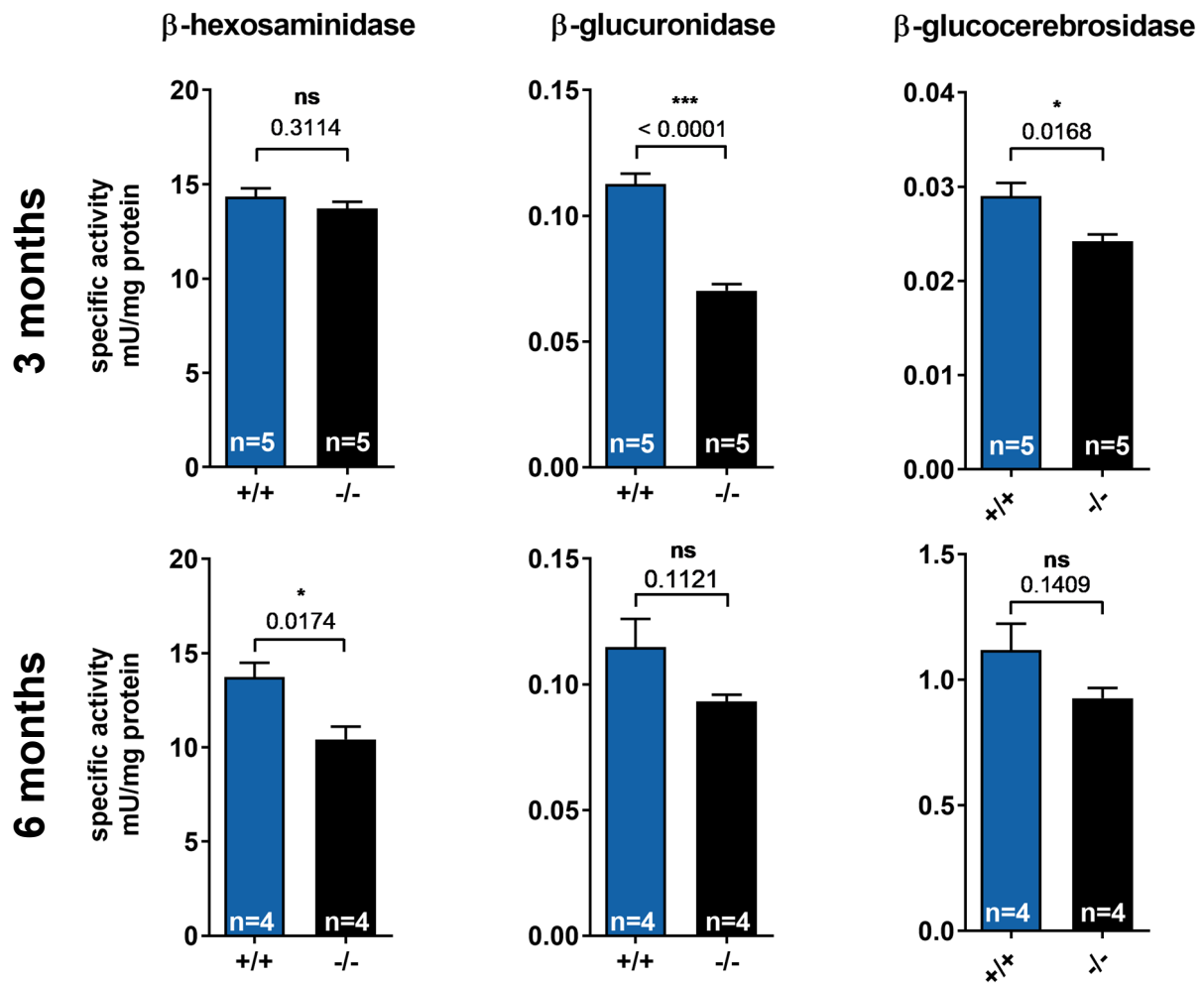


**Figure 43 | Pld3 KO mice have reduced lysosomal enzyme activity.** The lysosomal enzymes  $\beta$ -hexosaminidase,  $\beta$ -glucuronidase and  $\beta$ -glucocerebrosidase were analyzed in two cohorts of 3 months and 6 months old Pld3 WT versus Pld3 KO mice using total brain lysate. The absolute specific activity (mU/mg protein) for each enzyme was measured. Error bars represent SEM. \*\*\* $p < 0.001$ ; \* $p < 0.1$ ; unpaired Student's t test ( $n = 4 - 5$ ). ns, not significant.

Immunohistochemistry for CD68 revealed increased microglia immunoreactivity in the dentate gyrus of Pld3 KO mice when compared to WT sections (Figure 44). This observation was more evident on brain sections of adult mice (6 months old) and old mice (21 months old).

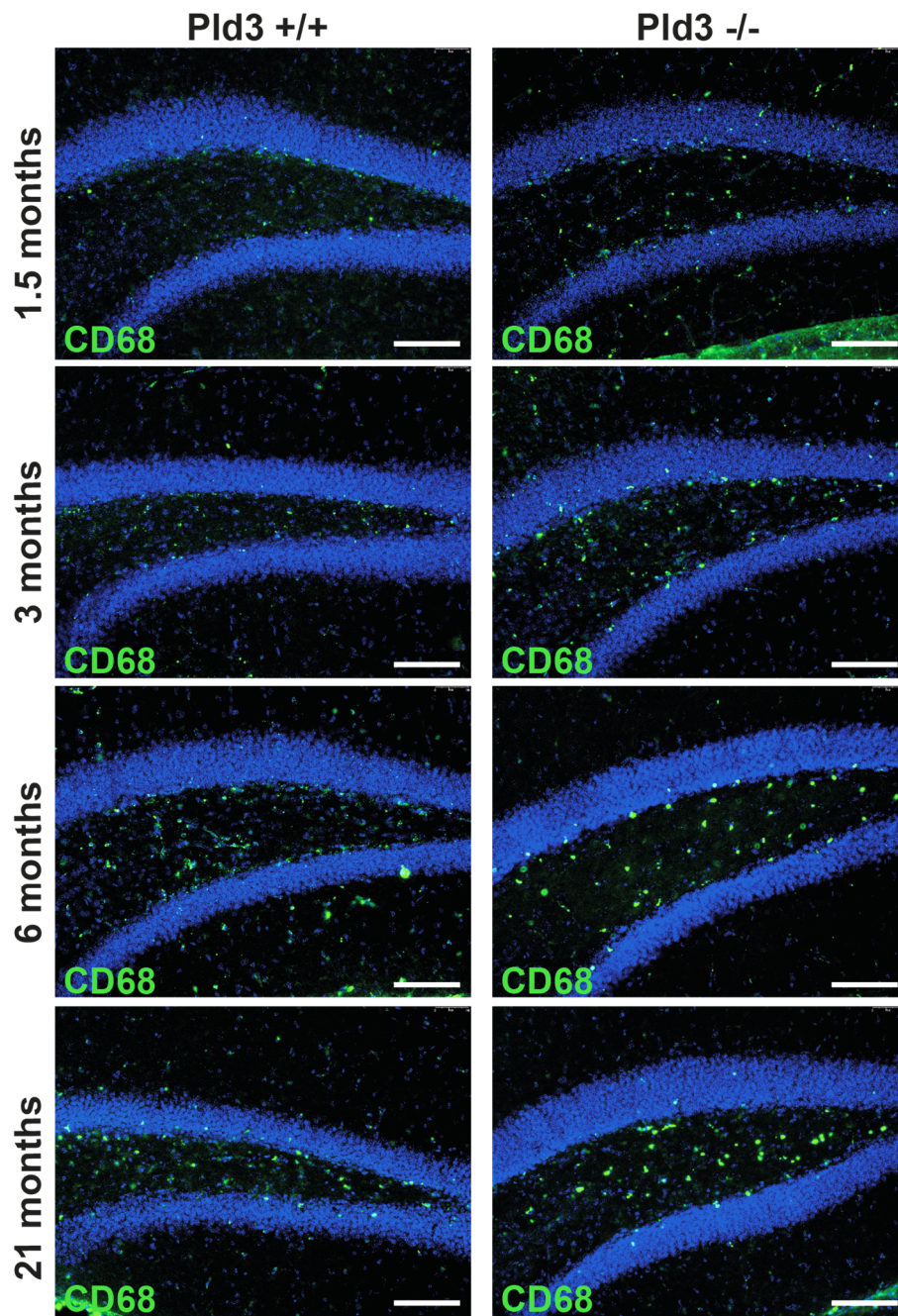


**Figure 44 | Pld3 KO mice show localized microglia activation in the dentate gyrus.** Dentate gyrus fluorescence images of 1.5, 3, 6 and 21 months old WT versus Pld3 KO mice. Sections were labeled with an anti-CD68 antibody as a marker of activated microglia, CD68 (green). Nuclei are stained with DAPI (blue). Scale bar, 50  $\mu$ m.

To confirm these results, brain sections of 12 months old WT and Pld3 KO mice were labeled with anti-CD68 and anti-GFAP antibodies. An increased microglia activation in the sections of Pld3 KO mice was not only observed in the dentate gyrus (DG) of the

hippocampus, but also in the subventricular zone (SVZ, Figure 45A), known to be the largest germinal zone of the adult mammalian brain and where adult neurogenesis takes place (Doetsch and Alvarez-Buylla, 1996).

Quantification of CD68 revealed significantly higher CD68 immunoreactivity in these two areas (DG and SVZ), as well as in the corpus callosum (CC) and the cerebellum (CB, Figure 45B). Although not significant, a tendency of increased CD68 labeling was also observed in the cerebral cortex (CX).

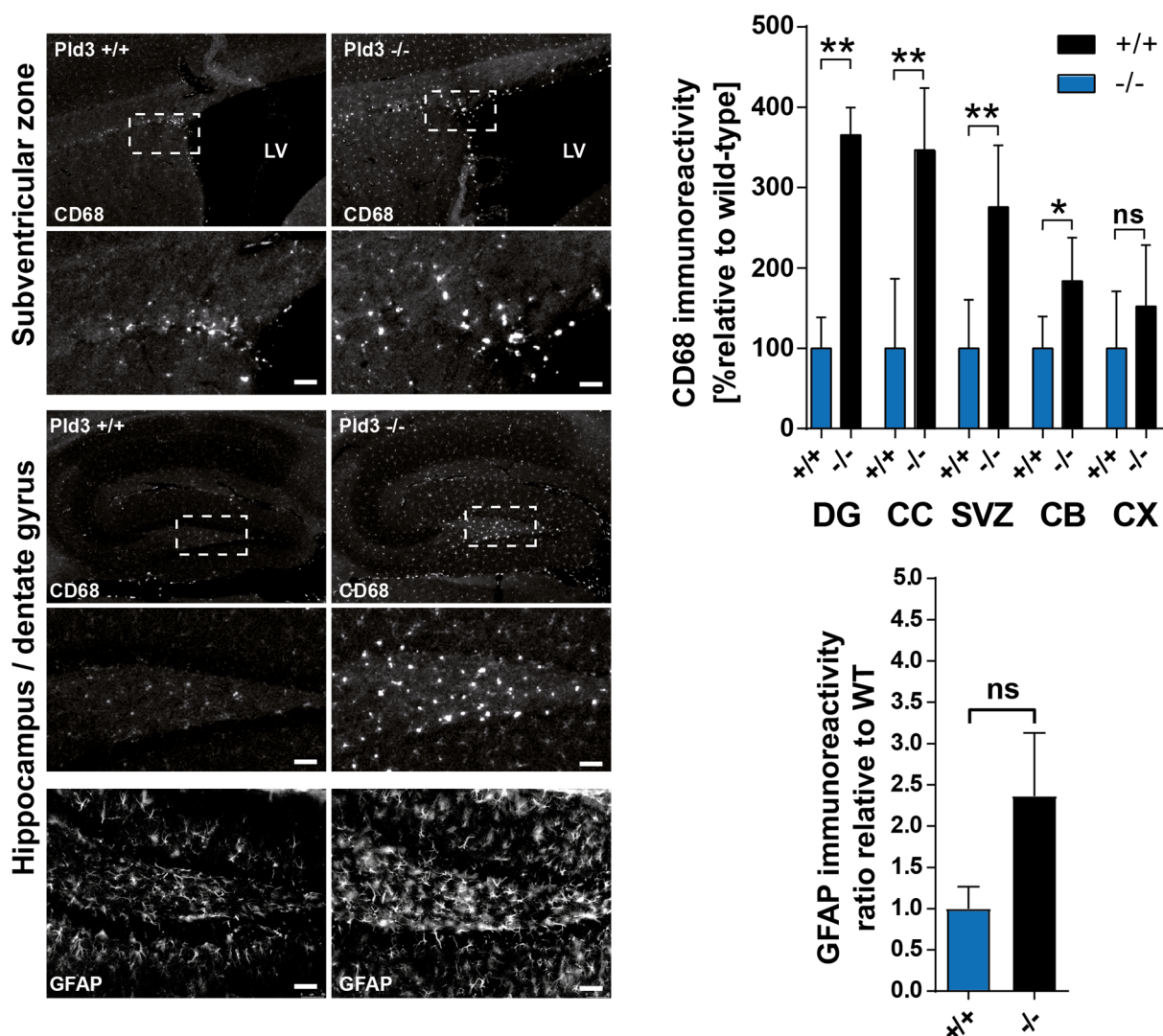


**Figure 45 | Pld3 KO mice have increased immunoreactivity of microglia and astrocytes markers.** A, 12 months old Pld3 WT and KO brain sections were labeled with the microglia marker (anti-CD68) or the astrocyte marker (anti-GFAP). Fluorescence images show the subventricular zone and the dentate gyrus of the hippocampus. B, Relative CD68 immunoreactivity was quantified in different brain regions. C, GFAP immunoreactivity was quantified in the dentate gyrus. Error bars represent SEM. \*\* $p < 0.01$ ; \* $p < 0.1$ ; unpaired Student's t test ( $n = 3$ ). ns, not significant. LV, lateral ventricle; DG, dentate gyrus; CC, corpus callosum; SVZ, subventricular zone; CB, cerebellum; CX, cortex. Scale bar, 50  $\mu$ m.

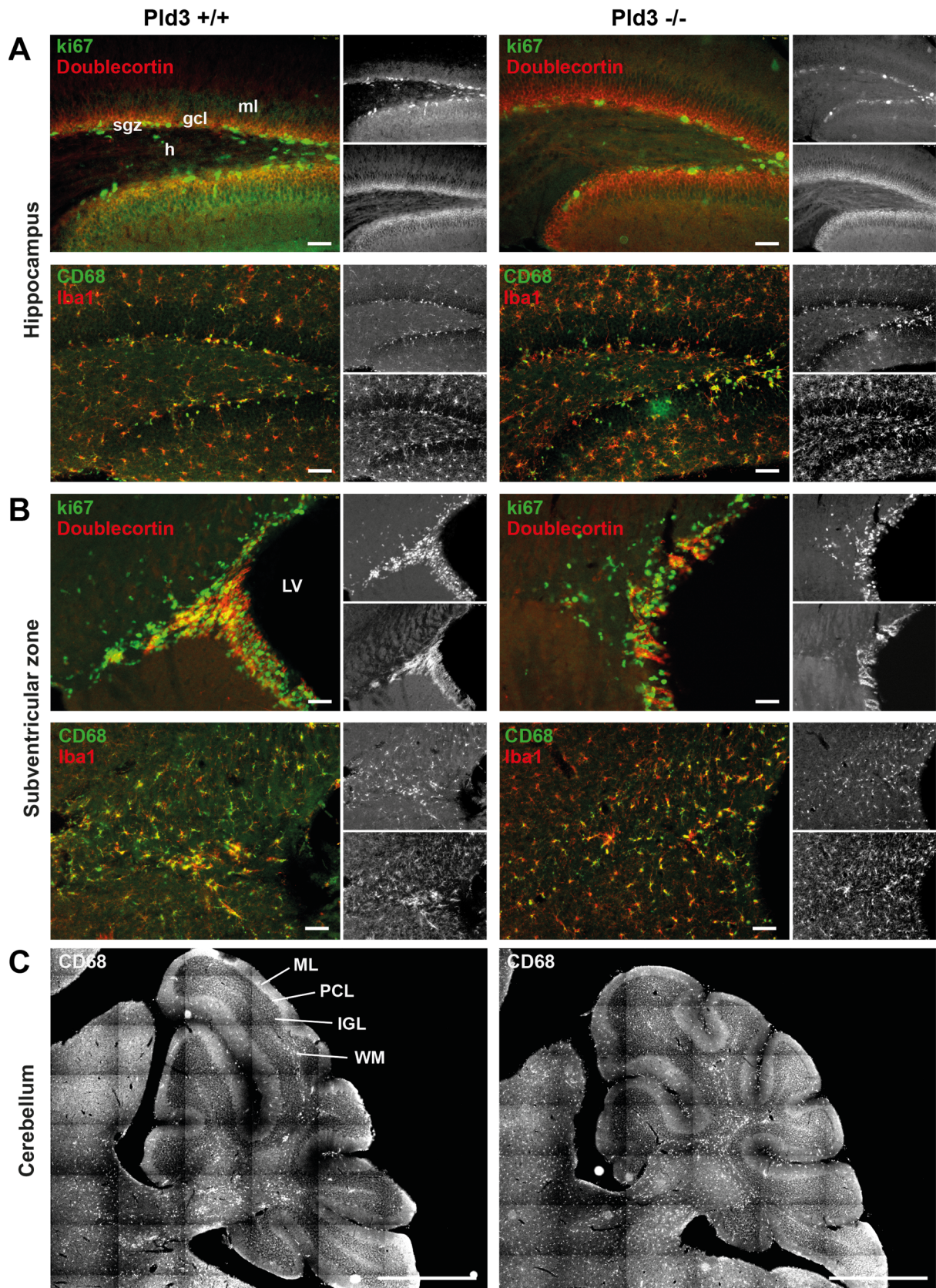


Immunofluorescence images of anti-GFAP staining in the DG (Figure 45A, lower panel) and further quantification (Figure 45C), revealed a tendency towards increased GFAP immunoreactivity. This marker is commonly used for the activation of astrocytes following injury or stress in the central nervous system (Zhang et al., 2017). Taken together, these data suggest that Pld3 deficiency leads to a subtle neuroinflammatory phenotype, especially in reported regions where new neurons are constantly and spontaneously born: the subgranular zone of the hippocampus (Altman and Das, 1965) and the subventricular zone (Altman, 1969).

We therefore hypothesized that Pld3 deficiency might alter neurogenesis in any of these described regions. Due to a higher rate of neuronal cell division in the first stage of mouse development (0 – 4 weeks), brain sections of 3 weeks old WT (+/+) and Pld3 KO (-/-) mice were co-labeled with fluorescence antibodies against Ki67 (neuronal mitotic marker) and doublecortin (DCX, marker of immature neurons). Immunohistochemistry images of the dentate gyrus and the subventricular zone did not reveal apparent differences in the staining of these two markers between WT and Pld3 KO sections (Figure 46). In the subgranular zone (sgz) of the dentate gyrus, less cells positive for Ki67 were observed in Pld3 -/-, yet this observation was not consistent when other brain sections were stained (data not shown). Additionally, staining against the CD68 antibody did not show increased immunoreactivity in the DG and SVZ as previously observed in older mice (Figure 44 and Figure 45). Nonetheless, a tendency of increased CD68 staining in Pld3 -/- sections was detected in the cerebellum, especially in the white matter (WM). In summary, these experiments suggest that Pld3 deficient mice develop a localized microgliosis in different brain regions, but this inflammatory phenotype does not seem to occur as a consequence of neurodegeneration.

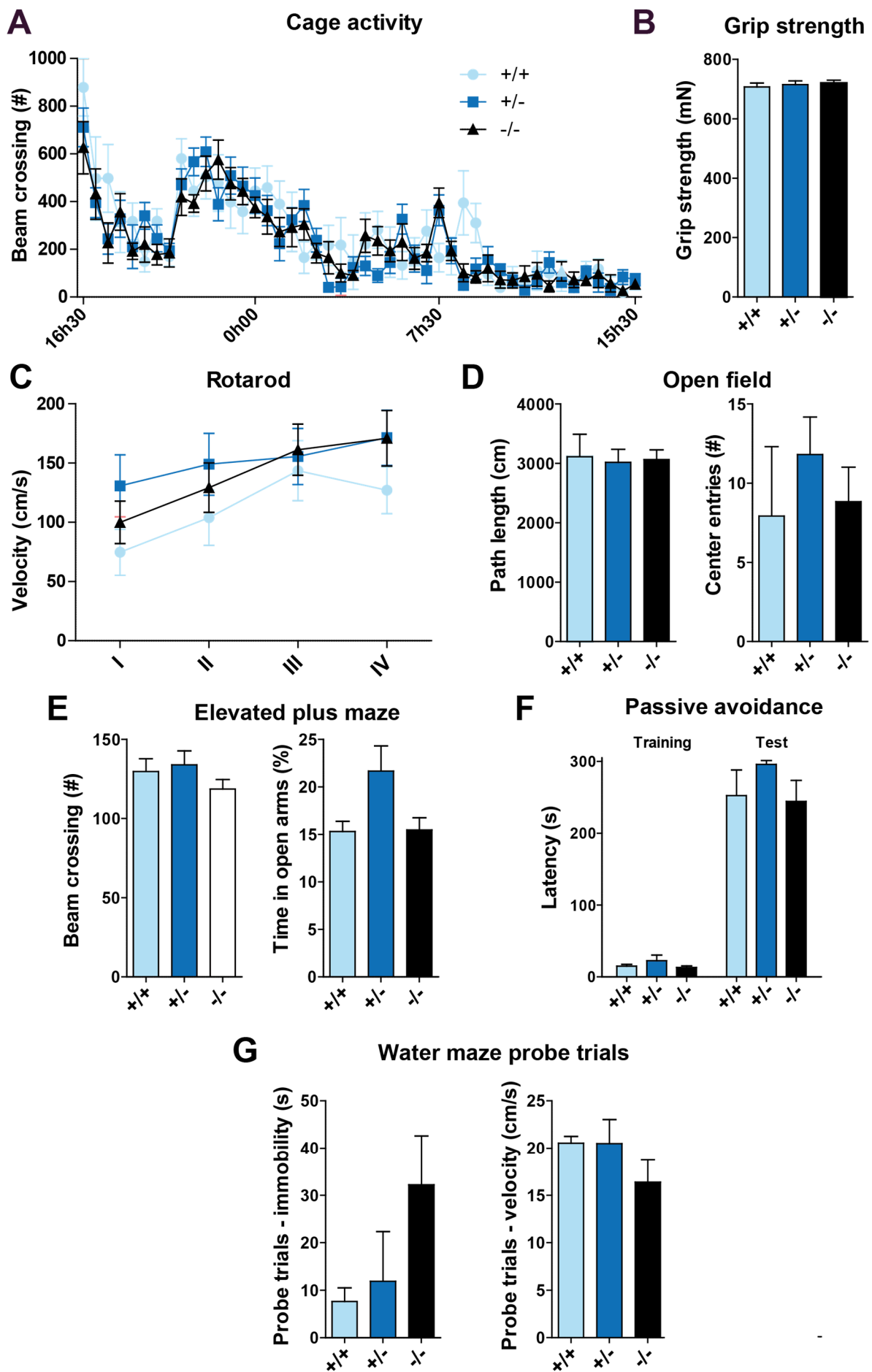
---

▼**Figure 46 | Pld3 KO mice show normal neurogenesis and cell proliferation.** Brain sections of 3 weeks old Pld3 WT and KO mice were co-labeled with markers of neurogenesis and cell proliferation (Doublecortin and Ki67) or with markers of microglia (Iba1 and CD68). Fluorescence images were acquired in different regions including the dentate gyrus of the hippocampus (*A*), the subventricular zone (*B*) and the cerebellum (*C*). For the dentate gyrus and the cerebellum main structures are listed. h, hilus; sgz, subgranular zone; gcl, granular cell layer; ml or ML, molecular layer; PCL, Purkinje cell layer; IGL, internal granular layer; WM, white matter. Scale bar, 50  $\mu$ m.



### **3.2.6 *Pld3* deficient mice show a depression-like behavior**

As a result of the increased CD68 immunoreactivity observed in brain regions of the *Pld3* deficient mice, we wanted to address if this inflammatory response has any effect on the behavior of *Pld3* KO mice. A large variety of rodent behavioral tests have been designed to evaluate traits such as sensory-motor function, social interactions, anxiety-like and depression-like behavior, substance dependence and various forms of cognitive functions (Hånell and Marklund, 2014). In collaboration with Dr. Stijn Stroobants from the University of Leuven (Belgium) different tests, including cage activity, grip strength, rotarod and open field, were used to test the locomotor activity and neuromuscular function in 5 months old WT (+/+), *Pld3* heterozygous (+/-) and *Pld3* KO (-/-) mice. Moreover, the exploratory activity was also evaluated. No differences appeared between the groups for cage activity (Figure 47A), grip strength (Figure 47B) and rotarod (Figure 47C), indicating similar neuromotor function. The groups showed comparable exploration in the open field test in terms of total activity (Figure 47D, left) and exploration of the center (Figure 47D, right). In the elevated plus maze, no changes between the groups were observed for total exploratory activity (Figure 47E). Passive avoidance test and water maze probe trials were used to evaluate learning and memory. All three groups performed successful passive avoidance learning (increase of step-through latencies (Figure 47F)). During the water maze probe trials, long-term retention of the platform location is tested. However, spatial preferences cannot be evaluated reliably when mice are highly immobile. Indeed, similar trends of increased immobility were observed in the probe trials. Therefore, all mice showing more than 15 % immobility were excluded to evaluate spatial preference. From the remaining animals, no differences were observed (Figure 47G). The Morris water maze is the most common test to evaluate cognitive functions related to learning and memory (Nunez, 2008). During water maze acquisition, *Pld3* KO mice tended to show increased escape latencies (Figure 48A, upper left), but did not travel more distance to reach the platform (Figure 48A, upper right). In fact, *Pld3* KO mice showed reduced swimming velocity depending on the time point of acquisition. When acquisition weeks were analyzed separately, knockout mice showed a progressive reduction of swimming velocity during the first week, in contrast to wildtype and heterozygous mice, which remained stable during the second week (Figure 48A, lower left).





**▲Figure 47 | Pld3 KO mice show normal neuromotor and cognitive function.** Locomotor activity, anxiety and willingness for the mice to explore was measured by cage activity, grip strength, rotarod, open field and elevated plus maze behavioral tasks. Passive avoidance and water maze probe trials were used to evaluate learning and memory. A total of 31 animals (5 months old) were analyzed for these trials (9 wild-type, 11 heterozygous, 11 Pld3 knockout). Error bars represent SEM. All tests were performed in collaboration with Dr. Stijn Stroobants at the Laboratory of Biological Psychology in Leuven (Belgium).

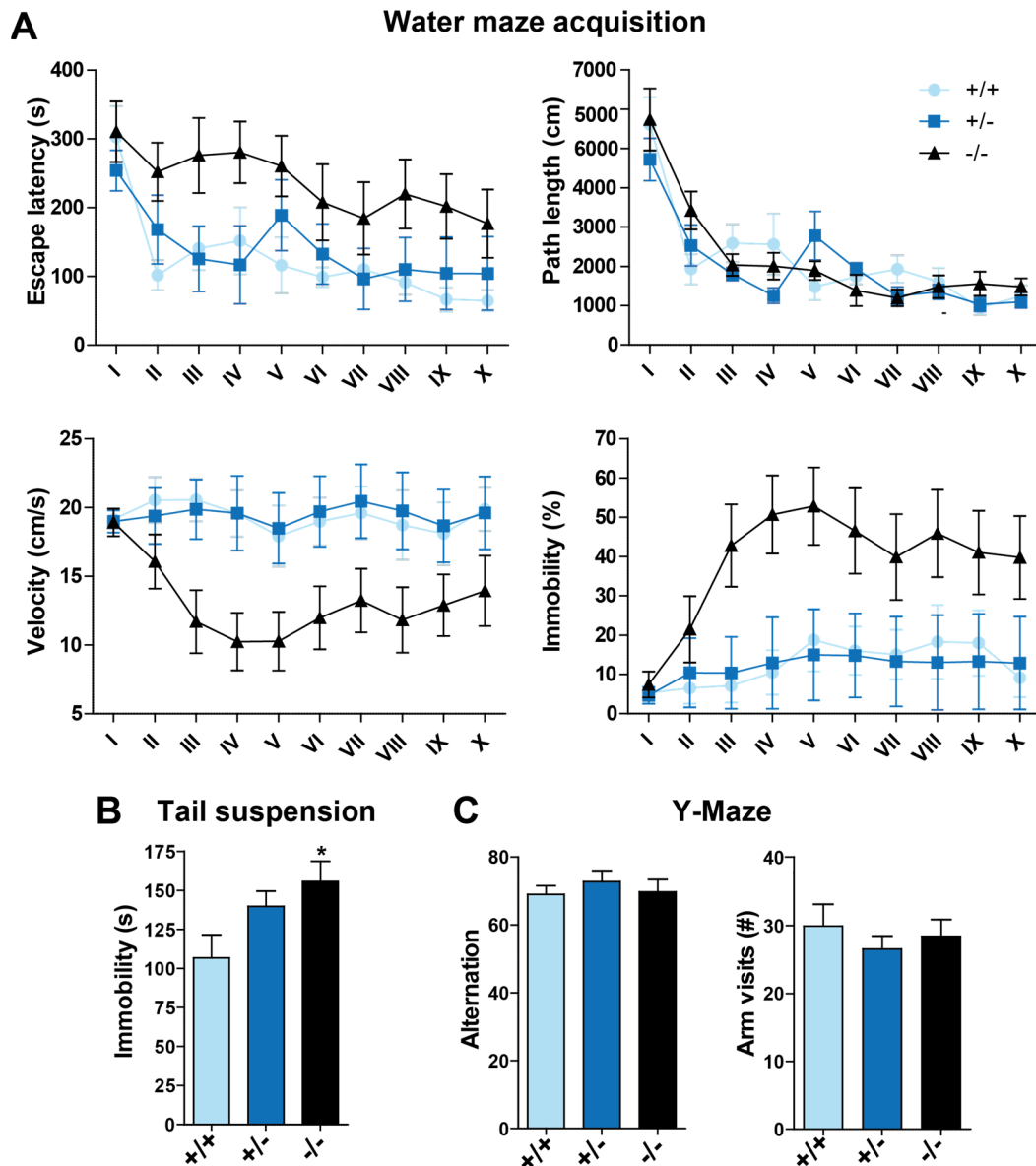


**Figure 48 | Pld3 KO mice show a depression-like behavior.** Spatial learning, memory and depression-like phenotype were evaluated by water maze acquisition, tail suspension and Y-Maze. A total of 31 animals (5 months old) were analyzed for these trials (9 wild-type, 11 heterozygous, 11 Pld3 knockout). All tests were performed in collaboration with Dr. Stijn Stroobants at the Laboratory of Biological Psychology in Leuven (Belgium). Error bars represent SEM. \* $p < 0.1$ .

This reduction of swimming velocity appeared to be due to increased floating behavior in the majority of knockout mice (=immobility in the water). Similar to the related velocity graph, knockout mice showed a progressive increase of immobility during the first week of acquisition, with floating behavior remaining at similar levels during the second week (Figure 48A, lower right). These results indicate an increased susceptibility for behavioral despair in knockout mice. To confirm a depression-like phenotype, a tail suspension test was performed. There were significant differences between the groups for the time spent immobile when suspended from the tail. Pld3 KO mice spent more time immobile than WT mice (Figure 48B). However, during Y-maze exploration, all groups showed a similar alternation behavior (Figure 48C, left) and similar amount of arm visits (Figure 48C, right), indicating intact working memory. All behavioral tests were re-tested in the same animals at 9 months of age, showing the same results and tendencies observed when tested at 5 months old (data not shown). These data indicate that Pld3 deficient mice have normal locomotor activity and no alterations in cognitive function related to memory and learning. However, Pld3 KO mice seems to develop a depression-like behavior.

### **3.3 Functional analysis of PLD3**

#### **3.3.1 *Pld3 deficient mice show subtle alterations in lipid species***

PLD3 has been grouped to the phospholipase D family members due to the presence of a conserved HKD motif. Enzymes belonging to this family, like PLD1 and PLD2 catalyze the hydrolysis of phosphatidylcholine (PC) to phosphatidic acid (PA) and choline (Hanahan and Chaikoff, 1947; Heller, 1978; Oude Weernink et al., 2007). In order to indirectly test for PLD activity, a high-throughput lipidomics analysis was performed. This analysis was carried out in collaboration with Dr. Dominik Schwudke from the Research Center Borstel, Germany. Due to the predominant Pld3 expression observed in the brain (section 3.2.1), especially in neuronal cells (section 3.2.3), wild-type (WT) and Pld3-deficient (KO) whole brain lysates were used for methyl-tert-butyl ether (MTBE) -based lipid extraction (Matyash et al., 2008) and further analyzed by mass spectrometry. A total of 220 lipid species divided in 13 classes were reported (Supplementary Table 23). From all the lipids

analyzed, only significant differences for ceramides (Cer) species were observed (Figure 49). However, for most of the detected species, the lipid content was too low, making it difficult to interpret. Moreover, no major differences were detected for phosphatidic acid (PA) as a classical end product of PLD enzyme activity. These data suggest that PLD3 does not have typical phospholipase D activity.

### 3.3.2 *PLD3 is a 5'-exonuclease*

To further analyze possible functions for PLD3 at the cellular level, a stable PLD3-knockout (KO) HeLa cell line was generated by CRISPR-Cas9 technology (clustered regularly interspaced short palindromic repeats, see section 2.3.5). To this end, HeLa cells were transfected with a pCMV-Cas9-GFP vector (Figure 6), containing a 22 bp target region of exon 4 of the human *PLD3* gene (Figure 50). The RNA-guided Cas9 promotes genome editing by stimulation of DNA-double stranded breaks at the target genomic locus (i.e. PLD3 target region) (Hsu and Zhang, 2012; Urnov et al., 2010). This region is associated with a protospacer adjacent motif (PAM), necessary for Cas9 to cleave the sequence (Barrangou et al., 2007; Brouns et al., 2008).

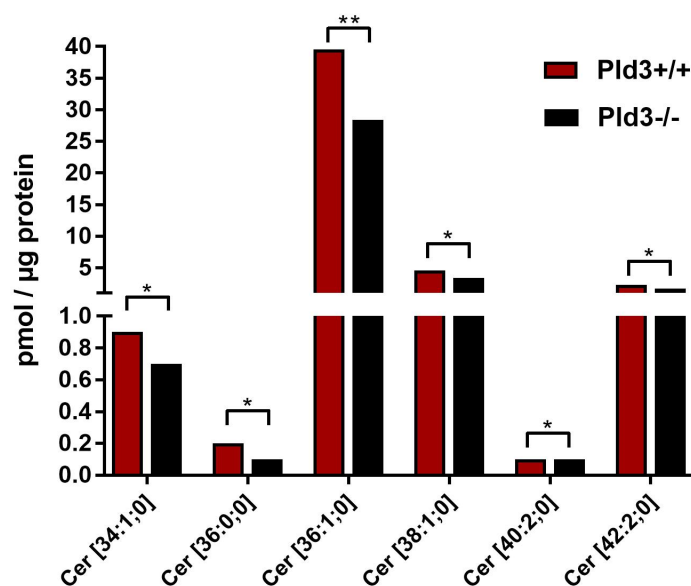


**Figure 49 | High-throughput lipidomics analysis of WT and KO Pld3 mice.** Lipid extraction of whole brain lysates of 4 WT vs. 4 Pld3 KO mice were performed via methyl-tert-butyl ether- (MTBE) and further analyzed by mass spectrometry. The graph shows significant values of different ceramide (Cer) species denoted as [carbon atoms:double bonds]. Error bars represent SD. \*p < 0.05, \*\*p < 0.05; unpaired Student's t test (n = 4).

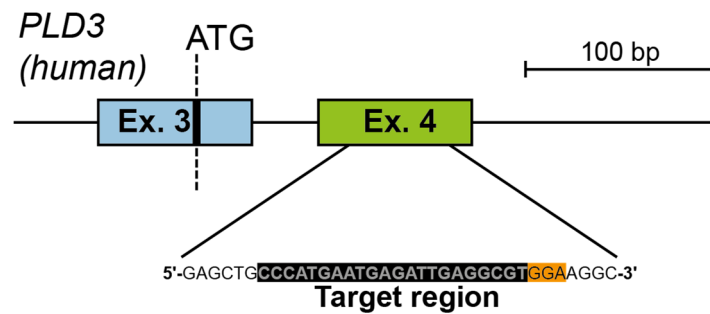


**Figure 50 | Schematic representation of sgRNA target site of the human PLD3 gene.** A sgRNA target region located in exon 4 of *PLD3* gene was used for the generation of PLD3-deficient HeLa cells using the CRISPR-Cas9 technology. The protospacer adjacent motif (PAM) is highlighted in orange.

Different clonal cell populations from the GFP-positive transfected HeLa cells were isolated by FACS and further validated. Primers were designed for PCR amplification of a 394 bp long product encompassing exon 4. Agarose gels of the PCR products for clones #16 and #19 revealed large genetic deletions (Figure 51A). Sanger sequencing chromatograms shows that PLD3 KO clones #10, #16 and #19 carry heterozygous mutations, where double peaks are observed after the target sequence, indicating different allelic mutations. For the PLD3 KO clone #20, a single nucleotide was inserted between the target sequence, leading to a homozygous frameshift mutation (Figure 51B). Additionally, PLD3 KO clones were validated by Western blot with both PLD3-specific N-terminal and luminal antibodies, showing an absence of PLD3 full-length and PLD3 cleavage products, when compared to the parental HeLa cell line (Figure 51C). For further analyses, only the PLD3 KO clone #20 was used.

With the aim to get better insight if PLD3 deficiency could cause any morphological alterations in subcellular structures (e.g. enlarged lysosomes), PLD3 KO HeLa cells were stained with different antibodies against intracellular proteins of the endoplasmic reticulum (KDEL), Golgi-apparatus (GM130), early endosomes (EEA1), late endosomes (LBPA) and lysosomes (LAMP2, Cathepsin D and CD63). Immunofluorescence analysis did not show any evident alterations in the size, positioning or morphology of the evaluated intracellular organelles (Figure 52).

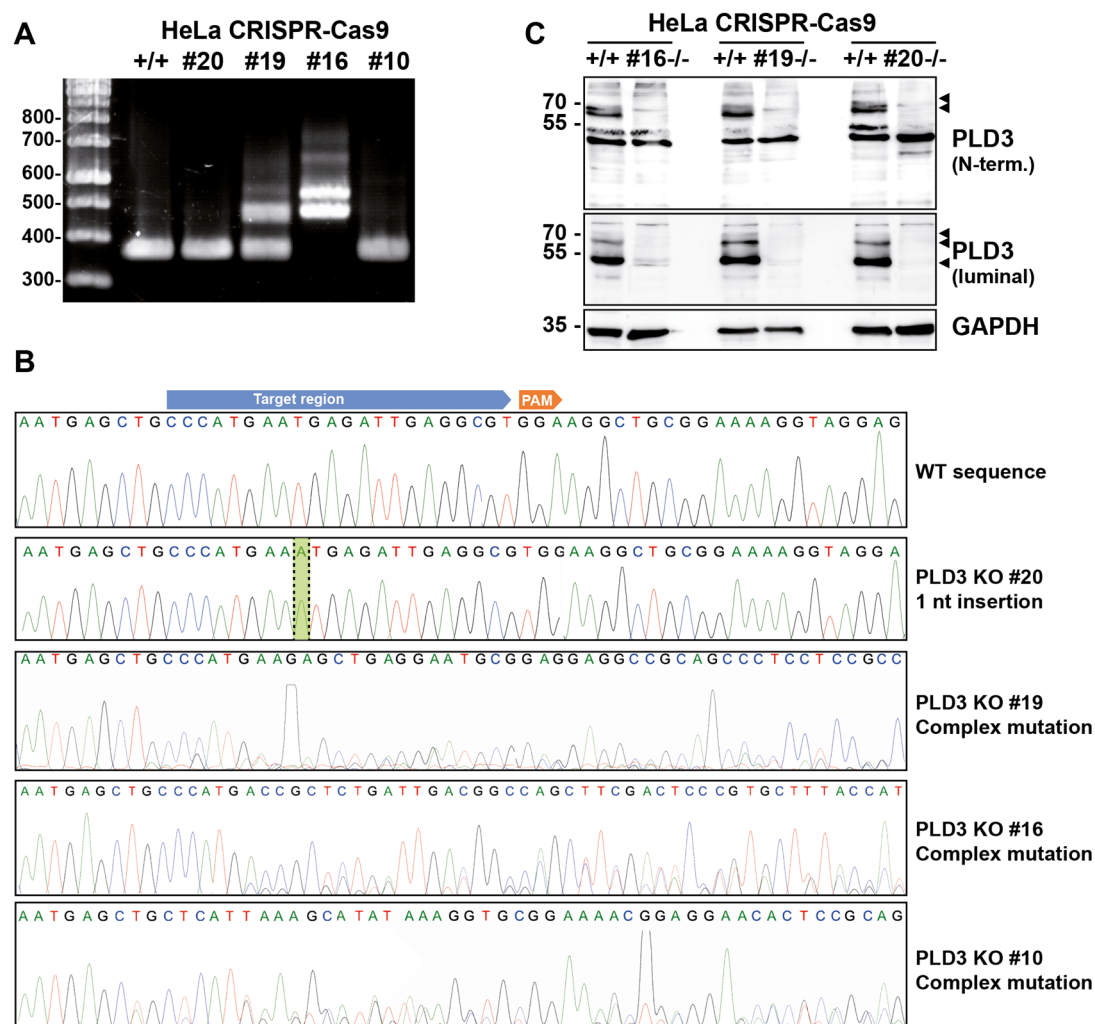


**Figure 51 | Validation of HeLa CRISPR-Cas9 clones.** Four different HeLa CRISPR-Cas9 clones were generated and validated for PLD3 deficiency. *A*, agarose gel analyses of PLD3 CRISPR-Cas9 clones amplifying by PCR a region of 394 bp long fragment covering exon 4 of WT PLD3 using genomic DNA as template. Clones #16 and #19 show large genetic deletions. *B*, Sanger sequencing chromatograms of all four PLD3 CRISPR-Cas9 clones and the corresponding sequence of the wild-type (WT) locus. Target region and protospacer adjacent motif (PAM) are indicated. *C*, Western blot analysis of three selected clones immunoblotted with PLD3-specific N-terminal and luminal antibodies. Comparison with the HeLa WT parental cell line is shown. Specific signals are labeled with black arrowheads. GAPDH is presented as a loading control.

Recently, in collaboration with the group of Dr. David Nemazee from The Scripps Research Institute, it was published that PLD3 and PLD4 (another homolog of the phospholipase D family) are lysosomal 5' single stranded acid exonucleases (Gavin et al., 2018). Pld3 protein expression analyses in different mouse organs (Figure 36 and Figure 37) showed that the spleen is the organ with second highest Pld3 expression. However, a

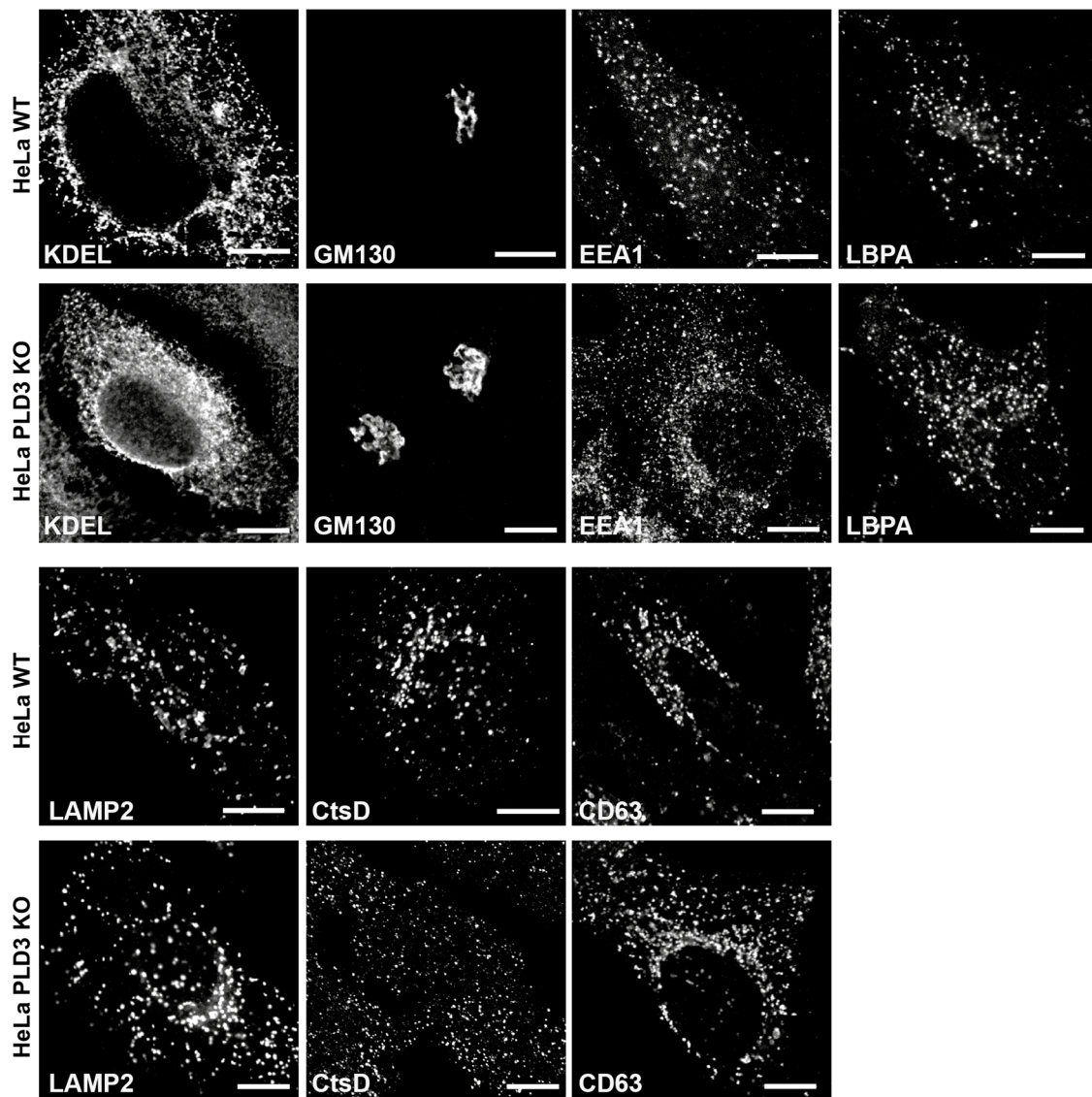
10-fold higher Pld3 expression was detected in the brain. Thus, we hypothesized that, if PLD3 and PLD4 have the same functions and/or similar physiological substrates, they might be tissue and/or cell-type specific.

Two different assays were established in order to investigate PLD3 nuclease activity. Both assays consisted on the *in vitro* incubation of cell or mouse organ lysates with specific 30 – 55 nucleotides long single-stranded deoxyribonucleic acid (ssDNA) in an acidic buffer condition. In the first (qualitative) assay, reaction products were separated in a DNA polyacrylamide gel electrophoresis (DNA-PAGE), stained with intercalating DNA agents and further visualized (for details, see section 2.5.12). In the second (quantitative) assay, ssDNA substrates were synthesized with a 5'-fluorescein amidite (FAM) dye and a 3'-BMN-Q530 quencher. Due to the low proximity between the dye and the quencher, FAM fluorescence is quenched; if 5' cleavage is occurring, FAM will be released from the sequence, allowing further quantification by spectrophotometry. We decided to name this assay as EFQO (End-Labeled Fluorescence-Quenced Oligonucleotide), assay that has been further developed and standardized by the MD student Cedric Cappel. The results that are discussed below are referred to the gel-based (qualitative) assay. Importantly, to make sure that no 3' exonuclease cleavage takes place in the reaction, the last 3' nucleotides of the sequence were modified with phosphorothioate (PS) bond modifications, which is known to render the internucleotide linkage resistance to degradation of most nucleases (Fisher et al., 1993).

First, PLD3 nuclease activity was studied at the cellular level by incubation of ssDNA as a substrate with lysates of WT HeLa or PLD3 KO HeLa cells. Analysis of the incubation products by DNA-PAGE revealed degradation of the substrate when incubated with WT HeLa cells lysates (Figure 53A). Degradation is evident by disappearance of the 50 nt ssDNA signal and appearance of smaller fragments. In contrast, similar to the negative control, where no lysate was added, limited substrate degradation was detected when incubated with PLD3 KO HeLa lysates (Figure 53A).

---

**Figure 52 | PLD3 KO HeLa cells do not show any morphological alterations in intracellular organelles.** Immunofluorescence images of PLD3 KO HeLa cells vs. WT HeLa cells stained with antibodies against marker proteins of the endoplasmic reticulum (KDEL), Golgi-apparatus (GM130), early endosomes (EEA1), late endosomes (LBPA) and late endosomes (LAMP2, Cathepsin D and CD63). Scale bar, 10  $\mu$ m.



The low nuclease activity detected in PLD3 KO HeLa cells, where faint signals of smaller DNA fragments are observed, could be due to PLD4 activity or other non-described nuclease(s). Next, PLD3 nuclease activity was evaluated under overexpressing conditions. Experiments with overexpressed constructs were always performed in PLD3 KO HeLa cells in order to avoid any endogenous (background) nuclease activity. As observed in Figure 53B, overexpression of *hPLD3* led to an increase of enzymatic activity, where substrate detection was very low after incubation at the indicated time points. This might be explained due to the high amount of PLD3 enzyme expressed. In summary, these experiments indicate that HeLa cells have endogenous PLD3 5' exonuclease activity and its overexpression leads to higher substrate degradation under the conditions used, making this a suitable assay to test the effect of different PLD3 variants on nuclease activity and further study PLD3 enzymological properties.



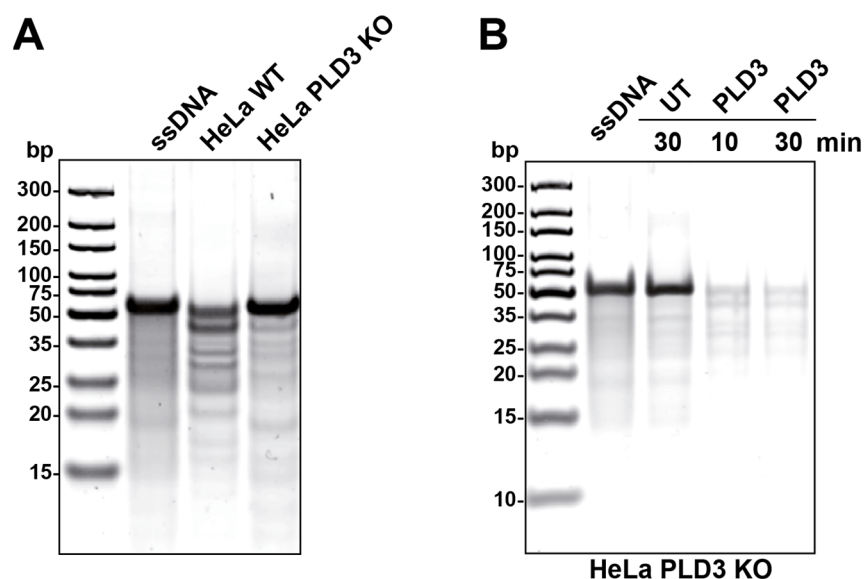


**Figure 53 | WT HeLa cells have endogenous PLD3 5'-nuclease activity.** Wild-type (WT) or PLD3 KO HeLa cell lysates (A) or *PLD3*-transfected cell lysates (B) were incubated with 4  $\mu$ M 55 nt-long ssDNA in reaction buffer (MES pH 4.5, 100 mM NaCl) at 37°C for the indicated time points. For the experiment shown in (A), incubation was performed for 2 h. A DNA polyacrylamide gel electrophoresis was run with reaction products in Tris-Borate-EDTA (TBE) buffer. Gels were incubated for 5 min in SYBR Gold Nucleic Acid Gel Stain and visualized at a 600 nm wavelength. For experiment B, only PLD3 KO HeLa cells were used.

As mentioned previously, PLD3 contains two HKD motifs, a key structural feature for phospholipase D family members. However, the second (in direction to the C-terminus) motif of PLD3 is not fully conserved, where the aspartic acid (D) is substituted by a glutamic acid (E). Therefore, we investigated if this amino acid might be important and dispensable for PLD3 nuclease activity, by its substitution with alanine (PLD3 E423A, Figure 54A). Besides, another HKD mutant (PLD3 K418R), located in the first motif, has been formerly reported to eliminate enzymatic activity for different PLD isoforms tested (Sung et al., 1997). Thus, both mutants were overexpressed in PLD3 KO HeLa cells and a nuclease assay was performed as discussed above. DNA-PAGE analysis revealed a complete abolishment of exonuclease activity for both mutants, where no substrate degradation was observed (Figure 54B). Mutants were also analyzed by immunocytochemistry by co-staining with the N-terminal and luminal specific anti-PLD3 antibodies and antibodies against the intracellular proteins KDEL (ER marker) and LAMP2 (lysosomal marker). PLD3 K418R, comparable to the WT, was localized to lysosomes, while PLD3 E423A expression led to its retention in the ER, where a high degree of co-localization with KDEL was observed (Figure 54C). This indicates that both



motifs are important for proper PLD3 exonuclease activity and that the glutamic acid position of the second motif might also be a key residue for proper PLD3 folding and, in consequence, for appropriate delivery to lysosomes.

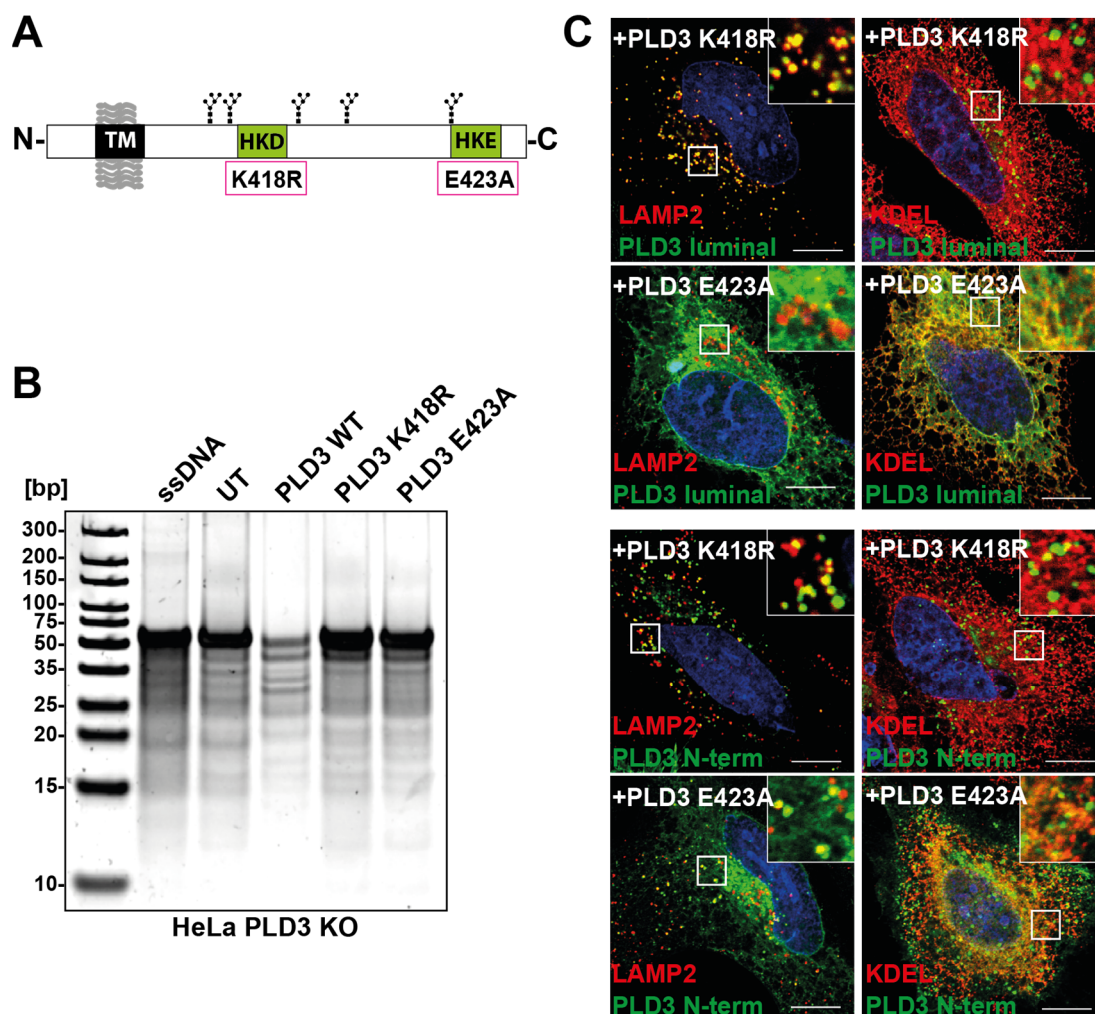


**Figure 54 | PLD3-HKD motif mutants have altered nuclease activity.** *A*, Schematic representation of PLD3 protein structure with both HKD/HKE motifs. The two PLD3-HKD mutants generated are encircled in red boxes. *B*, nuclease activity assay of PLD3 WT and both HKD/E mutants. Cell lysates (50  $\mu$ g) were incubated with 4  $\mu$ M 55 nt-long ssDNA in reaction buffer (MES pH 4.5, 100 mM NaCl) at 37°C for 30 min. Products were further analyzed by DNA PAGE, stained with SYBR Gold Nucleic Acid Gel Stain and visualized at a 600 nm wavelength. *C*, immunofluorescence images of HeLa cells transfected with both mutants and further co-stained with the N-terminal and luminal PLD3-specific antibodies (green) together with anti-KDEL (ER marker) and anti-LAMP2 (lysosomal marker) antibodies depicted in red. Scale bar, 10  $\mu$ m.

We have previously described that PLD3 proteolytic processing is pH-dependent and that its cleavage is abolished by inhibitors of lysosomal acidification (Figure 19B). To analyze if PLD3 nuclease activity is dependent on proteolytic processing, *PLD3*-transfected cells were incubated *in vivo* with the inhibitors Bafilomycin A, Chloroquine and ammonium chloride ( $\text{NH}_4\text{Cl}$ ). After incubation of the corresponding inhibitor treated-cell lysates with the ssDNA substrate and further separation of the products by DNA-PAGE, it was observed that interference with PLD3 cleavage did not inhibit its activity as a nuclease (Figure 55A). A slightly stronger DNA product signal was detected in the treated samples compared to untreated (DMSO) cells, suggesting a delay but not total inhibition of PLD3 nuclease activity. As a confirmation that all inhibitors used had an effect on PLD3 cleavage, a Western blot analysis with the same lysates was performed by immunoblotting with the antibody against the luminal domain of PLD3 (Figure 55B). In order to further investigate the enzymatic properties of PLD3, we analyzed the effect of different compounds on the modulation of PLD3 exonuclease activity (Figure 56 and Figure 57).

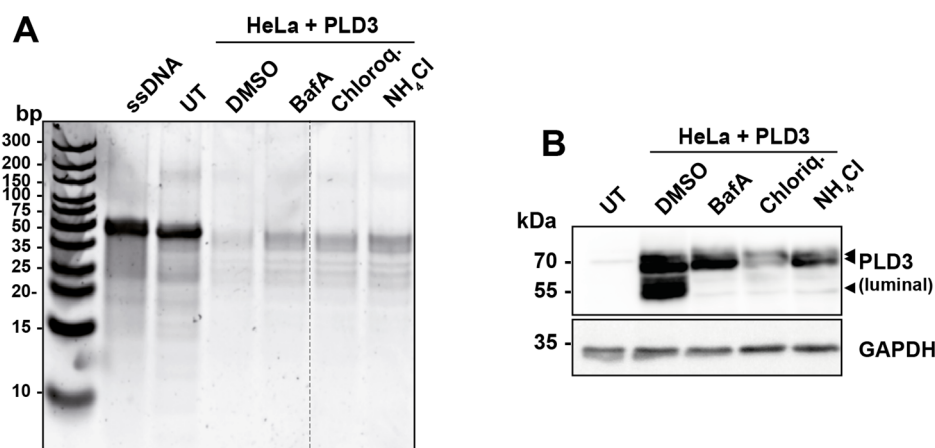


**Figure 55 | PLD3 nuclease activity is not cleavage-dependent.** *A*, *PLD3*-transfected cells were incubated *in vivo* with different inhibitors of lysosomal acidification described before to avoid PLD3 cleavage (Bafilomycin A, chloroquine and ammonium chloride). DMSO was used as a negative control of treatment. Cell lysates (50  $\mu\text{g}$ ) of treated and non-treated cells were incubated with 4  $\mu\text{M}$  55 nt-long ssDNA in reaction buffer (MES pH 4.5, 100 mM NaCl) at 37°C for 2 h. Products were further analyzed by DNA PAGE, stained with SYBR Gold Nucleic Acid Gel Stain and visualized at a 600 nm wavelength. *B*, Cells treated with the indicated inhibitors were analyzed by Western blot and further immunodetection with the PLD3-specific luminal antibody (PLD3-specific signal is shown with black arrowheads). GAPDH is depicted as a loading control.

Regulation of enzymes through metal ion complexation, accounting for 63 % of all cofactors, is widespread in biology underscoring a physiological need for enzyme stability and catalytic activity (Gohara and Cera, 2016). Moreover, it has been reported that the mouse Zuc (mZuc, also known as PLD6), another member of the phospholipase D family, also possesses single-strand-specific nuclease activity (Ipsaro et al., 2012; Nishimasu et al., 2012). This enzyme contains a Zn-binding domain known to be important for its catalytic activity. In order to test if PLD3 nuclease activity is dependent on metal cofactors, *PLD3*-transfected cell lysates were incubated *in vitro* with different divalent cations in the form of chloride salts or with described chelating agents, including ethylenediaminetetraacetic acid (EDTA) and 1,10-phenanthroline. A nuclease activity assay was applied by incubation of the treated lysates with a ssDNA substrate. In comparison to untreated lysates, DNA-PAGE analysis showed a complete absence of DNA products after incubation with EDTA, but not with phenanthroline (Figure 56). A similar result was observed after the addition of  $\text{CaCl}_2$ , suggesting that PLD3 activity might be induced by calcium as a divalent cation. In contrast, no apparent differences in substrate degradation was observed for the lysates incubated with either  $\text{Zn}^{2+}$ ,  $\text{Mg}^{2+}$  or  $\text{Cu}^{2+}$ , indicating that PLD3 exonuclease activity is not influenced by the presence of these divalent cations. Further analyses are required to address the activating effect of calcium ions in PLD3 enzymatic activity.

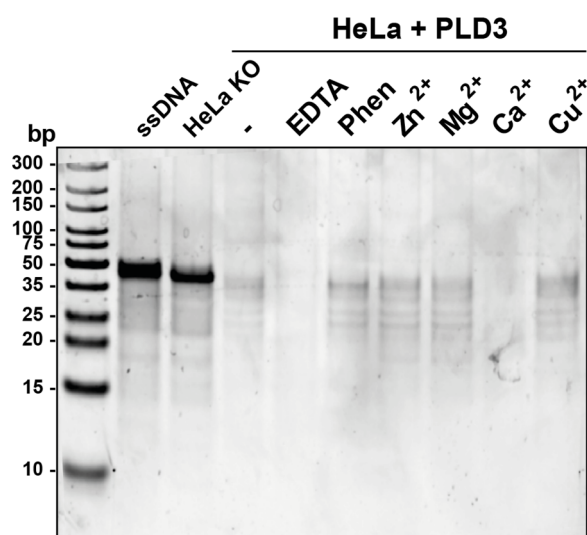


**Figure 56 | PLD3 nuclease activity is enhanced by EDTA and  $\text{Ca}^{2+}$ .** *PLD3* transfected cell lysates (50  $\mu\text{g}$ ) were pre-incubated *in vitro* with chelating agents (10 mM EDTA or 10 mM phenanthroline) or with different divalent cations (3 mM  $\text{ZnCl}_2$ , 3 mM  $\text{MgCl}_2$ , 3 mM  $\text{CaCl}_2$  and 1  $\mu\text{M}$   $\text{CuCl}_2$ ) for 30 min at 37 °C in reaction buffer (MES pH 4.5, 100 mM NaCl). Then, 4  $\mu\text{M}$  55 nt-long ssDNA was added and further incubated for 1 h at 37 °C. Products were analyzed by DNA PAGE, stained with SYBR Gold Nucleic Acid Gel Stain and visualized at a 600 nm wavelength.

As a result of PLD3 exonuclease activity, PLD3 can be grouped in the family of phosphodiesterases by cleavage of phosphodiester bonds from single-stranded DNA in a 5' → 3' direction. Phosphate ( $\text{PO}_4^{3-}$ ), sulfate ( $\text{SO}_4^{3-}$ ) and vanadate ( $\text{VO}_4^{3-}$ ) ions are polyatomic anions with a central atom (phosphorus, sulfur and vanadium, respectively) surrounded by four oxygen atoms in a tetrahedral arrangement. Due to this structural similarity, the effect of these anions (as competitive analogs) on PLD3 exonuclease activity was evaluated. Additionally, it is known that  $\beta$ -glycerophosphate, sodium pyrophosphate and sodium fluoride are phosphate inhibitors (Chung et al., 1992; Orriss et al., 2016). DNA-PAGE analysis of the products derived from the *in vitro* incubation of all these compounds with a ssDNA substrate revealed that vanadate ( $\text{VO}_4^{3-}$ ) completely inhibited the nuclease activity of PLD3 (Figure 57).  $\beta$ -glycerophosphate and pyrophosphate increased PLD3 exonuclease activity, where the substrate was almost completely degraded. In comparison to untreated lysates, sulfate, phosphate and fluoride did not show any effect on PLD3 activity (Figure 57). Taken together from our experiments we can conclude that PLD3 is a 5' specific single-stranded exonuclease endogenously expressed in HeLa cells. Both PLD3 HKD/E motifs are important for its catalytic activity and vanadate inhibits the PLD3 exonuclease activity.

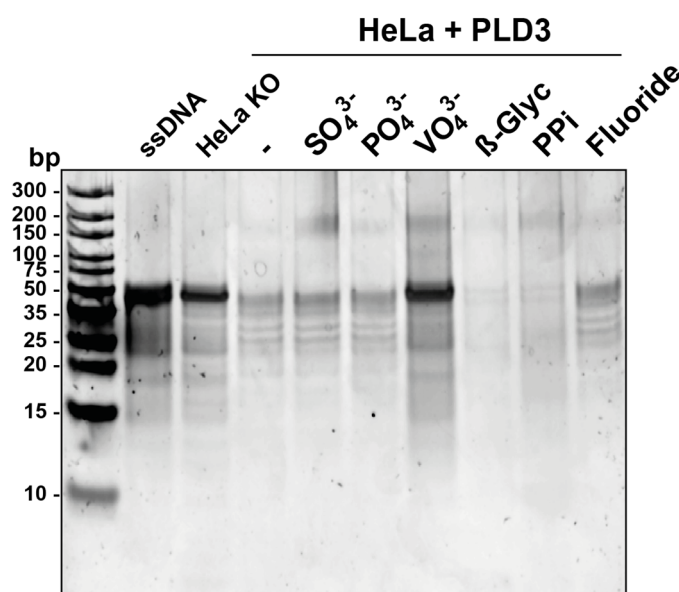


**Figure 57 | PLD3 nuclease activity is inhibited by vanadate ( $\text{Na}_3\text{VO}_4$ ).** PLD3 transfected cell lysates (50  $\mu\text{g}$ ) were pre-incubated *in vitro* with different anions (10 mM  $\text{Na}_2\text{SO}_4$ , 10 mM  $\text{NaH}_2\text{PO}_4$ , 5 mM  $\text{Na}_3\text{VO}_4$ ),  $\beta$ -glycerophosphate, 10 mM pyrophosphate (PPI) or 2 mM NaF for 30 min at 37 °C in reaction buffer (MES pH 4.5, 100 mM NaCl). Then, 4  $\mu\text{M}$  55 nt-long ssDNA was added and further incubated for 1 h at 37 °C. Products were analyzed by DNA PAGE, stained with SYBR Gold Nucleic Acid Gel Stain and visualized at a 600 nm wavelength.

### 3.3.3 *PLD3 is the main 5'-exonuclease in the brain*

As a result of the distinctive expression levels of PLD3 observed in the different mouse organs, we wanted to further investigate PLD3 exonuclease activity *in vivo* in mouse tissue. Hence, a nuclease assay was performed with brain, spleen and bone marrow lysates by incubation with the same substrate used for the cell-based analysis. As a control, wild-type (WT) mouse tissue lysates were compared with Pld3 knockout (KO) lysates at 0 h and after 4 h of incubation. DNA-PAGE analyses of the incubation products showed a complete substrate degradation in WT brain lysates, while in the Pld3 KO lysates no nuclease activity was observed (Figure 58, upper panel). Similar results were obtained for the spleen and the bone marrow. However, in the Pld3 KO lysates of these tissues approximately half of the substrate was degraded, shown by densitometric quantification of the ssDNA degradation signal (Figure 58, lower panel).

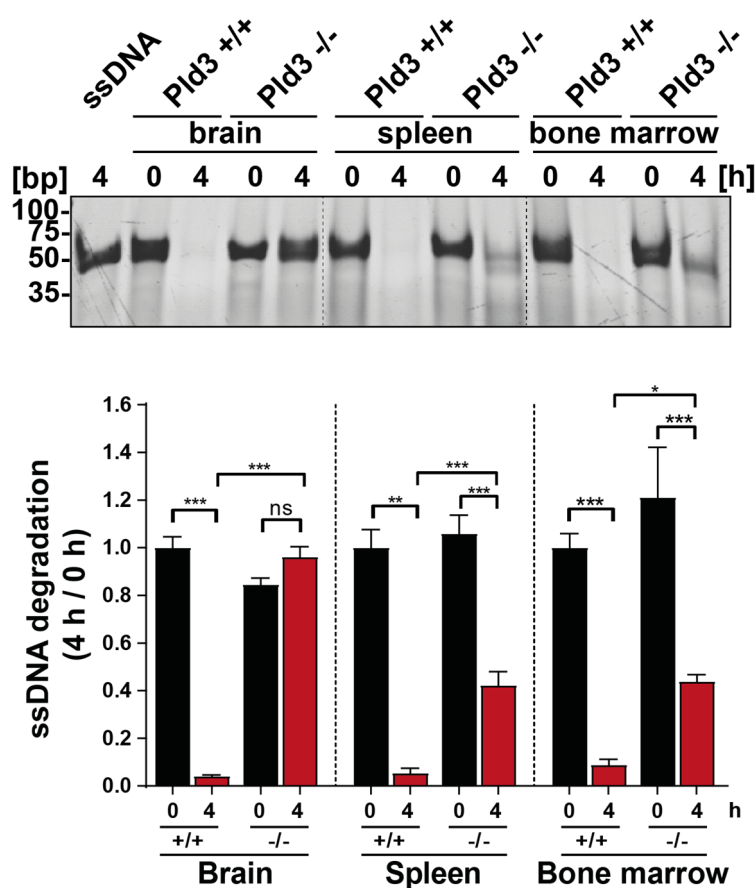


**Figure 58 | Pld3 is the main 5'-nuclease in the brain.** A, nuclease activity assay of brain, spleen and bone marrow lysates of WT (Pld3+/+) and KO (Pld3-/-) mice. Lysates (50 µg) were incubated with 4 µM 55 nt-long ssDNA in reaction buffer (MES pH 4.5, 100 mM NaCl) at 37°C for the indicated time points. Products were further analyzed by DNA PAGE, stained with Ethidium Bromide and visualized under UV light. The respective quantification of ssDNA degradation is shown. Error bars represent SEM. \*\*\*p < 0.001; \*\*p < 0.01; \*p < 0.1; unpaired Student's t test (n = 3). ns, not significant.



To confirm the observed Pld3-specific nuclease activity in the brain, increasing amounts (between 1 and 100  $\mu\text{g}$ ) of WT or Pld3 KO brain lysates were incubated with a ssDNA substrate and further analyzed by DNA-PAGE (Figure 59). Increasing concentrations of Pld3 enzyme led to progressive degradation of the ssDNA substrate until its disappearance with 100  $\mu\text{g}$  of lysate (Figure 59, left). Conversely, increasing amount of Pld3 KO brain lysate led only to a minor substrate degradation at very high concentrations. Altogether, these data indicate that Pld3 is the main 5' exonuclease in the brain and its absence in other organs is most likely compensated by Pld4 activity or other non-described 5' exonucleases.

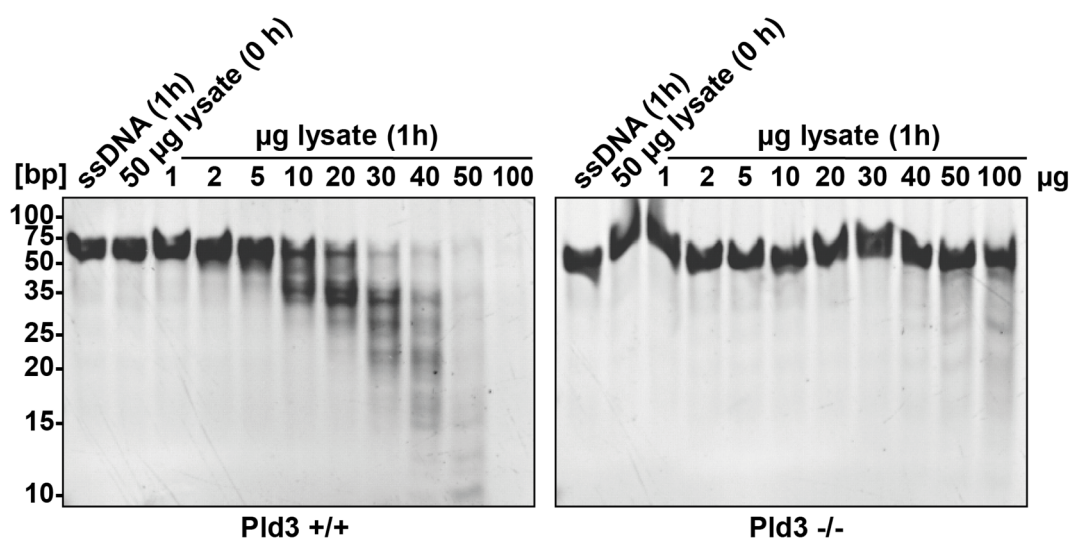


**Figure 59 | 5'-nuclease activity is abolished in the Pld3 KO mouse brain.** Increasing concentrations of WT and Pld3 KO mice brain lysates were analyzed for nuclease activity by incubation with 4  $\mu\text{M}$  55 nt-long ssDNA in reaction buffer (MES pH 4.5, 100 mM NaCl) at 37°C for the indicated time points. Products were further analyzed by DNA PAGE, stained with Ethidium Bromide and visualized under UV light.

### 3.4 Role of PLD3 variants as a genetic risk factor of Alzheimer's disease development

In 2014, Cruchaga et al. described a series of variants in *PLD3* that were either significantly associated with Alzheimer's disease (AD) risk (e.g. *PLD3* V232M variant) or variants that were only found in AD cases but not in healthy controls. Consequently, *PLD3* became of high interest to the scientific community. In follow-up genetic studies only one

group was able to reproduce the significant association of *PLD3* V232M and AD (van der Lee et al., 2015). However, other independent reports failed to reveal a risk effect of *PLD3* in AD (Heilmann et al., 2015; Hooli et al., 2015; Lambert et al., 2015). Despite the efforts, to date it is still in debate if there is a real genetic association of *PLD3* with Alzheimer's disease.

### 3.4.1 Described *Pld3* variants in AD patients exhibit different proteolytic processing and nuclease activity

We wanted to investigate the effect of different reported Alzheimer's disease-related variants on PLD3 proteolytic processing and nuclease activity. A set of these variants were generated by site directed mutagenesis (Figure 60), including the variant reported to significantly confer risk for AD (*PLD3* V232M), a conserved mutant located in the N-terminal *PLD3* sequence (*PLD3* M6R), mutations close to the possible *PLD3* cleavage site (*PLD3* G63S and *PLD3* P76A), a mutation found in AD cases of European-descent and African-American cases (*PLD3* K228R), glycosylation mutants (*PLD3* N236S and *PLD3* N284S) and a variant very close to the second HKE motif (*PLD3* T426A).

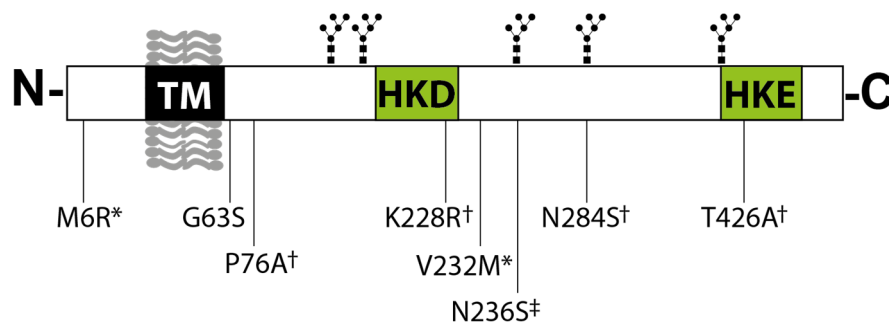


**Figure 60 | Schematic representation of different *PLD3* coding variants.** Scheme of *PLD3* variants generated for further analysis. \*Variants significantly associated with Alzheimer's disease risk. †Variants found only in Alzheimer's disease cases. ‡Variants that are more frequent in Alzheimer's disease cases than in controls. Data from Cruchaga et al.

After cDNA expression in HeLa cells, all *PLD3* variants were analyzed using Western blot (Figure 61) and immunodetection with antibodies against the N-terminal and luminal region of *PLD3*. In addition, for immunofluorescence analyses (Figure 62), *PLD3* was co-

stained with antibodies against protein expressed in the lysosomes (anti-LAMP2) and the ER (anti-KDEL). In spite of the different expression levels, PLD3 V232M, G63S, P76A, N284S and T426A had normal processing (Figure 61) and delivery to lysosomes (Figure 62). The weak signal observed for the full-length and N-terminal fragment of the PLD3 M6R expressed variant might be due to the amino acid change in the epitope and therefore a lower recognition with the N-terminal specific antibody. On the other hand, an altered proteolytic processing was observed after ectopic expression of the PLD3 variants K228R and N236S. Both PLD3 mutants were retained in the ER, shown by the high degree of co-localization with the KDEL marker (Figure 62). Interestingly, the PLD3 N236S mutant led to a shift to a lower molecular weight of full-length PLD3. This result that was also observed when glycosylation mutants were analyzed (Figure 14). These indicates that these two amino acids (K228 and N236) are key residues for proper PLD3 folding and correct transport to lysosomes.

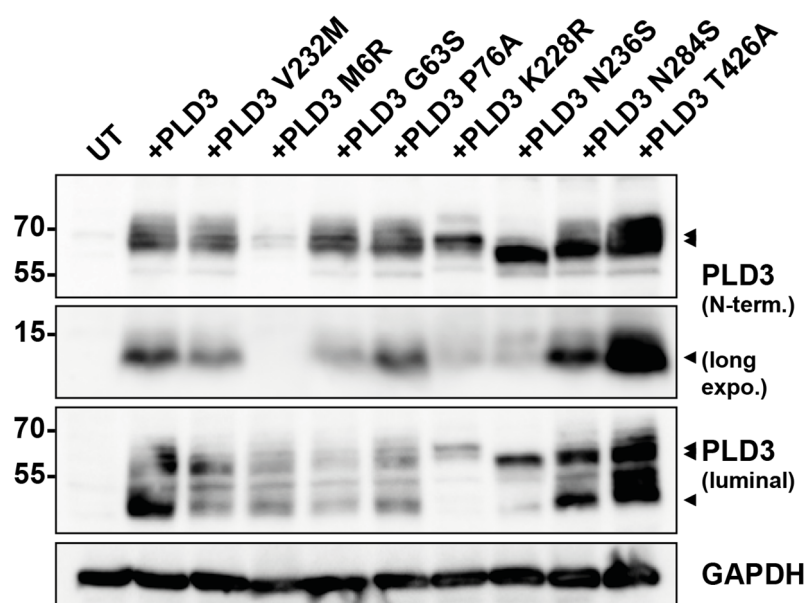
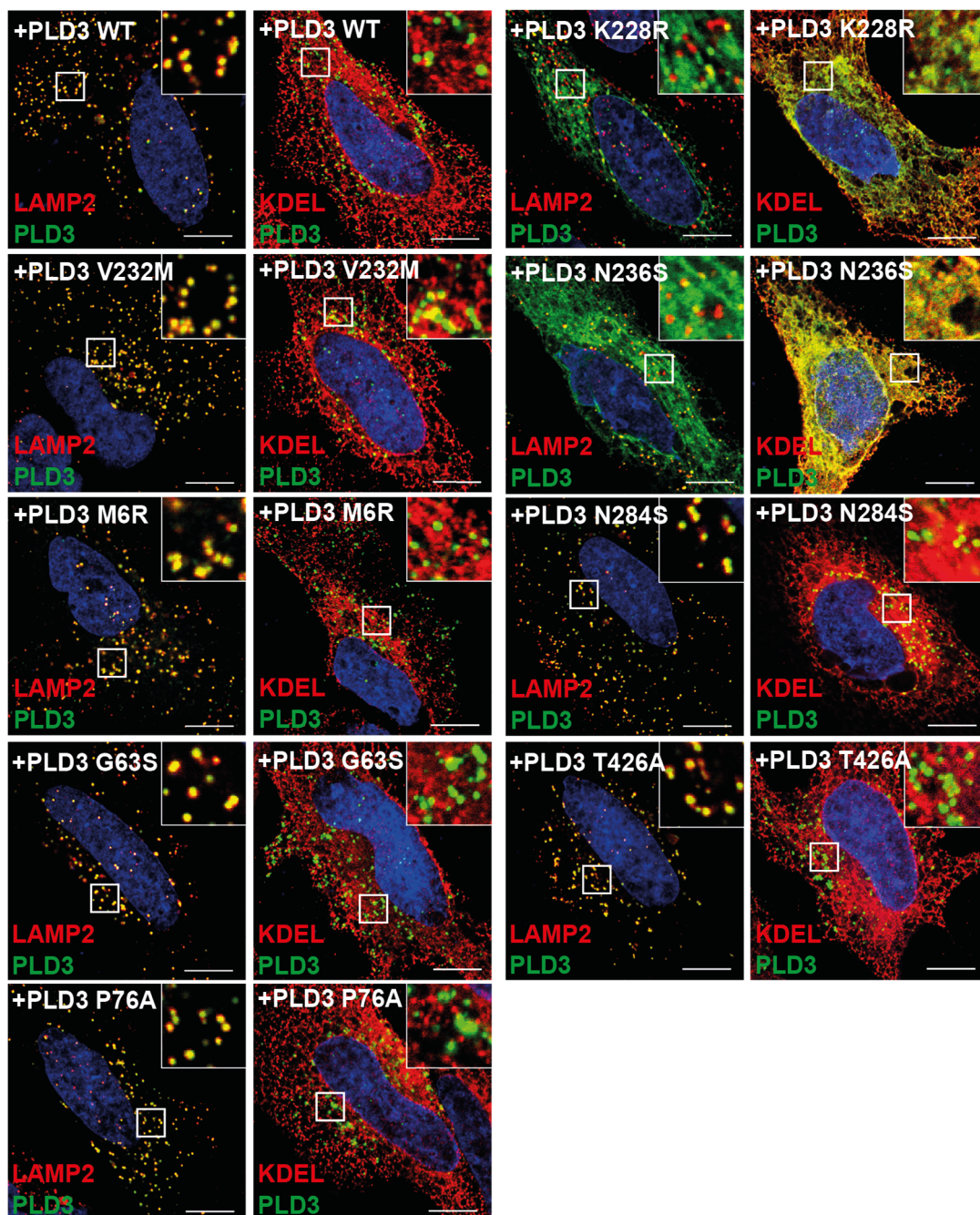


**Figure 61 | AD-related mutants exhibit differential PLD3 proteolytic processing.** Different Alzheimer's disease-related mutants were analyzed by Western blot by immunoblotting with both N-terminal and luminal PLD3-specific antibodies. The different and specific cleavage products are indicated with black arrowheads. GAPDH is presented as a loading control.

Next, we wanted to analyze the effect of the described *PLD3* variants on the nuclease activity. To this end, all mutants were overexpressed in *PLD3* KO HeLa cells and cell lysates were incubated with the ssDNA substrate. DNA-PAGE analysis revealed that the



expression of PLD3 K228R and PLD3 N236S led to decreased nuclease activity, especially for the first mutant (K228R) where most of the ssDNA substrate was not degraded (Figure 63). This result validates the assumption that proper folding and lysosomal delivery is necessary for suitable PLD3 5' exonuclease activity. For the other variants, a similar degradation pattern was observed when compared to PLD3 WT, arguing that these mutants do not have a high impact on PLD3 nuclease activity.



▲ **Figure 62 | AD-related mutants PLD3 K228R and N236S have abrogated delivery of PLD3 to lysosomes.** Alzheimer's disease-related PLD3 mutants were analyzed by immunocytochemistry, where transfected HeLa cells were further co-labeled with the luminal PLD3-specific antibody (green) and antibodies against the intracellular protein markers KDEL and LAMP2 (red). Insets show enlarged regions of the cell. Scale bar, 10  $\mu$ m.

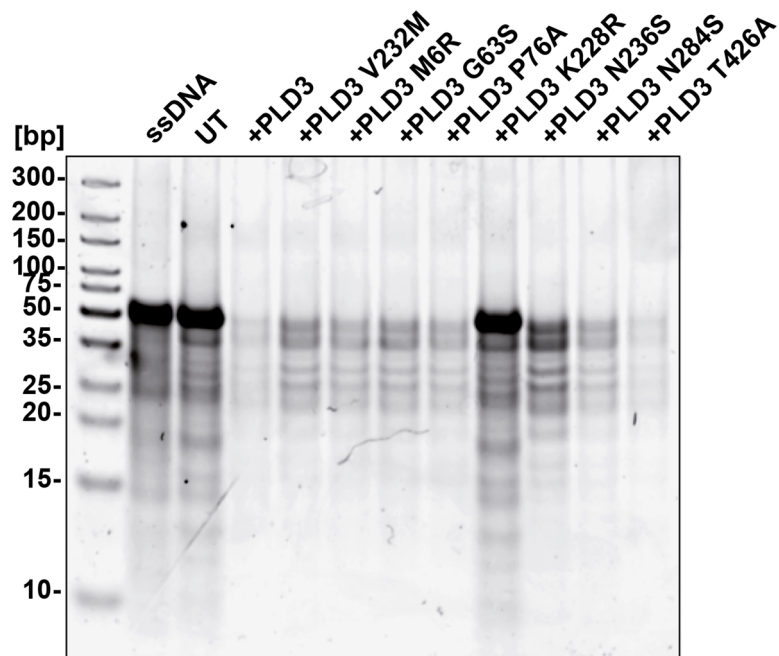


**Figure 63 | AD-related mutants PLD3 K228R and N236S have decreased 5'-exonuclease activity.** Cell lysates (50  $\mu$ g) of the different AD-related PLD3 mutants were incubated with 4  $\mu$ M 55 nt-long ssDNA in reaction buffer (MES pH 4.5, 100 mM NaCl) at 37°C for 30 min. Products were further analyzed by DNA PAGE, stained with SYBR Gold Nucleic Acid Gel Stain and visualized at a 600 nm wavelength.

### 3.4.2 Characterization of *Pld3* deficiency in the 5XFAD Alzheimer's mouse model

As previously mentioned, *PLD3* has been described as a genetic risk factor for Alzheimer's disease (AD). *Pld3* deficiency led to increased CD68 immunoreactivity within brain regions where adult neurogenesis occurs (e.g. the dentate gyrus of the hippocampus, section 3.2.5) together with a depression like behavior (section 3.2.6). Interestingly, AD pathogenesis is characterized by the deposition of amyloid beta ( $A\beta$ ) plaques, especially in the hippocampus (Kayed et al., 2003), as well as neuroinflammation (activated microglia and reactive astrocytes) (Wyss-Coray and Mucke, 2002). Therefore, we wanted to investigate how *Pld3* deficiency possibly contributes to the development of AD, especially in regard to APP biology.

#### 3.4.2.1 Protein levels of APP and its fragments are not altered in the *Pld3*<sup>-/-</sup> 5xFAD mice

The precise physiological function of the amyloid precursor protein (APP) remains unknown. However, it is well described that aberrant proteolytic processing of APP (increased amyloidogenic pathway) promotes the generation and oligomerization of the amyloid beta (A $\beta$ ) peptide, leading to different mechanisms of neurotoxicity (Glennner, 1983; Glennner and Wong, 1984; Masters et al., 1985). Moreover, Cruchaga et al. reported that overexpression of PLD3 decreased the extracellular levels of A $\beta$ 40 and A $\beta$ 42, while its knockdown had opposite effects.

Therefore, we first investigated whether PLD3 deficiency affects APP processing. Whole brain lysates of *Pld3* WT (+/+) and *Pld3* KO (-/-) mice were analyzed by Western blot and further immunodetected with different antibodies against full-length (FL) APP, APP proteolytic products (e.g. C-terminal fragments [CTFs] and soluble APP alpha [sAPP $\alpha$ ]) and key proteins involved in APP processing (e.g. Bace1 and presenilin). As observed in Figure 64, *Pld3* deficiency did not alter the overall processing of APP, where the levels of full-length (FL APP), the C-terminal fragments (CTFs) and soluble APP (sAPP $\alpha$ ) were unchanged. No changes in the protein levels of the proteases involved in APP amyloidogenic pathways (Bace1 and presenilin) were either observed.

The unaltered protein levels observed for APP and its cleavage products led us to hypothesize that breeding the *Pld3* knockout mice with the well-established AD-related mouse model (5xFAD) (Oakley et al., 2006), would help us to better decipher the role of *Pld3* on the turnover and processing of APP and A $\beta$ . Thus, 5xFAD *Pld3*<sup>-/-</sup> mice were generated (section 2.6.2). Western blot analysis of 6 months old 5xFAD and 5xFAD *Pld3*<sup>-/-</sup> mouse brain lysates were performed. Immunodetection against antibodies of full-length APP and its C-terminal fragments did not reveal any changes at the protein level between 5xFAD and 5xFAD *Pld3*<sup>-/-</sup> (Figure 65). As a control, an antibody against a lysosomal hydrolase (Cathepsin D) was used. Cathepsin D is known to be present in neuritic plaques (Cataldo et al., 1995; Ginsberg et al., 2000). Contradictory to what Cruchaga et al. reported in 2014, these results suggest that *Pld3* deficiency do not lead to any alterations on APP proteolytic processing *in vivo*.

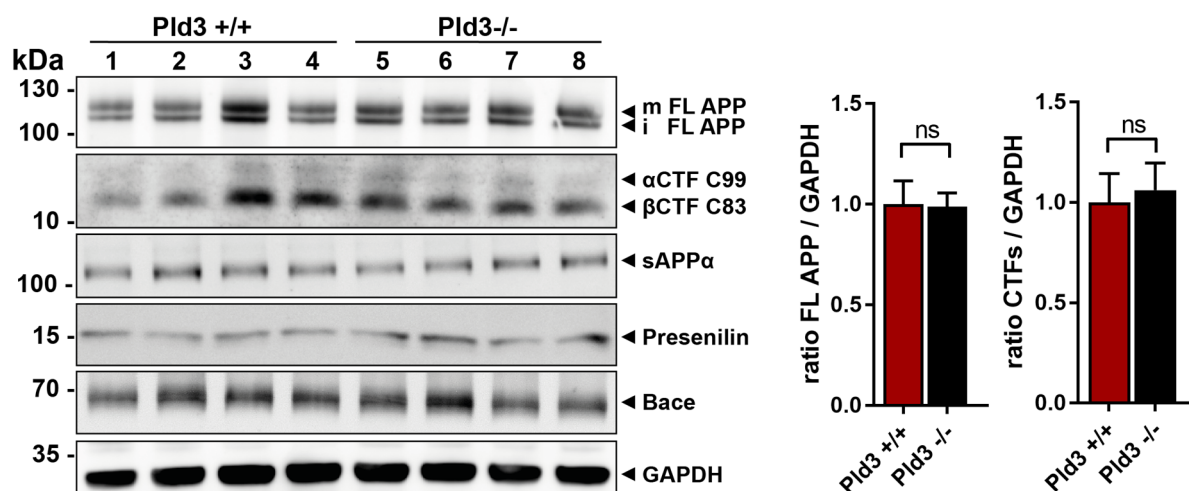


**Figure 64 | APP processing is not affected in Pld3 deficient mice.** Brain lysates of 6 months old Pld3 WT (+/+) and Pld3 KO (-/-) mice were analyzed by Western blot and further immunodetection with antibodies against full-length (FL) APP (anti-APP, clone 22C11), C-terminal fragments (CTFs, anti-APP, clone A8717), soluble APP alpha (sAPP $\alpha$ ) and the proteases Bace1 and preselinin. GAPDH is presented as a loading control. Densitometry quantification of FL APP and CTFs are presented in the graphs. Error bars represent SEM, unpaired Student's t test (n = 4). ns, not significant, m, mature; i, immature.

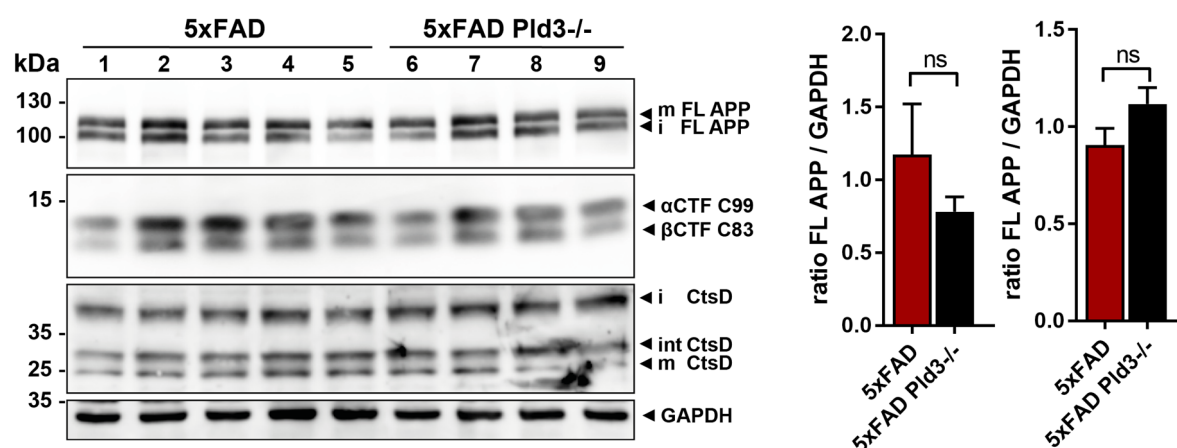


**Figure 65 | APP processing is not affected in 5xFAD Pld3<sup>-/-</sup> mice.** Western blot analyses of 6 months old 5xFAD and 5xFAD Pld3<sup>-/-</sup> mouse brain lysates. Membrane were immunodetected with antibodies against full-length (FL) APP (anti-APP, clone 22C11) and the cathepsin D (CtsD). Densitometry quantification of FL APP and CTFs are presented in the graphs. Error bars represent SEM, unpaired Student's t test (n = 4-5). ns, not significant, m, mature; i, immature, int, intermediate.

### 3.4.2.2 *Pld3 is localized to Amyloid beta (A $\beta$ ) plaques*

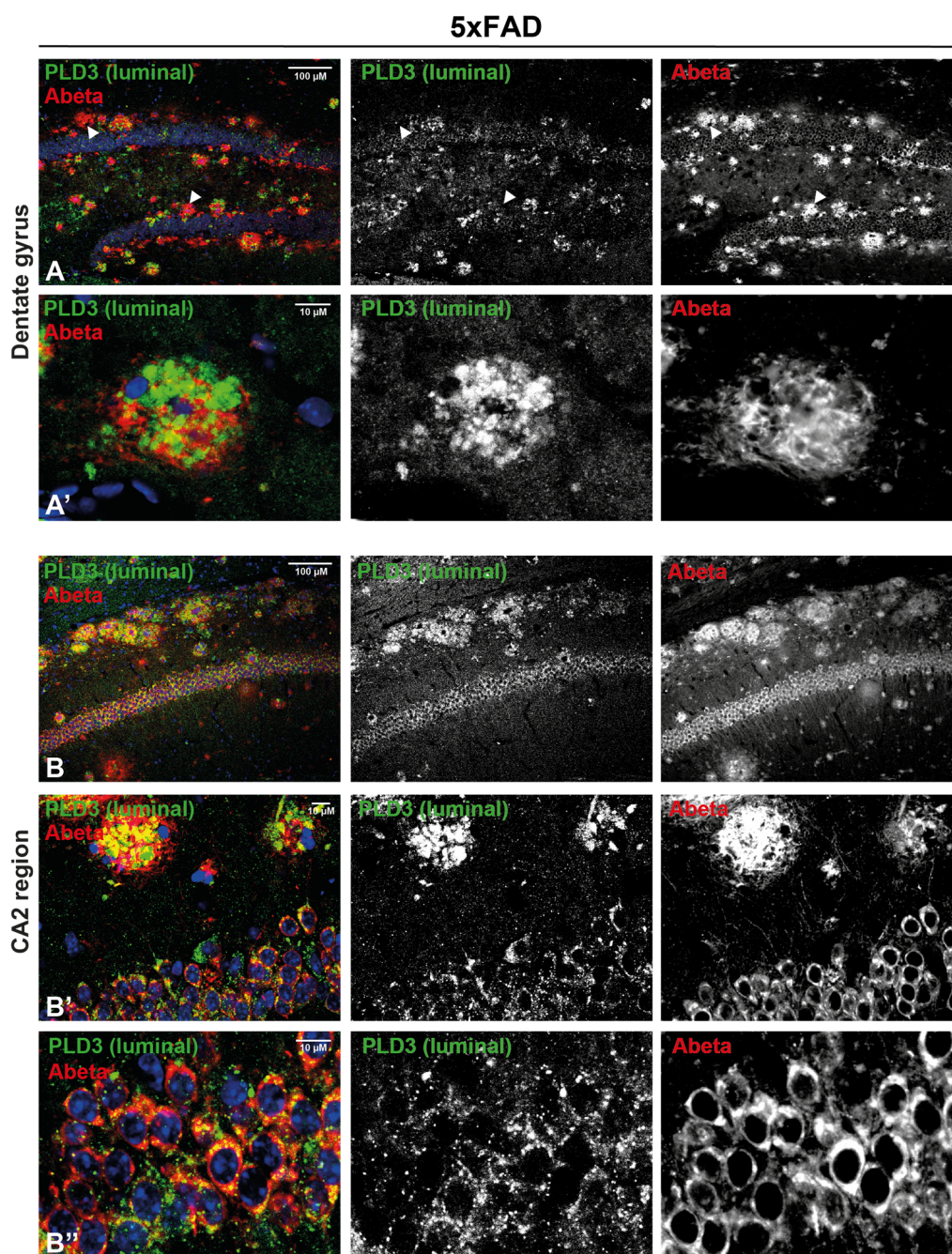
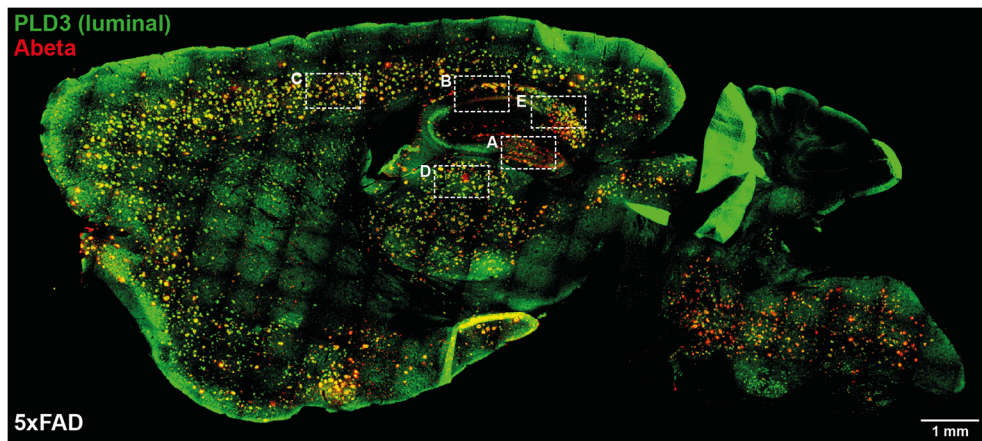
It has been shown that lysosomes which are rich in membrane proteins but with low levels of soluble hydrolases, accumulate in dystrophic neurites around amyloid plaques (Gowrishankar et al., 2015). To investigate the Pld3 localization, 5xFAD brain sections were fluorescence labeled with an anti-PLD3 luminal specific antibody and an anti-A $\beta$  (clone 6E10) antibody. Fluorescence microscopy revealed that Pld3 is found within the same brain regions where A $\beta$  plaques are concentrated, especially in the murine cortex and the hippocampus (Figure 66). With higher magnification, Pld3 staining is observed around extracellular A $\beta$  deposits, an observation that was consistent within the different brain regions, including the CA2 region and subiculum of the hippocampus (Figure 66B and Figure 67E) and the cortex (Figure 67C). In the dentate gyrus, compared to other regions, several A $\beta$  positive plaques were not stained with Pld3 (shown with white arrowheads, Figure 66A). Surprisingly, high levels of Pld3 surrounding A $\beta$  deposits were observed in the thalamus (Figure 67D), a region where very low detection of Pld3 was found in wild-type mice (Figure 38A and Figure 39). Lower Pld3 labeling around plaques was observed in the brainstem (Figure 66). These data suggest that Pld3 accumulates around A $\beta$  plaques, similar to what was reported for LAMP1, which resides in swollen axons that contact the amyloid deposits (Gowrishankar et al., 2015).

## 3.5 PLD3 and spinocerebellar ataxia

### 3.5.1 *A Pld3 variant linked to spinocerebellar ataxia shows altered proteolytic processing, intracellular localization and nuclease activity*

During the course of my PhD studies, PLD3 was described as a novel gene for autosomal dominant spinocerebellar ataxia (SCA) via a combination of whole exome sequencing (WES) and gene network analysis (Nibbeling et al., 2017). More exactly, a PLD3 variation (c.923T>C; p.Leu308Pro) resulting in reduced phospholipase D activity was identified in undiagnosed families. The same group showed that overexpression of turboGFP-PLD3-WT in Cos7 cells, led to an ER localization of PLD3. As described in this thesis, PLD3 is a lysosomal protein (section 3.1) and no significant changes or accumulation of lipid species as products of phospholipase D activity were observed in brain lysates Pld3 KO mice (section 3.3.1).







▲ **Figure 66 | Pld3 accumulates within the same brain regions as amyloid beta (A $\beta$ ) plaques.** Immunofluorescence staining of a 6 months old 5xFAD brain section. Pld3 was labeled with an antibody against its luminal domain (green) and an anti-A $\beta$  (clone 6E10) antibody (red). Fluorescence image was generated by acquisition of more than 300 single images and further stitching overlapping. Boxes (A-E) correspond to brain regions with higher magnification (see also Figure 67). A', B' and B'' represent images of the same region from the dentate gyrus and CA2 region, respectively, taken at a higher magnification.

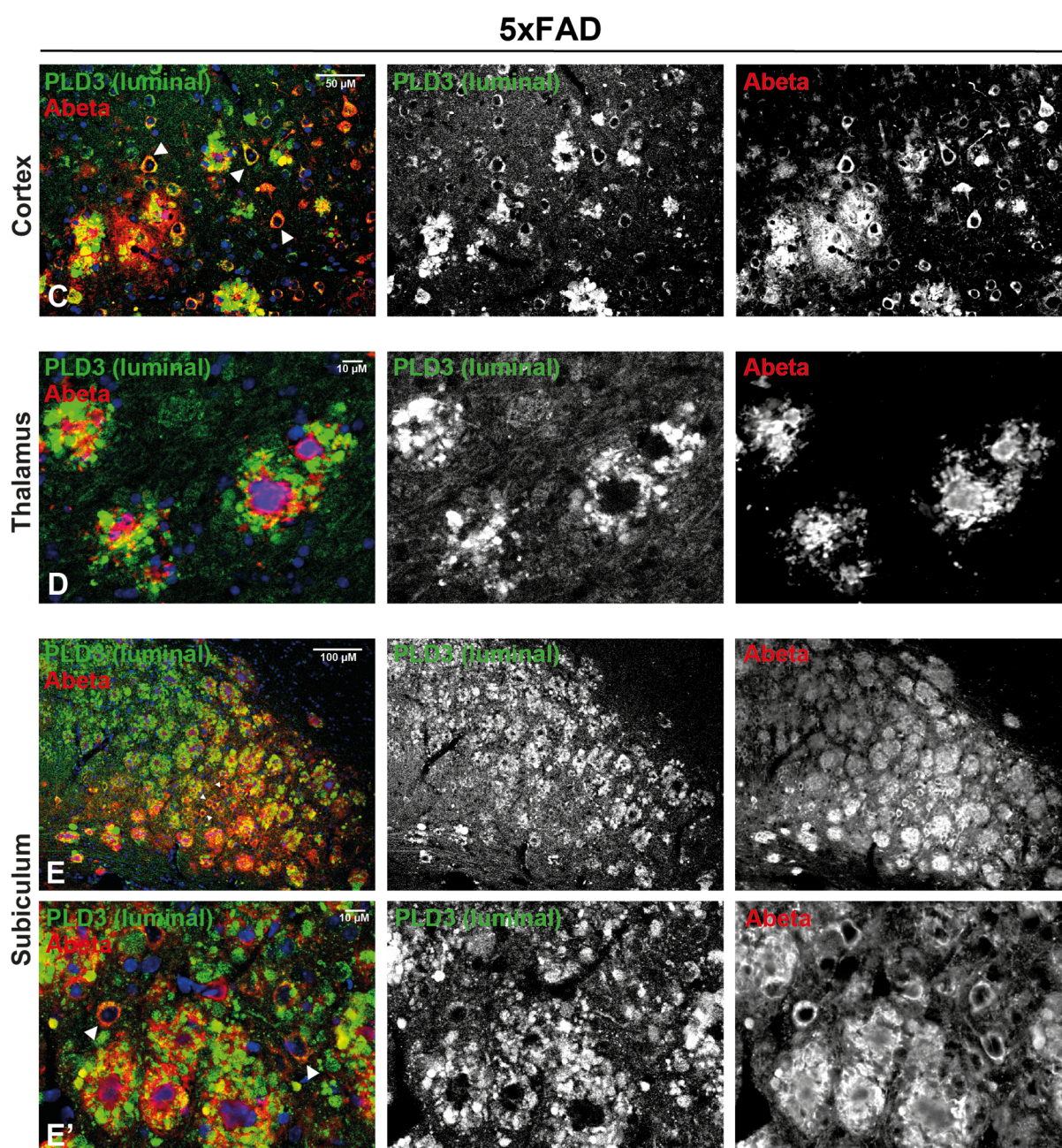


**Figure 67 | Pld3 accumulates around amyloid beta (A $\beta$ ) plaques in the cortex, the thalamus and the subiculum in 5x FAD mice.** Enlarged fluorescence images of the cerebral cortex (C), the thalamus (D) and the subiculum (E) from the stitching fluorescence picture shown in Figure 66. A 6 months old 5xFAD brain section was co-labeled with an antibody against the luminal domain of PLD3 (green) and with an anti-A $\beta$  (clone 6E10) antibody (red). E' represents an image of the same region taken at a higher magnification.

Therefore, the effect of this PLD3 variant on intracellular localization, proteolytic processing and nuclease activity was analyzed in more detail. Immunofluorescence images of HeLa cells transfected with either *hPLD3 WT* or *hPLD3 L308P* and further staining using both N-terminal and luminal PLD3-specific antibodies, showed that this PLD3 variant is mostly localized in the endoplasmic reticulum (ER) (Figure 68). In contrast, as already described in the first section of my results, PLD3 WT is confined to lysosomes.

In order to analyze any changes on the proteolytic processing of PLD3 L308P, Western blot analyses were performed in technical triplicates and immunodetected with both described PLD3-specific antibodies. When the membrane was detected with the antibody against the luminal domain of PLD3, a significant reduction of the PLD3 processed form (~50kDa) was observed, also confirmed by densitometric quantification of the luminal / full length (FL) PLD3 signal (Figure 69). Intriguing, no apparent reduction of the PLD3 N-terminal fragment (~12 kDa) was observed in cells transfected with the L308P variant, suggesting a partial abolishment of PLD3 cleavage.

Our functional analyses together with the data reported by Gavin et al. revealed that PLD3 is a 5'-exonuclease. Thus, lysates of HeLa cells transfected with the *hPLD3 L308P* variant were incubated with a ssDNA substrate and a nuclease assay was performed. DNA-PAGE analysis of the incubation products showed a basal nuclease activity for the PLD3 L308P, comparable to the activity observed for untransfected (UT) cells, arguing for a loss of function (Figure 70). In contrast, in *PLD3 WT* transfected cells, all the substrate was degraded after 2 h of incubation. These results were also validated by desintometric quantification of the signal between transfected (+PLD3) and untransfected (UT) cells. Together, these results indicate that the PLD3 L308P variant leads to a loss of function, probably due to improper folding and in consequence defective sorting to lysosomes.

---

▼ **Figure 68 | The spinocerebellar ataxia variant PLD3 L308P is localized in the ER.** HeLa cells were transfected either with *hPLD3 WT* or the SCA variant *hPLD3 L308P* and further co-stained with antibodies against PLD3 N-terminal and luminal domains (green) and antibodies against the intracellular markers LAMP2 (lysosomal marker) or KDEL (ER marker) depicted in red. The corresponding Pearson correlation coefficient (PCC) values between PLD3 and each marker are shown. Error bars represent SEM. \*\*\* $p < 0.001$ ; unpaired Student's t test ( $n = 12$ ). Scale bar, 10  $\mu\text{m}$ . ns, not significant.



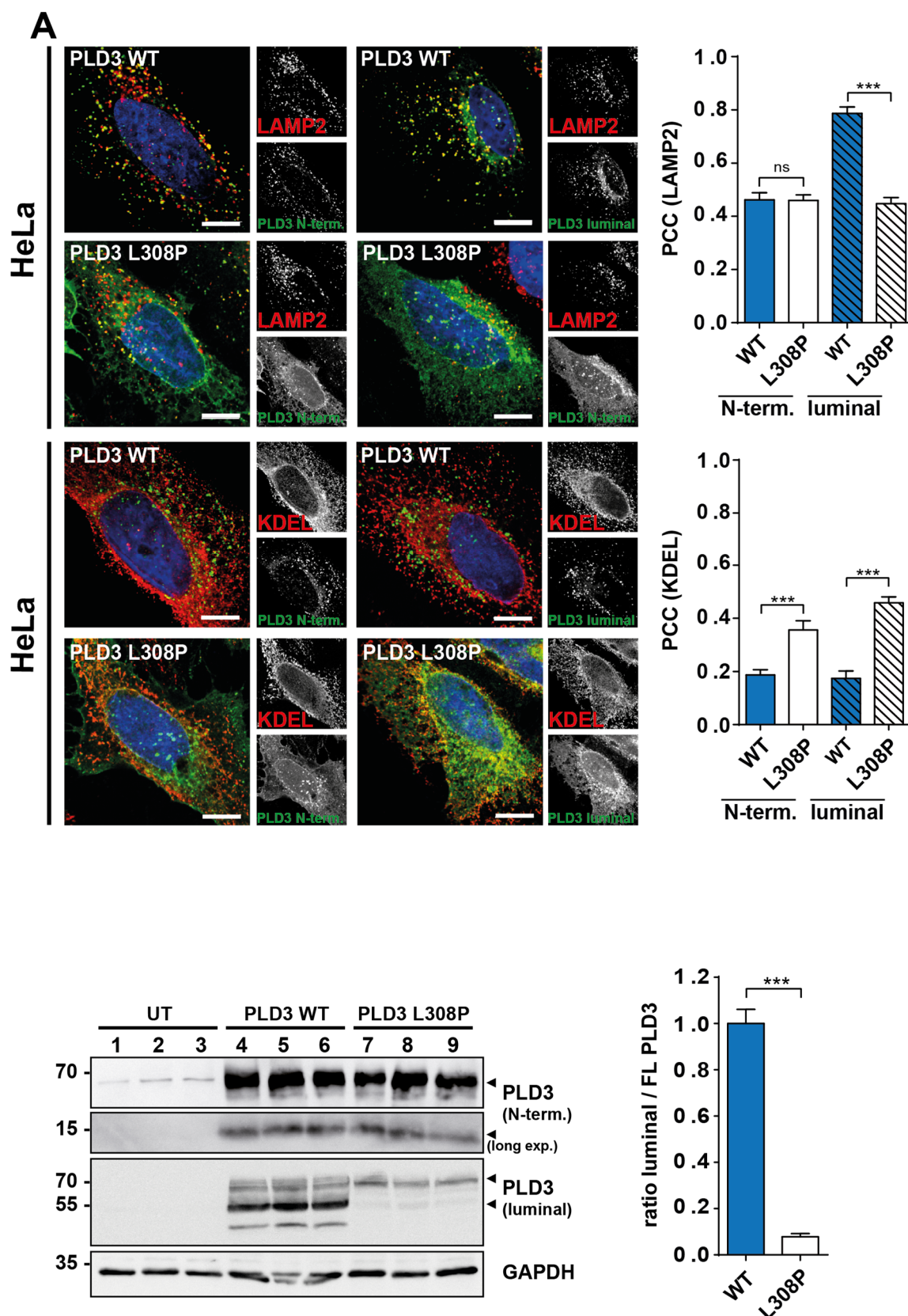


**Figure 69 | The PLD3 L308P variant shows altered proteolytic processing.** Western blot analyses of cell lysates transfected in technical replicates with either *hPLD3* WT or *PLD3* L308P and immunoblotted with both PLD3-specific antibodies. GAPDH is presented as a loading control. The respective densitometric quantification of luminal / full length (FL) PLD3 signal is shown. Error bars represent SEM. \*\*\**p* < 0.001; unpaired Student's *t* test (*n* = 3).

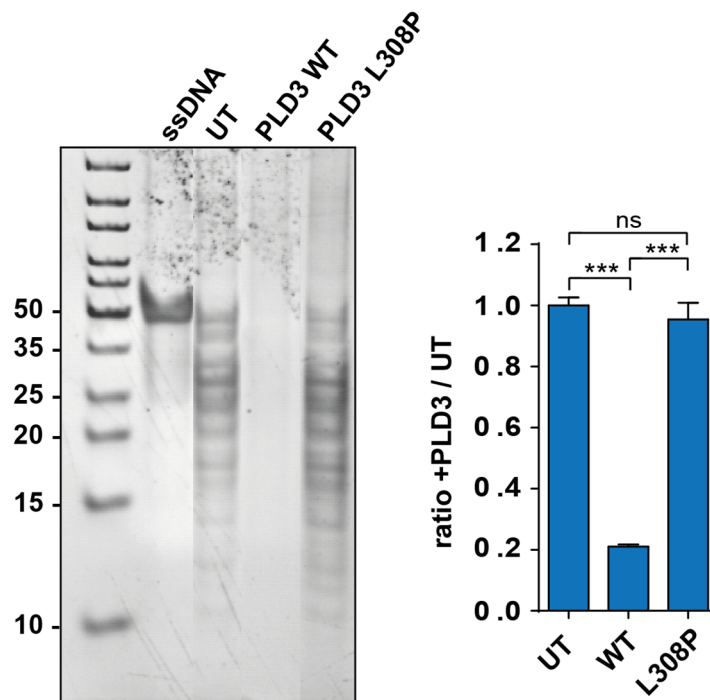
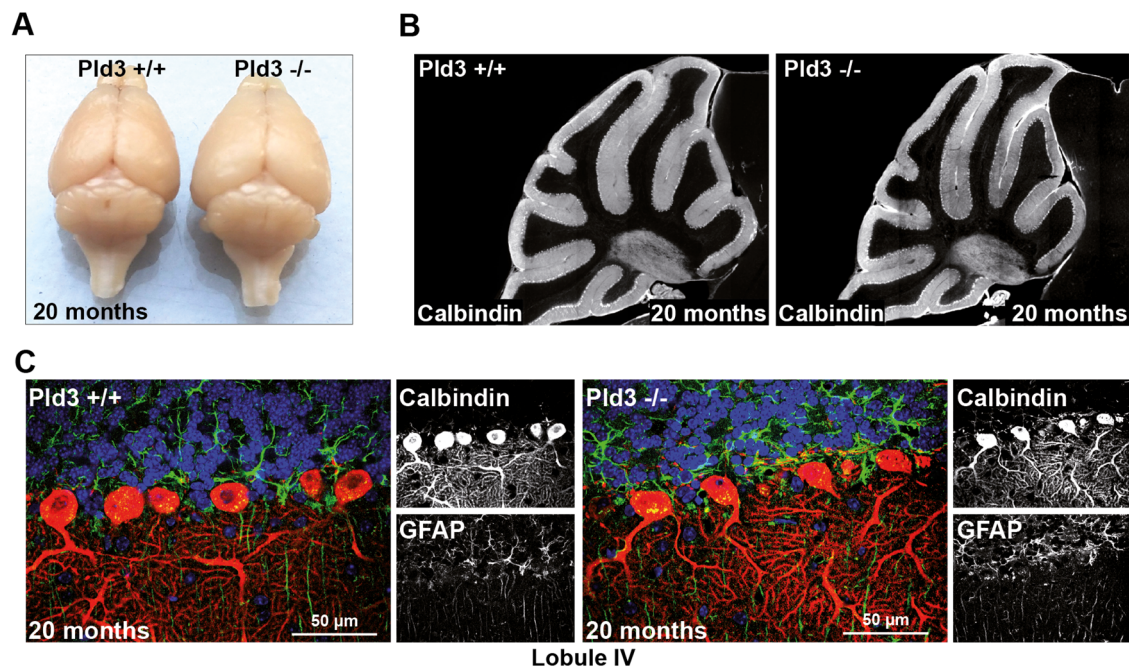


**Figure 70 | Nuclease activity of the PLD3 L308P variant is impaired.** Indicated transfected cell lysates (50  $\mu$ g) were incubated with ssDNA substrate (2  $\mu$ M) in reaction buffer (50 mM MES buffer, pH 4.5 and 100 mM NaCl) for 2 h at 37  $^{\circ}$ C and further analyzed by DNA-PAGE. Polyacrylamide gels were stained with Ethidium Bromide. The corresponding quantification of PLD3 / UT ratio is shown. Error bars represent SEM. \*\*\* $p$  < 0.001; unpaired Student's t test ( $n$  = 3). ns, not significant.

### 3.5.2 *Pld3*-deficient mice show unaltered cerebellar morphology or cerebellar dysfunction

When *Pld3* expression levels were analyzed in different brain regions, very low or no protein expression was observed in the cerebellum (Figure 38 and Figure 39). Additionally, X-gal staining of mouse brain sections also showed very low  $\beta$ -galactosidase activity (Figure 38B). Accordingly, we were surprised that *PLD3* was described as a causative gene of spinocerebellar ataxia (SCA, Nibbeling et al., 2017). To have a closer look, we analyzed any changes on the cerebellar function or morphology. First, no evident changes in the size or whole brain structure of 20 months old WT and *Pld3* knockout (KO) mice were observed (Figure 71A).

▼ **Figure 71 | *Pld3* deficient mice do not show cerebellar alterations.** *A*, photograph of the brain of a 20 months old *Pld3* wild-type (*Pld3* +/+) and a *Pld3* deficient (*Pld3* -/-) mouse. *B*, calbindin immunofluorescence staining of 20 months old *Pld3* wild-type and *Pld3* deficient mice. *C*, brain sections of the molecular layer in lobule IV of 20 months old *Pld3* wild-type and *Pld3* deficient mice were fluorescence labeled with antibodies against calbindin (red) and GFAP (green). Nuclei are stained with DAPI (blue). Scale bar, 50  $\mu$ m.



Additionally, immunofluorescence labeling of 20 months old brain sections with calbindin did not reveal loss of Purkinje cells in the cerebellum (Figure 71B) or sign of Bergmann astrogliosis or demyelination (Figure 71C). Rotarod is a widely used test to evaluate the motor coordination of rodents and is especially sensitive in detecting cerebellar dysfunction (Caston et al., 1995; Lalonde et al., 1995). Consequently, behavioral studies via rotarod test of two cohort of adult mice (5 months and 9 months), did not show any sign of cerebellar dysfunction (Figure 72). Altogether, these data did not revealed hints of cerebellar dysfunction in the PLD3 deficient mice, suggesting that PLD3 is not the described causative gene of spinocerebellar ataxia by Nibbeling et al.

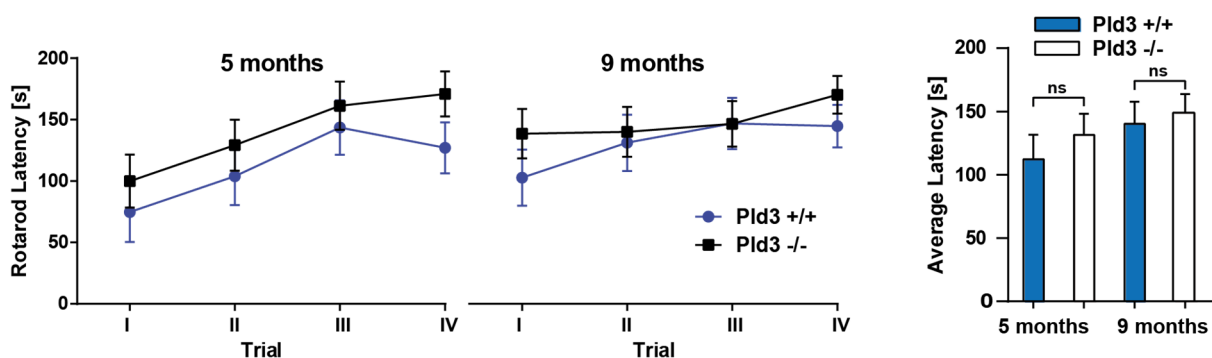


**Figure 72 | Behavior analyses of Pld3 deficient mice do not show any sign of cerebellar dysfunction.** Rotarod performance test of 5 months and 9 month Pld3 wild-type and deficient animals in four independent trials. The corresponding average latency (s) is shown for both set of mice (n = 9 – 11). ns, not significant. Rotarod test was performed in collaboration with Dr. Stijn Stroobants at the Laboratory of Biological Psychology in Leuven (Belgium).



## 4 DISCUSSION

### 4.1 Biochemical characterization of PLD3

PLD3 is a member of the PLD protein superfamily. Due to the presence of two motifs characteristic of this family, it has been suggested that PLD3 exerts a role in lipid metabolism, as described for other family members like PLD1 and PLD2 (Cao et al., 1997). However, PLD3 is still a poorly characterized member of the PLD superfamily and no canonical phospholipase activity has yet been described. Although PLD3 was proposed to be associated to the endoplasmic reticulum (Munck et al., 2005), opposite findings provided evidence that PLD3 is a bona fide lysosomal protein (Palmieri et al., 2011; Sleat et al., 2013). In order to gain better insight in the biology of PLD3, a detailed biochemical characterization was performed. This analysis was fundamental for the follow-up study of PLD3's physiological function and its possible involvement in the development of Alzheimer's disease and other neurodegenerative disorders.

#### 4.1.1 *PLD3 is a lysosomal protein*

Despite the few reports on PLD3, initial studies support a localization of PLD3 in the endoplasmic reticulum (ER) (Munck et al., 2005; Nibbeling et al., 2017; Osisami et al., 2012). Other groups revealed that PLD3 is localized to lysosomes (Fazzari et al., 2017; Palmieri et al., 2011; Sleat et al., 2013). Our own data show that PLD3 is a lysosomal protein, as revealed by its co-localization with an anti-LAMP2 antibody as a marker for this compartment. These observations were validated under PLD3 overexpression and endogenous conditions in SH-SY5Y cells and human brain sections, respectively.

In addition, treatment with different glycosidases demonstrated that PLD3 is mainly decorated with complex-type glycans, modifications that occur in post-ER compartments. Lysosomal localization is also supported by the work of Palmieri et al. in 2011, where *PLD3* was reported as a member of the CLEAR (Coordinated Lysosomal Expression and Regulation) gene network. PLD3 is transcriptionally regulated by the transcription factor EB (TFEB), the master regulator of lysosomal biogenesis. TFEB directly binds to specific E-box sites at the promoter of PLD3 (Palmieri et al., 2011). In addition, a database search

reported a set of genes that are co-expressed with PLD3. This molecular network corresponds to lysosomal proteins including cathepsin A, cathepsin D and progranulin (Sato et al., 2014).

#### **4.1.2 *PLD3 is proteolytically processed into a stable soluble form***

##### *4.1.2.1 PLD3 is proteolytically processed by acidic cysteine proteases*

Using antibodies against the N-terminus and C-terminus of PLD3, Western blot analysis revealed several PLD3-specific polypeptides with different molecular mass, arguing for post-translational modifications. The results obtained during this work indicate that full-length PLD3 is not only modified with complex- and high-mannose-type glycans, but it is further cleaved at an amino acid position C-terminal of the transmembrane domain yielding a soluble lysosomal peptide and a short membrane-bound N-terminal peptide.

Notably, PLD3 proteolytic processing occurs under acidic conditions, where PLD3 cleavage is abrogated after adding inhibitors of lysosomal acidification. This result provides additional evidence that PLD3 leaves the ER to be transported to endocytic compartments where cleavage takes place.

The primary intracellular proteases that exhibit proteolytic activity in acidified vesicles are “cathepsins”, classified in different groups based on their structure and catalytic site (Müller et al., 2012). Incubation of *PLD3*-transfected HeLa cells with inhibitors of different classes of proteases suggests that PLD3 cleavage is mediated by one or several cysteine protease(s). This group constitutes the largest among the cathepsin family (Rawlings et al., 2010). However, brain lysates of mice deficient for the most abundant cysteine proteases, including cathepsin B, L and legumain (another member of the cysteine protease superfamily) revealed normal PLD3 proteolytic processing, suggesting that other protease(s) of this class are involved in the initial PLD3 cleavage event. However, this can be also explained by the redundancy reported for cysteine proteases, most of them having a broad substrate specificity (Turk et al., 2012). For instance, mutual compensation between cathepsin B and L *in vivo* has been suggested, where double knockout mice exhibited an early-onset neurodegeneration. These mice were lethal during the second to fourth week in life (Felbor et al., 2002; Stahl et al., 2007).



#### 4.1.2.2 *PLD3 is N-glycosylated*

It is known that the vast majority of lysosomal proteins are heavily glycosylated (Tokhtaeva et al., 2017). This modification plays an important role in protein sorting and trafficking towards different intracellular compartments, and it influences the catalytic properties of lysosomal enzymes (Wang et al., 2005; Wei et al., 2005). Treatment with glycosidases under endogenous and overexpression conditions showed that PLD3 is mainly decorated with complex-type glycans. More specifically, analysis of predicted *N*-glycosylation sites in the luminal PLD3 domain, where single mutants were generated by substitution of the asparagine amino acids to alanine, revealed that the positions N97, N132, N236, N387 and N432 are glycosylated (Figure 73). Although Munck et al. reported that PLD3 is *N*-glycosylated, so far no experimental data have revealed which asparagine positions of PLD3 are modified. Noteworthy, Western blot and immunocytochemistry analyses showed that glycosylation of position N236 is indispensable for proper PLD3 folding and lysosomal sorting.

Western blot analysis of the described *N*-glycosylation mutants also revealed that the PLD3 N-terminal peptide of all the evaluated mutants was not shifted towards a lower molecular weight after deglycosylation, indicating that this short peptide is not *N*-glycosylated. This observation led to the assumption that PLD3 proteolytic processing occurs N-terminal to amino acid position N97. N97 is the most *N*-terminal asparagine position of the PLD3 sequence that was experimentally proven to be *N*-glycosylated. Molecular mass prediction of the first 97 amino acids of the PLD3 sequence computed a theoretical value of ~11 kDa, which matches with the observed size of the N-terminal PLD3 peptide. Therefore, it can be assumed that cleavage must take place after the transmembrane domain (TMD) and before position N97 (Figure 73). Several single alanine mutants replacing the amino acids located after the TMD (E61) and position N97 did not reveal alterations in PLD3 proteolytic processing when analyzed by Western blot (data not shown). Edman sequencing and LC-MS/MS analysis of *PLD3* transfected cells followed by immunoprecipitation with an antibody against the luminal domain of PLD3, also failed to decipher the cleaved neo-N-terminal peptide, possibly due to potential post-translational modifications after the cleavage process that hamper the peptide identification (data not shown). It should be noted that all these approaches were performed under overexpression conditions of *PLD3*-transfected HeLa cells.



In order to investigate PLD3 cleavage site under endogenous conditions, we established a collaboration with Dr. Ole Greiner-Tollersrud from the Department of Medical Biology at the Arctic University of Norway – University of Tromsø. The analysis was performed with a pool of porcine brain where high concentrations of PLD3 could be obtained after several purification steps, including heat treatment, concanavalin A, hydroxyapatite and diethylaminoethanol (DEAE)-Sepharose ion exchange chromatography. This procedure was followed by MS/MS analysis, where intramolecular cleavage of endogenous PLD3 was assigned to amino acid position Q72 (Greiner-Tollersrud, personal communication) (Figure 73). Generation of PLD3 mutants, where three blocks of ~10 amino acids between positions E61 and I89 were deleted, suggests that the initial cleavage takes place between amino acids 61 and 65 (Cedric Cappel, personal communication). Thus, additional trimming from the N-terminus of the PLD3 luminal domain until position Q72 cannot be excluded (Figure 73). Further analyses are required to validate these results, especially to learn if this cleavage site is conserved among other mammals, e.g. in the human and mouse PLD3 protein.

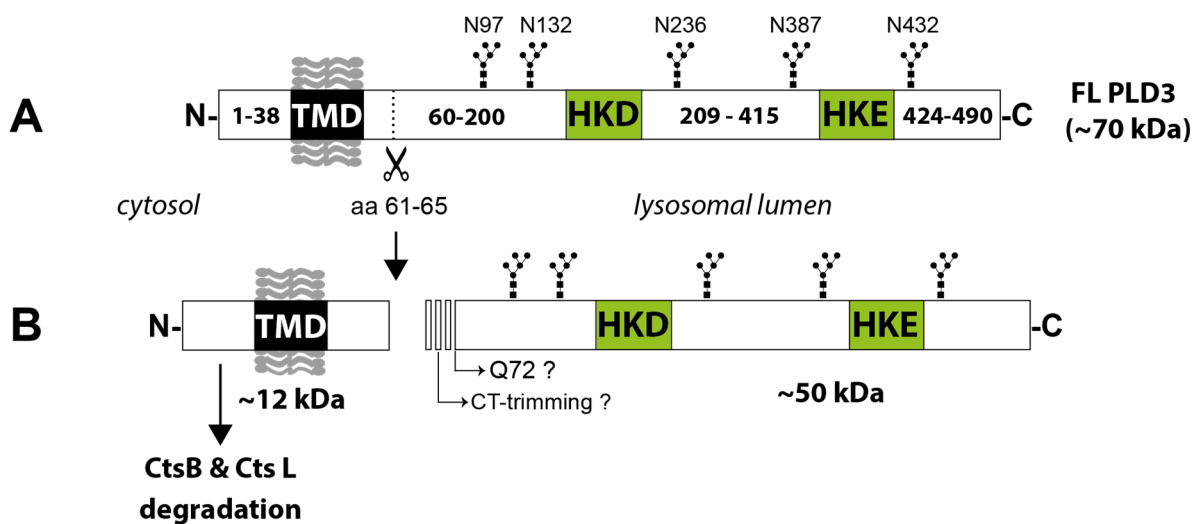


**Figure 73 | Schematic representation of PLD3 proteolytic processing.** Full length (FL) PLD3 is proteolytically processed by an unidentified protease at an amino acid closer to the transmembrane domain (TMD) (A), yielding a luminal domain (~50 kDa) and a short (~12 kDa) N-terminal peptide (B). This membrane-bound peptide is further degraded by cathepsin B and L. Initial cleavage site at position Q72 or possible C-terminal (CT) trimming remain to be validated. Described N-glycosylation sites at amino acid position N97, N132, N236, N387 and N432 are also depicted.

#### 4.1.2.3 *The PLD3 N-terminal peptide is degraded by cathepsin B and L*

Western blot analysis revealed strikingly increased levels of the ~11 kDa N-terminal peptide when lysates of CtsB/L double knockout (dKO) were analyzed. A similar result was observed when *PLD3*-transfected cells were treated with the cysteine protease inhibitor E64D. These observations suggest that the cysteine proteases CtsB and CtsL are responsible for the degradation of the short membrane-bound N-terminal peptide but are not involved in the initial *PLD3* cleavage that generates the soluble peptide. Of note, subcellular fractionation and LC-MS/MS analysis of brain lysosomes, revealed several *PLD3* peptides that were four-fold increased in CtsB/L dKO samples (Stahl et al., 2007). However, the identified *PLD3* peptides were not reported.

#### 4.1.2.4 *PLD3 is transported via the plasma membrane*

According to our data, *PLD3* follows a similar pathway and processing as the lysosomal acid phosphatase (LAP) protein. Although LAP has a type-I topology, it contains, comparable to *PLD3*, seven or eight N-linked oligosaccharides, a single transmembrane domain and a short cytosolic tail of 18 amino acids (Pohlmann et al., 1988; Waheed et al., 1988). LAP is transported to the cell surface where it is rapidly endocytosed via a tyrosine-based sorting motif in the short cytosolic tail. From early endosomes, LAP follows several cycles of rapid recycling (Braun et al., 1989; Peters et al., 1990). Once LAP reaches lysosomes, two sequential cleavage steps occur: (1) a thiol protease cleaves at the outside of the lysosomal membrane releasing the cytosolic LAP tail, and (2) an aspartyl protease cleaves within the luminal domain close to the transmembrane domain, which generates the soluble mature form of LAP (Gottschalk et al., 1989).

Our data indicate that *PLD3* is transported through the plasma membrane. However, mutation of the tyrosine at position 7 in the cytosolic region of *PLD3*, which we identified as a conserved tyrosine-based motif with the sequence YQEL, did not abolish transport of *PLD3* to lysosomes. However, *PLD3* localization was increased at the plasma membrane. This suggests that *PLD3* may partially follow either the “indirect” or the “direct” transport pathway described for lysosomal membrane proteins (Figure 1). Additional evidence for a transport via the plasma membrane comes from a study of Kuhn et al., in 2016, where *Pld3* levels were increased in the cellular membrane glycoproteome

of ADAM10-deficient neurons. Two years later, the same group identified following cell surface membrane glycoprotein biotinylation, that surface expression of Pld3 was significantly changed after BACE-1 inhibition (Herber et al., 2018). Despite these findings, own studies of *PLD3*-transfected HeLa cells treated with ADAM10 and BACE-1 inhibitors or analysis of mouse embryonic fibroblasts (MEFs) and brain lysates deficient from ADAM10 or BACE1, did not reveal alterations in the PLD3 proteolytic cleavage pattern (data not shown).

Interestingly, PLD3 levels were decreased in the cerebrospinal fluid (CSF) from primary central nervous system lymphoma (PCNSL) patients (Waldera-Lupa et al., 2017). These data indicate that PLD3 is mainly sorted to lysosomes, most likely via the “direct” pathway, to exert the main function in this compartment. Yet, a smaller fraction of PLD3 could be alternatively transported to the cell surface where further processing takes place to release the luminal domain in the extracellular matrix.

PLD3 proteolytic processing is complex and most likely tightly regulated in order to reach late endosomal-/lysosomal- compartments. *N*-glycosylation plays a pivotal role in PLD3 stability and may function as a protective mechanism to avoid degradation by acidic proteases.

### **4.1.3 *ESCRT-dependent delivery of PLD3 to lysosomes***

#### *4.1.3.1 PLD3 is localized to intraluminal vesicles within multivesicular bodies*

It appears that PLD3 behaves as a hybrid between a membrane and a soluble protein. First, PLD3 is transported through the secretory and early endocytic pathway as a full-length membrane-bound protein. After cleavage in acidic compartments, a stable PLD3 soluble protein is released in the lysosomal lumen. PLD3 was initially identified as a novel lysosomal protein by mass spectrometry analysis, suggesting to be modified with mannose 6-phosphate residues (Sleat et al., 2008; Sleat et al., 2013). This study proposes that PLD3 is transported to lysosomes via the M6P pathway. Immunofluorescence staining of MEF cells deficient for the cation independent M6P receptor (CI-M6PR /MPR300) or the GlnNac-1-phosphotransferase, did not reveal alterations on the localization of endogenous Pld3 in lysosomes (data not shown). Moreover, affinity purification of immobilized bovine soluble CI-MPR was not able to immunoprecipitate

the possible M6P-modified PLD3 protein (data not shown). This data indicate that PLD3 is not transported via the M6P pathway. However, it cannot be excluded that PLD3 may interact with M6P-modified proteins in the Golgi apparatus as an indirect mechanism of transport to early endosomes.

Co-transfection of *PLD3* with a dominant active form of Rab5 (Rab5-Q79L) revealed a distinct staining with both PLD3-specific antibodies. Particularly, a punctate-like PLD3 staining within enlarged endosomes was observed with the N-terminal PLD3-specific antibody. This pattern resembles the formation of intraluminal vesicles (ILVs) of multivesicular bodies (MVBs). PLD3 labeling co-localized with the staining of an anti-CD63 antibody, a marker of ILVs.

To date, the best characterized pathway for delivery of proteins into ILVs is through the ESCRT (endosomal sorting complexes required for transport) machinery (see section 1.2). However, eukaryotes have developed alternative, ESCRT-independent, routes for sorting of protein into ILVs. CD63 itself directly participates in the ESCRT-independent sorting of the premelanosome protein (PMEL), a component of melanocyte lysosome-related organelles (LROs), to ILVs. Similar to PLD3, PMEL undergoes proteolytic processing yielding a stable luminal polypeptide (van Niel et al., 2011). However, immunocytochemistry analysis of CD63-deficient MEFs cells did not reveal alterations in PLD3 sorting to lysosomes. In other cell systems, ESCRT-independent formation of ILVs requires ceramide. The only reported cargo sorted via this pathway is the proteolipid protein (PLP), where ILV formation depends on the sphingolipid ceramide, localized to raft-based microdomains important for the lateral segregation of the cargo within the endosomal membrane (Trajkovic et al., 2007). Treatment of *PLD3*-transfected HeLa cells with the neutral sphingomyelinase inhibitor GW4869, neither altered PLD3 processing and lysosomal localization. These results indicate that PLD3 is not sorted to ILVs via its interaction with CD63 or ceramide.

#### *4.1.3.2 PLD3 is transported to lysosomes via the ESCRT pathway in a PtdIns3P-dependent manner*

The data characterized so far from PLD3 proteolytic processing and transport to lysosomes resembles in several aspects the pathway described for carboxypeptidase S

(CPS) in yeast. CPS is synthesized as a type II transmembrane precursor protein (pCPS) which transits the secretory pathway to the endosomal system and requires a functional multivesicular body (MVB) sorting pathway. Delivery to the lumen of the vacuoles results in hydrolytic clipping of pCPS to its mature soluble form (mCPS) (Odorizzi et al., 1998; Spormann et al., 1992). This pathway is not only dependent on the synthesis of PtdIns(3,5)P<sub>2</sub> (Odorizzi et al., 1998), but also depends on the ubiquitination of the endosomal cargo, here CPS, which serves as a signal for the sorting into the vesicles that invaginate into the MVB (Katzmann et al., 2001).

Although the ESCRT pathway has been mainly described for rapid cargo downregulation and degradation by fusion of MVBs with lysosomes (Felder et al., 1990; Gruenberg and Maxfield, 1995), we investigated the possibility that PLD3 is transported to lysosomes in an ESCRT-dependent manner as a biosynthetic pathway.

Experiments where key components of the ESCRT machinery were either overexpressed or downregulated, like Hrs (member of the ESCRT-0 complex) and Vps4a (responsible for the final step of ILV formation), revealed that PLD3 processing and PLD3 lysosomal sorting was abrogated. Notably, overexpression and knockdown of Hrs prevented the localization of PLD3 to ILVs. The PLD3 signal was mainly restricted to the limiting endosomal membrane, comparable to CD63. A similar effect was observed when *PLD3*-transfected HeLa cells were treated with the fungal metabolite Wortmannin, an inhibitor of the Vps34 kinase (phosphatidylinositol 3-kinase, PtdIns 3-kinase) responsible for the conversion of PtdIns into PtdIns3P and its derivative PtdIns(3,5)P<sub>2</sub> (Powis et al., 1994). In Wortmannin-treated cells, PLD3 was also exclusively detected in the limiting membrane of endosomes. PtdIns 3-kinases are key regulators of protein sorting to the lysosome/vacuole in both yeast and mammalian cells. Moreover, PtdIns3P binding is essential for the recruitment/activation of components in the PtdIns 3-kinase signaling cascade at unique membrane sites (Burd and Emr, 1998; Herman et al., 1991; Patki et al., 1998). These data indicate that PLD3, comparable to CPS, is transported via the ESCRT machinery in a PtdIns3P- or PtdIns(3,5)P<sub>2</sub>-dependent manner, required for the invagination of the endosomal membrane (ILV formation) and subsequent formation of MVBs.

#### 4.1.3.3 *PLD3 is ubiquitinated*

A prerequisite for endosomal sorting in the MVB pathway is cargo ubiquitination, as extensively described for several membrane proteins, e.g. for the downregulation of activated epidermal growth factor receptor (EGFR) (Huang et al., 2006; Pennock and Wang, 2008; Raiborg and Stenmark, 2009). Our data indicate that PLD3 is ubiquitinated at different lysine residues at the N-terminus, suggesting that ubiquitin-binding is the major signal for PLD3 ESCRT-recognition. However, it cannot be excluded that other sorting mechanisms are responsible for PLD3 transport to ILVs of MVBs. For example, protein-protein interaction with ESCRT proteins (Mageswaran et al., 2014) or non-canonical ubiquitination, where ubiquitin is covalently added to the N-terminal amide group of the protein, the hydroxyl group of serine and threonine residues or to the thiol groups of cysteine residues, regulate the activity and fate of several proteins (McDowell and Philpott, 2013). This might explain why mutating all lysine residues did not completely abrogate PLD3 ubiquitination. PLD3 was still sorted to ILVs after overexpression of this mutant.

Noteworthy, PLD3 was identified in multiple screens for proteins that are ubiquitinated (Lee et al., 2011; Liu et al., 2012; Pridgeon et al., 2009; Shi et al., 2011). One site of PLD3 ubiquitination was found at position K11 of the short cytoplasmic N-terminal domain (Lee et al., 2011). Interestingly, a TUBE-based assay for evaluation of PLD3 ubiquitination, revealed that the PLD3 mutant K11R showed a slight decrease ubiquitination compared to the other mutants. This suggests that this lysine position is important for PLD3 ubiquitination. Since PLD3 was identified as a ubiquitinated substrate of HRD1, an E3 ubiquitin ligase (Lee et al., 2011), it would be interesting to know if abrogation of this enzyme influences the delivery of PLD3 to ILVs.

A new alternative pathway in mammalian cells for the sorting of a lysosomal protein is proposed (Figure 74). PLD3 is synthesized as a type II transmembrane protein in the ER (1) and transported to endocytic compartments via an “indirect” pathway through the plasma membrane (2) and further endocytosis (3), or via a “direct” pathway from the Golgi apparatus (4). PLD3 ubiquitination (5) acts then as a signal for ESCRT-dependent invagination of endosomes leading to the formation of ILVs within MVBs (6). Fusion of MVBs with lysosomes (7) leads to cysteine protease-dependent PLD3 proteolytic processing in a position close to the transmembrane domain, releasing a mature and

stable soluble peptide in the lumen of lysosomes, where PLD3 might exert its main function (Figure 74). This work opens up the concept that the ESCRT pathway is not purely involved in cargo degradation, but also in protein sorting. If other hitherto undescribed mammalian proteins follow the same pathway for lysosomal delivery remains to be elucidated.

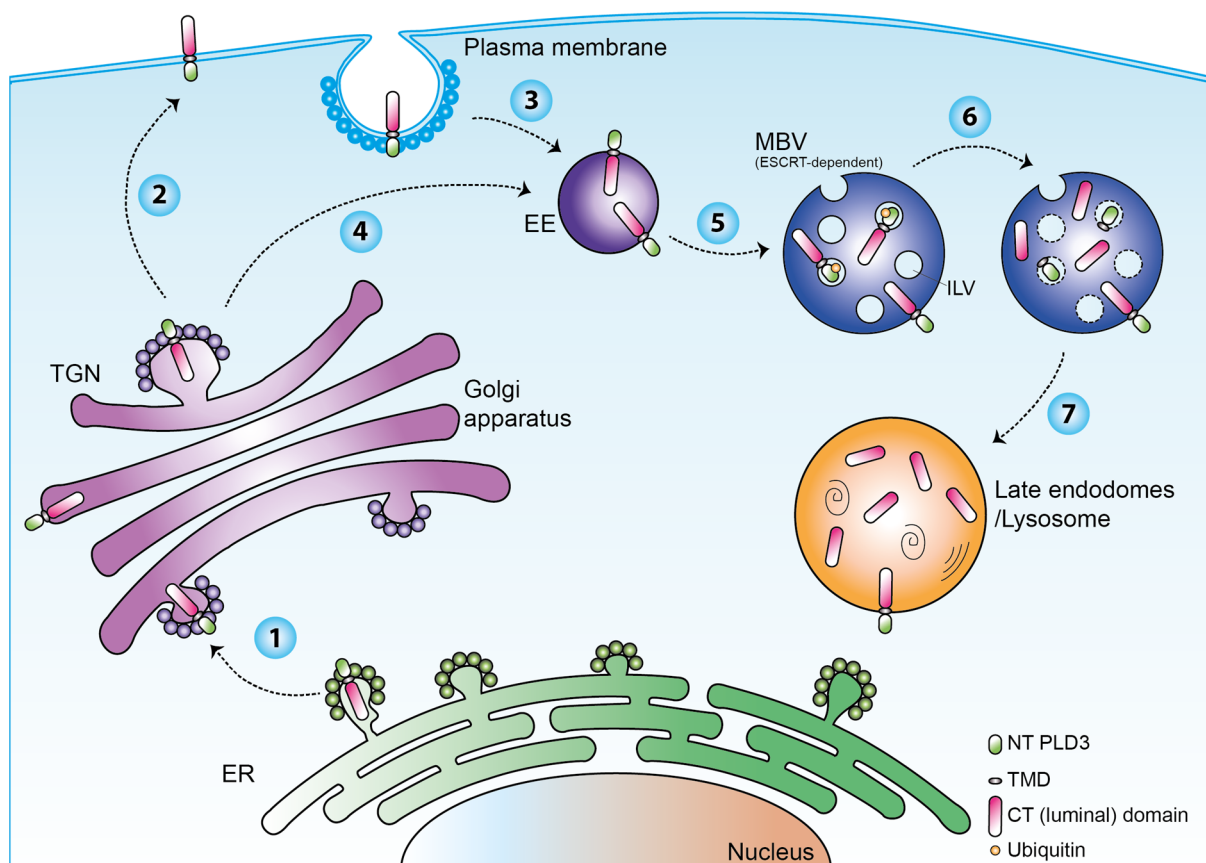


**Figure 74 | Schematic representation of PLD3 transport and its route to lysosomes.** After proper folding and subsequent processing of carbohydrates in the endoplasmic reticulum (ER) and Golgi apparatus (1), PLD3 is either partially transported to the plasma membrane (2 and 3) or directly transported to endosomes (4) (data not analyzed). Ubiquitination of PLD3 (5) acts as a signal for transport to intraluminal vesicles (ILVs) within multivesicular bodies (MBVs) (6) dependent on the ESCRT machinery. After fusion of MBVs with acidic lysosomal structures (7), PLD3 will be processed to generate a stable PLD3 luminal domain. The membrane-bound N-terminal peptide is degraded by cathepsin B and L. TGN, trans-Golgi network; NT, N-terminal; TMD, transmembrane domain; CT, C-terminal.

## 4.2 *In vivo* characterization of PLD3 function

PLD3 expression analysis by *in situ* hybridization revealed a pronounced localization in mature neurons of the forebrain (Pedersen et al., 1998). Later, PLD3 expression was found upregulated during skeletal muscle differentiation (myogenesis) (Lee et al., 2011;



Tomczak et al., 2004). PLD3 was also expressed in an enriched insulin granule fraction from the rat insulin-secreting cell line INS-1E (Brunner et al., 2007). Munck et al. showed ubiquitous PLD3 mRNA levels in a range of tissues, with highest levels in the brain (Munck et al., 2005). Our characterization of PLD3 as a lysosomal protein prompted a further study of its expression pattern and tissue distribution in mice.

#### **4.2.1 *Pld3 is a neuronal protein***

Compared to other mouse tissues, the highest Pld3 expression was observed in the brain. Further characterization of Pld3 expression in the brain revealed that the cerebral cortex and the hippocampus are the major regions where Pld3 is expressed. In agreement with this results, *PLD3* gene expression analysis of mouse and human brain tissue revealed high *PLD3* levels in the frontal, temporal and occipital cortices and in the hippocampus (Cruchaga et al., 2014; Hawrylycz et al., 2012; Lein et al., 2007). Nibbeling et al., proposed a role of *PLD3* in the etiology of spinocerebellar ataxia. However, Western blot analysis and X-gal staining of mouse brains sections revealed only low expression levels of Pld3 in the cerebellum.

Primary mixed co-cultures of neurons, astrocytes and microglia cells prepared from newborn WT mice embryos showed that Pld3 is exclusively found in neuronal cells. Pld3 immunostaining of mouse brain sections showed high levels of co-localization with the anti-NeuN neuronal marker, both in the hippocampus and the cerebral cortex. Similar results were reported by Pedersen et al., with pronounced Pld3 expression in the forebrain of mature neurons. Interestingly, low levels of Pld3 mRNA were reported in the neurons of early mouse embryos (between P7 and P10). Instead, a progressive upregulation of *PLD3* expression until mouse adulthood was observed (Pedersen et al., 1998). Immunohistochemistry analyses also indicate that Pld3 expression is restricted to distinct neuronal sub-types.

RNA transcriptome analyses have shown that Pld3 is also expressed in microglia cells (Schaum et al., 2018; Zhang et al., 2014). Immunocytochemistry analysis of murine BV-2 microglia cells did not show any staining for Pld3 (data not shown). Of note, in human brain sections, reactive astrocytes and activated microglia accumulating around senile plaques, did not express PLD3 (Sato et al., 2014). However, Western blot analysis of the

BV-2 cells revealed a faint band of the luminal domain of Pld3. Thus, it cannot be excluded that minor levels of Pld3 are expressed in microglia cells. In summary, Pld3 is mainly a neuronal protein most likely expressed in selective sub-types of cells. Additional studies are necessary to validate Pld3 expression in other cells types, e.g. microglia.

#### **4.2.2 *Pld3-deficient mice show a subtle phenotype***

Lysosomes are the key cellular hub for macromolecule catabolism, recycling and signaling. Mutations in genes encoding lysosomal proteins, such as lysosomal glycosidases, proteases or integral membrane proteins, cause the accumulation of undigested or partially digested macromolecules in lysosomes ('storage'), leading to the development of lysosomal storage disorders (LSDs) (Platt et al., 2018). If PLD3 is responsible for the bulk hydrolysis of a certain substrate, an enlargement of lysosomes should be expected. This is a common cellular phenotype observed in many LSDs. However, staining of PLD3 KO HeLa cells with an anti-LAMP2 antibody and electron microscopy analysis of neuronal lysosomes of Pld3 KO mice (data not shown), did not show obvious alterations on the size of lysosomes.

Analysis of three different lysosomal enzymes ( $\beta$ -hexosaminidase,  $\beta$ -glucuronidase and  $\beta$ -glucocerebrosidase) revealed a decrease in their activity in Pld3 KO brain lysates, compared to WT mice. Although no substrate accumulation was evident, Pld3 deficiency may induce secondary effects leading to a mild lysosomal dysfunction, disturbing the activity of some lysosomal enzymes. Noteworthy, Fazzari et al. reported an increased lysosomal density, size and total area occupied by electron microscopy of Pld3-deficient CA1 neurons. Several of these lysosomes showed electron-transparent inclusions compatible with lipid droplets (Fazzari et al., 2017). It is tempting to speculate that such lysosomal inclusions could correspond to undigested DNA, as it will be later discussed in regard to PLD3 enzymatic activity.

Behavioral studies of Pld3 KO mice suggest that these mice develop a depression-like behavior. Additionally, immunohistochemistry of Pld3 KO brain revealed an increased immunoreactivity of the microglia marker CD68, especially pronounced in the dentate gyrus of the hippocampus and the subventricular zone, known to be the largest regions where adult neurogenesis takes place (Doetsch and Alvarez-Buylla, 1996). Decreased

neurogenesis has been implicated in the pathogenesis of anxiety and depression, but direct evidence for this role is lacking (Drew and Hen, 2007; Sapolsky, 2004). Moreover, microglia cells are involved in shaping neuronal circuits in perinatal and postnatal stages, regulating adult hippocampal neurogenesis (Cunningham et al., 2013; Reemst et al., 2016; Sierra et al., 2010; Ueno et al., 2013).

Using antibodies against a neuronal mitotic marker (anti-Ki67) and a marker of immature neurons (anti-DCX, doublecortin), the possibility that *Pld3*-deficient mice may alter the process of neurogenesis was analyzed. However, no clear differences were observed in the staining of Ki67- or DCX-positive cells in brain sections between WT and *Pld3* KO mice. An alternative approach would be BrdU (Bromodeoxyuridine / 5-bromo-2'-deoxyuridine) labeling, which is an analogue of the nucleoside thymidine used to identify proliferating cells *in vivo* (Kee et al., 2002).

It is known that the majority of newborn cells during neurogenesis undergo death by apoptosis, which are rapidly cleared through phagocytosis of microglia (Sierra et al., 2010). Thus, analysis of the interplay between neurogenesis and neuronal death should be considered. Due to the *Pld3* expression pattern observed in the dentate gyrus of the mouse brain at different postnatal stages, Pedersen et al. suggests that *Pld3* is involved in processes associated with target cell innervation, neurotransmission and neuronal survival, but less involved in early developmental processes, such as axonal growth, neurogenesis and neuronal migration (Pedersen et al., 1998). Further studies are necessary to unravel if the microglia activation and the behavioral despair are explained by a role of *Pld3* in neuronal homeostasis or is merely a secondary response of *Pld3* deficiency.

#### **4.2.3 *Pld3* is a 5' exonuclease**

The phospholipase D (PLD) members, PLD1 and PLD2, catalyze the conversion of phosphatidylcholine (PC) to choline and phosphatidic acid (PA), inducing a variety of intracellular signal transduction events, which are involved in the regulation of membrane and vesicle trafficking, cell proliferation, migration and actin cytoskeleton dynamics (Cockcroft, 2001; Riebeling et al., 2009; Roth, 2008; Rudge and Wakelam, 2009). The non-classical PLD members PLD3 and PLD4, do not exhibit typical PLD

enzymatic activity for conversion of PC to choline and PA (Munck et al., 2005; Pedersen et al., 1998). PLD3 and PLD4, both share structural similarities composed of a short N-terminal cytoplasmic tail, a transmembrane domain, and a long C-terminal region (Munck et al., 2005; Yoshikawa et al., 2010).

Considering the high Pld3 expression levels in the murine brain, a lipidomic analysis of brain lysates between WT and Pld3 KO mice was performed in order to investigate a possible accumulation of putative substrate lipid species. However, from the 220 lipid species analyzed, no significant changes were detected in the levels of phosphatidic acid species, where a decrease was expected if PLD3 would be a classical PLD enzyme. A decrease in some ceramide species was observed, though the changes were subtle, making it difficult to draw any clear conclusions. It is worth mentioning that if PLD3 and/or PLD4 may function as possible phospholipases, other substrates should be considered. In comparison to PLD1 and PLD2 which are facing the cytosol, the catalytic domains of PLD3 and PLD4 are facing the lumen of endo-lysosomes. Thus, only lipids present in the inner leaflet of the lysosomal membrane are putative substrates. These data strengthen the hypothesis that PLD3 does not exert a classical PLD enzymatic phospholipase D activity as previously reported.

In the course of this doctoral project, PLD3 and PLD4 were identified as lysosomal single-stranded exonucleases (Gavin et al., 2018). *In vitro* incubation of the recombinant luminal domain of mouse PLD3 and PLD4 with different DNA substrates only led to a degradation of single-stranded DNA (ssDNA) in the 5' to 3' direction, showing high substrate specificity. As a consequence of these findings, PLD3 nuclease activity was further evaluated. To this end, a nuclease cell-based assay was established and standardized by incubation in an acidic buffer of the same ssDNA substrate reported by Gavin et al. (a 55 nucleotide (nt) ssDNA) with lysates of untransfected or *PLD3*-transfected HeLa cells. The degradation products of this incubation were further analyzed by DNA-PAGE. Nuclease activity analysis of WT and PLD3 KO HeLa cells revealed endogenous enzymatic activity in WT, but not in PLD3 KO HeLa cells, suggesting that PLD3 is the major 5'-exonuclease in this cell line. It would be interesting to investigate if PLD3 represents the main 5'-exonuclease in other cell lines, e.g. SH-SY5Y cells.

Comparison of untransfected HeLa cells and *PLD3*-transfected cells revealed a high PLD3-dependent nuclease activity, where most of the substrate was degraded after 30 min of

incubation. This assay via ectopic expression was therefore a suitable approach to further analyze the effect of different described PLD3 variants on their catalytic activity.

PLD1 and PLD2 mediate their catalytic activity via a pair of HKD motifs, described to form the catalytic center (Jenkins and Frohman, 2005). PLD3 also contains two of these motifs. However, the most C-terminal motif is not conserved, where an aspartic acid (D) is substituted by a glutamic acid (E) at position 423. Analysis of the PLD3 variant E423A revealed that this amino acid is indispensable not only for the 5'-exonuclease activity but also for proper folding and appropriate delivery to lysosomes. Another HKD mutant (PLD3 K418) previously shown to eliminate the enzymatic activity of all PLD isoforms (Sung et al., 1997), also showed impaired nuclease activity. These results indicate that the HKD motifs are not only important for the catalytic activity of the classical phospholipases, but also, as report here, essential for nucleases.

Conservation of the HKD motifs is the most important feature for the inclusion of a protein in the PLD superfamily because these enzymes share a two-step ( $S_N2$ ) ping-pong mechanism that proceeds through a covalent phospho-protein intermediate in phosphodiester hydrolysis (Stanacev and Stuhne-Sekalec, 1970; Yang et al., 1967). Several studies propose a reaction mechanism where the N-terminal histidine residue within the HKD motif, nucleophilically attacks the phosphate group of the substrate (step 1), and forms a covalent phospho-histidine intermediate. The histidine residue of the C-terminal HKD/E motif serves as a general acid and donates a proton to the leaving group (step 2) (Gottlin et al., 1998; Rudolph et al., 1999). Structural data support the proposed  $S_N2$  mechanism, as the catalytic cores of PLD superfamily enzymes are predicted to share a bilobal structure similar to that of the conserved HKD residues oriented adjacent to one another in the active site. Thus, this reaction mechanism is thought to extend to all PLD superfamily enzymes (Selvy et al., 2011). PLD3 shares high homology (48 %) with the *Vaccinia* virus protein K4L, reported to exhibit nuclease and viral DNA condensation function (Eckert et al., 2005). This suggests that the viral protein has evolved from one or more eukaryotic genes to finally incorporate the conserved HKD motifs and perform similar cellular processes (Cao et al., 1997). If K4L also have similar substrate specificity like PLD3 remains unclear.

Several of the here analyzed enzymatic properties of PLD3 are reminiscent of the activity previously described as 'spleen acid exonuclease' or 'spleen phosphodiesterase'. This

enzyme, purified from hog spleen, has 5' single-strand specificity in an acidic milieu (Bernardi and Bernardi, 1968; Hilmoe, 1960; Razzell, 1961). As observed for PLD3, ethylenediaminetetraacetic acid (EDTA) was described as an activator for the spleen acid exonuclease (Hilmoe, 1960). Addition of the divalent cations  $Mg^{2+}$ ,  $Zn^{2+}$  and  $Cu^{2+}$  did not either affect PLD3 activity. This result indicates that PLD3 is a metal-independent nuclease. Substrate specificity studies of the spleen exonuclease showed that this enzyme degrades in the preferred nucleotide order guanine (G) > adenine (A) > uracil (U)  $\geq$  cytosine (C) (Bernardi and Bernardi, 1968; Holý, 1974). Preliminary data where the 5' nucleotide of the substrate was replaced with A, C, T, U or G, revealed that 5'-G-ssDNA was preferentially degraded by PLD3, followed by 5'-T, 5'-A and 5'-U which were catalyzed with slower but comparable kinetics (data not shown). 5'-C-ssDNA was a poor substrate, as described for the spleen exonuclease.

Regarding the intracellular localization, using synthetic substrates, spleen exonuclease was found in the mitochondrial-lysosomal fraction (Razzell, 1961). Subsequent work confirmed the hypothesis that acid exonuclease is a lysosomal enzyme like other acid hydrolases that degrade nucleic acids (Erecińska et al., 1969; Van Dyck and Wattiaux, 1968). Mass spectrometry analysis of the commercially available phosphodiesterase II from bovine spleen identified six PLD3 peptides (Gavin et al., 2018). However, the gene encoding spleen exonuclease has never been cloned. These data support the idea that PLD3 and/or PLD4 represent the long sought 'spleen exonuclease'. Since the spleen exonuclease was also identified to degrade RNA, additional experimental data is required to decipher if ribonucleic acids would be also cleaved by PLD3 with such a high specificity.

Protein structure prediction tools suggest that PLD3 does not form a dimer to exert its catalytic activity, as described e.g. for PLD6, an endonuclease member of the PLD family (Ipsaro et al., 2012; Nishimasu et al., 2012). Instead, the large C-terminal region of PLD3 would fold itself into two globular domains, each containing one HKD/E motif. PLD3 crystallization could provide more information in regard to protein structure and the mechanism behind substrate binding. As shown for several PLD members, other cofactors that could regulate PLD3 activity should be considered, e.g. regulatory proteins or alternative post-translational modifications. Of note, treatment of *PLD3*-transfected cells with different inhibitors of lysosomal acidification did not alter PLD3 exonuclease activity. Additionally, membrane separation by ultracentrifugation followed by nuclease

activity analysis, revealed a comparable nuclease activity between the soluble PLD3 fraction and the membrane-bound full-length PLD3 fraction (data not shown). These results indicate that in acidic milieu proteolytic processing is dispensable for its enzymatic activity. This raises the question, why such a regulated mechanism of PLD3 trafficking and proteolytic cleavage to produce a soluble stable form in lysosomes does not influence PLD3 nuclease activity. A better accessibility of the soluble PLD3 enzyme to the substrate in comparison to the membrane-bound form of PLD3 could be envisaged. Further analyses are required to elucidate this assumption.

#### **4.2.4 *Pld3 is the main 5' exonuclease in the brain***

In the light of the findings that Pld3 is mainly expressed in the brain, an analysis of Pld3 exonuclease activity was performed using tissue lysates of WT and Pld3-deficient mice. Noteworthy, besides the highest Pld3 expression observed in the mouse brain, a substantial protein expression level was also detected in the spleen and the bone marrow, both primary immune competent tissues. Nuclease analysis revealed a high 5' exonuclease activity of all WT tissues (brain, spleen and bone marrow), where the substrate was completely degraded after 4 h of incubation. Strikingly, no nuclease activity was detected in the brain lysates of Pld3 KO mice. In contrast, ~40 % of substrate degradation was depicted in the spleen and bone marrow of Pld3 KO mice. Increasing amounts of PLD3 KO brain lysates only revealed minor nuclease activity at very high concentrations. These results indicate that Pld3 is the major 5' exonuclease in the brain. It can be speculated that the remaining nuclease activity observed in the spleen and the bone marrow and the minor activity observed with very high concentrations of Pld3 KO brain lysates, is due to Pld4 activity.

Both enzymes were identified as ssDNA exonucleases with overlapping functions (Gavin et al., 2018). The expression of Pld3 and Pld4 is likely tissue-specific. A previous study using Pld4 KO mice showed that Pld4 was mainly expressed in the marginal zone of the spleen and white matter tracks in the brain, including the corpus callosum and cerebellar white matter (Yoshikawa et al., 2010). The same group later described that Pld4 is implicated in the proliferation and phagocytosis function of microglia in the central nervous system (Otani et al., 2011). Proteomics data suggest high expression of PLD4 in



dendritic cells (DCs) and other myeloid cells and low expression in B cells. Moreover, studies have linked *PLD4* gene polymorphisms to systemic sclerosis, rheumatoid arthritis (Chen et al., 2017; Terao et al., 2013) and more recently, to systemic lupus erythematosus (Akizuki et al., 2019). These findings suggest a functional involvement of PLD4 in the development of autoimmunity through controlling functions of immune cells.

It can be hypothesized that in the brain, the major 5' exonuclease activity comes from PLD3 expression in neuronal cells, whereas a minor activity can be expected from PLD4 expression in microglia or other immune-related cells. Moreover, it can be speculated that in lymphatic organs, including the spleen and the bone marrow, PLD3 and PLD4 play a coordinated role in the specific degradation of ssDNA. Gavin et al. reported that wild-type macrophages had a high expression of *Pld3* and low expression of *Pld4*, whereas wild-type dendritic cells showed the opposite pattern of expression. Analysis of *Pld3*-deficient macrophages and *Pld4*-deficient dendritic cells revealed a large inflammatory response, marked by elevated levels of interferon- $\gamma$  (IFN- $\gamma$ ) and interleukin-6 (IL-6). These abnormalities were dependent on toll-like receptor 9 (TLR9) (Gavin et al., 2018). Toll-like receptors (TLRs) are type-I transmembrane proteins that mediate innate immunity by the recognition of pathogen- or damage-associated patterns (P/DAMPs) (Gordon, 2002). TLR9 resides in endo-/lysosomes and senses single-stranded DNA (ssDNA) containing unmethylated CpG dinucleotides (Krieg, 2002). Several classes of synthetic ligands, assigned as oligodeoxynucleotides (ODNs), which mimic the immunostimulatory activity of bacterial DNA, have been described and activate downstream signaling of TLR9 (Guiducci et al., 2006; Vollmer et al., 2004). Gavin et al. propose that PLD3 and PLD4 trim the 5' end of single-stranded ODNs, degrading them and limit their ability to stimulate TLR9. Thus, we hypothesize that the increased CD68 immunoreactivity at sites of neurogenesis observed in *Pld3*-deficient mice could correspond to an inflammatory response due to TLR9 overstimulation. TLR9 regulates aberrant adult neurogenesis upon injury (Matsuda et al., 2015). However, it should be noted that an analysis of *Pld3*<sup>-/-</sup> *Tlr9*<sup>-/-</sup> mice did not reveal a rescue of the phenotype of the *Pld3* KO mice (data not shown). This indicates that the increased CD68 immunoreactivity was not necessarily dependent on TLR9. Since TLR9 stimulation activates a downstream signaling cascade, measurement of activated transcription factors or proinflammatory cytokines should be considered.

The assay of the PLD3 exonuclease activity described here and the proposed function of PLD3 as a nucleic acid degrading enzyme of TLR9 ligands were all performed with synthetic or artificial ssDNA substrates. However, the physiological substrate of PLD3 is still unknown. Danger signals can arise not only from pathogens, but also from endogenous damage-associated molecular patterns (DAMPs), which can either be secreted from cells or be released following cell injury and death (Kono and Rock, 2008; Krysko et al., 2011). These endogenous molecules can include extracellular matrix, cytosolic compounds and fragments of damaged organelles (McCarthy et al., 2014).

An example of such DAMPs is mitochondrial DNA (mtDNA). mtDNA contains unmethylated CpG dinucleotides, known to stimulate TLR9 (Krysko et al., 2011; Oka et al., 2012; Zhang et al., 2010). Thus, a natural substrate of PLD3 could be mtDNA. After translocation to the lysosomal lumen, autophagic substrates undergo degradation by catabolic enzymes. RNase T2 and DNaseII are a well-characterized lysosomal RNases and DNases, respectively. DNaseII is an endonuclease that cleaves double-stranded DNA with low sequence specificity (Evans and Aguilera, 2003). The contribution of DNaseII to autophagic degradation of mtDNA, which prevents inflammation, has also been reported (Oka et al., 2012).

Interestingly, the successful purification of the initially described 'spleen exonuclease' was largely dependent on the choice of the oligonucleotides obtained by digestion of DNA by DNaseII (Bernardi and Bernardi, 1968). Moreover, it has been shown that DNaseII-dependent digestion is required for DNA sensing by TLR9 (Chan et al., 2015). Thus, it can be speculated that, upon autophagy-mediated mitochondrial degradation ('mitophagy') (Rodriguez-Enriquez et al., 2006), mtDNA is accessible for its degradation by DNaseII to produce ssDNA fragments of approximately 10 nucleotides. This natural 'ODNs' would then stimulate TLR9.

Downregulation of this response is then regulated by the degradation of these shorter oligonucleotides by means of the 5' exonuclease activity of PLD3 and/or PLD4. If this hypothesis holds true, a bulk DNA degradation is not expected. Considering the similarities in the enzymatic activities of PLD3 and PLD4, it can be suggested that these nucleases have redundant functions in key cell types. In fact, mice deficient in both genes did not survive to the age of weaning. However, only a single allele of either *Pld3* or *Pld4* was required to allow survival (Gavin et al., 2018).

### 4.3 PLD3 and its role in neurodegenerative disorders

#### 4.3.1 *PLD3 and Alzheimer's disease*

An increasing interest for PLD3 has evolved in the past years, especially after a polymorphism in the *PLD3* gene (*PLD3* V232M variant), was associated with a higher probability to develop late-onset Alzheimer's disease (LOAD) (Cruchaga et al., 2014). Later studies attempted to reproduce this genetic association (Heilmann et al., 2015; Hooli et al., 2015; Lambert et al., 2015). However, only one group reported that the frequency of the *PLD3* V232M variant was higher in AD cases compared to controls (van der Lee et al., 2015).

The functional consequences of the *PLD3* variants on the nuclease activity, however, has not yet been investigated. Besides *PLD3* V232M, other variants were also associated with AD risk or were more frequent in AD cases than in controls (Cruchaga et al., 2014). From some of the *PLD3* variants reported by Cruchaga et al., *PLD3* K228R and N236S showed alterations in PLD3 proteolytic processing. This can be explained by an ER retention. As expected, *PLD3* K228R and N236S also revealed lower exonuclease activity, indicating that these amino acid positions are conserved and important for proper PLD3 folding, transport and nuclease activity. It would be interesting to evaluate the PLD3 exonuclease activity using brain lysates of post-mortem AD cases. However, sequencing of *PLD3* alleles of each individual case should be performed in order to directly compare *PLD3* variants and PLD3 activity.

Cruchaga et al. and Satoh et al. reported that PLD3 mRNA and protein levels are lower in neurons from AD brains compared to control brains. Moreover, overexpression of PLD3 led to a significant decrease of the intracellular amyloid precursor protein (APP) (Cruchaga et al., 2014). Western blot analysis of WT and *Pld3* KO brain lysates did not reveal alterations on APP protein levels, APP cleavage products or the levels of proteases involved in APP amyloidogenic pathway (Bace1 and presenilin). It can be assumed that a possible effect of PLD3 on APP processing is only revealed under conditions of high expression of human APP. However, analysis of 5xFAD and 5xFAD *Pld3*<sup>-/-</sup> brain lysates showed comparable protein levels of APP and its cleavage products. In agreement with these findings, Fazzari et al., using an APP knock-in mice (*App<sup>ki</sup>*) also reported that *Pld3* deficiency did not directly affect APP metabolism.

### 4.3.2 *PLD3 and spinocerebellar ataxia*

Based on a combination of exome sequencing, *PLD3* was identified as a novel causative gene of autosomal dominant spinocerebellar ataxia (SCA) (Nibbeling et al., 2017). The described *PLD3* variant (L308P) associated to the disease, was localized to the endoplasmic reticulum and exhibited a reduced phospholipase D activity. As described along this thesis, no canonical phospholipase D activity was conferred to *PLD3*. Instead, the *PLD3* L308P mutant revealed impaired exonuclease activity and abrogated *PLD3* proteolytic processing. This hereditary neurodegenerative disorder is characterized by loss of coordination and balance, gait abnormalities and slurred speech (Durr, 2010; Klockgether, 2011). However, behavioral studies and calbindin labeling of *Pld3* KO brain sections did not reveal any signs of impaired motor coordination or loss of Purkinje cells in the cerebellum, respectively. These data support the finding by Nibbeling et al. that the *PLD3* L308P variant leads to a loss of function. However, the *Pld3* KO analysis as performed here, suggests that *PLD3* is not a causative gene of spinocerebellar ataxia.

## 4.4 Concluding remarks

The detailed biochemical characterization of *PLD3* performed here revealed a new biosynthetic intracellular pathway, where the ESCRT machinery is essential for the transport and delivery of *PLD3* to lysosomes. In late endosomes/lysosomes *PLD3* undergoes proteolytic cleavage releasing the mature soluble form. *PLD3* shows highest expression in the brain and localizes to distinct neuronal cell populations. *PLD3* acts as a 5' exonuclease specifically cleaving single-stranded DNA. Elucidating *PLD3*'s natural substrate will further clarify the role of *PLD3* as an exonuclease in the brain and in the regulation of neuronal function. It remains to be investigated how genetic polymorphisms within the *PLD3* gene affect and modulate the development of neurodegenerative disorders.



## 5 REFERENCES

- Aizawa, S., Contu, V. R., Fujiwara, Y., Hase, K., Kikuchi, H., Kabuta, C., Wada, K. and Kabuta, T.** (2016a). Lysosomal membrane protein SIDT2 mediates the direct uptake of DNA by lysosomes. *Autophagy* **8627**, 1–5.
- Aizawa, S., Fujiwara, Y., Contu, V. R., Hase, K., Takahashi, M., Kikuchi, H., Kabuta, C., Wada, K. and Kabuta, T.** (2016b). Lysosomal putative RNA transporter SIDT2 mediates direct uptake of RNA by lysosomes. *Autophagy* **12**, 565–78.
- Akizuki, S., Ishigaki, K., Kochi, Y., Law, S.-M., Matsuo, K., Ohmura, K., Suzuki, A., Nakayama, M., Iizuka, Y., Koseki, H., et al.** (2019). PLD4 is a genetic determinant to systemic lupus erythematosus and involved in murine autoimmune phenotypes. *Ann. Rheum. Dis.* annrheumdis-2018-214116.
- Altman, J.** (1969). Autoradiographic and histological studies of postnatal neurogenesis. IV. Cell proliferation and migration in the anterior forebrain, with special reference to persisting neurogenesis in the olfactory bulb. *J. Comp. Neurol.* **137**, 433–457.
- Altman, J. and Das, G. D.** (1965). Autoradiographic and histological evidence of postnatal hippocampal neurogenesis in rats. *J. Comp. Neurol.* **124**, 319–335.
- Aoyagi, T., Takeuchi, T., Matsuzaki, A., Kawamura, K., Kondo, S., Masa Hamada, Maeda, K. and Umezawa, H.** (1969). Leupeptins, new protease inhibitors from actinomycetes. *J. Antibiot. (Tokyo)*. **22**, 283–286.
- Ascoli, G. A., Donohue, D. E. and Halavi, M.** (2007). NeuroMorpho.Org: a central resource for neuronal morphologies. *J. Neurosci.* **27**, 9247–51.
- Axe, E. L., Walker, S. A., Manifava, M., Chandra, P., Roderick, H. L., Habermann, A., Griffiths, G. and Ktistakis, N. T.** (2008). Autophagosome formation from membrane compartments enriched in phosphatidylinositol 3-phosphate and dynamically connected to the endoplasmic reticulum. *J. Cell Biol.* **182**, 685–701.
- Babst, M., Sato, T. K., Banta, L. M. and Emr, S. D.** (1997). Endosomal transport function in yeast requires a novel AAA-type ATPase, Vps4p. *EMBO J.* **16**, 1820–31.
- Babst, M., Katzmann, D. J., Estepa-Sabal, E. J., Meerloo, T. and Emr, S. D.** (2002a). Escrt-III: an endosome-associated heterooligomeric protein complex required for mvb sorting. *Dev. Cell* **3**, 271–82.
- Babst, M., Katzmann, D. J., Snyder, W. B., Wendland, B. and Emr, S. D.** (2002b).

- Endosome-associated complex, ESCRT-II, recruits transport machinery for protein sorting at the multivesicular body. *Dev. Cell* **3**, 283–9.
- Bainton, D. F.** (1981). The discovery of lysosomes. *J. Cell Biol.* **91**, 66s–76s.
- Baldwin, S. A., Yao, S. Y. M., Hyde, R. J., Ng, A. M. L., Foppolo, S., Barnes, K., Ritzel, M. W. L., Cass, C. E. and Young, J. D.** (2005). Functional characterization of novel human and mouse equilibrative nucleoside transporters (hENT3 and mENT3) located in intracellular membranes. *J. Biol. Chem.* **280**, 15880–7.
- Barrangou, R., Fremaux, C., Deveau, H., Richards, M., Boyaval, P., Moineau, S., Romero, D. A. and Horvath, P.** (2007). CRISPR provides acquired resistance against viruses in prokaryotes. *Science* **315**, 1709–12.
- Barrett, A. J.** (1980). The Lysosome and its Membrane. *Biochem. Soc. Trans.*
- Bekris, L. M., Yu, C.-E., Bird, T. D. and Tsuang, D. W.** (2010). Genetics of Alzheimer disease. *J. Geriatr. Psychiatry Neurol.* **23**, 213–27.
- Bernardi, A. and Bernardi, G.** (1968). Studies on acid hydrolases. IV. Isolation and characterization of spleen exonuclease. *Biochim. Biophys. Acta* **155**, 360–70.
- Bertram, L. and Tanzi, R. E.** (2005). The genetic epidemiology of neurodegenerative disease. *J. Clin. Invest.* **115**, 1449–57.
- Bishop, N., Horman, A. and Woodman, P.** (2002). Mammalian class E vps proteins recognize ubiquitin and act in the removal of endosomal protein-ubiquitin conjugates. *J. Cell Biol.* **157**, 91–101.
- Blasi, E., Barluzzi, R., Bocchini, V., Mazzolla, R. and Bistoni, F.** (1990). immortalization of murine microglial cells by a v-raf/v-myc carrying retrovirus. *J. Neuroimmunol.* **27**, 229–37.
- Bonifacino, J. S.** (2004). Insights into the biogenesis of lysosome-related organelles from the study of the Hermansky-Pudlak syndrome. *Ann. N. Y. Acad. Sci.* **1038**, 103–14.
- Bonifacino, J. S. and Glick, B. S.** (2004). The mechanisms of vesicle budding and fusion. *Cell* **116**, 153–66.
- Bonifacino, J. S. and Traub, L. M.** (2003). Signals for Sorting of Transmembrane Proteins to Endosomes and Lysosomes. *Annu. Rev. Biochem.* **72**, 395–447.
- Braulke, T. and Bonifacino, J. S.** (2009). Sorting of lysosomal proteins. *Biochim. Biophys. Acta - Mol. Cell Res.* **1793**, 605–614.
- Braun, M., Waheed, A. and von Figura, K.** (1989). Lysosomal acid phosphatase is transported to lysosomes via the cell surface. *EMBO J.* **8**, 3633–40.



- Brouns, S. J. J., Jore, M. M., Lundgren, M., Westra, E. R., Slijkhuis, R. J. H., Snijders, A. P. L., Dickman, M. J., Makarova, K. S., Koonin, E. V and van der Oost, J.** (2008). Small CRISPR RNAs guide antiviral defense in prokaryotes. *Science* **321**, 960–4.
- Brown, W. J., DeWald, D. B., Emr, S. D., Plutner, H. and Balch, W. E.** (1995). Role for phosphatidylinositol 3-kinase in the sorting and transport of newly synthesized lysosomal enzymes in mammalian cells. *J. Cell Biol.* **130**, 781–96.
- Brown, F. D., Thompson, N., Saqib, K. M., Clark, J. M., Powner, D., Thompson, N. T., Solari, R. and Wakelam, M. J.** (1998). Phospholipase D1 localises to secretory granules and lysosomes and is plasma-membrane translocated on cellular stimulation. *Curr. Biol.* **8**, 835–8.
- Brunner, Y., Couté, Y., Iezzi, M., Foti, M., Fukuda, M., Hochstrasser, D. F., Wollheim, C. B. and Sanchez, J.-C.** (2007). Proteomics analysis of insulin secretory granules. *Mol. Cell. Proteomics* **6**, 1007–17.
- Burd, C. G. and Emr, S. D.** (1998). Phosphatidylinositol(3)-phosphate signaling mediated by specific binding to RING FYVE domains. *Mol. Cell* **2**, 157–62.
- Burn, S. F.** (2012). Detection of  $\beta$ -Galactosidase Activity: X-gal Staining. pp. 241–250. Humana Press, Totowa, NJ.
- Callahan, J. W., Bagshaw, R. D. and Mahuran, D. J.** (2009). The integral membrane of lysosomes: its proteins and their roles in disease. *J. Proteomics* **72**, 23–33.
- Canfield, W. M., Johnson, K. F., Ye, R. D., Gregory, W. and Kornfeld, S.** (1991). Localization of the signal for rapid internalization of the bovine cation-independent mannose 6-phosphate/insulin-like growth factor-II receptor to amino acids 24–29 of the cytoplasmic tail. *J. Biol. Chem.* **266**, 5682–8.
- Cao, X. and Südhof, T. C.** (2001). A transcriptionally [correction of transcriptively] active complex of APP with Fe65 and histone acetyltransferase Tip60. *Science* **293**, 115–20.
- Cao, J., Koop, B. and Upton, C.** (1997). A human homolog of the vaccinia virus HindIII K4L gene is a member of the phospholipase D superfamily. *Virus Res.* **48**, 11–18.
- Carlsson, S. R. and Fukuda, M.** (1992). The lysosomal membrane glycoprotein lamp-1 is transported to lysosomes by two alternative pathways. *Arch. Biochem. Biophys.* **296**, 630–9.
- Carlsson, S. R., Roth, J., Piller, F. and Fukuda, M.** (1988). Isolation and characterization of human lysosomal membrane glycoproteins, h-lamp-1 and h-lamp-2. Major

- sialoglycoproteins carrying polylactosaminoglycan. *J. Biol. Chem.* **263**, 18911–9.
- Caston, J., Jones, N. and Stelz, T.** (1995). Role of preoperative and postoperative sensorimotor training on restoration of the equilibrium behavior in adult mice following cerebellectomy. *Neurobiol. Learn. Mem.* **64**, 195–202.
- Cataldo, A. M., Barnett, J. L., Berman, S. A., Li, J., Quarless, S., Bursztajn, S., Lippa, C. and Nixon, R. A.** (1995). Gene expression and cellular content of cathepsin D in Alzheimer's disease brain: Evidence for early up-regulation of the endosomal-lysosomal system. *Neuron* **14**, 671–680.
- Chadwick, W., Brenneman, R., Martin, B. and Maudsley, S.** (2010). Complex and multidimensional lipid raft alterations in a murine model of Alzheimer's disease. *Int. J. Alzheimers. Dis.* **2010**, 604792.
- Chan, M. P., Onji, M., Fukui, R., Kawane, K., Shibata, T., Saitoh, S., Ohto, U., Shimizu, T., Barber, G. N. and Miyake, K.** (2015). DNase II-dependent DNA digestion is required for DNA sensing by TLR9. *Nat. Commun.* **6**, 5853.
- Chapel, A., Kieffer-Jaquinod, S., Sagné, C., Verdon, Q., Ivaldi, C., Mellal, M., Thirion, J., Jadot, M., Bruley, C., Garin, J., et al.** (2013). An Extended Proteome Map of the Lysosomal Membrane Reveals Novel Potential Transporters. *Mol. Cell. Proteomics* **12**, 1572–1588.
- Chen, J. W., Cha, Y., Yuksel, K. U., Gracy, R. W. and August, J. T.** (1988). Isolation and sequencing of a cDNA clone encoding lysosomal membrane glycoprotein mouse LAMP-1. Sequence similarity to proteins bearing onco-differentiation antigens. *J. Biol. Chem.* **263**, 8754–8.
- Chen, W.-C., Wang, W.-C., Okada, Y., Chang, W.-P., Chou, Y.-H., Chang, H.-H., Huang, J.-D., Chen, D.-Y., Chang, W.-C. and Chang, W.-C.** (2017). rs2841277 (PLD4) is associated with susceptibility and rs4672495 is associated with disease activity in rheumatoid arthritis. *Oncotarget* **8**, 64180–64190.
- Chow, V. W., Mattson, M. P., Wong, P. C. and Gleichmann, M.** (2010). An overview of APP processing enzymes and products. *Neuromolecular Med.* **12**, 1–12.
- Chung, C. H., Golub, E. E., Forbes, E., Tokuoka, T. and Shapiro, I. M.** (1992). Mechanism of action of beta-glycerophosphate on bone cell mineralization. *Calcif. Tissue Int.* **51**, 305–11.
- Cockcroft, S.** (2001). Signalling roles of mammalian phospholipase D1 and D2. *Cell. Mol. Life Sci.* **58**, 1674–87.

- Colley, W. C., Sung, T. C., Roll, R., Jenco, J., Hammond, S. M., Altshuler, Y., Bar-Sagi, D., Morris, A. J. and Frohman, M. A.** (1997). Phospholipase D2, a distinct phospholipase D isoform with novel regulatory properties that provokes cytoskeletal reorganization. *Curr. Biol.* **7**, 191–201.
- Cowles, C. R., Snyder, W. B., Burd, C. G. and Emr, S. D.** (1997). Novel Golgi to vacuole delivery pathway in yeast: identification of a sorting determinant and required transport component. *EMBO J.* **16**, 2769–82.
- Crews, L. and Masliah, E.** (2010). Molecular mechanisms of neurodegeneration in Alzheimer's disease. *Hum. Mol. Genet.* **19**, R12–R20.
- Cruchaga, C., Karch, C. M., Jin, S. C., Benitez, B. A., Cai, Y., Guerreiro, R., Harari, O., Norton, J., Budde, J., Bertelsen, S., et al.** (2014). Rare coding variants in the phospholipase D3 gene confer risk for Alzheimer's disease. *Nature* **505**, 550–554.
- Cunningham, C. L., Martinez-Cerdeno, V. and Noctor, S. C.** (2013). Microglia Regulate the Number of Neural Precursor Cells in the Developing Cerebral Cortex. *J. Neurosci.* **33**, 4216–4233.
- Darsow, T., Burd, C. G. and Emr, S. D.** (1998). Acidic di-leucine motif essential for AP-3-dependent sorting and restriction of the functional specificity of the Vam3p vacuolar t-SNARE. *J. Cell Biol.* **142**, 913–22.
- De Duve, C., Pressman, B. C., Gianetto, R., Wattiaunx, R. and Appelmans, F.** (1955). Tissue fractionation studies. 6. Intracellular distribution patterns of enzymes in rat-liver tissue. *Biochem. J.* **60**, 604–17.
- DeKosky, S. T. and Scheff, S. W.** (1990). Synapse loss in frontal cortex biopsies in Alzheimer's disease: correlation with cognitive severity. *Ann. Neurol.* **27**, 457–64.
- DeKosky, S. T., Scheff, S. W. and Styren, S. D.** (1996). Structural correlates of cognition in dementia: quantification and assessment of synapse change. *Neurodegeneration* **5**, 417–21.
- Dell'Angelica, E. C., Mullins, C., Caplan, S. and Bonifacino, J. S.** (2000). Lysosome-related organelles. *FASEB J.* **14**, 1265–78.
- Della Valle, M. C., Sleat, D. E., Sohar, I., Wen, T., Pintar, J. E., Jadot, M. and Lobel, P.** (2006). Demonstration of lysosomal localization for the mammalian ependymin-related protein using classical approaches combined with a novel density shift method. *J. Biol. Chem.* **281**, 35436–45.

- DeMasi, J., Du, S., Lennon, D. and Traktman, P.** (2001). Vaccinia virus telomeres: interaction with the viral I1, I6, and K4 proteins. *J. Virol.* **75**, 10090–105.
- Deshpande, R. A. and Shankar, V.** (2002). Ribonucleases from T2 family. *Crit. Rev. Microbiol.* **28**, 79–122.
- Dice, J. F.** (2007). Chaperone-mediated autophagy. *Autophagy* **3**, 295–9.
- Dimou, L. and Götz, M.** (2014). Glial Cells as Progenitors and Stem Cells: New Roles in the Healthy and Diseased Brain. *Physiol. Rev.* **94**, 709–737.
- Dittmer, F., Ulbrich, E. J., Hafner, A., Schmahl, W., Meister, T., Pohlmann, R. and von Figura, K.** (1999). Alternative mechanisms for trafficking of lysosomal enzymes in mannose 6-phosphate receptor-deficient mice are cell type-specific. *J. Cell Sci.* **112** (Pt 10), 1591–7.
- Doetsch, F. and Alvarez-Buylla, A.** (1996). Network of tangential pathways for neuronal migration in adult mammalian brain. *Proc. Natl. Acad. Sci. U. S. A.* **93**, 14895–900.
- Drew, M. R. and Hen, R.** (2007). Adult hippocampal neurogenesis as target for the treatment of depression. *CNS Neurol. Disord. Drug Targets* **6**, 205–18.
- Du, G., Altshuler, Y. M., Kim, Y., Han, J. M., Ryu, S. H., Morris, A. J. and Frohman, M. A.** (2000). Dual requirement for rho and protein kinase C in direct activation of phospholipase D1 through G protein-coupled receptor signaling. *Mol. Biol. Cell* **11**, 4359–68.
- Du, G., Altshuler, Y. M., Vitale, N., Huang, P., Chasserot-Golaz, S., Morris, A. J., Bader, M.-F. and Frohman, M. A.** (2003). Regulation of phospholipase D1 subcellular cycling through coordination of multiple membrane association motifs. *J. Cell Biol.* **162**, 305–15.
- Durr, A.** (2010). Autosomal dominant cerebellar ataxias: polyglutamine expansions and beyond. *Lancet. Neurol.* **9**, 885–94.
- Eckert, D., Williams, O., Meseda, C. A. and Merchlinsky, M.** (2005). Vaccinia virus nicking-joining enzyme is encoded by K4L (VACWR035). *J. Virol.* **79**, 15084–90.
- Edgar, J. R., Willén, K., Gouras, G. K. and Futter, C. E.** (2015). ESCRTs regulate amyloid precursor protein sorting in multivesicular bodies and intracellular amyloid- $\beta$  accumulation. *J. Cell Sci.* **128**, 2520–2528.
- Erecińska, M., Sierakowska, H. and Shugar, D.** (1969). Intracellular localization of phosphodiesterases I and II in rat liver. *Eur. J. Biochem.* **11**, 465–71.

- Erickson, A. H., Ginns, E. I. and Barranger, J. A.** (1985). Biosynthesis of the lysosomal enzyme glucocerebrosidase. *J. Biol. Chem.* **260**, 14319–14324.
- Evans, C. J. and Aguilera, R. J.** (2003). DNase II: genes, enzymes and function. *Gene* **322**, 1–15.
- Fazzari, P., Horre, K., Arranz, A. M., Frigerio, C. S., Saito, T., Saido, T. C. and De Strooper, B.** (2017). PLD3 gene and processing of APP. *Nature* **541**, E1–E2.
- Felbor, U., Kessler, B., Mothes, W., Goebel, H. H., Ploegh, H. L., Bronson, R. T. and Olsen, B. R.** (2002). Neuronal loss and brain atrophy in mice lacking cathepsins B and L. *Proc. Natl. Acad. Sci.* **99**, 7883–7888.
- Felder, S., Miller, K., Moehren, G., Ullrich, A., Schlessinger, J. and Hopkins, C. R.** (1990). Kinase activity controls the sorting of the epidermal growth factor receptor within the multivesicular body. *Cell* **61**, 623–34.
- Feyder, S., De Craene, J.-O., Bär, S., Bertazzi, D. L. and Friant, S.** (2015). Membrane trafficking in the yeast *Saccharomyces cerevisiae* model. *Int. J. Mol. Sci.* **16**, 1509–25.
- Fisher, T. L., Terhorst, T., Cao, X. and Wagner, R. W.** (1993). Intracellular disposition and metabolism of fluorescently-labeled unmodified and modified oligonucleotides microinjected into mammalian cells. *Nucleic Acids Res.* **21**, 3857–65.
- Fratz-Berilla, E. J., Ketcham, S. A., Parhiz, H., Ashraf, M. and Madhavarao, C. N.** (2017). An improved purification method for the lysosomal storage disease protein  $\beta$ -glucuronidase produced in CHO cells. *Protein Expr. Purif.* **140**, 28–35.
- Frohman, M. A.** (2015). The phospholipase D superfamily as therapeutic targets. *Trends Pharmacol. Sci.* **36**, 137–144.
- Fujiwara, Y., Furuta, A., Kikuchi, H., Aizawa, S., Hatanaka, Y., Konya, C., Uchida, K., Yoshimura, A., Tamai, Y., Wada, K., et al.** (2013a). Discovery of a novel type of autophagy targeting RNA. *Autophagy* **9**, 403–409.
- Fujiwara, Y., Kikuchi, H., Aizawa, S., Furuta, A., Hatanaka, Y., Konya, C., Uchida, K., Wada, K. and Kabuta, T.** (2013b). Direct uptake and degradation of DNA by lysosomes. *Autophagy* **9**, 1167–71.
- Fujiwara, Y., Wada, K. and Kabuta, T.** (2017). Lysosomal degradation of intracellular nucleic acids-multiple autophagic pathways. *J. Biochem.* **161**, 145–154.
- Fukuda, M., Viitala, J., Matteson, J. and Carlsson, S. R.** (1988). Cloning of cDNAs encoding human lysosomal membrane glycoproteins, h-lamp-1 and h-lamp-2. Comparison of their deduced amino acid sequences. *J. Biol. Chem.* **263**, 18920–8.

- Gavin, A. L., Huang, D., Huber, C., Mårtensson, A., Tardif, V., Skog, P. D., Blane, T. R., Thinnes, T. C., Osborn, K., Chong, H. S., et al.** (2018). PLD3 and PLD4 are single-stranded acid exonucleases that regulate endosomal nucleic-acid sensing. *Nat. Immunol.* **19**, 942–953.
- Ghazi-Tabatabai, S., Saksena, S., Short, J. M., Pobbati, A. V., Veprintsev, D. B., Crowther, R. A., Emr, S. D., Egelman, E. H. and Williams, R. L.** (2008). Structure and disassembly of filaments formed by the ESCRT-III subunit Vps24. *Structure* **16**, 1345–56.
- Gill, D. J., Teo, H., Sun, J., Perisic, O., Veprintsev, D. B., Vallis, Y., Emr, S. D. and Williams, R. L.** (2007). Structural studies of phosphoinositide 3-kinase-dependent traffic to multivesicular bodies. *Biochem. Soc. Symp.* **74**, 47.
- Ginsberg, S. D., Hemby, S. E., Lee, V. M.-Y., Eberwine, J. H. and Trojanowski, J. Q.** (2000). Expression profile of transcripts in Alzheimer's disease tangle-bearing CA1 neurons. *Ann. Neurol.* **48**, 77–87.
- Glennner, G. G.** (1983). Alzheimer's disease. The commonest form of amyloidosis. *Arch. Pathol. Lab. Med.* **107**, 281–2.
- Glennner, G. G. and Wong, C. W.** (1984). Alzheimer's disease: initial report of the purification and characterization of a novel cerebrovascular amyloid protein. *Biochem. Biophys. Res. Commun.* **120**, 885–90.
- Gohara, D. W. and Cera, E. Di** (2016). Molecular Mechanisms of Enzyme Activation by Monovalent Cations. *J. Biol. Chem.* **291**, 20840.
- Gordon, S.** (2002). Pattern recognition receptors: doubling up for the innate immune response. *Cell* **111**, 927–30.
- Gottlin, E. B., Rudolph, A. E., Zhao, Y., Matthews, H. R. and Dixon, J. E.** (1998). Catalytic mechanism of the phospholipase D superfamily proceeds via a covalent phosphohistidine intermediate. *Proc. Natl. Acad. Sci. U. S. A.* **95**, 9202–7.
- Gottschalk, S., Waheed, A., Schmidt, B., Laidler, P. and von Figura, K.** (1989). Sequential processing of lysosomal acid phosphatase by a cytoplasmic thiol proteinase and a lysosomal aspartyl proteinase. *EMBO J.* **8**, 3215–9.
- Gowrishankar, S., Yuan, P., Wu, Y., Schrag, M., Paradise, S., Grutzendler, J., De Camilli, P. and Ferguson, S. M.** (2015). Massive accumulation of luminal protease-deficient axonal lysosomes at Alzheimer's disease amyloid plaques. *Proc. Natl. Acad. Sci.* **112**, E3699–E3708.

- Greenbaum, L. M. and Sutherland, J. H.** (1983). Host cathepsin D response to tumor in the normal and pepstatin-treated mouse. *Cancer Res.* **43**, 2584–7.
- Griffin, W. S. T.** (2006). Inflammation and neurodegenerative diseases. *Am. J. Clin. Nutr.* **83**, 470S–474S.
- Groux-Degroote, S., van Dijk, S. M., Wolthoorn, J., Neumann, S., Theos, A. C., De Mazière, A. M., Klumperman, J., van Meer, G. and Sprong, H.** (2008). Glycolipid-dependent sorting of melanosomal from lysosomal membrane proteins by luminal determinants. *Traffic* **9**, 951–63.
- Gruenberg, J. and Maxfield, F. R.** (1995). Membrane transport in the endocytic pathway. *Curr. Opin. Cell Biol.* **7**, 552–63.
- Gruenberg, J. and Stenmark, H.** (2004). The biogenesis of multivesicular endosomes. *Nat. Rev. Mol. Cell Biol.* **5**, 317–23.
- Guiducci, C., Ott, G., Chan, J. H., Damon, E., Calacsan, C., Matray, T., Lee, K.-D., Coffman, R. L. and Barrat, F. J.** (2006). Properties regulating the nature of the plasmacytoid dendritic cell response to Toll-like receptor 9 activation. *J. Exp. Med.* **203**, 1999–2008.
- Haass, C.** (2004). Take five--BACE and the gamma-secretase quartet conduct Alzheimer's amyloid beta-peptide generation. *EMBO J.* **23**, 483–8.
- Haass, C., Kaether, C., Thinakaran, G. and Sisodia, S.** (2012). Trafficking and proteolytic processing of APP. *Cold Spring Harb. Perspect. Med.* **2**, a006270.
- Hanahan, D. J. and Chaikoff, I. L.** (1947). A new phospholipide-splitting enzyme specific for the ester linkage between the nitrogenous base and the phosphoric acid grouping. *J. Biol. Chem.* **169**, 699–705.
- Hånell, A. and Marklund, N.** (2014). Structured evaluation of rodent behavioral tests used in drug discovery research. *Front. Behav. Neurosci.* **8**, 252.
- Hanson, P. I., Roth, R., Lin, Y. and Heuser, J. E.** (2008). Plasma membrane deformation by circular arrays of ESCRT-III protein filaments. *J. Cell Biol.* **180**, 389–402.
- Harter, C. and Mellman, I.** (1992). Transport of the lysosomal membrane glycoprotein lgp120 (lgp-A) to lysosomes does not require appearance on the plasma membrane. *J. Cell Biol.* **117**, 311–25.
- Hasilik, A., Waheed, A. and von Figura, K.** (1981). Enzymatic phosphorylation of lysosomal enzymes in the presence of UDP-N-acetylglucosamine. Absence of the activity in I-cell fibroblasts. *Biochem. Biophys. Res. Commun.* **98**, 761–7.

- Hawrylycz, M. J., Lein, E. S., Guillozet-Bongaarts, A. L., Shen, E. H., Ng, L., Miller, J. A., van de Lagemaat, L. N., Smith, K. A., Ebbert, A., Riley, Z. L., et al.** (2012). An anatomically comprehensive atlas of the adult human brain transcriptome. *Nature* **489**, 391–399.
- Heilmann, S., Drichel, D., Clarimon, J., Fernández, V., Lacour, A., Wagner, H., Thelen, M., Hernández, I., Fortea, J., Alegret, M., et al.** (2015). PLD3 in non-familial Alzheimer's disease. *Nature* **520**, E3–E5.
- Helenius, A. and Aebi, M.** (2001). Intracellular functions of N-linked glycans. *Science* **291**, 2364–9.
- Heller, M.** (1978). Phospholipase D. *Adv. Lipid Res.* **16**, 267–326.
- Hemmi, H., Takeuchi, O., Kawai, T., Kaisho, T., Sato, S., Sanjo, H., Matsumoto, M., Hoshino, K., Wagner, H., Takeda, K., et al.** (2000). A Toll-like receptor recognizes bacterial DNA. *Nature* **408**, 740–745.
- Henne, W. M., Buchkovich, N. J. and Emr, S. D.** (2011). The ESCRT Pathway. *Dev. Cell* **21**, 77–91.
- Herber, J., Njavro, J., Feederle, R., Schepers, U., Müller, U. C., Bräse, S., Müller, S. A. and Lichtenthaler, S. F.** (2018). Click Chemistry-mediated Biotinylation Reveals a Function for the Protease BACE1 in Modulating the Neuronal Surface Glycoproteome. *Mol. Cell. Proteomics* **17**, 1487–1501.
- Herman, P. K., Stack, J. H. and Emr, S. D.** (1991). A genetic and structural analysis of the yeast Vps15 protein kinase: evidence for a direct role of Vps15p in vacuolar protein delivery. *EMBO J.* **10**, 4049–60.
- Hiller, G., Eibl, H. and Weber, K.** (1981). Characterization of intracellular and extracellular vaccinia virus variants: N1-isonicotinoyl-N2-3-methyl-4-chlorobenzoylhydrazine interferes with cytoplasmic virus dissemination and release. *J. Virol.* **39**, 903–13.
- Hilmoe, R. J.** (1960). Purification and properties of spleen phosphodiesterase. *J. Biol. Chem.* **235**, 2117–21.
- Hjerpe, R., Aillet, F., Lopitz-Otsoa, F., Lang, V., England, P. and Rodriguez, M. S.** (2009). Efficient protection and isolation of ubiquitylated proteins using tandem ubiquitin-binding entities. *EMBO Rep.* **10**, 1250–8.
- Holý, A.** (1974). Substrate specificity of spleen acid exonuclease and spleen cyclic phosphodiesterase. *Collect. Czechoslov. Chem. Commun.* **39**, 310–332.



- Honing, S., Sandoval, I. V and von Figura, K.** (1998). A di-leucine-based motif in the cytoplasmic tail of LIMP-II and tyrosinase mediates selective binding of AP-3. *EMBO J.* **17**, 1304–1314.
- Hooli, B. V., Lill, C. M., Mullin, K., Qiao, D., Lange, C., Bertram, L. and Tanzi, R. E.** (2015). PLD3 gene variants and Alzheimer’s disease. *Nature* **520**, E7–E8.
- Hopperton, K. E., Mohammad, D., Trépanier, M. O., Giuliano, V. and Bazinet, R. P.** (2018). Markers of microglia in post-mortem brain samples from patients with Alzheimer’s disease: a systematic review. *Mol. Psychiatry* **23**, 177–198.
- Hsu, P. D. and Zhang, F.** (2012). Dissecting Neural Function Using Targeted Genome Engineering Technologies. *ACS Chem. Neurosci.* **3**, 603–610.
- Huang, F., Kirkpatrick, D., Jiang, X., Gygi, S. and Sorkin, A.** (2006). Differential Regulation of EGF Receptor Internalization and Degradation by Multiubiquitination within the Kinase Domain. *Mol. Cell* **21**, 737–748.
- Huang, H., Gao, Q., Peng, X., Choi, S.-Y., Sarma, K., Ren, H., Morris, A. J. and Frohman, M. A.** (2011). piRNA-associated germline nuage formation and spermatogenesis require MitoPLD profusogenic mitochondrial-surface lipid signaling. *Dev. Cell* **20**, 376–87.
- Hughes, W. E. and Parker, P. J.** (2001). Endosomal localization of phospholipase D 1a and 1b is defined by the C-termini of the proteins, and is independent of activity. *Biochem. J.* **356**, 727–36.
- Huotari, J. and Helenius, A.** (2011). Endosome maturation. *EMBO J.* **30**, 3481–3500.
- Hurley, J. H.** (2008). ESCRT complexes and the biogenesis of multivesicular bodies. *Curr. Opin. Cell Biol.* **20**, 4–11.
- Ipsaro, J. J., Haase, A. D., Knott, S. R., Joshua-Tor, L. and Hannon, G. J.** (2012). The structural biochemistry of Zucchini implicates it as a nuclease in piRNA biogenesis. *Nature* **491**, 279–282.
- Ishidoh, K. and Kominami, E.** (2002). Processing and activation of lysosomal proteinases. *Biol. Chem.* **383**, 1827–31.
- Ivanov, A., Pawlikowski, J., Manoharan, I., van Tuyn, J., Nelson, D. M., Rai, T. S., Shah, P. P., Hewitt, G., Korolchuk, V. I., Passos, J. F., et al.** (2013). Lysosome-mediated processing of chromatin in senescence. *J. Cell Biol.* **202**, 129–43.

- Jang, J.-H., Lee, C. S., Hwang, D. and Ryu, S. H.** (2012). Understanding of the roles of phospholipase D and phosphatidic acid through their binding partners. *Prog. Lipid Res.* **51**, 71–81.
- Janvier, K. and Bonifacino, J. S.** (2005). Role of the Endocytic Machinery in the Sorting of Lysosome-associated Membrane Proteins. *Mol. Biol. Cell* **16**, 4231–4242.
- Jenkins, G. M. and Frohman, M. A.** (2005). Phospholipase D: A lipid centric review. *Cell. Mol. Life Sci.* **62**, 2305–2316.
- Johansen, T. and Lamark, T.** (2011). Selective autophagy mediated by autophagic adapter proteins. *Autophagy* **7**, 279–96.
- Kandel, E., James, S., Thomas, J., Steven, S. & A, H.** (2012). *Principles of Neural Science*.
- Katzmann, D. J., Babst, M. and Emr, S. D.** (2001a). Ubiquitin-dependent sorting into the multivesicular body pathway requires the function of a conserved endosomal protein sorting complex, ESCRT-I. *Cell* **106**, 145–55.
- Katzmann, D. J., Babst, M. and Emr, S. D.** (2001b). Ubiquitin-Dependent Sorting into the Multivesicular Body Pathway Requires the Function of a Conserved Endosomal Protein Sorting Complex, ESCRT-I. *Cell* **106**, 145–155.
- Kayed, R., Head, E., Thompson, J. L., McIntire, T. M., Milton, S. C., Cotman, C. W. and Glabe, C. G.** (2003). Common structure of soluble amyloid oligomers implies common mechanism of pathogenesis. *Science* **300**, 486–9.
- Kee, N., Sivalingam, S., Boonstra, R. and Wojtowicz, J. M.** (2002). The utility of Ki-67 and BrdU as proliferative markers of adult neurogenesis. *J. Neurosci. Methods* **115**, 97–105.
- Klockgether, T.** (2011). Update on degenerative ataxias. *Curr. Opin. Neurol.* **24**, 339–45.
- Kong, W., Mou, X., Liu, Q., Chen, Z., Vanderburg, C. R., Rogers, J. T. and Huang, X.** (2009). Independent component analysis of Alzheimer's DNA microarray gene expression data. *Mol. Neurodegener.* **4**, 5.
- Kono, H. and Rock, K. L.** (2008). How dying cells alert the immune system to danger. *Nat. Rev. Immunol.* **8**, 279–89.
- Koonin, E. V** (1996). A duplicated catalytic motif in a new superfamily of phosphohydrolases and phospholipid synthases that includes poxvirus envelope proteins. *Trends Biochem. Sci.* **21**, 242–3.
- Körner, C., Herzog, A., Weber, B., Rosorius, O., Hemer, F., Schmidt, B. and Braulke, T.** (1994). In vitro phosphorylation of the 46-kDa mannose 6-phosphate receptor by

- casein kinase II. Structural requirements for efficient phosphorylation. *J. Biol. Chem.* **269**, 16529–32.
- Kornfeld, S. and Mellman, I.** (1989). The Biogenesis of Lysosomes. *Annu. Rev. Cell Biol.* **5**, 483–525.
- Kornfeld, R., Bao, M., Brewer, K., Noll, C. and Canfield, W.** (1999). Molecular cloning and functional expression of two splice forms of human N-acetylglucosamine-1-phosphodiester alpha-N-acetylglucosaminidase. *J. Biol. Chem.* **274**, 32778–85.
- Kraft, C., Deplazes, A., Sohrmann, M. and Peter, M.** (2008). Mature ribosomes are selectively degraded upon starvation by an autophagy pathway requiring the Ubp3p/Bre5p ubiquitin protease. *Nat. Cell Biol.* **10**, 602–10.
- Krieg, A. M.** (2002). CpG Motifs in Bacterial DNA and Their Immune Effects. *Annu. Rev. Immunol.* **20**, 709–760.
- Krysko, D. V., Agostinis, P., Krysko, O., Garg, A. D., Bachert, C., Lambrecht, B. N. and Vandenabeele, P.** (2011). Emerging role of damage-associated molecular patterns derived from mitochondria in inflammation. *Trends Immunol.* **32**, 157–164.
- Kuhn, P. H., Colombo, A. V., Schusser, B., Dreymueller, D., Wetzels, S., Schepers, U., Herber, J., Ludwig, A., Kremmer, E., Montag, D., et al.** (2016). Systematic substrate identification indicates a central role for the metalloprotease ADAM10 in axon targeting and synapse function. *Elife* **5**, 1–29.
- Lalonde, R., Bensoula, A. N. and Filali, M.** (1995). Rotorod sensorimotor learning in cerebellar mutant mice. *Neurosci. Res.* **22**, 423–426.
- Lambert, J.-C., Grenier-Boley, B., Bellenguez, C., Pasquier, F., Campion, D., Dartigues, J.-F., Berr, C., Tzourio, C. and Amouyel, P.** (2015). PLD3 and sporadic Alzheimer's disease risk. *Nature* **520**, E1–E1.
- Lata, S., Schoehn, G., Jain, A., Pires, R., Piehler, J., Gottlinger, H. G. and Weissenhorn, W.** (2008). Helical structures of ESCRT-III are disassembled by VPS4. *Science* **321**, 1354–7.
- Lazzarino, D. A. and Gabel, C. A.** (1989). Mannose processing is an important determinant in the assembly of phosphorylated high mannose-type oligosaccharides. *J. Biol. Chem.* **264**, 5015–23.
- Lee, Y. B., Nagai, A. and Kim, S. U.** (2002). Cytokines, chemokines, and cytokine receptors in human microglia. *J. Neurosci. Res.* **69**, 94–103.

- Lee, K. A., Hammerle, L. P., Andrews, P. S., Stokes, M. P., Mustelin, T., Silva, J. C., Black, R. A. and Doedens, J. R.** (2011). Ubiquitin ligase substrate identification through quantitative proteomics at both the protein and peptide levels. *J. Biol. Chem.* **286**, 41530–41538.
- Lein, E. S., Hawrylycz, M. J., Ao, N., Ayres, M., Bensinger, A., Bernard, A., Boe, A. F., Boguski, M. S., Brockway, K. S., Byrnes, E. J., et al.** (2007). Genome-wide atlas of gene expression in the adult mouse brain. *Nature* **445**, 168–176.
- Lippincott-Schwartz, J. and Fambrough, D. M.** (1987). Cycling of the integral membrane glycoprotein, LEP100, between plasma membrane and lysosomes: kinetic and morphological analysis. *Cell* **49**, 669–77.
- Liscovitch, M., Czarny, M., Fiucci, G. and Tang, X.** (2000). Phospholipase D: molecular and cell biology of a novel gene family. *Biochem. J.* **345 Pt 3**, 401–15.
- Liu, B., Zheng, Y., Wang, T.-D., Xu, H.-Z., Xia, L., Zhang, J., Wu, Y.-L., Chen, G.-Q. and Wang, L.-S.** (2012). Proteomic identification of common SCF ubiquitin ligase FBXO6-interacting glycoproteins in three kinds of cells. *J. Proteome Res.* **11**, 1773–81.
- Loschen, G., Flohé, L. and Chance, B.** (1971). Respiratory chain linked H<sub>2</sub>O<sub>2</sub> production in pigeon heart mitochondria. *FEBS Lett.* **18**, 261–264.
- Lübke, T., Lobel, P. and Sleat, D. E.** (2009). Proteomics of the lysosome. *Biochim. Biophys. Acta - Mol. Cell Res.* **1793**, 625–635.
- Luzio, J. P., Pryor, P. R. and Bright, N. A.** (2007). Lysosomes: fusion and function. *Nat. Rev. Mol. Cell Biol.* **8**, 622–32.
- Mageswaran, S. K., Dixon, M. G., Curtiss, M., Keener, J. P. and Babst, M.** (2014). Binding to any ESCRT can mediate ubiquitin-independent cargo sorting. *Traffic* **15**, 212–29.
- Marks, M. S., Ohno, H., Kirchner, T. and Bonracino, J. S.** (1997). Protein sorting by tyrosine-based signals: adapting to the Ys and wherefores. *Trends Cell Biol.* **7**, 124–128.
- Marsh, M., Schmid, S., Kern, H., Harms, E., Male, P., Mellman, I. and Helenius, A.** (1987). Rapid analytical and preparative isolation of functional endosomes by free flow electrophoresis. *J. Cell Biol.* **104**, 875–86.
- Masters, C. L., Simms, G., Weinman, N. A., Multhaup, G., McDonald, B. L. and Beyreuther, K.** (1985). Amyloid plaque core protein in Alzheimer disease and Down syndrome. *Proc. Natl. Acad. Sci. U. S. A.* **82**, 4245–9.

- Matsuda, T., Murao, N., Katano, Y., Juliandi, B., Kohyama, J., Akira, S., Kawai, T. and Nakashima, K.** (2015). TLR9 signalling in microglia attenuates seizure-induced aberrant neurogenesis in the adult hippocampus. *Nat. Commun.* **6**, 1–10.
- Matyash, V., Liebisch, G., Kurzchalia, T. V., Shevchenko, A. and Schwudke, D.** (2008). Lipid extraction by methyl- *tert* -butyl ether for high-throughput lipidomics. *J. Lipid Res.* **49**, 1137–1146.
- McCarthy, C. G., Goulopoulou, S., Wenceslau, C. F., Spitler, K., Matsumoto, T. and Webb, R. C.** (2014). Toll-like receptors and damage-associated molecular patterns: novel links between inflammation and hypertension. *Am. J. Physiol. Circ. Physiol.* **306**, H184–H196.
- McDowell, G. S. and Philpott, A.** (2013). Non-canonical ubiquitylation: Mechanisms and consequences. *Int. J. Biochem. Cell Biol.* **45**, 1833–1842.
- Melling, T. and Westermayer, K.** (2011). Optimization of Procedures for Establishing Mouse Primary Cortical Cultures and siRNA Knockdowns for Studying Huntington's Disease Proteins.
- Misumi, Y., Misumi, Y., Miki, K., Takatsuki, A., Tamura, G. and Ikehara, Y.** (1986). Novel blockade by brefeldin A of intracellular transport of secretory proteins in cultured rat hepatocytes. *J. Biol. Chem.* **261**, 11398–11403.
- Mizushima, N.** (2007). Autophagy: process and function. *Genes Dev.* **21**, 2861–2873.
- Mizushima, N. and Komatsu, M.** (2011). Autophagy: Renovation of Cells and Tissues. *Cell* **147**, 728–741.
- Möhlmann, T., Bernard, C., Hach, S. and Ekkehard Neuhaus, H.** (2010). Nucleoside transport and associated metabolism\*. *Plant Biol.* **12**, 26–34.
- Morel, E., Chamoun, Z., Lasiecka, Z. M., Chan, R. B., Williamson, R. L., Vetanovetz, C., Dall'Armi, C., Simoes, S., Point Du Jour, K. S., McCabe, B. D., et al.** (2013). Phosphatidylinositol-3-phosphate regulates sorting and processing of amyloid precursor protein through the endosomal system. *Nat. Commun.* **4**, 2250.
- Motabar, O., Goldin, E., Leister, W., Liu, K., Southall, N., Huang, W., Marugan, J. J., Sidransky, E. and Zheng, W.** (2012). A high throughput glucocerebrosidase assay using the natural substrate glucosylceramide. *Anal. Bioanal. Chem.* **402**, 731–9.
- Müller, U. C. and Zheng, H.** (2012). Physiological functions of APP family proteins. *Cold Spring Harb. Perspect. Med.* **2**, a006288.

- Müller, S., Dennemärker, J. and Reinheckel, T.** (2012). Specific functions of lysosomal proteases in endocytic and autophagic pathways. *Biochim. Biophys. Acta - Proteins Proteomics* **1824**, 34–43.
- Munck, A., Böhm, C., Seibel, N. M., Hashemol Hosseini, Z. and Hampe, W.** (2005). HUK4 is a ubiquitously expressed type 2 transmembrane protein associated with the endoplasmic reticulum. *FEBS J.* **272**, 1718–1726.
- Nelson, R. K. and Frohman, M. A.** (2015). Physiological and pathophysiological roles for phospholipase D. *J. Lipid Res.* **56**, 2229–2237.
- Nibbeling, E. A. R., Duarri, A., Verschuuren-Bemelmans, C. C., Fokkens, M. R., Karjalainen, J. M., Smeets, C. J. L. M., de Boer-Bergsma, J. J., van der Vries, G., Dooijes, D., Bampi, G. B., et al.** (2017). Exome sequencing and network analysis identifies shared mechanisms underlying spinocerebellar ataxia. *Brain* **140**, 2860–2878.
- Nickerson, D. P., West, M., Henry, R. and Odorizzi, G.** (2010). Regulators of Vps4 ATPase Activity at Endosomes Differentially Influence the Size and Rate of Formation of Intraluminal Vesicles. *Mol. Biol. Cell* **21**, 1023–1032.
- Nikolaev, A., McLaughlin, T., O’Leary, D. D. M. and Tessier-Lavigne, M.** (2009). APP binds DR6 to trigger axon pruning and neuron death via distinct caspases. *Nature* **457**, 981–9.
- Nishimasu, H., Ishizu, H., Saito, K., Fukuhara, S., Kamatani, M. K., Bonnefond, L., Matsumoto, N., Nishizawa, T., Nakanaga, K., Aoki, J., et al.** (2012). Structure and function of Zucchini endoribonuclease in piRNA biogenesis. *Nature* **491**, 284–287.
- Novick, P., Ferro, S. and Schekman, R.** (1981). Order of events in the yeast secretory pathway. *Cell* **25**, 461–9.
- Nunez, J.** (2008). Morris Water Maze Experiment. *J. Vis. Exp.*
- O’Neill, R. A.** (1996). Enzymatic release of oligosaccharides from glycoproteins for chromatographic and electrophoretic analysis. *J. Chromatogr. A* **720**, 201–215.
- Oakley, H., Cole, S. L., Logan, S., Maus, E., Shao, P., Craft, J., Guillozet-Bongaarts, A., Ohno, M., Disterhoft, J., Van Eldik, L., et al.** (2006). Intraneuronal beta-Amyloid Aggregates, Neurodegeneration, and Neuron Loss in Transgenic Mice with Five Familial Alzheimer’s Disease Mutations: Potential Factors in Amyloid Plaque Formation. *J. Neurosci.* **26**, 10129–10140.
- Obermüller, S., Kiecke, C., von Figura, K. and Höning, S.** (2002). The tyrosine motifs of

- Lamp 1 and LAP determine their direct and indirect targeting to lysosomes. *J. Cell Sci.* **115**, 185–94.
- Odorizzi, G., Babst, M. and Emr, S. D.** (1998). Fab1p PtdIns(3)P 5-kinase function essential for protein sorting in the multivesicular body. *Cell* **95**, 847–58.
- Oka, T., Hikoso, S., Yamaguchi, O., Taneike, M., Takeda, T., Tamai, T., Oyabu, J., Murakawa, T., Nakayama, H., Nishida, K., et al.** (2012). Mitochondrial DNA that escapes from autophagy causes inflammation and heart failure. *Nature* **485**, 251–5.
- Orriss, I. R., Arnett, T. R. and Russell, R. G. G.** (2016). Pyrophosphate: a key inhibitor of mineralisation. *Curr. Opin. Pharmacol.* **28**, 57–68.
- Osisami, M., Ali, W. and Frohman, M. A.** (2012). A role for phospholipase D3 in myotube formation. *PLoS One* **7**,.
- Otani, Y., Yamaguchi, Y., Sato, Y., Furuichi, T., Ikenaka, K., Kitani, H. and Baba, H.** (2011). PLD4 is involved in phagocytosis of microglia: Expression and localization changes of PLD4 are correlated with activation state of microglia. *PLoS One* **6**,.
- Oude Weernink, P. A., Han, L., Jakobs, K. H. and Schmidt, M.** (2007). Dynamic phospholipid signaling by G protein-coupled receptors. *Biochim. Biophys. Acta - Biomembr.* **1768**, 888–900.
- Pak, Y., Glowacka, W. K., Bruce, M. C., Pham, N. and Rotin, D.** (2006). Transport of LAPT5 to lysosomes requires association with the ubiquitin ligase Nedd4, but not LAPT5 ubiquitination. *J. Cell Biol.* **175**, 631–45.
- Palmieri, M., Impey, S., Kang, H., di Ronza, A., Pelz, C., Sardiello, M. and Ballabio, A.** (2011a). Characterization of the CLEAR network reveals an integrated control of cellular clearance pathways. *Hum. Mol. Genet.* **20**, 3852–3866.
- Palmieri, M., Impey, S., Kang, H., di Ronza, A., Pelz, C., Sardiello, M. and Ballabio, A.** (2011b). Characterization of the CLEAR network reveals an integrated control of cellular clearance pathways. *Hum. Mol. Genet.* **20**, 3852–66.
- Patki, V., Lawe, D. C., Corvera, S., Virbasius, J. V and Chawla, A.** (1998). A functional PtdIns(3)P-binding motif. *Nature* **394**, 433–4.
- Peden, A. A., Oorschot, V., Hesser, B. A., Austin, C. D., Scheller, R. H. and Klumperman, J.** (2004). Localization of the AP-3 adaptor complex defines a novel endosomal exit site for lysosomal membrane proteins. *J. Cell Biol.* **164**, 1065–76.
- Pedersen, K. M., Finsen, B., Celis, J. E. and Jensen, N. A.** (1998). Expression of a novel

- murine phospholipase D homolog coincides with late neuronal development in the forebrain. *J. Biol. Chem.* **273**, 31494–31504.
- Peng, X. and Frohman, M. A.** (2012). Mammalian phospholipase D physiological and pathological roles. *Acta Physiol. (Oxf)*. **204**, 219–26.
- Pennock, S. and Wang, Z.** (2008). A Tale of Two Cbls: Interplay of c-Cbl and Cbl-b in Epidermal Growth Factor Receptor Downregulation. *Mol. Cell. Biol.* **28**, 3020–3037.
- Peters, C., Braun, M., Weber, B., Wendland, M., Schmidt, B., Pohlmann, R., Waheed, A. and Figura, K. Von** (1990). Targeting of a lysosomal membrane protein: a tyrosine-containing endocytosis signal in the cytoplasmic tail of lysosomal acid phosphatase is necessary and sufficient for targeting to lysosomes. *EMBO J.* **9**, 3497–3506.
- Piaceri, I., Nacmias, B. and Sorbi, S.** (2013). Genetics of familial and sporadic Alzheimer's disease. *Front. Biosci. (Elite Ed)*. **5**, 167–77.
- Piper, R. C. and Katzmann, D. J.** (2007). Biogenesis and Function of Multivesicular Bodies. *Annu. Rev. Cell Dev. Biol.* **23**, 519–547.
- Platt, F. M., d'Azzo, A., Davidson, B. L., Neufeld, E. F. and Tiffit, C. J.** (2018). Lysosomal storage diseases. *Nat. Rev. Dis. Prim.* **4**, 27.
- Pohlmann, R., Krentler, C., Schmidt, B., Schröder, W., Lorkowski, G., Culley, J., Mersmann, G., Geier, C., Waheed, A. and Gottschalk, S.** (1988). Human lysosomal acid phosphatase: cloning, expression and chromosomal assignment. *EMBO J.* **7**, 2343–50.
- Ponting, C. P. and Kerr, I. D.** (1996). A novel family of phospholipase D homologues that includes phospholipid synthases and putative endonucleases: identification of duplicated repeats and potential active site residues. *Protein Sci.* **5**, 914–22.
- Poole, B. and Ohkuma, S.** (1981). Effect of weak bases on the intralysosomal pH in mouse peritoneal macrophages. *J. Cell Biol.* **90**, 665–9.
- Powis, G., Bonjouklian, R., Berggren, M. M., Gallegos, A., Abraham, R., Ashendel, C., Zalkow, L., Matter, W. F., Dodge, J., Grindey, G., et al.** (1994). Wortmannin, a potent and selective inhibitor of phosphatidylinositol-3-kinase. *Cancer Res.* **54**, 2419–23.
- Pridgeon, J. W., Webber, E. A., Sha, D., Li, L. and Chin, L.-S.** (2009). Proteomic analysis reveals Hrs ubiquitin-interacting motif-mediated ubiquitin signaling in multiple cellular processes. *FEBS J.* **276**, 118–31.



- Raiborg, C. and Stenmark, H.** (2009). The ESCRT machinery in endosomal sorting of ubiquitylated membrane proteins. *Nature* **458**, 445–452.
- Rawlings, N. D., Barrett, A. J. and Bateman, A.** (2010). MEROPS: the peptidase database. *Nucleic Acids Res.* **38**, D227-33.
- Razzell, W. E.** (1961). Tissue and intracellular distribution of two phosphodiesterases. *J. Biol. Chem.* **236**, 3028–30.
- Reczek, D., Schwake, M., Schröder, J., Hughes, H., Blanz, J., Jin, X., Brondyk, W., Van Patten, S., Edmunds, T. and Saftig, P.** (2007). LIMP-2 is a receptor for lysosomal mannose-6-phosphate-independent targeting of beta-glucoocerebrosidase. *Cell* **131**, 770–83.
- Reddy, M. K. and Bauer, W. R.** (1989). Activation of the vaccinia virus nicking-joining enzyme by trypsinization. *J. Biol. Chem.* **264**, 443–9.
- Reemst, K., Noctor, S. C., Lucassen, P. J. and Hol, E. M.** (2016). The Indispensable Roles of Microglia and Astrocytes during Brain Development. *Front. Hum. Neurosci.* **10**, 566.
- Reggiori, F. and Pelham, H. R.** (2001). Sorting of proteins into multivesicular bodies: ubiquitin-dependent and -independent targeting. *EMBO J.* **20**, 5176–86.
- Rehling, P., Darsow, T., Katzmann, D. J. and Emr, S. D.** (1999). Formation of AP-3 transport intermediates requires Vps41 function. *Nat. Cell Biol.* **1**, 346–353.
- Riebeling, C., Morris, A. J. and Shields, D.** (2009). Phospholipase D in the Golgi apparatus. *Biochim. Biophys. Acta* **1791**, 876–80.
- Roberts, R.** (2005). Lysosomal cysteine proteases: structure, function and inhibition of cathepsins. *Drug News Perspect.* **18**, 605–14.
- Rodriguez-Enriquez, S., Kim, I., Currin, R. T. and Lemasters, J. J.** (2006). Tracker dyes to probe mitochondrial autophagy (mitophagy) in rat hepatocytes. *Autophagy* **2**, 39–46.
- Rohrer, J. and Kornfeld, R.** (2001). Lysosomal hydrolase mannose 6-phosphate uncovering enzyme resides in the trans-Golgi network. *Mol. Biol. Cell* **12**, 1623–31.
- Rosorius, O., Issinger, O. G. and Braulke, T.** (1993). Phosphorylation of the cytoplasmic tail of the 300-kDa mannose 6-phosphate receptor is required for the interaction with a cytosolic protein. *J. Biol. Chem.* **268**, 21470–3.
- Roth, M. G.** (2008). Molecular Mechanisms of PLD Function in Membrane Traffic. *Traffic*

- 9, 1233–1239.
- Ruddock, L. W. and Molinari, M.** (2006). N-glycan processing in ER quality control. *J. Cell Sci.* **119**, 4373–80.
- Rudge, S. A. and Wakelam, M. J. O.** (2009). Inter-regulatory dynamics of phospholipase D and the actin cytoskeleton. *Biochim. Biophys. Acta* **1791**, 856–61.
- Rudolph, A. E., Stuckey, J. A., Zhao, Y., Matthews, H. R., Patton, W. A., Moss, J. and Dixon, J. E.** (1999). Expression, characterization, and mutagenesis of the *Yersinia pestis* murine toxin, a phospholipase D superfamily member. *J. Biol. Chem.* **274**, 11824–31.
- S. Kornfeld, W. .** (2001). Sly, I-cell disease and pseudo-Hurler polydystrophy: disorders of lysosomal enzyme phosphorylation and localization. In *The Metabolic and Molecular Bases of Inherited Disease* (ed. C.R. Scriver, A. L.) and Beaudet, W.S. Sly, D. V.), pp. 3421–3452. New York: McGraw-Hill.
- Saftig, P. and Klumperman, J.** (2009). Lysosome biogenesis and lysosomal membrane proteins: Trafficking meets function. *Nat. Rev. Mol. Cell Biol.* **10**, 623–635.
- Saftig, P., Beertsen, W. and Eskelinen, E.-L.** (2008). LAMP-2: a control step for phagosome and autophagosome maturation. *Autophagy* **4**, 510–2.
- Sahu, R., Kaushik, S., Clement, C. C., Cannizzo, E. S., Scharf, B., Follenzi, A., Potalicchio, I., Nieves, E., Cuervo, A. M. and Santambrogio, L.** (2011). Microautophagy of cytosolic proteins by late endosomes. *Dev. Cell* **20**, 131–9.
- Saksena, S., Wahlman, J., Teis, D., Johnson, A. E. and Emr, S. D.** (2009). Functional reconstitution of ESCRT-III assembly and disassembly. *Cell* **136**, 97–109.
- Sapolsky, R. M.** (2004). Is impaired neurogenesis relevant to the affective symptoms of depression? *Biol. Psychiatry* **56**, 137–9.
- Satoh, J. I., Kino, Y., Yamamoto, Y., Kawana, N., Ishida, T., Saito, Y. and Arima, K.** (2014). PLD3 is accumulated on neuritic plaques in Alzheimer's disease brains. *Alzheimer's Res. Ther.* **6**, 1–13.
- Schaum, N., Karkanias, J., Neff, N. F., May, A. P., Quake, S. R., Wyss-Coray, T., Darmanis, S., Batson, J., Botvinnik, O., Chen, M. B., et al.** (2018). Single-cell transcriptomics of 20 mouse organs creates a Tabula Muris. *Nature* **562**, 367–372.
- Schmidt, O. and Teis, D.** (2012). The ESCRT machinery. *Curr. Biol.* **22**, R116–20.
- Schöls, L., Bauer, P., Schmidt, T. and Schulte, T.** (2004). Autosomal dominant cerebellar ataxias: clinical features, genetics, and pathogenesis. *Lancet Neurol.* **3**,

- Schröder, B., Wrocklage, C., Pan, C., Jäger, R., Kösters, B., Schäfer, H., Elsässer, H.-P., Mann, M. and Hasilik, A.** (2007). Integral and Associated Lysosomal Membrane Proteins. *Traffic* **8**, 1676–1686.
- Schröder, J., Lüllmann-Rauch, R., Himmerkus, N., Pleines, I., Nieswandt, B., Orinska, Z., Koch-Nolte, F., Schröder, B., Bleich, M. and Saftig, P.** (2009). Deficiency of the tetraspanin CD63 associated with kidney pathology but normal lysosomal function. *Mol. Cell. Biol.* **29**, 1083–94.
- Schwake, M., Schröder, B. and Saftig, P.** (2013). Lysosomal Membrane Proteins and Their Central Role in Physiology. *Traffic* **14**, 739–748.
- Selvy, P. E., Lavieri, R. R., Brown, Lindsley, C. W. and Alex, H. B.** (2011). Phospholipase D - enzymology, functionality, and chemical modulation. *Chem. Rev.* **111**, 6064–6119.
- Seubert, P., Vigo-Pelfrey, C., Esch, F., Lee, M., Dovey, H., Davis, D., Sinha, S., Schlossmacher, M., Whaley, J., Swindlehurst, C., et al.** (1992). Isolation and quantification of soluble Alzheimer's beta-peptide from biological fluids. *Nature* **359**, 325–7.
- Shen, D., Wang, X., Li, X., Zhang, X., Yao, Z., Dibble, S., Dong, X., Yu, T., Lieberman, A. P., Showalter, H. D., et al.** (2012). Lipid storage disorders block lysosomal trafficking by inhibiting a TRP channel and lysosomal calcium release. *Nat. Commun.* **3**, 731.
- Shi, Y., Chan, D. W., Jung, S. Y., Malovannaya, A., Wang, Y. and Qin, J.** (2011). A Data Set of Human Endogenous Protein Ubiquitination Sites. *Mol. Cell. Proteomics* **10**, M110.002089.
- Sierra, A., Encinas, J. M., Deudero, J. J. P., Chancey, J. H., Enikolopov, G., Overstreet-Wadiche, L. S., Tsirka, S. E. and Maletic-Savatic, M.** (2010). Microglia shape adult hippocampal neurogenesis through apoptosis-coupled phagocytosis. *Cell Stem Cell* **7**, 483–95.
- Skarnes, W. C., Rosen, B., West, A. P., Koutsourakis, M., Bushell, W., Iyer, V., Mujica, A. O., Thomas, M., Harrow, J., Cox, T., et al.** (2011). A conditional knockout resource for the genome-wide study of mouse gene function. *Nature* **474**, 337–342.
- Slaugenhaupt, S. A.** (2002). The molecular basis of mucopolipidosis type IV. *Curr. Mol. Med.* **2**, 445–50.
- Sleat, D. E., Zheng, H., Qian, M. and Lobel, P.** (2006). Identification of sites of mannose

- 6-phosphorylation on lysosomal proteins. *Mol. Cell. Proteomics* **5**, 686–701.
- Sleat, D. E., Valle, M. C. D., Zheng, H., Moore, D. F. and Lobel, P.** (2008). The mannose 6-phosphate glycoprotein proteome. *J. Proteome Res.* **7**, 3010–3021.
- Sleat, D. E., Sun, P., Wiseman, J. A., Huang, L., El-Banna, M., Zheng, H., Moore, D. F. and Lobel, P.** (2013). Extending the Mannose 6-Phosphate Glycoproteome by High Resolution/Accuracy Mass Spectrometry Analysis of Control and Acid Phosphatase 5-Deficient Mice. *Mol. Cell. Proteomics* **12**, 1806–1817.
- Slot, J. W. and Geuze, H. J.** (2007). Cryosectioning and immunolabeling. *Nat. Protoc.* **2**, 2480–2491.
- Spormann, D. O., Heim, J. and Wolf, D. H.** (1992). Biogenesis of the yeast vacuole (lysosome). The precursor forms of the soluble hydrolase carboxypeptidase yscS are associated with the vacuolar membrane. *J. Biol. Chem.* **267**, 8021–9.
- Stahl, S., Reinders, Y., Asan, E., Mothes, W., Conzelmann, E., Sickmann, A. and Felbor, U.** (2007). Proteomic analysis of cathepsin B- and L-deficient mouse brain lysosomes. *Biochim. Biophys. Acta* **1774**, 1237–46.
- Stanacev, N. Z. and Stuhne-Sekalec, L.** (1970). On the mechanism of enzymatic phosphatidylation. Biosynthesis of cardiolipin catalyzed by phospholipase D. *Biochim. Biophys. Acta* **210**, 350–2.
- Stauber, T. and Jentsch, T. J.** (2013). Chloride in vesicular trafficking and function. *Annu. Rev. Physiol.* **75**, 453–77.
- Stenmark, H., Parton, R. G., Steele-Mortimer, O., Lütcke, A., Gruenberg, J. and Zerial, M.** (1994). Inhibition of rab5 GTPase activity stimulates membrane fusion in endocytosis. *EMBO J.* **13**, 1287–96.
- Stepp, J. D., Huang, K. and Lemmon, S. K.** (1997). The yeast adaptor protein complex, AP-3, is essential for the efficient delivery of alkaline phosphatase by the alternate pathway to the vacuole. *J. Cell Biol.* **139**, 1761–74.
- Stuchell-Brereton, M. D., Skalicky, J. J., Kieffer, C., Karren, M. A., Ghaffarian, S. and Sundquist, W. I.** (2007). ESCRT-III recognition by VPS4 ATPases. *Nature* **449**, 740–744.
- Stuckey, J. A. and Dixon, J. E.** (1999). Crystal structure of a phospholipase D family member. *Nat. Struct. Biol.* **6**, 278–84.
- Sung, T. C., Roper, R. L., Zhang, Y., Rudge, S. A., Temel, R., Hammond, S. M., Morris, A.**

- J., Moss, B., Engebrecht, J. and Frohman, M. A.** (1997). Mutagenesis of phospholipase D defines a superfamily including a trans-Golgi viral protein required for poxvirus pathogenicity. *EMBO J.* **16**, 4519–30.
- Takahashi, R. H., Milner, T. A., Li, F., Nam, E. E., Edgar, M. A., Yamaguchi, H., Beal, M. F., Xu, H., Greengard, P. and Gouras, G. K.** (2002). Intraneuronal Alzheimer abeta42 accumulates in multivesicular bodies and is associated with synaptic pathology. *Am. J. Pathol.* **161**, 1869–79.
- Takahashi, R. H., Almeida, C. G., Kearney, P. F., Yu, F., Lin, M. T., Milner, T. A. and Gouras, G. K.** (2004). Oligomerization of Alzheimer's -Amyloid within Processes and Synapses of Cultured Neurons and Brain. *J. Neurosci.* **24**, 3592–3599.
- Tamai, M., Hanada, K., Adachi, T., Oguma, K., Kashiwagi, K., Omura, S. and Ohzeki, M.** (1981). Papain inhibitions by optically active E-64 analogs. *J. Biochem.* **90**, 255–7.
- Tartakoff, A., Vassalli, P. and Détraz, M.** (1978). Comparative studies of intracellular transport of secretory proteins. *J. Cell Biol.* **79**, 694–707.
- Terao, C., Ohmura, K., Kawaguchi, Y., Nishimoto, T., Kawasaki, A., Takehara, K., Furukawa, H., Kochi, Y., Ota, Y., Ikari, K., et al.** (2013). PLD4 as a novel susceptibility gene for systemic sclerosis in a Japanese population. *Arthritis Rheum.* **65**, 472–80.
- Theos, A. C., Truschel, S. T., Tenza, D., Hurbain, I., Harper, D. C., Berson, J. F., Thomas, P. C., Raposo, G. and Marks, M. S.** (2006). A lumenal domain-dependent pathway for sorting to intraluminal vesicles of multivesicular endosomes involved in organelle morphogenesis. *Dev. Cell* **10**, 343–354.
- Tokhtaeva, E., Mareninova, O. A., Gukovskaya, A. S. and Vagin, O.** (2017). Analysis of N- and O-Glycosylation of Lysosomal Glycoproteins. pp. 35–42. Humana Press, New York, NY.
- Tomczak, K. K., Marinescu, V. D., Ramoni, M. F., Sanoudou, D., Montanaro, F., Han, M., Kunkel, L. M., Kohane, I. S. and Beggs, A. H.** (2004). Expression profiling and identification of novel genes involved in myogenic differentiation. *FASEB J.* **18**, 403–5.
- Trajkovic, K., Hsu, C., Chiantia, S., Rajendran, L., Wenzel, D., Wieland, F., Schwille, P., Brügger, B. and Simons, M.** (2007). Ceramide Triggers Budding of Exosome Vesicles into Multivesicular Endosomes. **319**,.
- Turk, V., Stoka, V., Vasiljeva, O., Renko, M., Sun, T., Turk, B. and Turk, D.** (2012).

- Cysteine cathepsins: From structure, function and regulation to new frontiers. *Biochim. Biophys. Acta - Proteins Proteomics* **1824**, 68–88.
- Turner, P. R., O'Connor, K., Tate, W. P. and Abraham, W. C.** (2003). Roles of amyloid precursor protein and its fragments in regulating neural activity, plasticity and memory. *Prog. Neurobiol.* **70**, 1–32.
- Ueno, M., Fujita, Y., Tanaka, T., Nakamura, Y., Kikuta, J., Ishii, M. and Yamashita, T.** (2013). Layer V cortical neurons require microglial support for survival during postnatal development. *Nat. Neurosci.* **16**, 543–51.
- Urbé, S., Sachse, M., Row, P. E., Preisinger, C., Barr, F. A., Strous, G., Klumperman, J. and Clague, M. J.** (2003). The UIM domain of Hrs couples receptor sorting to vesicle formation. *J. Cell Sci.* **116**, 4169–79.
- Urnov, F. D., Rebar, E. J., Holmes, M. C., Zhang, H. S. and Gregory, P. D.** (2010). Genome editing with engineered zinc finger nucleases. *Nat. Rev. Genet.* **11**, 636–46.
- van der Lee, S. J., Holstege, H., Wong, T. H., Jakobsdottir, J., Bis, J. C., Chouraki, V., van Rooij, J. G. J., Grove, M. L., Smith, A. V., Amin, N., et al.** (2015). PLD3 variants in population studies. *Nature* **520**, E2–E3.
- Van Dyck, J. M. and Wattiaux, R.** (1968). [Intracellular distribution of acid exonuclease in rat liver]. *Eur. J. Biochem.* **7**, 13–20.
- van Meel, E. and Klumperman, J.** (2008). Imaging and imagination: understanding the endo-lysosomal system. *Histochem. Cell Biol.* **129**, 253–66.
- van Niel, G., Charrin, S., Simoes, S., Romao, M., Rochin, L., Saftig, P., Marks, M. S., Rubinstein, E. and Raposo, G.** (2011a). The Tetraspanin CD63 Regulates ESCRT-Independent and -Dependent Endosomal Sorting during Melanogenesis. *Dev. Cell* **21**, 708–721.
- Varvel, N. H., Bhaskar, K., Patil, A. R., Pimplikar, S. W., Herrup, K. and Lamb, B. T.** (2008). Abeta oligomers induce neuronal cell cycle events in Alzheimer's disease. *J. Neurosci.* **28**, 10786–93.
- Vingtdeux, V., Sergeant, N. and Buée, L.** (2012). Potential Contribution of Exosomes to the Prion-Like Propagation of Lesions in Alzheimer's Disease. *Front. Physiol.* **3**, 229.
- Voigt, F., Reuter, M., Kasaruho, A., Schulz, E. C., Pillai, R. S. and Barabas, O.** (2012). Crystal structure of the primary piRNA biogenesis factor Zucchini reveals similarity to the bacterial PLD endonuclease Nuc. *RNA* **18**, 2128–34.
- Vollmer, J., Weeratna, R., Payette, P., Jurk, M., Schetter, C., Laucht, M., Wader, T.,**

- Tluk, S., Liu, M., Davis, H. L., et al.** (2004). Characterization of three CpG oligodeoxynucleotide classes with distinct immunostimulatory activities. *Eur. J. Immunol.* **34**, 251–62.
- von Figura, K. and Hasilik, A.** (1986). Lysosomal enzymes and their receptors. *Annu. Rev. Biochem.* **55**, 167–93.
- von Rotz, R. C., Kohli, B. M., Bosset, J., Meier, M., Suzuki, T., Nitsch, R. M. and Konietzko, U.** (2004). The APP intracellular domain forms nuclear multiprotein complexes and regulates the transcription of its own precursor. *J. Cell Sci.* **117**, 4435–48.
- Waheed, A., Pohlmann, R., Hasilik, A., von Figura, K., van Elsen, A. and Leroy, J. G.** (1982). Deficiency of UDP-N-acetylglucosamine:lysosomal enzyme N-acetylglucosamine-1-phosphotransferase in organs of I-cell patients. *Biochem. Biophys. Res. Commun.* **105**, 1052–8.
- Waheed, A., Gottschalk, S., Hille, A., Krentler, C., Pohlmann, R., Braulke, T., Hauser, H., Geuze, H. and von Figura, K.** (1988). Human lysosomal acid phosphatase is transported as a transmembrane protein to lysosomes in transfected baby hamster kidney cells. *EMBO J.* **7**, 2351–8.
- Waldera-Lupa, D. M., Etemad-Parishanzadeh, O., Brocksieper, M., Kirchgassler, N., Seidel, S., Kowalski, T., Montesinos-Rongen, M., Deckert, M., Schlegel, U. and Stühler, K.** (2017). Proteomic changes in cerebrospinal fluid from primary central nervous system lymphoma patients are associated with protein ectodomain shedding. *Oncotarget* **8**, 110118–110132.
- Walker, D. G. and Lue, L.-F.** (2015). Immune phenotypes of microglia in human neurodegenerative disease: challenges to detecting microglial polarization in human brains. *Alzheimers. Res. Ther.* **7**, 56.
- Wang, Y., Norgård, M. and Andersson, G.** (2005). N-glycosylation influences the latency and catalytic properties of mammalian purple acid phosphatase. *Arch. Biochem. Biophys.* **435**, 147–156.
- Warner, J. R.** (1999). The economics of ribosome biosynthesis in yeast. *Trends Biochem. Sci.* **24**, 437–40.
- Wartosch, L., Bright, N. A. and Luzio, J. P.** (2015). Lysosomes. *Curr. Biol.* **25**, R315–R316.

- Wei, Y. D., Lee, S. J., Lee, K. S., Gui, Z. Z., Yoon, H. J., Kim, I., Je, Y. H., Guo, X., Sohn, H. D. and Jin, B. R.** (2005). N-glycosylation is necessary for enzymatic activity of a beetle (*Apriona germari*) cellulase. *Biochem. Biophys. Res. Commun.* **329**, 331–336.
- Weidemann, A., König, G., Bunke, D., Fischer, P., Salbaum, J. M., Masters, C. L. and Beyreuther, K.** (1989). Identification, biogenesis, and localization of precursors of Alzheimer's disease A4 amyloid protein. *Cell* **57**, 115–26.
- Wendeler, M. and Sandhoff, K.** (2009). Hexosaminidase assays. *Glycoconj. J.* **26**, 945–952.
- Williams, R. L. and Urbé, S.** (2007). The emerging shape of the ESCRT machinery. *Nat. Rev. Mol. Cell Biol.* **8**, 355–68.
- Winans, S. C. and Walker, G. C.** (1983). Genetic localization and characterization of a pKM101-coded endonuclease. *J. Bacteriol.* **154**, 1117–25.
- Winchester, B. G.** (2001). Lysosomal membrane proteins. *Eur. J. Paediatr. Neurol.* **5**, 11–19.
- Wollert, T., Yang, D., Ren, X., Lee, H. H., Im, Y. J. and James, H.** (2009a). The ESCRT machinery at a glance. *J. Cell Sci.* **122**, 2163–2166.
- Wollert, T., Wunder, C., Lippincott-Schwartz, J. and Hurley, J. H.** (2009b). Membrane scission by the ESCRT-III complex. *Nature* **458**, 172–7.
- Wyant, G. A., Abu-Remaileh, M., Frenkel, E. M., Laqtom, N. N., Dharamdasani, V., Lewis, C. A., Chan, S. H., Heinze, I., Ori, A. and Sabatini, D. M.** (2018). NUFIP1 is a ribosome receptor for starvation-induced ribophagy. *Science* **360**, 751–758.
- Wyss-Coray, T. and Mucke, L.** (2002). Inflammation in Neurodegenerative Disease—A Double-Edged Sword. *Neuron* **35**, 419–432.
- Xu, H. and Ren, D.** (2015). Lysosomal Physiology. *Annu. Rev. Physiol.* **77**, 57–80.
- Yakes, F. M. and Van Houten, B.** (1997). Mitochondrial DNA damage is more extensive and persists longer than nuclear DNA damage in human cells following oxidative stress. *Proc. Natl. Acad. Sci. U. S. A.* **94**, 514–9.
- Yang, S. F., Freer, S. and Benson, A. A.** (1967). Transphosphatidylolation by phospholipase D. *J. Biol. Chem.* **242**, 477–84.
- Yoshikawa, F., Banno, Y., Otani, Y., Yamaguchi, Y., Nagakura-Takagi, Y., Morita, N., Sato, Y., Saruta, C., Nishibe, H., Sadakata, T., et al.** (2010). Phospholipase D family member 4, a transmembrane glycoprotein with no phospholipase D activity, expression in spleen and early postnatal microglia. *PLoS One* **5**, e13932.



- 
- Zhang, Q., Raoof, M., Chen, Y., Sumi, Y., Sursal, T., Junger, W., Brohi, K., Itagaki, K. and Hauser, C. J.** (2010). Circulating mitochondrial DAMPs cause inflammatory responses to injury. *Nature* **464**, 104–107.
- Zhang, Y., Chen, K., Sloan, S. A., Bennett, M. L., Scholze, A. R., O’Keeffe, S., Phatnani, H. P., Guarnieri, P., Caneda, C., Ruderisch, N., et al.** (2014). An RNA-Sequencing Transcriptome and Splicing Database of Glia, Neurons, and Vascular Cells of the Cerebral Cortex. *J. Neurosci.* **34**, 11929–11947.
- Zhang, S., Wu, M., Peng, C., Zhao, G. and Gu, R.** (2017). GFAP expression in injured astrocytes in rats. *Exp. Ther. Med.* **14**, 1905–1908.
- Zimmerman, U. J. P. and Schlaepfer, W. W.** (1982). Characterization of a brain calcium-activated protease that degrades neurofilament proteins. *Biochemistry* **21**, 3977–3983.





526.3	LPE [22:5]	0.000	0.001	0.004	0.002	0.001	0.004	0.003	0.001	0.839	None
528.3	LPE [22:4]	0.007	0.026	0.040	0.022	0.015	0.053	0.034	0.011	0.733	None
760.5	PS [34:1]	0.008	0.076	0.043	0.024	0.030	0.057	0.042	0.022	0.979	PS [18:1 / 16:0], PS [18:0 / 16:1]
774.5	PS [35:1]	0.000	0.007	0.004	0.001	0.001	0.003	0.003	0.001	0.571	PS [18:1 / 17:0]
784.5	PS [36:3]	0.000	0.005	0.003	0.001	0.002	0.005	0.003	0.001	0.697	PS [18:2 / 18:1], PS [16:0 / 20:3]
786.5	PS [36:2]	0.030	0.348	0.196	0.107	0.143	0.284	0.204	0.103	0.871	PS [18:1 / 18:1], PS [18:2 / 18:0], PS [16:0 / 20:2]
788.5	PS [36:1]	0.103	0.986	0.544	0.309	0.412	0.814	0.585	0.304	0.850	PS [18:0 / 18:1]
806.5	PS [38:6]	0.002	0.023	0.010	0.007	0.007	0.013	0.009	0.008	0.853	PS [16:0 / 22:6]
808.5	PS [38:5]	0.003	0.035	0.020	0.011	0.013	0.027	0.018	0.009	0.996	PS [20:4 / 18:1]
810.5	PS [38:4]	0.022	0.237	0.139	0.076	0.098	0.191	0.135	0.071	0.919	PS [20:4 / 18:0], PS [18:1 / 20:3], PS [22:4 / 16:0]
814.6	PS [38:2]	0.004	0.051	0.028	0.014	0.020	0.043	0.029	0.014	0.857	PS [20:1 / 18:1], PS [18:0 / 20:2]
816.6	PS [38:1]	0.011	0.111	0.057	0.031	0.044	0.094	0.065	0.033	0.801	PS [18:0 / 20:1], PS [18:1 / 20:0]
832.5	PS [40:7]	0.006	0.067	0.038	0.022	0.027	0.053	0.035	0.019	0.978	PS [18:1 / 22:6]
834.5	PS [40:6]	0.272	2.728	1.604	0.940	1.200	2.230	1.567	0.819	0.914	PS [18:0 / 22:6]
838.6	PS [40:4]	0.020	0.206	0.121	0.070	0.088	0.169	0.118	0.062	0.918	PS [22:4 / 18:0], PS [20:4 / 20:0]
842.6	PS [40:2]	0.003	0.036	0.019	0.010	0.014	0.030	0.019	0.010	0.865	PS [18:1 / 22:1], PS [20:1 / 20:1]
844.6	PS [40:1]	0.003	0.030	0.018	0.009	0.016	0.032	0.021	0.011	0.548	PS [18:1 / 22:0], PS [18:0 / 22:1], PS [20:1 / 20:0]
866.6	PS [42:4]	0.000	0.007	0.004	0.002	0.003	0.007	0.004	0.002	0.721	PS [20:4 / 22:0]
719.5	PG [32:1]	0.001	0.008	0.006	0.003	0.004	0.008	0.005	0.004	0.725	PG [16:1 / 16:0]
721.5	PG [32:0]	0.016	0.076	0.050	0.028	0.028	0.069	0.050	0.036	0.839	PG [16:0 / 16:0]
745.5	PG [34:2]	0.004	0.021	0.014	0.008	0.007	0.017	0.012	0.009	0.941	PG [16:1 / 18:1], PG [16:0 / 18:2]
747.5	PG [34:1]	0.088	0.422	0.292	0.165	0.160	0.363	0.272	0.196	0.947	PG [16:0 / 18:1], PG [16:1 / 18:0]
749.5	PG [34:0]	0.005	0.023	0.016	0.009	0.009	0.023	0.016	0.012	0.745	PG [16:0 / 18:0], PG [17:0 / 17:0]
761.5	PG [35:1]	0.001	0.008	0.006	0.002	0.002	0.004	0.004	0.002	0.500	PG [17:0 / 18:1], PG [16:0 / 19:1]
767.5	PG [36:5]	0.001	0.005	0.003	0.002	0.002	0.004	0.003	0.002	0.902	PG [16:1 / 20:4]
769.5	PG [36:4]	0.023	0.103	0.072	0.041	0.039	0.087	0.066	0.047	0.987	PG [16:0 / 20:4], PG [18:2 / 18:2], PG [20:3 / 16:1]
771.5	PG [36:3]	0.003	0.013	0.008	0.004	0.004	0.011	0.007	0.005	0.947	PG [18:1 / 18:2], PG [20:3 / 16:0]
773.5	PG [36:2]	0.023	0.095	0.069	0.037	0.036	0.076	0.061	0.046	0.950	PG [18:1 / 18:1], PG [20:2 / 16:0], PG [18:0 / 18:2], PG [16:1 / 20:1]
775.5	PG [36:1]	0.007	0.037	0.026	0.015	0.014	0.034	0.025	0.018	0.844	PG [18:1 / 18:0], PG [16:0 / 20:1]
783.5	PG [37:4]	0.000	0.003	0.002	0.001	0.001	0.001	0.001	0.001	0.220	PG [17:0 / 20:4]
791.5	PG [38:7]	0.001	0.004	0.003	0.001	0.001	0.003	0.002	0.002	0.881	PG [16:1 / 22:6]
793.5	PG [38:6]	0.007	0.032	0.021	0.012	0.013	0.030	0.021	0.015	0.817	PG [22:6 / 16:0], PG [18:2 / 20:4]
795.5	PG [38:5]	0.012	0.054	0.038	0.022	0.020	0.044	0.035	0.026	0.982	PG [18:1 / 20:4], PG [16:1 / 22:4]
797.5	PG [38:4]	0.037	0.164	0.115	0.066	0.063	0.134	0.101	0.076	0.960	PG [18:0 / 20:4], PG [20:3 / 18:1], PG [16:0 / 22:4]
819.5	PG [40:7]	0.010	0.043	0.029	0.018	0.017	0.036	0.029	0.021	0.921	PG [22:6 / 18:1], PG [20:3 / 20:4], PG [22:5 / 18:2]

	821.5	PG [40:6]	0.005	0.019	0.014	0.008	0.008	0.008	0.017	0.013	0.010	0.845	PG [18:0 / 22:6], PG [22:5 / 18:1], PG [18:2 / 22:4], PG [20:2 / 20:4], PG [20:3 / 20:3]
599.3	LPI [18:0]	0.003	0.016	0.011	0.007	0.008	0.008	0.008	0.016	0.012	0.005	0.804	None
619.3	LPI [20:4]	0.004	0.025	0.025	0.011	0.011	0.010	0.010	0.040	0.021	0.007	0.726	None
698.5	CL [68:5]		0.002	0.001	0.000	0.000	0.000	0.000	0.001	0.000	0.000	0.327	None
699.5	CL [68:4]	0.001	0.009	0.005	0.003	0.003	0.003	0.003	0.007	0.004	0.002	0.833	None
700.5	CL [68:3]	0.000	0.006	0.004	0.002	0.002	0.002	0.002	0.004	0.003	0.001	0.781	None
710.5	CL [70:7]	0.002	0.019	0.012	0.006	0.006	0.005	0.005	0.015	0.009	0.005	0.801	None
711.5	CL [70:6]	0.001	0.011	0.008	0.004	0.004	0.004	0.004	0.009	0.007	0.003	0.924	None
712.5	CL [70:5]	0.002	0.021	0.013	0.007	0.007	0.007	0.007	0.016	0.011	0.005	0.850	None
713.5	CL [70:4]	0.005	0.046	0.029	0.016	0.016	0.014	0.014	0.033	0.023	0.012	0.751	None
714.5	CL [70:3]	0.001	0.009	0.006	0.003	0.003	0.003	0.003	0.007	0.005	0.002	0.744	None
720.5	CL [71:4]		0.002	0.001	0.000	0.000	0.000	0.000	0.001	0.000	0.000	0.137	None
721.5	CL [72:10]	0.001	0.010	0.006	0.003	0.003	0.003	0.003	0.008	0.005	0.002	0.857	None
722.5	CL [72:9]	0.001	0.012	0.008	0.004	0.004	0.004	0.004	0.009	0.006	0.003	0.792	None
723.5	CL [72:8]	0.005	0.035	0.024	0.013	0.013	0.013	0.013	0.029	0.020	0.010	0.903	None
724.5	CL [72:7]	0.008	0.068	0.039	0.025	0.025	0.022	0.022	0.049	0.035	0.018	0.784	None
725.5	CL [72:6]	0.004	0.036	0.020	0.013	0.013	0.014	0.014	0.027	0.019	0.010	0.907	None
726.5	CL [72:5]	0.007	0.057	0.034	0.021	0.021	0.020	0.020	0.040	0.029	0.014	0.757	None
727.5	CL [72:4]	0.009	0.078	0.044	0.025	0.025	0.021	0.021	0.055	0.038	0.020	0.759	None
731.5	CL [73:7]		0.002	0.001	0.001	0.001	0.000	0.000	0.001	0.001	0.006	0.194	None
734.5	CL [74:11]	0.002	0.022	0.014	0.007	0.007	0.007	0.007	0.017	0.012	0.006	0.866	None
735.5	CL [74:10]	0.008	0.054	0.035	0.021	0.021	0.020	0.020	0.043	0.030	0.015	0.837	None
736.5	CL [74:9]	0.009	0.070	0.047	0.026	0.026	0.026	0.026	0.056	0.039	0.020	0.863	None
737.5	CL [74:8]	0.011	0.087	0.052	0.032	0.032	0.032	0.032	0.061	0.046	0.022	0.787	None
738.5	CL [74:7]	0.012	0.106	0.059	0.041	0.041	0.036	0.036	0.075	0.054	0.027	0.772	None
742.5	CL [75:10]		0.001	0.001	0.000	0.000	0.000	0.000	0.001	0.000	0.020	0.240	None
748.5	CL [76:11]	0.009	0.070	0.044	0.027	0.027	0.026	0.026	0.051	0.039	0.020	0.821	None
749.5	CL [76:10]	0.012	0.091	0.053	0.036	0.036	0.031	0.031	0.066	0.051	0.024	0.797	None
750.5	CL [76:9]	0.011	0.091	0.052	0.034	0.034	0.033	0.033	0.070	0.049	0.025	0.892	None
809.5	PI [32:0]	0.001	0.004	0.002	0.001	0.001	0.002	0.002	0.001	0.002	0.002	0.499	PI [16:0 / 16:0]
837.5	PI [34:0]	0.002	0.017	0.008	0.005	0.005	0.005	0.005	0.010	0.007	0.005	0.753	PI [16:0 / 18:0]
857.5	PI [36:4]	0.047	0.329	0.211	0.121	0.121	0.160	0.160	0.286	0.210	0.111	0.847	PI [16:0 / 20:4]
861.5	PI [36:2]	0.002	0.015	0.009	0.005	0.005	0.007	0.007	0.012	0.009	0.004	0.855	PI [18:1 / 18:1], PI [18:0 / 18:2]

863.6	PI [36:1]	0.007	0.043	0.025	0.016	0.021	0.038	0.026	0.015	0.809	PI [18:1 / 18:0], PI [16:0 / 20:1], PI [16:1 / 20:0]
865.6	PI [36:0]	0.002	0.001	0.000	0.000	0.000	0.001	0.000		0.567	PI [18:0 / 18:0]
871.5	PI [37:4]	0.002	0.014	0.010	0.004	0.005	0.008	0.006	0.003	0.490	PI [17:0 / 20:4]
881.5	PI [38:6]	0.012	0.086	0.050	0.027	0.040	0.079	0.051	0.028	0.772	PI [22:6 / 16:0], PI [18:2 / 20:4], PI [16:1 / 22:5]
883.5	PI [38:5]	0.050	0.413	0.245	0.138	0.187	0.342	0.236	0.123	0.910	PI [18:1 / 20:4]
885.5	PI [38:4]	0.290	1.950	1.164	0.694	0.945	1.662	1.155	0.624	0.869	PI [18:0 / 20:4]
891.6	PI [38:1]	0.000	0.002	0.001	0.001	0.001	0.002	0.001	0.001	0.859	PI [20:1 / 18:0]
907.5	PI [40:7]	0.002	0.017	0.010	0.005	0.008	0.015	0.010	0.005	0.814	PI [18:1 / 22:6]
909.5	PI [40:6]	0.017	0.128	0.071	0.039	0.061	0.110	0.072	0.043	0.793	PI [22:6 / 18:0]
913.6	PI [40:4]	0.002	0.012	0.008	0.005	0.007	0.012	0.008	0.005	0.618	PI [18:0 / 22:4]
483.3	LPG [16:0]	0.001	0.005	0.005	0.002	0.002	0.006	0.004	0.002	0.804	None
507.3	LPG [18:2]	0.000	0.001	0.001	0.000	0.000	0.001	0.001	0.000	0.515	None
509.3	LPG [18:1]	0.004	0.016	0.013	0.008	0.006	0.016	0.014	0.008	0.881	None
511.3	LPG [18:0]	0.000	0.001	0.001	0.000	0.000	0.001	0.001	0.000	0.628	None
531.3	LPG [20:4]	0.000	0.002	0.003	0.002	0.001	0.003	0.002	0.001	0.849	None
555.3	LPG [22:6]	0.001	0.005	0.004	0.003	0.002	0.006	0.004	0.002	0.791	None
716.5	PE [34:1]	0.007	0.015	0.012	0.007	0.009	0.017	0.013	0.009	0.624	PE [18:1 / 16:0]
730.5	PE [35:1]	0.011	0.020	0.015	0.010	0.000	0.001	0.000	0.000	0.229	PE [17:1 / 18:0]
744.6	PE [36:1]	0.016	0.025	0.017	0.013	0.012	0.020	0.016	0.011	0.751	PE [18:0 / 18:1], PE [20:1 / 16:0]
762.5	PE [38:6]	0.007	0.019	0.012	0.008	0.011	0.014	0.018	0.014	0.959	PE [22:6 / 16:0], PE [20:4 / 18:2]
764.5	PE [38:5]	0.038	0.079	0.054	0.038	0.047	0.064	0.052	0.037	0.875	PE [20:4 / 18:1]
766.5	PE [38:4]	0.001	0.002	0.001	0.001	0.001	0.002	0.002	0.001	0.830	PE [20:4 / 18:0], PE [22:4 / 16:0], PE [18:1 / 20:3]
772.6	PE [40:7]	0.005	0.002	0.002	0.003	0.004	0.001	0.001	0.004	0.507	PE [18:0 / 20:1]
788.5	PE [40:6]	0.062	0.122	0.081	0.058	0.080	0.104	0.082	0.059	0.714	PE [22:6 / 18:1]
790.5	PE [40:5]	0.002	0.007	0.004	0.002	0.003	0.005	0.004	0.003	0.967	PE [22:6 / 18:0]
792.6	PE [40:4]	0.005	0.011	0.008	0.006	0.007	0.010	0.008	0.005	0.919	PE [22:4 / 18:1], PE [20:4 / 20:1], PE [18:0 / 22:5]
794.6	PE [42:7]	0.000	0.001	0.001	0.001	0.000	0.001	0.001	0.000	0.943	PE [22:4 / 18:0]
816.6	PE [42:6]	0.000	0.001	0.000	0.001	0.000	0.001	0.001	0.000	0.820	PE [20:1 / 22:6]
818.6	PE [34:2]	0.010	0.021	0.011	0.008	0.011	0.013	0.012	0.011	0.647	PE [22:6 / 20:0]
700.5	PE-O [34:2]	0.004	0.007	0.004	0.003	0.004	0.004	0.004	0.003	0.793	PE-O [16:1 / 18:1]
722.5	PE-O [36:5]	0.020	0.045	0.022	0.016	0.023	0.029	0.025	0.019	0.450	PE-O [16:1 / 20:4]
726.5	PE-O [36:3]	0.014	0.026	0.014	0.011	0.016	0.019	0.018	0.015	0.794	PE-O [18:2 / 18:1]
728.6	PE-O [36:2]	0.001	0.001	0.001	0.001	0.001	0.001	0.001	0.001	0.891	PE-O [18:1 / 18:1]

746.5	PE-O [38:7]	0.016	0.034	0.018	0.015	0.019	0.022	0.019	0.017	0.726	PE-O [16:1 / 22:6]
748.5	PE-O [38:6]	0.007	0.009	0.002	0.004	0.007	0.004	0.004	0.003	0.613	PE-O [18:2 / 20:4]
750.5	PE-O [38:5]	0.018	0.037	0.019	0.016	0.020	0.024	0.021	0.017	0.759	PE-O [18:1 / 20:4], PE-O [16:1 / 22:4], PE-O [18:2 / 20:3]
774.5	PE-O [40:7]	0.030	0.061	0.032	0.026	0.039	0.041	0.035	0.029	0.882	PE-O [18:1 / 22:6]
776.6	PE-O [40:6]	0.007	0.015	0.008	0.006	0.009	0.011	0.009	0.007	0.937	PE-O [18:2 / 22:4]
778.6	PE-O [40:5]	0.007	0.015	0.008	0.007	0.009	0.011	0.009	0.007	0.935	PE-O [18:1 / 22:4]
<b>positive ion mode</b>											
703.6	SM [34:1:0]	0.014	0.017	0.014	0.011	0.014	0.015	0.015	0.015	0.486	
705.6	SM [33:1:1]	0.000	0.000		0.000	0.000	0.000	0.000	0.001	0.729	
731.6	SM [36:1:0]	0.363	0.418	0.343	0.296	0.339	0.364	0.364	0.382	0.794	
733.6	SM [36:0:0]	0.002	0.003	0.002	0.002	0.002	0.003	0.002	0.002	0.589	
745.6	SM [37:1:0]	0.001	0.001	0.001	0.000	0.000	0.000	0.000		0.252	
759.6	SM [38:1:0]	0.025	0.030	0.025	0.021	0.025	0.027	0.028	0.029	0.400	
787.7	SM [40:1:0]	0.008	0.012	0.010	0.008	0.011	0.013	0.013	0.012	0.069	
801.7	SM [41:1:0]	0.002	0.003	0.002	0.002	0.003	0.003	0.003	0.002	0.064	
805.7	SM [40:0:1]	0.001	0.001	0.001	0.001	0.001	0.001	0.001	0.001	0.581	
811.7	SM [42:3:0]	0.003	0.003	0.003	0.002	0.002	0.003	0.003	0.003	0.401	
815.7	SM [41:2:1]	0.000	0.001		0.000	0.000	0.000	0.000		0.403	
815.7	SM [42:1:0]	0.011	0.012	0.010	0.008	0.011	0.012	0.013	0.012	0.110	
584.5	DAG [32:1]	0.001	0.001	0.001	0.001	0.001	0.001	0.001	0.001	0.598	
586.5	DAG [32:0]	0.006	0.007	0.006	0.004	0.006	0.006	0.006	0.005	0.789	
610.5	DAG [34:2]	0.002	0.003	0.002	0.001	0.002	0.002	0.002	0.002	0.699	
612.6	DAG [34:1]	0.045	0.051	0.043	0.036	0.046	0.047	0.044	0.043	0.730	
614.6	DAG [34:0]	0.002	0.003	0.003	0.002	0.002	0.003	0.003	0.002	0.863	
634.5	DAG [36:4]	0.014	0.017	0.015	0.012	0.015	0.016	0.015	0.014	0.650	
636.6	DAG [36:3]	0.001	0.002	0.001	0.001	0.001	0.001	0.001		0.884	
638.6	DAG [36:2]	0.017	0.020	0.016	0.013	0.017	0.016	0.015	0.015	0.704	
640.6	DAG [36:1]	0.036	0.036	0.029	0.028	0.032	0.033	0.031	0.033	0.981	
658.5	DAG [38:6]	0.007	0.009	0.008	0.006	0.007	0.008	0.008	0.005	0.938	
660.6	DAG [38:5]	0.008	0.009	0.008	0.006	0.008	0.009	0.008	0.007	0.993	
662.6	DAG [38:4]	0.069	0.082	0.074	0.056	0.070	0.080	0.074	0.065	0.768	
664.6	DAG [38:3]	0.001	0.001	0.001	0.001	0.001	0.001	0.001	0.001	0.612	
666.6	DAG [38:2]	0.004	0.004	0.003	0.003	0.004	0.004	0.004	0.003	0.295	
668.6	DAG [38:1]	0.003	0.003	0.002	0.002	0.003	0.003	0.003	0.002	0.691	

686.6	DAG [40:6]	0.005	0.006	0.005	0.004	0.005	0.006	0.006	0.006	0.004	0.798
688.6	DAG [40:5]	0.001	0.001	0.001	0.001	0.001	0.001	0.001	0.001	0.000	0.595
690.6	DAG [40:4]	0.003	0.003	0.002	0.002	0.003	0.003	0.003	0.003	0.002	0.431
694.6	DAG [40:2]	0.001	0.001		0.000	0.001	0.001	0.000	0.000	0.000	0.486
564.5	Cer [36:2;0]	0.006	0.004	0.004	0.006	0.006	0.007	0.008	0.007	0.007	<b>0.015</b>
566.6	Cer [36:1;0]	0.034	0.036	0.031	0.027	0.027	0.030	0.033	0.029	0.029	0.351
594.6	Cer [38:1;0]	0.004	0.004	0.004	0.003	0.003	0.004	0.004	0.003	0.003	0.670
596.6	Cer [37:1;1]	0.001	0.000		0.000	0.000	0.000	0.000	0.000	0.000	0.101
620.6	Cer [40:2;0]	0.001	0.001	0.001	0.001	0.001	0.001	0.002	0.001	0.001	0.157
622.6	Cer [39:2;1]	0.001	0.001	0.001	0.001	0.001	0.001	0.001	0.000	0.000	0.258
624.6	Cer [39:1;1]	0.001	0.001	0.001	0.001	0.001	0.001	0.001	0.001	0.001	0.898
638.6	Cer [40:1;1]	0.000			0.000	0.000	0.000	0.000	0.000	0.001	0.089
648.6	Cer [42:2;0]	0.003	0.004	0.003	0.003	0.003	0.004	0.004	0.003	0.003	0.226
650.6	Cer [41:2;1]	0.001	0.000		0.000	0.000	0.000	0.000	0.000	0.000	0.321
652.6	Cer [41:1;1]	0.001	0.001		0.000	0.001	0.001	0.001	0.001	0.000	0.675
820.7	TAG [48:2]	0.001	0.004	0.002		0.001	0.001	0.001	0.001	0.001	0.134
822.8	TAG [48:1]	0.004	0.008	0.004	0.002	0.004	0.004	0.005	0.002	0.002	0.666
824.8	TAG [48:0]	0.012	0.013	0.010	0.007	0.011	0.011	0.015	0.008	0.008	0.799
846.8	TAG [50:3]	0.003	0.012	0.006	0.001	0.002	0.003	0.001	0.003	0.003	0.234
848.8	TAG [50:2]	0.010	0.024	0.012	0.005	0.008	0.011	0.008	0.006	0.006	0.311
850.8	TAG [50:1]	0.026	0.029	0.021	0.015	0.023	0.026	0.029	0.016	0.016	0.857
852.8	TAG [50:0]	0.012	0.009	0.009	0.007	0.010	0.011	0.014	0.007	0.007	0.631
872.8	TAG [52:4]	0.009	0.021	0.011	0.004	0.007	0.010	0.006	0.006	0.006	0.339
876.8	TAG [52:2]	0.003	0.022	0.011	0.006	0.012	0.015	0.016	0.006	0.006	0.698
878.8	TAG [52:1]	0.016	0.014	0.011	0.009	0.014	0.015	0.017	0.008	0.008	0.697
880.8	TAG [52:0]	0.004	0.003	0.002	0.002	0.003	0.003	0.004	0.001	0.001	0.847
898.8	TAG [54:5]	0.008	0.015	0.008	0.003	0.006	0.010	0.008	0.004	0.004	0.544
900.8	TAG [54:4]	0.012	0.020	0.011	0.006	0.010	0.013	0.010	0.007	0.007	0.517
902.8	TAG [54:3]	0.008	0.013	0.006	0.003	0.006	0.008	0.005	0.003	0.003	0.407
904.8	TAG [54:2]	0.006	0.007	0.004	0.003	0.006	0.006	0.007	0.003	0.003	0.713
906.8	TAG [54:1]	0.002	0.001	0.001	0.001	0.001	0.002	0.002			0.141
920.8	TAG [56:8]	0.002	0.001	0.001	0.000	0.001	0.002	0.001			0.222
922.8	TAG [56:7]	0.021	0.019	0.013	0.011	0.018	0.022	0.022	0.010	0.010	0.625
926.8	TAG [56:5]	0.005	0.005	0.003	0.002	0.005	0.005	0.005	0.002	0.002	0.573
928.8	TAG [56:4]	0.003	0.002	0.001	0.001	0.002	0.003	0.003	0.003	0.001	0.608



948.8	TAG [58:8]	0.003	0.002	0.001	0.001	0.002	0.004	0.003	0.001	0.335
950.8	TAG [58:7]	0.004	0.003	0.001	0.001	0.003	0.003	0.004	0.001	0.577
726.6	GlcCer [36:2;0]	0.001	0.000	0.001	0.000	0.001	0.001	0.001	0.001	0.052
728.6	GlcCer [36:1;0]	0.007	0.008	0.007	0.006	0.008	0.009	0.010	0.009	<b>0.011</b>
744.6	GlcCer [36:1;1]	0.006	0.007	0.006	0.005	0.006	0.007	0.007	0.007	<b>0.045</b>
754.6	GlcCer [38:2;0]	0.001	0.001	0.001	0.000	0.000	0.001	0.001	0.001	0.413
756.6	GlcCer [38:1;0]	0.001	0.001	0.001	0.001	0.001	0.002	0.002	0.002	<b>0.003</b>
772.6	GlcCer [38:1;1]	0.008	0.009	0.007	0.006	0.007	0.008	0.009	0.009	0.590
780.6	GlcCer [40:3;0]	0.000	0.000	0.000	0.000	0.000	0.000	0.000	0.000	0.697
782.7	GlcCer [40:2;0]	0.014	0.016	0.013	0.011	0.015	0.017	0.016	0.015	0.108
784.7	GlcCer [40:1;0]	0.008	0.011	0.008	0.007	0.011	0.013	0.014	0.014	<b>0.005</b>
786.7	GlcCer [40:0;0]	0.001	0.001	0.001	0.000	0.001	0.001	0.001	0.001	0.174
796.7	GlcCer [41:2;0]	0.007	0.008	0.006	0.005	0.006	0.007	0.007	0.005	0.690
798.6	GlcCer [40:2;1]	0.006	0.008	0.006	0.005	0.006	0.007	0.007	0.007	0.556
798.7	GlcCer [41:1;0]	0.005	0.006	0.005	0.004	0.006	0.007	0.007	0.006	<b>0.030</b>
800.7	GlcCer [40:1;1]	0.082	0.096	0.077	0.064	0.085	0.096	0.097	0.097	0.102
802.7	GlcCer [40:0;1]	0.008	0.010	0.007	0.005	0.007	0.008	0.008	0.008	0.956
808.7	GlcCer [42:3;0]	0.009	0.010	0.008	0.007	0.010	0.011	0.011	0.011	<b>0.037</b>
810.7	GlcCer [42:2;0]	0.109	0.125	0.099	0.081	0.114	0.130	0.134	0.126	0.068
812.7	GlcCer [42:1;0]	0.005	0.004	0.003	0.003	0.009	0.010	0.009	0.007	<b>0.001</b>
814.7	GlcCer [41:1;1]	0.037	0.044	0.037	0.028	0.034	0.037	0.040	0.038	0.859
814.7	GlcCer [42:0;0]	0.001	0.001	0.000	0.000	0.001	0.001	0.001	0.001	0.441
824.7	GlcCer [42:3;1]	0.006	0.003	0.003	0.001	0.003	0.003	0.003	0.003	0.687
826.7	GlcCer [42:2;1]	0.054	0.071	0.055	0.041	0.051	0.057	0.061	0.057	0.864
828.7	GlcCer [42:1;1]	0.076	0.091	0.072	0.059	0.083	0.092	0.096	0.090	0.074
830.7	GlcCer [42:0;1]	0.002	0.002	0.002	0.001	0.002	0.002	0.002	0.002	0.829
840.7	GlcCer [43:2;1]	0.001	0.001	0.001	0.001	0.001	0.001	0.001	0.001	0.156
704.5	PC [30:1]	0.000	0.001	0.000	0.000	0.000	0.001	0.001	0.000	0.447
706.5	PC [30:0]	0.048	0.054	0.044	0.037	0.046	0.056	0.057	0.047	0.268
730.5	PC [32:2]	0.003	0.005	0.003	0.003	0.003	0.004	0.004	0.003	0.619
732.6	PC [32:1]	0.244	0.283	0.234	0.188	0.249	0.305	0.309	0.241	0.195
734.6	PC [32:0]	2.880	3.071	2.520	2.225	2.776	3.152	3.344	2.824	0.182
758.6	PC [34:2]	0.179	0.220	0.157	0.118	0.202	0.243	0.199	0.151	0.326
760.6	PC [34:1]	6.096	6.816	5.542	4.661	6.021	6.886	7.160	5.755	0.277
780.6	PC [36:5]	0.046	0.035	0.029	0.020	0.031	0.036	0.031	0.031	0.945

782.6	PC [36:4]	2.304	1.784	1.526	1.272	1.576	1.691	1.823	1.574	0.816
784.6	PC [36:3]	0.174	0.120	0.097	0.074	0.121	0.135	0.127	0.109	0.761
786.6	PC [36:2]	0.579	0.672	0.545	0.433	0.583	0.663	0.686	0.515	0.421
788.6	PC [36:1]	2.068	2.277	1.801	1.557	1.966	2.301	2.361	1.876	0.349
802.5	PC [38:8]	0.004	0.002	0.002	0.001	0.002	0.002	0.002	0.002	0.630
806.6	PC [38:6]	1.062	1.213	1.015	0.809	1.097	1.274	1.279	0.982	0.272
808.6	PC [38:5]	0.388	0.385	0.327	0.265	0.317	0.357	0.377	0.298	0.905
810.6	PC [38:4]	1.482	1.317	1.094	0.944	1.158	1.283	1.344	1.076	0.967
812.6	PC [38:3]	0.020	0.023	0.019	0.016	0.026	0.029	0.030	0.024	<b>0.009</b>
814.6	PC [38:2]	0.082	0.097	0.076	0.059	0.084	0.099	0.102	0.077	0.267
816.6	PC [38:1]	0.082	0.089	0.069	0.057	0.081	0.098	0.101	0.075	0.169
818.7	PC [38:0]	0.000	0.000			0.001	0.001	0.001	0.000	0.247
830.6	PC [40:8]	0.068	0.044	0.036	0.029	0.037	0.040	0.038	0.035	0.460
832.6	PC [40:7]	0.420	0.359	0.296	0.246	0.324	0.366	0.368	0.279	0.934
834.6	PC [40:6]	0.707	0.783	0.650	0.544	0.734	0.822	0.835	0.628	0.274
836.6	PC [40:5]	0.043	0.045	0.036	0.029	0.037	0.040	0.043	0.033	0.979
838.6	PC [40:4]	0.078	0.077	0.064	0.053	0.069	0.078	0.081	0.064	0.500
840.6	PC [40:3]	0.001	0.001	0.001	0.001	0.001	0.002	0.002	0.001	0.059
842.7	PC [40:2]	0.020	0.024	0.020	0.015	0.022	0.027	0.026	0.020	0.140
844.7	PC [40:1]	0.018	0.021	0.017	0.013	0.023	0.028	0.026	0.020	<b>0.031</b>
858.6	PC [42:8]	0.013	0.011	0.009	0.007	0.010	0.010	0.010	0.008	0.661
860.6	PC [42:7]	0.033	0.032	0.025	0.020	0.028	0.032	0.033	0.024	0.721
864.6	PC [42:5]	0.007	0.006	0.005	0.004	0.006	0.007	0.007	0.005	0.660
870.7	PC [42:2]	0.014	0.016	0.012	0.010	0.016	0.021	0.019	0.015	0.059
872.7	PC [42:1]	0.014	0.015	0.011	0.010	0.018	0.023	0.021	0.016	<b>0.018</b>
494.3	LPC [16:1]	0.000	0.001	0.003	0.001	0.001	0.003	0.002	0.001	0.728
496.3	LPC [16:0]	0.053	0.067	0.087	0.051	0.055	0.092	0.080	0.063	0.514
520.3	LPC [18:2]	0.000	0.001	0.001	0.000	0.001	0.001	0.001	0.000	0.514
522.4	LPC [18:1]	0.029	0.039	0.054	0.027	0.031	0.062	0.049	0.032	0.543
524.4	LPC [18:0]	0.020	0.023	0.024	0.017	0.019	0.026	0.025	0.022	0.443
550.4	LPC [20:1]	0.001	0.002	0.004	0.001	0.001	0.004	0.003	0.001	0.571
568.3	LPC [22:6]	0.010	0.015	0.017	0.009	0.011	0.019	0.017	0.011	0.566
572.4	LPC [22:4]	0.000	0.000	0.001	0.000	0.000	0.001	0.001	0.001	0.372
714.5	PC-O [32:3]	0.001	0.002	0.001	0.001	0.001	0.001	0.001	0.001	0.461
716.6	PC-O [32:2]	0.004	0.006	0.004	0.003	0.003	0.002	0.002	0.003	0.080

718.6	PC-O [32:1]	0.015	0.016	0.011	0.010	0.013	0.013	0.015	0.013	0.724
720.6	PC-O [32:0]	0.022	0.023	0.019	0.016	0.019	0.023	0.024	0.020	0.498
738.5	PC-O [34:5]	0.003	0.003	0.003	0.002	0.001	0.001	0.001	0.002	<b>0.012</b>
740.6	PC-O [34:4]	0.003	0.003	0.002	0.002	0.002	0.002	0.002	0.003	0.830
742.6	PC-O [34:3]	0.006	0.006	0.004	0.004	0.004	0.004	0.004	0.005	0.427
744.6	PC-O [34:2]	0.017	0.022	0.013	0.011	0.015	0.015	0.015	0.015	0.742
746.6	PC-O [34:1]	0.069	0.080	0.065	0.049	0.064	0.076	0.079	0.063	0.568
748.6	PC-O [34:0]	0.012	0.013	0.011	0.009	0.011	0.013	0.013	0.011	0.541
764.6	PC-O [36:6]	0.002	0.002	0.001	0.001	0.001	0.001	0.001	0.002	0.325
766.6	PC-O [36:5]	0.008	0.008	0.006	0.006	0.006	0.006	0.006	0.007	0.407
768.6	PC-O [36:4]	0.020	0.016	0.013	0.010	0.013	0.013	0.014	0.012	0.491
770.6	PC-O [36:3]	0.010	0.012	0.008	0.007	0.008	0.009	0.008	0.009	0.548
772.6	PC-O [36:2]	0.014	0.014	0.009	0.008	0.012	0.012	0.013	0.011	0.563
774.6	PC-O [36:1]	0.010	0.012	0.010	0.007	0.011	0.012	0.013	0.010	0.238
790.6	PC-O [38:7]	0.006	0.007	0.005	0.004	0.005	0.005	0.005	0.006	0.656
794.6	PC-O [38:5]	0.006	0.007	0.005	0.004	0.006	0.006	0.007	0.004	0.921
796.6	PC-O [38:4]	0.005	0.004	0.004	0.003	0.003	0.004	0.004	0.003	0.611
798.6	PC-O [38:3]	0.002	0.004	0.002	0.001	0.002	0.002	0.002	0.001	0.480
800.7	PC-O [38:2]	0.001	0.001	0.000	0.000		0.000	0.000		0.448
804.7	PC-O [38:0]	0.000	0.000		0.000	0.000	0.001	0.001	0.001	<b>0.043</b>
816.6	PC-O [40:8]	0.001	0.001	0.000		0.001	0.000	0.001		0.366
818.6	PC-O [40:7]	0.002	0.003	0.002	0.002	0.002	0.002	0.003	0.001	0.645

This data was generated in collaboration with Dr. Dominik Schwudke from the Research Center Borstel, Germany.

## 7 LIST OF FIGURES AND TABLES

### 7.1 List of figures

Figure 1   <i>Schematic representation of lysosomal protein sorting</i> .....	4
Figure 2   <i>Schematic representation of carboxypeptidase S (CPS) biogenesis</i> .....	6
Figure 3   <i>Scheme of ubiquitin-dependent sorting of proteins by the ESCRT machinery</i> .....	8
Figure 4   <i>Schematic diagram of selective delivery of DNA and RNA to lysosomes</i> .....	10
Figure 5   <i>Domain alignment of different PLD superfamily enzymes</i> . ....	13
Figure 6   <i>Schematic representation of CRISPR-Cas9 plasmid for the generation of stable PLD3-deficient HeLa cells</i> .....	34
Figure 7   <i>Isolation of hippocampus and cortex</i> .....	37
Figure 8   <i>Schematic representation of the gene-trap cassette for the generation of Pld3 KO mice</i> .....	47
Figure 9   <i>Schematic representation of 5xFAD Pld3<sup>-/-</sup> mice</i> .....	47
Figure 10   <i>Western blot analysis of PLD3 transfected cells</i> . ....	55
Figure 11   <i>PLD3 localizes to late endosomes and lysosomes</i> .....	57
Figure 12   <i>Endogenous PLD3 localizes to lysosomes</i> . ....	59
Figure 13   <i>PLD3 is N-glycosylated</i> . ....	60
Figure 14   <i>PLD3 is N-glycosylated at multiple sites</i> .....	61
Figure 15   <i>Reducing conditions do not affect the generation of PLD3 cleavage products</i> . .....	62
Figure 16   <i>Membrane separation of PLD3 transfected HeLa cells</i> .....	63
Figure 17   <i>Membrane-bound and soluble PLD3 show different compartmentalization in lysosomes</i> . ....	64
Figure 18   <i>PLD3 shows distinct subcellular distribution as visualized by Percoll density centrifugation experiment</i> . ....	65
Figure 19   <i>Proteolytic processing of PLD3 is mediated by acidic cysteine proteases</i> .....	66
Figure 20   <i>Confocal images of PLD3-transfected HeLa cells with different inhibitors</i> .....	68
Figure 21   <i>Degradation of PLD3 N-terminus is mediated by cathepsin B and L</i> .....	69
Figure 22   <i>PLD3 is partially sorted to the plasma membrane (PM)</i> .....	70
Figure 23   <i>PLD3 is localized to ILVs of MVBs</i> .....	72

---

Figure 24   <i>PLD3 reaches lysosomes in CD63 deficient MEFs.</i> .....	73
Figure 25   <i>Effect of the ceramide inhibitor GW4869 on the processing and localization of PLD3.</i> .....	73
Figure 26   <i>PLD3 is transported to MVBs dependent on PtdIns(3)P.</i> .....	75
Figure 27   <i>PLD3 is retained in intracellular membranes upon co-expression of Hrs</i> .....	77
Figure 28   <i>PLD3 processing is altered upon co-expression with Hrs.</i> .....	77
Figure 29   <i>PLD3 transport to lysosomes is altered upon co-expression with Vps4a.</i> .....	78
Figure 30   <i>PLD3 processing is altered upon co-expression with Vps4a.</i> .....	79
Figure 31   <i>PLD3 processing and localization is altered upon Hrs knockdown.</i> .....	80
Figure 32   <i>PLD3 is ubiquitinated.</i> .....	81
Figure 33   <i>PLD3 is ubiquitinated at multiple lysine (K) residues.</i> .....	82
Figure 34   <i>PLD3 ubiquitination is altered after mutation of all N-terminal lysine (K) residues.</i> .....	83
Figure 35   <i>Lysine residue 11 (K11) might be a key residue of PLD3 ubiquitination.</i> .....	84
Figure 36   <i>Pld3 is highly expressed in the brain.</i> .....	85
Figure 37   <i>Pld3 is expressed in the spleen.</i> .....	86
Figure 38   <i>Pld3 is mainly expressed in the cortex and the hippocampus.</i> .....	87
Figure 39   <i>Image stitching of Pld3 expression in the brain.</i> .....	88
Figure 40   <i>Pld3 is mainly expressed in neuronal cells.</i> .....	90
Figure 41   <i>Pld3 is highly expressed in neurons.</i> .....	90
Figure 42   <i>Pld3 is hardly expressed in microglia cells.</i> .....	91
Figure 43   <i>Pld3 KO mice have reduced lysosomal enzyme activity.</i> .....	93
Figure 44   <i>Pld3 KO mice show localized microglia activation in the dentate gyrus.</i> .....	94
Figure 45   <i>Pld3 KO mice have increased immunoreactivity of microglia and astrocytes markers.</i> .....	95
Figure 46   <i>Pld3 KO mice show normal neurogenesis and cell proliferation.</i> .....	96
Figure 47   <i>Pld3 KO mice show normal neuromotor and cognitive function.</i> .....	100
Figure 48   <i>Pld3 KO mice show a depression-like behavior.</i> .....	100
Figure 49   <i>High-throughput lipidomics analysis of WT and KO Pld3 mice.</i> .....	102
Figure 50   <i>Schematic representation of sgRNA target site of the human PLD3 gene.</i> ....	103
Figure 51   <i>Validation of HeLa CRISPR-Cas9 clones.</i> .....	104
Figure 52   <i>PLD3 KO HeLa cells do not show any morphological alterations in intracellular organelles.</i> .....	105

---

Figure 53   <i>WT HeLa cells have endogenous PLD3 5'-nuclease activity.</i> .....	107
Figure 54   <i>PLD3-HKD motif mutants have altered nuclease activity.</i> .....	108
Figure 55   <i>PLD3 nuclease activity is not cleavage-dependent.</i> .....	109
Figure 56   <i>PLD3 nuclease activity is enhanced by EDTA and Ca<sup>2+</sup>.</i> .....	110
Figure 57   <i>PLD3 nuclease activity is inhibited by vanadate (Na<sub>3</sub>VO<sub>4</sub>).</i> .....	111
Figure 58   <i>Pld3 is the main 5'-nuclease in the brain.</i> .....	112
Figure 59   <i>5'-nuclease activity is abolished in the Pld3 KO mouse brain.</i> .....	113
Figure 60   <i>Schematic representation of different PLD3 coding variants.</i> .....	114
Figure 61   <i>AD-related mutants exhibit differential PLD3 proteolytic processing.</i> .....	115
Figure 62   <i>AD-related mutants PLD3 K228R and N236S have abrogated delivery of PLD3 to lysosomes.</i> .....	117
Figure 63   <i>AD-related mutants PLD3 K228R and N236S have decreased 5'-exonuclease activity.</i> .....	117
Figure 64   <i>APP processing is not affected in Pld3 deficient mice.</i> .....	119
Figure 65   <i>APP processing is not affected in 5xFAD Pld3<sup>-/-</sup> mice.</i> .....	119
Figure 66   <i>Pld3 accumulates within the same brain regions as amyloid beta (A<math>\beta</math>) plaques.</i> .....	122
Figure 67   <i>Pld3 accumulates around amyloid beta (A<math>\beta</math>) plaques in the cortex, the thalamus and the subiculum in 5x FAD mice.</i> .....	122
Figure 68   <i>The spinocerebellar ataxia variant PLD3 L308P is localized in the ER.</i> .....	123
Figure 69   <i>The PLD3 L308P variant shows altered proteolytic processing.</i> .....	124
Figure 70   <i>Nuclease activity of the PLD3 L308P variant is impaired.</i> .....	125
Figure 71   <i>Pld3 deficient mice do not show cerebellar alterations.</i> .....	125
Figure 72   <i>Behavior analyses of Pld3 deficient mice do not show any sign of cerebellar dysfunction.</i> .....	126
Figure 73   <i>Schematic representation of PLD3 proteolytic processing.</i> .....	132
Figure 74   <i>Schematic representation of PLD3 transport and its route to lysosomes.</i> .....	138

## 7.2 List of tables

Table 1. <i>List of laboratory chemicals</i> .....	18
Table 2. <i>List of reagents, solutions, media and buffers</i> .....	19
Table 3. <i>List of cell lines</i> .....	20
Table 4. <i>List of transgenic mouse lines</i> .....	21
Table 5. <i>List of primary antibodies</i> .....	21
Table 6. <i>List of secondary antibodies</i> .....	22
Table 7. <i>List of protein and DNA standards</i> .....	23
Table 8. <i>List of enzymes</i> .....	23
Table 9. <i>List of artificial substrates for lysosomal enzyme activity</i> .....	23
Table 10. <i>List of plasmids</i> .....	24
Table 11. <i>List of expression constructs</i> .....	24
Table 12. <i>Oligonucleotides used for genotyping</i> .....	25
Table 13. <i>Oligonucleotides used for site directed mutagenesis</i> .....	26
Table 14. <i>Oligonucleotide used for nuclease activity assay</i> .....	28
Table 15. <i>List of equipment</i> .....	28
Table 16. <i>List of software</i> .....	29
Table 17. <i>List of consumables</i> .....	29
Table 18. <i>List of commercial kits</i> .....	30
Table 19. <i>siRNA transfection volumes per dish/well</i> .....	34
Table 20. <i>Composition of SDS polyacrylamide gels</i> .....	43
Table 21. <i>PCR components for genotyping determination</i> .....	48
Table 22. <i>PCR cycle conditions applied for genotyping</i> .....	49
Table 23. <i>List of lipid species after high- throughput lipidomics analysis between WT and Pld3 KO mouse brain</i> .....	180

## 8 DECLARATION

Herewith I declare that:

Apart from the supervisor's guidance, I have prepared the present thesis autonomously and only using the sources listed.

This thesis has not been submitted partially or wholly as part of a doctoral degree to another examining body.

This thesis has been prepared in accordance with the Rules of Good Scientific Practice of the German Research Foundation.

No academic degree has been withdrawn.

Part of this work have been published in the following articles:

**Gonzalez, A. C., Schweizer, M., Jagdmann, S., Bernreuther, C., Reinheckel, T., Saftig, P. and Damme, M.** (2018). Unconventional Trafficking of Mammalian Phospholipase D3 to Lysosomes. *Cell Rep.* **22**, 1040–1053.

**Gonzalez, A. C., Stroobants, S., Reisdorf, P., Gavin, A. L., Nemazee, D., Schwudke, D., D'Hooge, R., Saftig, P. and Damme, M.** (2018). PLD3 and spinocerebellar ataxia. *Brain* **141**, e78–e78.





## 9 CURRICULUM VITAE

### Adriana Gonzalez

Olshausenstr. 12

24118 Kiel

Born: 12<sup>th</sup> May 1988 in Caracas (Venezuela)

### *Education*

Since May 2015 **PhD student** in the working group of Prof. Dr. Paul Saftig and PD. Dr. Markus Damme, Biochemical Institute, University of Kiel.

*2015-2017: Member of the Research Training Group 1459: Sorting and Interaction between Proteins of Subcellular Compartments*

*Title: Biochemical characterization and functional analysis of phospholipase D3 (PLD3)*

09/2012-01/2015 **M.Sc. Molecular Cell Biology and Neurobiology**  
University of Kaiserslautern

*Title: Transport analysis of the amyloid precursor protein (APP) after induced dimerization and ubiquitination analysis of APLP2*

09/2005-11/2010 **B.Sc. Biology**

“Simon Bolivar” University, Caracas, Venezuela

*Title: Molecular study of CFTR gene mutations in Venezuelan patients with cystic fibrosis*

## 10 PUBLICATIONS AND SCIENTIFIC PARTICIPATION

### *Publications*

**Gonzalez, A. C.**, Stroobants, S., Reisdorf, P., Gavin, A. L., Nemazee, D., Schwudke, D., D'Hooge, R., Saftig, P. and Damme, M. (2018). PLD3 and spinocerebellar ataxia. *Brain* 141, e78–e78.

**Gonzalez, A. C.**, Schweizer, M., Jagdmann, S., Bernreuther, C., Reinheckel, T., Saftig, P. and Damme, M. (2018). Unconventional Trafficking of Mammalian Phospholipase D3 to Lysosomes. *Cell Rep.* 22, 1040–1053.

Eggert, S., **Gonzalez, A. C.\***, Thomas, C., Schilling, S., Schwarz, S. M., Tischer, C., Adam, V., Strecker, P., Schmidt, V., Willnow T. E., Hermey, G., Pietrzik, C. U., Koo, E. H., Kins, S. (2018). Dimerization leads to changes in APP (amyloid precursor protein) trafficking mediated by LRP1 and SorLA. *Cellular and Molecular Life Science*, Jan; 75(2):301-322.

\*Eggert S and Gonzalez AC are first authors and contributed equally to this work

### *Participation in meetings*

05/2018 ***EMBO Workshop on Lysosomes and Metabolism***

Telethon Institute of Genetics and Medicine (TIGEM), Naples, Italy (Poster presentation)

10/2017 ***17<sup>th</sup> Eibsee Meeting on Cellular Mechanisms of Neurodegeneration***

German Center for Neurodegenerative Diseases, Munich, Germany.  
Participation as part of the Awarded Alzheimer Research Scholarship (Poster presentation)

06/2017 ***4<sup>th</sup> International Symposium on Protein Trafficking in Health and Disease***

University Medical Center, Hamburg-Eppendorf, Germany (Poster presentation, 1<sup>st</sup> poster prize)

- 
- 03/2017 ***Gordon Research Seminar and Conference on Lysosomal Diseases***  
Barga, Italy (Poster presentation)
- 09/2016 ***13<sup>th</sup> Horizons in Molecular Biology***  
Max Plack Institute for Biophysical Chemistry, Göttingen, Germany (Awarded Student Talk & Poster presentation)
- 10/2013 ***EMBO/EMBL Symposium***  
Seeing is Believing – Imaging the Processes of Life, EMBL Heidelberg, Germany

### ***Scientific awards***

- 2017-current ***Awarded Alzheimer Research Scholarship***  
The Hans and Ilse Breuer Foundation, Germany.
- 06/2017 ***1<sup>st</sup> poster prize***  
4<sup>th</sup> International Symposium on Protein Trafficking in Health and Disease, University Medical Center, Hamburg, Germany
- 09/2016 ***Awarded Student Talk***  
13<sup>th</sup> Horizons in Molecular Biology, Max Planck Institute for Biophysical Chemistry, Göttingen, Germany



## 11 ACKNOWLEDGEMENTS

This journey has come to an end...

I want to specially thank my supervisors Dr. Markus Damme and Prof. Dr. Paul Saftig for giving me the opportunity to do my PhD in your lab and work in such an exciting project. Thanks for the enriched discussions, ideas, advice and for all the support behind the preparation of my thesis, I really appreciate it. I have certainly learned a lot from both of you.

Thanks to Prof. Dr. Thomas Röder for being the second supervisor of my thesis.

I want to thank all the members of the GRK1459 Research group, where I participated in the first two years of my PhD. Special thanks to Dr. Dorthé Labonté and Prof. Dr. Thomas Braulke for the coordination and organization of the seminars, practical courses, workshops and symposia. Thanks to the group for the amazing moments and the scientific talks. For all you, all the success in your further scientific career.

Special thanks to all the members of the 'Hans und Ilse Breuer Stiftung-Alzheimer Forschungs und Hilfe' for financing the last two years of my PhD.

Thanks to all the collaboration partners and institutions for their contributions to this work: The Immunology department at the University Hospital Schleswig-Holstein, Dr. Michaela Schweizer, Dr. Christian Bernreuther, Dr. Thomas Reinheckel, Dr. Stijn Stroobants, Dr. Dominik Schwudke, Dr. Ole Tollersrud, Dr. Amanda Gavin and Dr. David Nemazee.

Thanks to all the previous and actual members of the AG Saftig. What a wonderful group. David, Marlies, Florencia, Andrè and Cedric, you made my days much brighter and joyful in the lab. Maike, thanks for the support with experiments. Saskia and Lisor, my office buddies, thanks for all the nice chats and for helping me improve my German. Also for all of you, all the success, I know we will meet again 😊

I want to thank my family and friends. Even kilometres away, I have felt your support and love. Dani, thanks for sharing with me part of this Journey. Martha, gracias por apoyarme en estos últimos meses y estar a mi lado en las buenas y en las malas. Gracias Madre por tu amor incondicional y apoyo, sin tí, no estaría aquí.

*Gracias a todos*